Dissertation

submitted to the

Combined Faculty of Mathematics, Engineering and Natural Sciences

of Heidelberg University, Germany

for the degree of

Doctor of Natural Sciences

Put forward by

Alexander Magunia

born in Recklinghausen, Germany

Oral examination: July 19th, 2024

Time-and-Energy–Resolved Electron Dynamics in Atoms and Molecules with Intense Short-Wavelength Light

Referees: Prof. Dr. Thomas Pfeifer

Prof. Dr. Markus Oberthaler

Towards a future as bright
as our laser pulses,
and as rich in possibilities
as our quantum states.

Zusammenfassung: Zeit- und Energie-Aufgelöste Elektronen-Dynamik in Atomen und Molekülen mit Intensiven Kurzwelligem Licht

In dieser Arbeit wird die Wechselwirkung von ultrakurzen, extrem ultravioletten (XUV) und weichen Röntgen-Laserpulsen mit Atomen und Molekülen in der Gasphase untersucht. Insgesamt wird das Thema aus vier verschiedenen Blickwinkeln erforscht, die alle auf den kurzlebig-kohärenten elektonischen Reaktionen auf die Laserpulse basieren, sowie mit transienter Absorptionsspektroskopie gemessen werden. Erstens zeigt eine theoretische Studie, wie transiente Energieverschiebungen elektronischer Dressed-States in Atomen, die durch einen intensiven XUV-Freie-Elektronen-Laser (FEL) erzeugt werden, zu zeitlichen Dipolphasenverschiebungen und Absorptionslinienänderungen führen. Zweitens werden in einer Folgestudie die Rabi-Zyklen der elektronischen Populationen untersucht, die den Absorptionslinienänderungen der ersten Studie entsprechen. Ein faltendes neuronales Netzwerk wird eingesetzt, um die zeitliche Populationsdynamik aus den simulierten spektralen Absorptionsänderungen zu rekonstruieren. Die Inversion von einer Absorptions- zu einer Emissionslinie wird beschrieben und ein möglicher experimenteller Nachweis in Helium wird diskutiert. Drittens ermöglichen dichte Gase die Verstärkung des ansonsten unwahrscheinlichen, und nichtlinearen Prozesses der stimulierten resonanten inelastischen Röntgenstreuung (engl.: RIXS), sowie eine auf Propagationseffekte basierende räumlich-spektrale Umformung der FEL Pulse. Zu diesem Zweck ist ein neuer Versuchsapparat aufgebaut worden, welcher in einem Röntgen-FEL RIXS-Experiment in dichtem Neongas eingesetzt wurde. Viertens wird ein neuartiges Experiment zur Kombination von XUV-Pulsen aus der Erzeugung von hohen Harmonischen und XUV-FEL-Pulsen demonstriert, bei dem eine photochemische Reaktion in molekularem Sauerstoff zeitlich aufgelöst wird. Ein FEL Puls initiiert Dissoziationsprozesse mit der gekoppelten Kern- und Elektronenbewegung der molekularen Sauerstoffionen, die auf Femto- und Pikosekunden-Zeitskalen aufgelöst werden, indem die Reaktionsprodukte in den Absorptionsspektren der zeitlich verzögerten hohen Harmonischen identifiziert werden. Eine FEL-Photonenenergie aufgelöste Studie der Fragmente wird durchgeführt, um die Ergebnisse der Absorptionsspektroskopie mit kinetischen Energiespektren zu vergleichen, die parallel mit einem Reaktionsmikroskop aufgenommen wurden.

Abstract: Time-and-Energy–Resolved Electron Dynamics in Atoms and Molecules with Intense Short-Wavelength Light

This thesis investigates the interaction of ultrashort, extreme-ultraviolet (XUV) and soft x-ray laser pulses with atoms and molecules in the gas phase. In total, the subject is explored from four different perspectives, which are all based on the short-lived–coherent electronic responses to the laser pulses, and measured with transient absorption spectroscopy. First, a theoretical study reveals how transient energy shifts of electronic dressed states in atoms driven by an intense XUV Free-Electron Laser (FEL) lead to temporal dipole phase shifts and absorption-line changes. Second, a follow-up study investigates the electronic-population Rabi-cycles corresponding to the absorption-line changes of the first study. A convolutional neural network is employed to reconstruct the temporal population dynamics from the simulated spectral absorption modifications. The inversion from an absorption to an emission line is described and a potential experimental demonstration in helium is discussed. Third, dense gas targets enable amplification of the otherwise improbable, non-linear process of stimulated resonant inelastic x-ray scattering (RIXS), as well as x-ray FEL propagation-based spatial-spectral reshaping. To this end, a new experimental setup is built and utilized in an x-ray FEL driven RIXS experiment in dense neon gas. Fourth, a novel experiment combining XUV pulses from high-order harmonic generation (HHG) and XUV-FEL pulses is demonstrated by time-resolving a photochemical reaction in molecular oxygen. An FEL pulse initiates coupled nuclear-electronic dissociation pathways from molecular oxygen ions, which are time-resolved on femto- and picosecond time scales by identifying the reaction products in the time-delayed HHG absorption spectra. A FEL-photon-energy–resolved study of the fragments is performed to compare findings from absorption spectroscopy with kinetic energy release spectra recorded in parallel with a reaction microscope.

List of Publications

This cumulative dissertation is based on the following three publications:

[1] Alexander Magunia et al. "Bound-State Electron Dynamics Driven by Near-Resonantly Detuned Intense and Ultrashort Pulsed XUV Fields"
Applied Sciences 10(18) 6153 (2020)
doi: 10.3390/APP10186153

[2] Daniel Richter, Alexander Magunia, Marc Rebholz, Christian Ott and Thomas Pfeifer "Electronic Population Reconstruction from Strong-Field-Modified Absorption Spectra with a Convolutional Neural Network"
Optics 5(1) 88–100 (2024)
doi: 10.3390/opt5010007

[3] Alexander Magunia et al. " Time-resolving state-specific molecular dissociation with XUV broadband absorption spectroscopy"
Science Advances 9(47) eadk1482 (2023)
doi: 10.1126/sciadv.adk1482

Further published results with own contribution can be found in:

[4] Christian Ott et al. "Strong-Field Extreme-Ultraviolet Dressing of Atomic Double Excitation"
Physical Review Letters 123(16) 163201 (2019)
doi: 10.1103/PhysRevLett.123.163201

[5] Yu He et al. "Direct manipulation of atomic excitation with intense extreme-ultraviolet laser fields"
Physical Review A 105(4) 043113 (2022)
doi: 10.1103/PhysRevA.105.043113

[6] Lennart Aufleger et al. "Pulse length effects on autoionizing states under the influence of intense SASE XUV fields"
Journal of Physics B: Atomic, Molecular and Optical Physics 53(23) 234002 (2020)
doi: 10.1088/1361-6455/ABBE2D

[7] Lennart Aufleger et al. "Line-shape broadening of an autoionizing state in helium at high XUV intensity"
New Journal of Physics 24(1) 013014 (2022)
doi: 10.1088/1367-2630/AC3B2E

[8] Michael Straub et al. "Differential Measurement of Electron Ejection after Two-Photon Two-Electron Excitation of Helium"
Physical Review Letters 129(18) 183204 (2022)
doi: 10.1103/PhysRevLett.129.183204

[9] Thomas Ding et al. "Nonlinear Coherence Effects in Transient-Absorption Ion Spectroscopy with Stochastic Extreme-Ultraviolet Free-Electron Laser Pulses"
Physical Review Letters 123(10) 103001 (2019)
doi: 10.1103/PhysRevLett.123.103001

[10] Thomas Ding et al. "XUV pump–XUV probe transient absorption spectroscopy at FELs"
Faraday Discussions 228 519-536 (2021)
doi: 10.1039/D0FD00107D

[11] Thomas Ding et al. "Measuring the frequency chirp of extreme-ultraviolet free-electron laser pulses by transient absorption spectroscopy"
Nature Communications 12(643) (2021)
doi: 10.1038/s41467-020-20846-1

[12] Marc Rebholz et al. "XUV-Initiated Dissociation Dynamics of Molecular Oxygen (O_2)"
Journal of Physical Chemistry A 125(47) 10138–10143 (2021)
doi: 10.1021/acs.jpca.1c06033

[13] Marc Rebholz et al. "All-XUV Pump-Probe Transient Absorption Spectroscopy of the Structural Molecular Dynamics of Di-iodomethane"
Physical Review X 11(3) 031001 (2021)
doi: 10.1103/PhysRevX.11.031001

[14] Patrick Rupprecht et al. "Laser Control of Electronic Exchange Interaction within a Molecule"
Physical Review Letters 128(15) 153001 (2022)
doi: 10.1103/PhysRevLett.128.153001

[15] Patrick Rupprecht et al. "Resolving vibrations in a polyatomic molecule with femtometer precision via x-ray spectroscopy"
Physical Review A 108(3) 032816 (2023)
doi: 10.1103/PhysRevA.108.032816

[16] Patrick Rupprecht, Alexander Magunia, Lennart Aufleger, Christian Ott and Thomas Pfeifer "Flexible experimental platform for dispersion-free temporal characterization of ultrashort pulses"
Optics Express 31(24) 39821–39831 (2023)
doi: 10.1364/OE.503731

Contents

1. Conceptual Background: Scientific Introduction into Four Questions

The interaction of light with matter can be found in natural process often and is frequently used in technological devices as well. These processes can be understood quite well, if one looks into the details: The light interacts with the constituents of matter—molecules or solids made of atoms which in turn are made of electrons and nuclei. The fundamental questions to ask for understanding these processes and break them down in a *top-down* manner are quite intuitive: What light is interacting—i.e. which photon energies does it contain? What atoms or molecules are interacting—i.e. how are they structured? And which parts of the atom/molecule are interacting with which spectral parts of the light?

Examples of the many natural light-driven processes on Earth range from chemical cycles in the atmosphere to photosynthesis allowing biology—and thus life—to harvest energy from sunlight, drawing a blueprint for human-made solar cells. Most of them are based on infrared (IR), visible (VIS) or ultraviolet (UV) light, whereas other radiation types are either not produced by our Sun in large quantities, or do not penetrate Earth's atmosphere significantly—or both. Studying the interaction of *extreme-ultraviolet (XUV)* or *x-ray* radiation with atoms or molecules is, thus, often only possible when looking towards extraterrestrial processes or, alternatively, in laboratory-based experiments. Yet, it allows for novel insights into the structure and dynamics of atoms and molecules and might, ultimately, be utilized for novel technologies in a *bottom-up* approach. It is the large photon energies of the XUV/x-ray light—translating to *short wavelengths* with respect to visible light—which enables it to address *inner-shell* and *core-state* electrons. While outer valence-electrons are involved in the formation of delocalized molecular bonds, inner-shell/core electrons stay localized at their parent atom within the molecule. Furthermore, electron states in different atomic species have different ionization and excitation energies, thus the interaction with inner-shell/core-electrons in hetero-nuclear molecules—consisting of at least two different atomic species, e.g. water [H_2O] molecules—also allows for so-called *site- or element-specificity*.

The electronic states and corresponding orbitals govern the chemical binding within molecules, but also their chemical properties with regards to their environment. This microscopic world of electrons, atoms and molecules is governed by the rules of quantum mechanics, where the properties of all quantum particles are non-deterministic and instead guided by *probabilistic* wave functions. An electron, for example, can thus be in the superposition of two (or even more) states at the same time. This quantum behavior can be initiated by using laser light and further utilized

in technologies, and thus brought to the everyday world—most notably qubits and hence quantum computers are based on probabilistic properties. But this behavior also appears in atoms and molecules naturally, and can lead to a variety of processes: an electron leaving the atom/molecule, or an electron/atom tunneling through an energetically-forbidden area, or a molecule having several pathways of breaking up into smaller molecules or atoms—and many more.
This further implies that the initial reaction of quantum particles when interacting with light, leads to further processes both within the atom/molecule and with its environment. This kind of *photochemical reaction* is not instantaneous, but has to be understood as dynamical, i.e. time-dependent, process with a finite duration. Yet, such reactions can be extremely fast—on the order of picoseconds [ps = 10^{-12} s], femtoseconds [fs = 10^{-15} s] or even attoseconds [as = 10^{-18} s]—and are, thus, often neither measured in a time-resolved manner nor well understood, yet. The emergence of ultrashort XUV and x-ray laser pulse sources by means of high-order harmonics generation (HHG) [17–19] has enabled investigating such fast electronic, atomic or molecular processes and has lead to the new research field of attosecond science. Furthermore, the advent of XUV/x-ray Free-Electron Lasers (FELs) has widened the scientific applications due to higher pulse energies and peak intensities while retaining femtosecond [20] or even attosecond [21, 22] temporal resolution.
Since then, many different measurement schemes and experiments have been developed, where two main parallel routes can be identified: Driving (or *pumping*) an atom/molecule with a visible, IR or UV pulse while detecting (or *probing*) with an XUV pulse, most often an HHG pulse, allows to unravel dynamics, which can in principle be used to study processes happening on Earth. Alternatively, using all–XUV FEL–pump and FEL–probe schemes allows for a complementary kind of quantum behavior to be studied, where the XUV excitation is expected to lead to novel dynamical processes. Further, the type of detection of these processes determines which information can be extracted. Since XUV/x-ray light ionizes any atomic or molecular species, the measurement of photo-electrons and ionic fragments as a function of their kinetic energies is a widespread investigation method. Yet, processes in an intact molecule or in neutral fragments cannot be detected by this measurement technique. In contrast, looking at the spectra of the laser pulses, for example by means of absorption spectroscopy, allows to identify neutral and ionic atomic/molecular species due to their unique spectral absorption imprints, as with the Fraunhofer Lines in the solar spectrum [23, 24].
This also demonstrates, not only interact lasers with matter, but the back-direction is also taking place: matter can be used to manipulate laser pulses. While the absorption features in the pulse spectrum are insightful to investigate the properties of independent atoms and molecules, many more processes need to be considered when a laser pulse travels through a dense gas cloud—where *propagation* effects determine the spectral, temporal or spatial reshaping of the pulse.

In view of the above presented scientific background, this thesis addresses the following questions:

(I) How are absorption changes in an XUV pulse spectrum related to the perturbation of the electronic structure of the interacting atom?

(II) How can temporal electron dynamics in atoms be reconstructed from spectral absorption measurements?

(III) How can high gas-density experiments be performed to include propagation effects during the interaction of XUV/x-ray pulses with atoms and molecules?

(IV) How can a novel combination of XUV laser pulses be used to investigate and time-resolve a photochemical reaction?

All four questions are related to the quantum-dynamics of atoms or molecules, which are governed by their electronic responses to the interaction with ultrafast XUV and x-ray pulses. While the dynamical processes evolve in time, their measurements are spectrally, i.e. energy-resolved. The answers to question (I), (II) and (IV) are given within the three publications in Chapter 4, whereas the answer to question (III) and a detailed discussion of how these topics are interconnected is provided in Chapter 5, including further theoretical and experimental results. To this end, a more detailed theoretical introduction to explain the common background of the four topics is given in Chapter 2. This theory background is especially important to the two simulation-based studies in the first two publications related to questions (I) and (II). The two experimental setups related to questions (III) and (IV) are presented in Chapter 3. The first setup is based on the combination of FEL and HHG pulses to time-resolve molecular dissociation dynamics, whereas the second setup is used for studying non-linear electron-excitations and propagation effects in dense target-gases. In the following, a detailed scientific context for the different questions is given, while comprehensive answers will be provided in Chapter 6.

The first publication (Section 4.1) discusses well-known electron-state couplings and population oscillations in atoms, but modified for ultrafast driving XUV pulses. Nandi et al. [25] have shown that so-called Rabi population oscillations can be brought to the XUV regime with femtosecond FEL pulses. But for the direct detection of this XUV-induced Rabi oscillations, the atom is further ionized, which breaks the electronic-state superposition. Instead, measuring the absorption spectrum of the driving XUV pulse, Ott et al. [4] have shown experimentally, but indirect, that a significant population transfer in a Rabi-coupling scheme leads to the modification of the corresponding absorption line. The theoretical study of this XUV-induced absorption-line changes presented in the first publication of this thesis leads to the intuitive picture of ultrafast, transient energy shifts as the mechanism leading to the observed absorption changes in the experiments.

Yet, in the work above the absorption profile is only altered within a confined driving-pulse intensity range. In the second publication (Section 4.2), increasing the peak intensity of the driving

XUV pulse further, the absorption line can be inverted to an emission line. A first experimental demonstration of this effect is provided in the discussion (Section 5.1). The absorption-to-emission–line inversion is directly connected to the Rabi-cycles of the electronic population, but, interestingly, not with population inversion. This also illustrates, that the temporal Rabi cycles are necessary to understand the spectral absorption changes. Reconstructing underlying quantum dynamics from spectral measurements is an often encountered challenge. To achieve such a reconstruction, a convolutional neural network (CNN) is used and presented in the second publication. As the field of machine learning—to which CNNs belong—is in general growing, also first applications to the ultrafast scientific field have been recently demonstrated. The second publication can therefore be regarded as extension of these efforts. Further, the spectral bandwidths of FEL pulses can be broad enough to excite several states simultaneously—thus launching an electronic wave packet with non-trivial temporal behavior. This scheme can also be reconstructed with the CNN and might allow for intensity-dependent control of electron-population transfer.

The back-action of electrons or atoms on the XUV/x-ray pulses they interact with is a crucial aspect of the research field. In fact, the existence of both ultrafast XUV/x-ray sources builds on this back-action: FEL pulses are generated by relativistic electrons interacting with their own emitted radiation, while high-harmonics are generated in gas clouds, where their phase matching while propagating though the could is an important aspect. Both processes will be explained further in Section 2.1. While high gas pressures ($\geq$1 atmospheric pressure) for the HHG process are utilized successfully for example in [26], the recent research of employing FEL or HHG pulses in dense gas clouds to further investigate their propagation behavior is often limited to moderate gas pressures ($\leq$1 atmospheric pressure). To this end, an experimental setup achieving high target pressures is presented in Section 3.2, and first results of a stimulated scattering process amplified via propagation through the dense cloud are presented in Section 5.1.

While the first two publications consider electron dynamics in atoms, in a molecule additional nuclear degrees of freedom as vibrations or dissociation exist. The initial photo-excitation of a molecular electron leads to responses of both nuclear and electronic degrees of freedom. Often the electron dynamics precede the nuclear motions, but for fast enough nuclear responses, they can become coupled. The investigation of such photochemical reactions thus demands a time-resolved experimental pump–probe scheme. For XUV/x-ray initiated molecular dynamics, FEL-pump–FEL-probe schemes have been demonstrated [12, 13], but lacking the important aspect of covering several atomic sites or fragments within the probing FEL spectrum. The third publication (Section 4.3) demonstrates, how a combination of FEL-pump and HHG-probe pulses is implemented for the first time and is used for a benchmark study of the state-specific dissociation of molecular oxygen. The coupled dissociation pathways via nuclear-tunneling dissociation and electronic pre-dissociation are resolved on picosecond time scales. Further, femtosecond time-scale and excitation-energy–dependent dissociations are discussed in Section 5.2.

2. Theoretical Background: XUV/X-Ray Lasers, Quantum Dynamics, Machine Learning

The previous chapter is meant to give an overview of the scientific questions this thesis is addressing and their relevance within a broader context. Yet, for a precise understanding of the results of this thesis, a more detailed introduction into the following topics is expected to be helpful to the reader. The structure of this chapter is chosen to match and help guide through the results presented in Chapters 4 and 5:
Since the interaction of ultrashort XUV laser pulses with atoms or molecules is the central aspect of this thesis, the two complimentary methods of producing such pulses, the Free-Electron Laser (FEL) and High-order Harmonic Generation (HHG), are discussed first (Section 2.1). The basic concepts of the electronic structure in atoms, especially in helium and oxygen atoms, is presented in Section 2.2. Furthermore, the dipole interaction of a laser with an electron within an atom is introduced for weak and strong fields, respectively. The induced dipole of an excited atom leads to light emission interfering with the incoming light and thereby creates absorption features in the spectrum, as discussed in Section 2.3. This three sections provide the basis for the results discussed in the first publication in Section 4.1. To reconstruct and eventually predict the induced electron dynamics from modified absorption spectra, a convolutional neural network (CNN) is used in the second publication (Section 4.2)—for which the working principle of neural networks is provided in Section 2.4. The final theory Section 2.5 shows how the electronic structure in atoms can be utilized to understand the formation of molecular bonds. This section includes how molecular electrons, in particular in O_2, behave in interplay with the nuclei when being photo-excited and, ultimately, how the molecule can break up and the electronic states regain atomic character again. This lays the foundation for the dissociation of molecular oxygen studied in the third publication (Section 4.3).

2.1. Ultrafast Extreme-Ultraviolet and X-Ray Laser Sources

While in Chapter 1 the wavelength (or photon *energy*) of light was emphasized to motivate the use of XUV/x-ray laser sources, it is equally important to consider its intensity (related to the *amount* of photons) to describe the interaction with atoms and molecules properly. For the

scope of this thesis, three cases will be considered. (i) For very low intensities, the quantum nature of the electromagnetic field, manifesting in photons, needs to be treated with quantum field theory (QFT)—which for the general description of the laser sources below is practically never the case. Yet, *while* interacting with an atom or molecule, often only a single (or few) photons are absorbed or emitted, thus the photon-picture is commonly used there—but classical perturbation theory is sufficient to describe this process without QFT. This will be described in more detail in Section 2.2.3. In general, the laser pulses contain large numbers of photons and can be described classically as electromagnetic waves obeying Maxwell's equations. The interaction of this electromagnetic waves with atoms can be considered *linear* for low intensities—(ii) the *weak-field* regime (Section 2.2.2)—or *non-linear* for high intensities in the (iii) *strong-field* regime (Section 2.2.3). The two complimentary methods of producing ultrafast XUV/x-ray pulses presented in the following are ideal examples for weak-fields in the case of HHG pulses (Section 2.1.1) and strong-fields in the case of FEL pulses (Section 2.1.2).

2.1.1. High-Order Harmonic Generation

For the purpose of this thesis, the usage of infrared (IR) pulsed lasers for time-resolving chemical reactions on femtosecond timescales is chosen as an introductory point about pulsed laser source development. It lays the foundation for the field of ultrafast science and won the Nobel Prize in Chemistry 1999 in [27]. In similar spirit, the advent of XUV attosecond pulses by generating high-order harmonics of IR pulses winning the Nobel Price in Physics recently in 2023, allows to resolve electronic motions within atoms and molecules [17–19]. The key factor to enable this process is the peak electric-field strength of the driving IR pulse being sufficiently high ($\sim 10^9\,\mathrm{V/m}$), so it becomes comparable with the strength of the electric-field between an electron and the nucleus it is bound to. In that case, the semi-classical "three-step model" [28] allows to explain this highly non-linear and non-perturbative HHG process—which is illustrated in Figure 1. A single cycle of the driving pulse is sufficient to cover all three steps (Figure 1a). Around the peak field strength, the laser bends the Coulomb potential of the atom linearly—since the driving IR wavelength (typically $\simeq 1\,\mu\mathrm{m}$) is much larger than the size of the atom (typically $\sim 1\,\text{Å}$)—such that the valence electron can tunnel-ionize through the remaining potential barrier (Figure 1b). A more formal foundation of this interaction will be presented in Section 2.2. Half an IR-cycle after the ionization, the electric field of the IR pulse changes its sign, hence it bends the potential into the other direction and thereby accelerates the electron back towards the parent ion (Figure 1c). During that time, the electron is considered quasi-free and gains kinetic energy by being accelerated in the ponderomotive potential of the IR pulse. Another quarter IR cycle later, the electric field of the laser is close to zero and the atomic potential is unperturbed. With a small probability (typical conversion factors are 10^{-5} to 10^{-6} [29, 30]), the electron can recombine with the parent ion and give away its excess energy in form of a single XUV or x-ray photon γ (Figure 1d). Since the complete HHG process is initiated at every electric-field peak, driving pulses with a duration of several cycles generate a pulse train, whereas in the

limit of a single-cycle pulse, an isolated attosecond pulse is generated [17] (Figure 1e), where pulse durations down to 43 as have been demonstrated [31]. Further, in isotropic media such as commonly used noble gases, the process is periodic in each half IR cycle, thus only odd harmonics of the driving pulse frequency ω_d are generated. The less attosecond pulses are generated in time, the broader the individual harmonic peaks are in spectral domain (Equation (3)), down to the isolated-pulse limit, where individual harmonics can be spectrally distinguished only barely, and the spectrum rather resembles a broadband source. The maximum photon energy of the HHG pulses is determined by the properties of the involved atom, in particular its ionization potential I_P, and the interaction of the laser pulse with the quasi-free electron due to its ponderomotive potential, which is governed by the driving-pulse peak intensity I_0 and its wavelength λ_d. With help of the full quantum-mechanical treatment [18] the maximal 'cutoff' energy of the HHG spectrum can be estimated to be:

$$E_{\text{cutoff}}\ [\text{eV}] = I_P\ [\text{eV}] + 3 \cdot 10^{-13} \cdot I_0 \left[\frac{\text{W}}{\text{cm}^2}\right] \cdot \lambda_d^2\ [\mu\text{m}] \tag{1}$$

An estimate of the cut-off energy for a typical pulse with $\lambda_d = 0.8\,\mu$m, reaching a peak intensity of $I_0 = 10^{14}\,\text{W/cm}^2$, and focused into a krypton cloud ($I_P = 14\,\text{eV}$) leads to $E_{\text{cutoff}} \sim 34\,\text{eV}$. Thus, the HHG spectrum spans into the extreme-ultraviolet (XUV) regime ($E_{ph}^{XUV} > 12.4\,\text{eV}$). Utilizing longer-wavelength driving pulses ($\lambda_d = 3.9\,\mu$m in [32]) allows to upscale the cutoff energy into the soft x-ray regime ($E_{ph}^{x-ray} > 124\,\text{eV}$), with, for example, spectra up to 1.6 keV reported in [32]. The exact border between XUV and x-ray radiation is not always consistent throughout scientific literature. The terms are used within this thesis with respect to the numbers above. Also, the usage of 'x-ray' in this thesis refers to the energetically lower half of the regime, often called soft x-ray, excluding nuclear transitions available to the hard x-ray regime.
The HHG process is an illustrative example of how the feedback of the IR-generated plasma

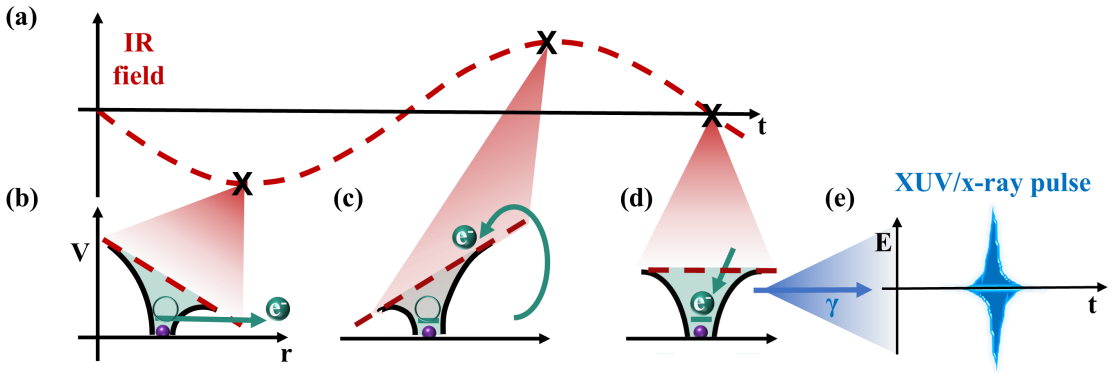

Figure 1.: Scheme of high-order harmonic generation. **(a)** Single cycle of the HHG-driving IR pulse in time. **(b)-(d)** Atomic potentials in the HHG three-step model in space, as discussed in the main text. **(e)** Resulting isolated XUV or x-ray HHG pulse in time.

manipulates the driving pulse. The generated XUV radiation is so different in nature from the driving IR pulse, it is commonly regarded as a new pulse instead of a spectral reshaping of the IR pulse (which technically is also correct). Furthermore, a single-atom response, as used in the three-step model, only includes a part of the complete interaction, since the XUV radiation needs to propagate through the gas cloud—typically some millimeters of length—after its generation. Although HHG intensities are typically low due to the low conversion factors, they are large enough to consider the HHG pulses as classical waves and, hence, apply classical propagation consideration: The individual harmonics ω_{2n+1} propagate differently throughout the medium, thus the pressure and dispersion $n(\omega)$ of the gas (Section 2.3), as well as the focusing geometry [33] are crucial factors for the phase-matching and propagation of the harmonics.
In total, the large bandwidth of the HHG pulses spanning into the XUV or soft x-ray regime, attosecond pulse durations, and weak peak-intensities make the HHG pulses ideal probing tools for time-resolved XUV/x-ray absorption spectroscopy as utilized in the results (Section 4.3).

2.1.2. Free-Electron Lasers

While the HHG process only takes place when the quasi-free IR-accelerated electrons recombine with their parent ions, accelerated electrons also emit radiation, in general, without (re-)combining with other particles. The emitted radiation can be brought to re-interact with the electrons, if the electrons co-propagate in a sinusoidal motion with the radiation and with comparable speed. In this case, the initially spontaneous emission can be amplified to generate forward-directed and coherent emission—as a laser does, but without the stimulated emission in a gain medium. What started in the 1940s and 50s as a theoretical consideration [34, 35], developed rapidly to be the main working principle for Free-Electron Lasers (FEL), first for IR and microwave [36], and later for XUV and x-ray FELs [20]. The scheme of *self-amplified spontaneous emission (SASE)* used in most modern-day FELs, in particular at the Free-Electron Laser in Hamburg (FLASH) at the Deutsches Elektronen-Synchrotron (DESY) and at the European X-ray Free-Electron Laser (EuXFEL), is illustrated in Figure 2: An electron source consisting of a photo-cathode illuminated with ultraviolet (UV) radiation provides electron bunches, which are captured by radio-frequency (RF) pulses and guided to a linear acceleration stage (Figure 2a). Due to the acceleration, the electrons reach relativistic velocities v_e with GeV levels of kinetic energy. After the electron bunches are compressed in a magnetic chicane, a chain of periodic and oppositely-poled magnets—called undulator—leads to the sinusoidal motion of the electron bunches perpendicular to both the propagation direction and magnetic field direction, while radiation is emitted in the forward direction of the electron propagation in a confined cone (Figure 2b). Under the right conditions (see Equation (2)), the ponderomotive force of the radiation back-acts on the initially randomly assembled electrons (Figure 2c) leading to *microbunching* of the electrons within the pulse (Figure 2d) [37]. The microbunches emit radiation more coherently and lead to the self-amplification of the resulting partially-coherent laser pulses (Figure 2e). This amplification only occurs for the correct wavelength λ of the emitted light (within a window of $\Delta\lambda/\lambda \approx 1\,\%$) [38]:

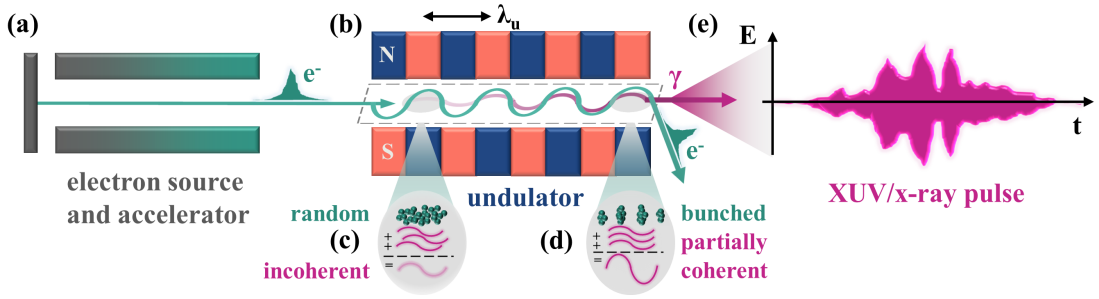

Figure 2.: Scheme of an Free-Electron Laser. **(a)** Electron pulses are accelerated close to the speed of light. **(b)** Within the undulator, the electrons start emitting incoherent radiation **(c)**, which back-acts on the electrons to forms microbunches **(d)**. As a result, a short, intense and partially-coherent XUV or x-ray pulse is produced **(e)**.

$$\lambda = \frac{\lambda_u}{2\gamma^2}\left(1 + \frac{e^2 B_0^2 \lambda_u^2}{8\pi^2 m_e^2 c^2}\right), \tag{2}$$

where λ_u is the undulator period, $\gamma = 1/\left(1 - v_e^2/c^2\right)^{1/2}$ is the Lorentz factor, B_0 is the undulator magnetic field, c is the speed of light and e and m_e are the charge and mass of the electron, respectively. As motivated in Chapter 1, the (central) wavelength of an FEL pulse is crucial for determining which processes can be initiated when interacting with an atom or molecule. Equation (2) shows that three parameters can be used to change that wavelength: the electron kinetic energy, the magnetic field strength and the undulator period. Changing the electron kinetic energy with the linear accelerator settings is often employed, but cannot be performed fast (as for example at FLASH1). In contrast, tuning the magnetic field strength allows for fast and precise scans of the FEL wavelength, with steps on the order of the FEL bandwidth within large ranges. This is achieved by changing the vertical gap size between the magnets with µm-precision as employed at the FLASH2 and SASE3-EuXFEL undulators. Such wavelength control is therefore available for the experiments presented in Chapters 4 and 5, which are performed at the FL26 beamline at FLASH and the Small Quantum System (SQS) endstation at EuXFEL. The most important FEL-pulse parameters are summarized in Table 2.1.

Table 2.1.: FEL pulse parameters at FLASH [39] and EUXFEL [40].

Parameter	**FLASH2**	**EuXFEL SASE3**
wavelength [nm]	4–60	0.4–3
average bandwidth [%]	0.7–2.0	∼1
pulse duration [fs]	≤50–200	1–30
average single-pulse energy [µJ]	10–500	≤10,000
pulses per second	10–7,500	27,000

The given single-pulse energies in Table 2.1 imply high peak intensities (as discussed in Section 2.2.3), whereas the wavelength ranges imply that FLASH2 operates from the XUV to soft x-ray region, whereas EuXFEL provides higher-energy soft x-ray radiation. The average bandwidth of $\sim$1 % is rather narrow compared to the HHG pulses presented in the previous section. Yet, single FEL spectra fluctuate on a shot-to-shot basis due to the only partially-coherent SASE process [41]. Typically, SASE FEL spectra contain several nearly-coherent spikes of comparable width, which determine the overall temporal pulse duration due to the Fourier uncertainty principle:

$$\Delta E \cdot \Delta t \geq \frac{\hbar}{2}. \tag{3}$$

Here, *coherence* implies a fixed phase-relation between all relevant spectral components. In a similar way, the temporal sub-pulses (see Figure 2e) determine the coherence time and spectral bandwidth of the FEL pulses. In case a laser pulse is fully coherent and all spectral components have the same phase (or the phase is given as a linear function), the pulses are called Fourier-transform limited and can minimize the uncertainty in Equation (3). So-called seeded FELs utilizing an external, coherent laser to initiate the electron emission can deliver fully-coherent FEL pulses [42]. Further, in Section 2.2.2 it will be used, that coherent pulses lead to coherent excitations in atoms, where the same principle of fixed phase relations applies to electronic states in an atom.

For SASE-FEL pulses, averaging over many spectrally-fluctuating pulse spectra leads to a more smooth, Gaussian-like shape [41, 43]. The simulation models utilized in the first two publications (Sections 4.1 and 4.2) employ this averaged Gaussian-like spectra, and hence, effectively simulate fully-coherent temporal (sub-)spikes. Thinking of the whole FEL pulse as a train of such spikes with slightly randomly varying properties as peak intensities and central photon energies, justifies this approximation. Therefore, coherence is mostly assumed within this thesis, if not state otherwise. The partial coherence of the SASE-FEL pulses might practically reduce the coherent effects discussed in this thesis, but as demonstrated by experiments with SASE-FEL pulses [4, 6, 7], such effects remain evident nevertheless.

Overall, the capability to tune the central wavelength in the XUV and x-ray regime while having narrow bandwidths, femtosecond pulse durations and high pulse energies make the FEL pulses an ideal tool for state-selective and non-linear pump pulses of ultrafast electron dynamics in atoms and molecules, as utilized throughout the different results presented in Chapters 4 and 5.

2.2. Electrons in Atoms

In contrast to the light sources above, the structure and behavior of electrons, atoms and molecules could historically not be explained with classical mechanics, and therefore gave rise to the formalism of quantum-mechanics. Quantum particles are postulated to (i) be described by probabilistic wavefunctions $|\psi\rangle$, and (ii) obey the Schrödinger equation in the non-relativistic regime—besides further postulates [44]. This section does not seek to explore this quantum nature itself, but rather uses it to introduce the electronic structure of atoms. This will further allow to describe and understand the interaction of atoms and laser, as well as molecular structures.

2.2.1. Unperturbed Atoms

As already illustrated for the HHG process in Section 2.1.1, an electron can be bound to an atomic nucleus within its Coulomb potential due to their electrostatic interaction. For its quantum-mechanical and non-relativistic treatment–which follows closely [45]—the Coulomb potential $\hat{V}$ is included in the Hamiltonian $\hat{\mathcal{H}}$:

$$\hat{\mathcal{H}} = \hat{V} + \hat{T}, \tag{4}$$

where $\hat{T}$ is the total kinetic energy of the electron and the nucleus. The Hamiltonian is used to formulate the time-dependent Schrödinger equation (TDSE):

$$i\hbar \frac{\partial \psi(\vec{r},t)}{\partial t} = \hat{\mathcal{H}}\psi(\vec{r},t), \tag{5}$$

where $\psi(\vec{r},t)$ is the electronic wavefunction. In the following, the reader is guided through the most important aspects of solving the TDSE following [45]. Only for single-electron, hydrogen-like atoms, the TDSE is analytically solvable leading to the eigenstates $\psi_{nlm}(\vec{r},t)$ and eigenenergies E_n as functions of the discrete quantum numbers n (main), l (orbital angular momentum), m_l (magnetic). The time dependence of the eigenstates is a trivial phase evolution and the states can be rewritten in time- and space-decoupled manner: $\psi_{nlm}(\vec{r},t) = e^{-iE_n t/\hbar}\psi_{nlm}(\vec{r})$. Since the hydrogen atom is spherically symmetric, the angular part of the wavefunctions can be expressed with help of the spherical harmonics $Y_l^m(\nu,\theta)$—which will be used later for both multi-electron systems and for the molecular electronic structure in Section 2.5. Using the eigenstates and -energies, the TDSE can be rewritten in a time-independent form:

$$\hat{\mathcal{H}}\,|\psi_{nlm}\rangle = E_n\,|\psi_{nlm}\rangle\,. \tag{6}$$

For the eigenenergies, the spin of an electron $|\vec{s}| = \frac{1}{2}$ needs also to be taken into account. This leads to the coupling of the spin $\vec{s}$ and orbital angular momentum $\vec{l}$ vectors and results in a splitting of the eigenenergies into E_{nls}. This *fine structure* splitting is small—e.g. <10 meV for the O^+: 2p $\rightarrow$ 3d transition—compared to the spectral resolution of the experimental setup, ∼30 meV (Chapter 3)—and will therefore not be discussed further.

For all other atoms containing (at least) a second electron, like helium, the electron-electron interaction makes the SEQ analytically unsolvable. This interaction contains the Coulomb potential between the electrons, but also the Pauli's exchange principle has to be considered—stating that the two-electron wavefunction has to be anti-symmetric under the parity operator $P : \vec{r} \rightarrow -\vec{r}$. Thus, when the total spatial wavefunction is symmetric, the total spin wavefunction has to be anti-symmetric and vice versa. For this consideration, the total orbital angular momentum $\vec{L} = \sum_i \vec{l_i}$ and total spin $\vec{S} = \sum_i \vec{s_i}$ are defined, where $i = \{1, 2\}$ denotes the individual electrons. The electronic states are typically labeled as ^{2S+1}L, where L is given in spectroscopic notation: $L = \{0, 1, 2, 3, ...\} \rightarrow \{S, P, D, F, ...\}$. To solve the SEQ including the Coulomb interaction between the two electrons, that term can be treated as perturbation [45]. Alternatively, leading to even more precise energies, a *variational method* [46] can be used for the helium ground state—$1s^2$ (^{1}S)—and its singly-excited states, e.g. the $1snp$ (^{1}P) Rydberg series, converging to the ionization threshold of 24.6 eV. Although electron interaction is necessary to estimate the correct energy values, the states are typically labeled in the single-electron notation $n_1 l_1 n_2 l_2$, which will be used throughout the thesis. Notably, the doubly-excited states of helium, e.g. the $sp_{2,n+}$ (^{1}P) series converging to the ionization threshold at 65.4 eV, lays above the first ionization threshold and, hence, can undergo the radiationless process of *autoionization*. As it will be presented in Section 2.3, this leads to asymmetric *Fano* absorption profiles [47]. The notation $sp_{2,n+}$ arises from the superposition of the $2snp$ and $2pns$ configurations [48]. The eigenenergies of the doubly-excited states can be determined with an R-matrix approach [49] and are shown—together with the singly excited states—in Figure 3a. With energies around 20 eV and 60 eV, respectively, they are ideal candidates to study XUV-excitation of correlated electrons.

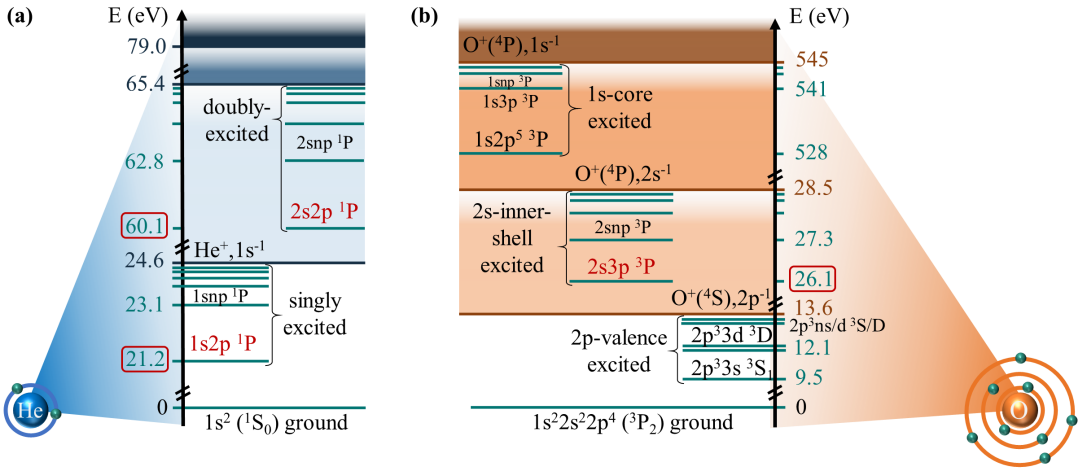

Figure 3.: Electronic states in **(a)** helium and **(b)** oxygen atoms. As discussed in Section 2.2.2, only states (green) which can be excited from the ground state are presented. The ionization thresholds are given in blue and orange, respectively. Relevant states and energies for the results in Chapters 4 and 5 are highlighted in red.

For atoms like oxygen with more than two electrons, the sum of all electron-electron Coulomb interactions between any two electrons can become significant and cannot be treated as perturbation anymore. Instead, the *central-field approximation* can be employed, where for every single electron the Coulomb interaction with all other electrons is treated as a mean field. As a benefit of doing so, the effective potential becomes spherically symmetric, and the spherical harmonics can be utilized for solving the angular part again. To solve the residual radial part, one typically starts with (hydrogen-like) single-electron states, and calculates new states and basis sets: For example, the *Slater determinant* allows to mix-up single electron orbitals and determine the minimum energy while ensuring Pauli's exchange principle. This than can be used in the *Hartree-Fock* variational method to estimate the eigenenergies of electronic states with reasonable precision. Regarding the spin-orbit coupling in many-electron systems, it has to be considered that the individual spins $\vec{s_i}$ and angular momenta $\vec{l_i}$ may couple to the total angular momenta $\vec{j_i} = \vec{l_i} + \vec{s_i}$ first, before coupling to the momenta of other electrons via: $\vec{J} = \sum_i^N \vec{j_i}$ (known as *jj*-coupling)—in contrast to the above described *ls*-coupling, where first the individual spins and angular orbital momenta would couple to $\vec{L}$ and $\vec{S}$ before those couple to $\vec{J} = \vec{L} + \vec{S}$. This will become relevant for understanding which transitions in an atom are allowed while interacting with an electromagnetic wave in the next subsection. For that purpose, it is also important to understand which of the states are actually populated in the electronic ground state of the atom. This is given by filling up the states starting from the lowest energy state, often correctly estimated by the *Madelung rule*: (i) filling states with increasing $n + l$, and (ii) for equal $n + l$ values, lower n states are filled first [50]. For a light enough element ($Z \leq 18$), these rules match the ordering of the hydrogen states: (i) the lowest n has the lowest energy, and for a given value of n, the lower l, the lower the state energy. For the oxygen atom, this leads to a ground state configuration of O(^{3}P): $1s^2\ 2s^2\ 2p^4$, where *Hund's rules* [45] are used to determine the ^{3}P total configuration. Eventually, there are many so called Post-Hartree-Fock methods, further increasing the precision of the electronic-state energies. For example using another variational method, the Hartree-Fock states can be linearly combined and the resulting state is optimized through the combination coefficients. This often employed procedure is known as *Configuration Interaction (CI)*. Turning to the oxygen atom, CI can be used to calculate the Rydberg series shown in Figure 3b, where an $n = 2, l = p$ (short: $2p$) electron of the O(^{3}P) ground state is excited to an ns (^{3}S) or nd (^{3}D) state (with $n \geq 3$) [51], which converges to the first ionization threshold, the *L-edge*, at 13.6 eV. Alternatively, a $2s$ electron can be excited to an np (^{3}P) autoionizing state (with $n \geq 3$) converging to the ionization limit at 28.5 eV. For these states, the R-matrix method can be utilized again [52, 53] in good agreement with experimental results [54, 55]. Lastly, a $1s$ electron can be excited to an np (^{3}P) state [56, 57] close to the *K-edge* ionization threshold at 545 eV [58]. These states can autoionize, but in addition the $n \geq 3$ states can also decay via the radiationless *Auger-Meitner* process, where an inner electron drops to the $1s$ state transferring its energy to ionize the outer-most electron. While many more electronic states exist in both helium and oxygen, only a small subset is presented to illustrate the different excitation and

decay mechanisms. To understand how electron excitations can take place and which transitions are allowed, the interaction with an electromagnetic field is considered in the following section.

2.2.2. Atoms in Weak Fields

After looking at XUV laser sources and electronic structure of atoms individually, this section will introduce the interaction of (weak) electromagnetic fields with bound electrons. For that purpose, the change of electron momentum ($\vec{p}$) due to the electron charge ($-e$) interacting with the vector potential of the electromagnetic field $\vec{A}$ needs to be considered: $\vec{p}^2 \rightarrow (\vec{p} + e\vec{A})^2$. For a weak field, the resulting $\vec{A}^2$-term can be neglected. Further, the *dipole approximation* can be utilized—stating that the electronic orbital size ($r \sim 10^{-10}\,\mathrm{m}$ to $10^{-11}\,\mathrm{m}$) is typically smaller than the wavelength of the light ($\lambda_{VIS/XUV} \sim 10^{-7}\,\mathrm{m}$ to $10^{-8}\,\mathrm{m}$), and thus, the spatial part of the electric field can be neglected by approximating: $e^{i\vec{k}\vec{r}} \approx 1$. This leads to the interaction term $\hat{\mathcal{H}}_1 = \hat{d} \cdot E(t)$ in the Hamiltonian, in addition to the unperturbed Hamiltonian ($\hat{\mathcal{H}}_0$):

$$\hat{\mathcal{H}} = \hat{\mathcal{H}}_0 + \hat{d} \cdot E(t). \tag{7}$$

Here, $E(t)$ is the electric field of the laser and $\hat{d}$ is the dipole operator between two unperturbed—or *bare*—electronic states $|\psi_a\rangle$ and $|\psi_b\rangle$ with the expectation value:

$$d_{ab} = \langle \hat{d} \rangle_{ab} = e \int \psi_a(\vec{r})\ \vec{r}\ \psi_b^*(\vec{r})\ d\vec{r} \tag{8}$$

The separation of the spatial and temporal parts of the wavefunctions, as introduced earlier, has been utilized to only consider the spatial part in Equation (8). For the time-dependent part, one can write the general state:

$$|\psi(t)\rangle = c_a(t)\,|\psi_a\rangle + c_b(t)\,|\psi_b\rangle \tag{9}$$

as superposition of the two bare states, where the probability to be in one of the states is given by $P_i(t) = |c_i(t)|^2$. Thus, if the electronic states and the dipole moments between them are given, one can use numerical methods to solve the time evolution under any given interaction with a laser (pulse). This is the approach utilized in the two publications in Sections 4.1 and 4.2. Yet, for an electromagnetic field with a frequency ω matching the transition frequency between the two states ω_{ba} and a *weak*, constant electric-field strength E_0, the small probability ($P \ll 1$) at time T to excite from the initial state, $|\psi_a\rangle$, into the initially unpopulated and non-degenerate $|\psi_b\rangle$ state is given by first-order perturbation theory as $P_{ba} = W_{ba} \cdot T$, where W_{ba} is the transition rate known as *Fermi's golden rule*:

$$W_{ba} = \frac{2\pi}{\hbar} |d_{ba} E_0(\omega = \omega_{ba})|^2. \tag{10}$$

In general, this also implies that an excitation laser (pulse) needs to have non-vanishing spectral intensity at the corresponding transition energy to initiate this *absorption* process, where the

energy of a single photon is transferred to the excited electron. A broad pulse can therefore excite several states simultaneously in a *coherent superposition*, which is also referred to as *electronic wavepacket*. Respectively, *stimulated photo-emission* occurs as well at discrete transition energies between two states. Furthermore, the emission can also take place *spontaneously* leading to a finite lifetime τ_b of the excited state, which translates into the spectral width $\Gamma_b = \frac{\hbar}{\tau_b}$ of the excited state. When several decaying mechanism compete, for example via spontaneous decays into several lower lying states, or in parallel to autoionization or Auger-Meitner decay, the total lifetime is equal to the sum of all individual lifetimes. Since XUV or x-ray photon energies typically excite into short-lived autoionizing or Auger-Meitner-decaying states (as– or fs–scales), the corresponding line widths are rather broad (meV– or eV–scales). In total, under the above given circumstances, the electronic structure within the atom is not perturbed and only a small amount of the electron wavefunction is transitioned to another state. This defines the use of the term *weak* with regards to the electromagnetic field within the scope of this thesis.
It should be noted, that this formalism can be used in general for any single- or multi-electronic system. While for a single electron (at position $\vec{r}$) the dipole moment is given as $\vec{d} = e\vec{r}$, the sum of all individual electrons (at positions $\vec{r_i}$) needs to be taken into account to define the dipole moment $\vec{D} = \sum_i e\vec{r_i}$ in a multi-electron atom. In any case, the probability to excite from state $|\psi_a\rangle$ to state $|\psi_b\rangle$ vanishes, when the dipole moment between the two states equals zero. To this end, the integral in Equation (8) needs to be evaluated, which depends on the spatial properties of the pair of wavefunctions and thus on their quantum numbers. For the hydrogen-like single-electron wavefunctions, the following set of *selection rules* can be derived from this evaluation:

$$\Delta l = \pm 1, \quad \Delta m = 0, \pm 1, \quad \text{change of parity}, \tag{11}$$

where the rule for Δm depends on the polarization direction of the electric field. In contrast, the general selection rules for multi-electron transitions depend on the J instead of the L quantum number:

$$\Delta J = 0, \pm 1 \ (J = 0 \rightarrow J' = 0 \text{ forbidden}), \quad \Delta M_J = 0, \pm 1, \quad \text{change of parity}. \tag{12}$$

If the multi-electron system is in the LS-coupling regime, as given in helium and oxygen atoms, the following conditions need to be fulfilled as well:

$$\Delta L = 0, \pm 1 \ (L = 0 \rightarrow L' = 0 \text{ forbidden}), \quad \Delta M_L = 0, \pm 1, \quad \Delta S = 0. \tag{13}$$

Since all of these selection rules are derived in the dipole approximation, the allowed transitions are called *electric dipole* or *E1 transitions*—inducing a oscillating dipole moment within the atom. Throughout this thesis, dipole-allowed single-electron excitations in a multi-electron system are considered, if not explicitly stated otherwise. For other types of transitions, like M1 and E2 transitions, when the dipole approximation is omitted, the reader is referred to [45] for more

details. Also, instead of using first-order perturbation theory as for Equation (10), higher orders can be used to derive multi-photon transitions, in case the electric-field strength is high enough. The two-photon excitation of an electron is a relevant example of such a process, which will be discussed in Section 5.2. A derivation of corresponding transition rules can be found in textbooks like [45, 59]. Further, inelastic processes as the *scattering* of a photon with different output than input energy can be described in second order perturbation theory [60]. This lays the foundation of *resonant inelastic x-ray scattering (RIXS)* investigated at the EuXFEL facility with help of the high gas-density setup presented in Section 3.2 and discussed in Section 5.1. The HHG process presented in Section 2.1.1 can be regarded as even more drastic, as it is non-perturbative and the whole Coulomb potential is modified. Where literature often refers to these regimes of laser intensities as *strong-field*, these term is used in this thesis with regards to the—also non-perturbative—strong-coupling of a two-state system presented in the next section.

2.2.3. Atoms in Strong Fields

In the previous section the electronic structure of an atom, i.e. the energy levels and state populations, did not change significantly through the interaction with a weak electromagnetic field. Yet, there are several cases where the electronic energy levels and populations can be modified, if the interacting fields become strong enough [45]. For monochromatic oscillating fields with a constant amplitude [45], examples are known as (perturbative) *AC-Stark* energy shifts—often used for non-resonant fields—or *Autler Townes (energy) splitting* [61] in case of a near-resonant and non-perturbative excitation. The later can be connected to temporal oscillations of the electronic-state populations known as *Rabi*-oscillations [62]. The Autler-Townes splitting can be regarded as the low-intensity limit of the dressed states picture, which accounts for the interaction of a (classical) electromagnetic wave with an atom in a non-perturbative way, for example when Floquet theory is used [63]. With the help of a full quantum field theory (QFT) treatment, the dressed states can be understood as combination of bare atomic states and Fock photon-number-states $|n\rangle$ of the electromagnetic field [64]. For the case of a moderately intense and near-resonant XUV pulse coupling the ground state to an excited state, as considered in the first two publications, the description based on the lowest-order coupling in the Floquet formalism (including only single-photon exchanges) leading to the Autler-Townes splitting [63] is sufficient—but needs to be adapted to account for a pulsed, instead of a continuous, driving laser. Considering a two-level system with electronic states $|\psi_a\rangle$, $|\psi_b\rangle$ with energies E_a, E_b, infinite lifetimes, a (real) dipole transition moment d_{ab} and an electric field $E(t)$ as in the previous section, the corresponding Hamiltonian (Equation (7)) can be expressed as matrix:

$$\mathcal{H}_{\text{2-lvl}} = \begin{pmatrix} E_a & d_{ab} \cdot E\,(t) \\ d_{ab} \cdot E\,(t) & E_b \end{pmatrix}. \tag{14}$$

By reducing the system to two energy levels, the Schrödinger Equation (6) becomes a pair of linear coupled differential equations for the time-dependent state coefficients $c_{a,b}(t)$. In general, these equations can be solved numerically—as in the publications in Sections 4.1 and 4.2. For a monochromatic, continuous wave: $E(t) = E_0\ cos(\omega_0 t)$, with a field strength E_0 and a frequency ω_0 close to the transition frequency $\omega_{ab} = (E_b - E_a)/\hbar$—such that the detuning $\Delta = \omega_0 - \omega_{ab}$ becomes small—the differential equations can be solved analytically by applying the *rotating-wave approximation (RWA)*. First, the phases of the state coefficients are rotated:

$$c_a(t) = \tilde{c}_a(t) \cdot e^{-i(\omega_a + \Delta/2)t}, \quad c_b(t) = \tilde{c}_b(t) \cdot e^{-i(\omega_b - \Delta/2)t}. \tag{15}$$

Then, neglecting the fast oscillation terms $(\omega_{ab} + \omega_0)$, Equation (14) can be re-written as:

$$\mathcal{H}_{\text{2-lvl}}^{\text{RWA}} = \frac{\hbar}{2} \begin{pmatrix} -\Delta & \Omega_R \\ \Omega_R & \Delta \end{pmatrix}. \tag{16}$$

Here, the Rabi frequency Ω_R is used, which is defined as $\Omega_R = d_{ab}E_0/\hbar$. As it will become apparent in the following, it is helpful to define the generalized Rabi frequency $\tilde{\Omega}_R$ for $\Delta \neq 0$ as:

$$\tilde{\Omega}_R = \sqrt{\Delta^2 + |\Omega_R|^2}. \tag{17}$$

With help of the eigenvalues of the RWA-matrix in Equation (16), the eigenenergies of the new eigenstates— the laser-dressed states—can be written as:

$$E_a^{\pm} = E_a - \frac{\Delta}{2} \pm \frac{\hbar\tilde{\Omega}_R}{2}, \quad E_b^{\pm} = E_b + \frac{\Delta}{2} \pm \frac{\hbar\tilde{\Omega}_R}{2}. \tag{18}$$

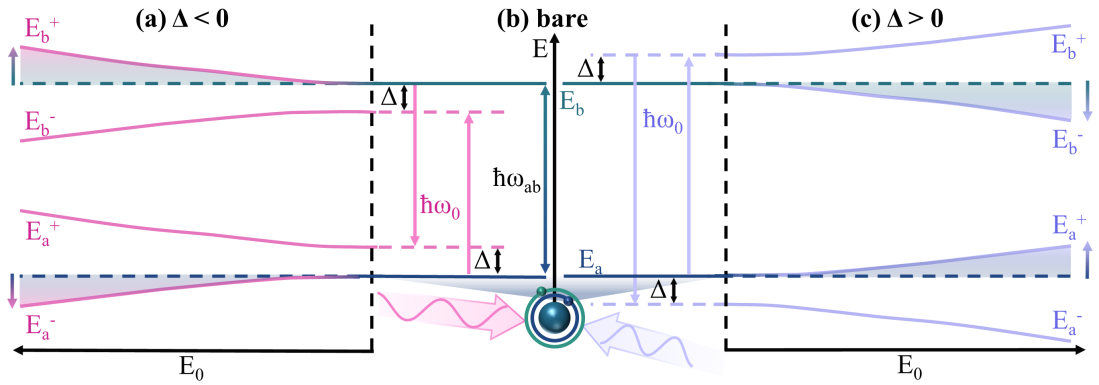

Figure 4.: Energy levels of laser-dressed states. **(b)** Two bare electronic states are coupled with a single laser creating four dressed states. **(a)** If the laser is red detuned, the energies of the dressed states differ from the blue detuned case in **(c)**, but in both cases, they depend on the electric-field strength of the laser. The energy shifts of the bare states used in Section 4.1 and discussed in Section 5.1 are shaded in green.

Since the generalized Rabi frequency increases with the peak electric-field strength, the eigenenergies in Equation (18) are field-strength dependent as well. Figure 4 illustrates how the bare atomic states (Figure 4b) transition into the dressed states for red detuning ($\Delta < 0$) in Figure 4a, and for blue detuning ($\Delta > 0$) of the driving laser in Figure 4c. These energy shifts and splittings can be measured from a third, unperturbed state [61] or in the fluorescence spectrum [65]. For short and intense driving pulses, the transient energy shifts within the interaction lead to line-shape asymmetry changes instead, as discussed in the first publication in Section 4.1. But for high intensities, the energy-shift-based argumentation comes to its limit, and it will be discussed in Chapter 5, that considering the dressed-state populations leads to a more precise description. To this end, the bare atomic states $|\psi_{a,b}\rangle$ are not eigenstates in the presence of the electromagnetic field anymore, thus the time-dependent coefficients $c_{a,b}(t)$ have to be calculated. In the case of only the $|\psi_a\rangle$ state being initially populated, following solutions can be derived for a continuous driving laser in the RWA [62]:

$$\tilde{c}_a(t) = \cos\left(\frac{\tilde{\Omega}_R t}{2}\right) + i\frac{\Delta}{\tilde{\Omega}_R} \cdot \sin\left(\frac{\tilde{\Omega}_R t}{2}\right), \tag{19}$$

$$\tilde{c}_b(t) = -i\frac{\Omega_R}{\tilde{\Omega}_R} \cdot \sin\left(\frac{\tilde{\Omega}_R t}{2}\right). \tag{20}$$

This allows to interpret the generalized Rabi-frequency as the oscillation frequency of the state populations (see Figure 5). In contrast to classical rate-equation models, this allows for a maximal population of the upper state $|\psi_b\rangle$. The coupling or superposition of states can be used in several scientific applications, for example it forms the basis for atomic qubits in quantum computers.

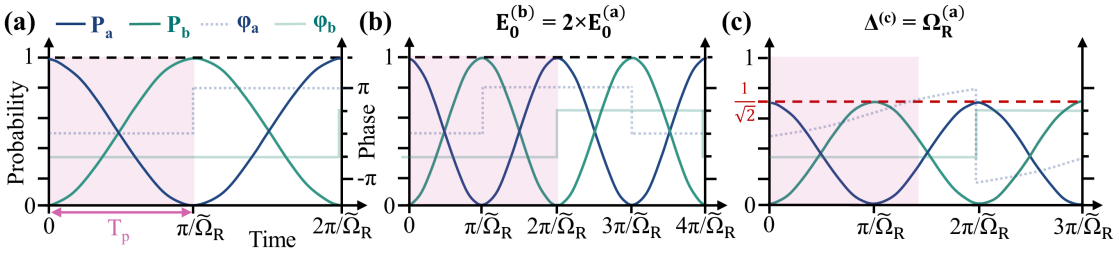

Figure 5.: Rabi oscillations of electronic-state populations in c.w. and rectangular-pulsed laser fields. **(a)** For a resonant c.w. laser, the two populations oscillate between 0 and 1 out-of-phase. At the population minima, phase jumps of π occurs. **(b)** Doubling the field strength of the driving pulse with respect to **(a)** leads to twice the Rabi frequency and the population oscillations and phase jumps occur twice as fast. **(c)** A detuning matching the Rabi-frequency in **(a)** leads to an increase of $\sqrt{2}$ for the generalized Rabi frequency and a decrease of $\sqrt{2}$ for the maximum population. The ground state phase ϕ_a increases continuously (besides periodic 2π-jumps), whereas the excited state phase ϕ_b still exhibit a π-jump. Using a rectangular-pulsed laser with the same duration T_P (pink area) in all three cases instead, leaves the populations and phases at different final values: e.g. (a) $P_a = 0$ vs. (b) P_a=1, which will be further discussed in Section 5.1

In such experiments, a resonant rectangular pulse can be utilized with duration (T_p) much longer than a laser cycle $T_0 = \frac{2\pi}{\omega_0}$, such that the monochromatic description above can still be used. Further, it becomes helpful to consider the final populations at the end of the pulse, which do not change afterwards without further influences. They depend on the laser pulse area $\Theta = \int dt\ E(t) = E_0 \cdot T_p$, which can be chosen to excite the system to $P_e(t = T_p) = 1$, what is known as π-pulse (Figure 5a). Introducing a detuning $\Delta \neq 0$, a full population transfer is not possible anymore (Figure 5c). Alternatively, doubling the pulse duration or doubling the peak field strength, a 2π-pulse can be achieved, which leaves the system unchanged in population with regards to the initial state $P_g(t = T_p) = P_g(t = 0) = 1$—but with phase jumps of π for both states (Figure 5b). Typically, this is achieved by a lower intensity to avoid effects like strong-field ionization, but long enough pulse durations. Yet, transferring this concept to investigate and control ultrafast coherences and dynamics, one needs high peak intensities, because the state lifetime becomes very short. This defines the usage of the term *strong-fields* in the sense of *strong-coupling* of states with ultrashort laser pulses. A generalized Rabi-formalism for pulsed lasers of arbitrary temporal envelope can be introduced with a time-dependent Rabi-frequency $\Omega_R(t) = d_{ab}E(t)/\hbar$ [5, 63], but the differential equations for the state coefficients need to be solved numerically (for non-vanishing Δ). Alternatively, the Hamiltonian in Equation (14) can be diagonalized numerically for every time step—which is the approach chosen in the publications in Sections 4.1 and 4.2.

2.3. Absorption Spectroscopy

Microscopic Dipoles and Macroscopic Polarizations

While the previous sections have introduced how a laser interacts with atoms depending on the electronic structure and the laser properties, it still needs to be considered how these interactions can be detected. For example, if ions and electrons are generated, or alternatively, photons are scattered, detecting those charged particles or the light diffracted away from the initial propagation direction are powerful tools to gain insights into the light-matter interaction and routinely employed in HHG or FEL experiments [66, 67]. Yet, they depend on the formation of such ions, electrons or scattered photons. In contrast, the transmitted light nearly always contains information about the interaction if a spectrally sufficient broad light source is used. As introduced in Sections 2.1 and 2.2, the here employed laser sources contain many photons, but only a few or single photons are involved in the absorption processes. Thus, a cloud of atoms needs to be excited to measure macroscopic changes in the laser spectrum. Here, clouds are considered, as this thesis studies light-matter–interactions solely in the gaseous phase. The photo-excitation of an atomic electron creates a dipole $d(t)$ in the individual atoms, which oscillates with a $\frac{\pi}{2}$-shift with respect to the driving electric field $E_{in}(t)$. If the number of atoms per volume is given as particle density η, their dipoles lead to a macroscopic polarization $P(t)$ of the gas cloud:

$$P(t) = \eta \; d(t). \tag{21}$$

In general, there are many effects to be considered to understand how the polarization of a medium can be generated and expressed as a function of the input electric field, which is typically expressed as a Taylor-expansion:

$$P(t) = \epsilon_0 \; \left[\chi^{(1)} E_{\text{in}}(t) \; + \; \chi^{(n)} E_{\text{in}}^{n}(t) \right], \tag{22}$$

where ϵ_0 is the vacuum permittivity, $\chi^{(1)}$ is the linear electric susceptibility and $\chi^{(2\leq n\in\mathbb{N})}$ are the nth-order nonlinear susceptibilities. The linear term is connected to the refractive index of the medium $n(\omega) = \sqrt{1+\chi(\omega)}$, which, in turn, is connected to the dispersion, $Re(n)$, and linear absorption, $\alpha = Im(n)$. The non-linear terms are connected to n-photon processes. In case of non-perturbative processes as the HHG or Rabi oscillations, the series in Equation (22) does not converge. To understand the back-action of the induced polarization on the driving field, Maxwell's equation can be employed and a wave equation for the total electric field can be derived [59], including the source-term $\frac{\partial^2 P}{\partial t^2}$ for a newly-generated electric field $E_{\text{gen}}(t)$. Classically, this can be interpreted as the Lamor theorem: accelerated charges—the oscillating dipole moment—emit light: $E_{\text{gen}}(t)$.

Absorption Line-Shape Changes in Low Gas Densities

For a sufficiently low gas density, the generated electric field is negligible compared to the original field and does not interact with the atoms in the gas cloud again [68]. Therefore, the whole (macroscopic) interaction can be simplified to a single-particle response in form of the induced dipole, linearly scaling with the number of atoms. In the case of a weak, thus linear-driving laser, exciting an atomic electron resonantly, the emitted light has the same frequency as the driving frequency, but is in total phase-shifted by π. This arises from a second $\frac{\pi}{2}$ shift between the generated electric field with respect to the dipole. The emitted light can be measured as fluorescence in any given direction but the forward propagation direction of the laser. There, the driving and induced electric field interfere destructively. Either scanning the wavelength of the laser across the resonance or, alternatively, using a pulsed laser with a bandwidth broader than the resonance width, this destructive interference can be measured as a minimum in the transmitted laser spectrum. To disentangle the contributions of the initial driving spectrum from the atomic absorption features, it is helpful to measure the spectrum before, $|E_{\text{in}}(\omega)|^2$, and after the interaction, $|E_{\text{tot}}(\omega) = E_{\text{in}}(\omega) + E_{\text{gen}}(\omega)|^2$, and calculate the *optical density (OD)*:

$$OD(\omega) = -log\left(\frac{|E_{\text{tot}}(\omega)|^2}{|E_{\text{in}}(\omega)|^2}\right) = -log\left(\frac{|E_{\text{in}}(\omega) + i\ \eta d(\omega)|^2}{|E_{\text{in}}(\omega)|^2}\right), \tag{23}$$

where Equation (21) and $e^{\frac{\pi}{2}} = i$ are used to express the generated electric field as $E_{\text{gen}}(\omega) = i\eta d(\omega)$. For the weak and linear interaction of the incoming field with the atoms, the OD is directly proportional to the linear absorption coefficient $\alpha(\omega)$ of the medium and thereby also proportional to the single-atom absorption cross section $\sigma(\omega) = \frac{\alpha(\omega)}{\eta}$. While the later is a commonly used quantity to describe and evaluate (linear) absorption experiments, in the case of intense driving lasers and hence non-linear interactions (in the spirit of the non-linear terms in Equation (22)), it is not a useful concept anymore. In contrast, the OD can always be defined and measured, and is therefore used within this thesis instead.

The connection of temporal dipole moment and spectral absorption as well as the changes in the OD due to ultrashort and intense driving pulses are illustrated in Figure 6 for a two electronic-level system. In Figure 6a, the temporal profile of a rectangular pulse (violet) and the induced temporal dipole (blue) are shown. The pulse duration T_P is much shorter than the exponential lifetime $\frac{1}{\Gamma}$ of the excited state, which is referred to as the *impulsive limit*. A spectral measurement of the OD (Equation (23)) can be performed (in principle) with a single pulse because the spectral bandwidth of the pulse is much broader than the resonance width Γ. The resulting OD in Figure 6b is a Lorentzian line:

$$OD_{\text{Lorentzian}}(\omega) \sim \frac{1}{1-\epsilon^2}, \quad \text{with } \epsilon = \frac{\hbar\omega - E_r}{\Gamma/2} \tag{24}$$

which is typical for an excited electron state decaying via spontaneous emission. If instead an autoionizing resonance is excited, as the doubly excited $sp_{2,n+}$ (^{1}P) states in helium (Section 2.2.2), the interference of the direct ionization pathway and autoionization via the doubly-excited state

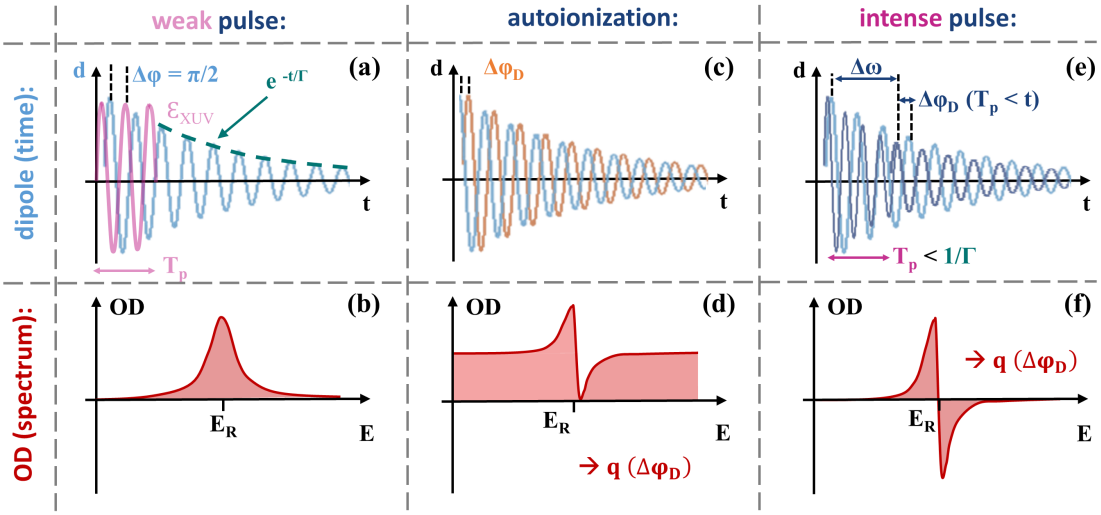

Figure 6.: Spectral absorption of an electronic resonance **(b),(d),(f)** for three different cases of induced dipole moments **(a),(c),(e)**. **(a)** A weak pulse of duration T_P (light violet) induces a dipole (light blue) in a two-level system, which decays exponentially with the excited-state lifetime $\frac{\hbar}{\Gamma}$. **(b)** Resulting absorption in the OD spectrum has a Lorentzian line shape. **(c)** A weak pulse (as in (a), not shown) excites an autoionizing state, inducing a dipole with phase shift $\Delta\varphi_D$ (orange) with respect to the dipole in (a). **(d)** The resulting absorption has an asymmetric Fano-shape. **(e)** If an intense pulse drives the two-level system, a phase shift in the dipole moment (dark blue) can be induced with respect to the weak case (light blue). **(f)** As in (d), this leads to a Fano-like line shape for the two-level system.

leads to an asymmetric line shape in the OD (Figure 6d):

$$OD_{\text{Fano}}(\omega) \sim \frac{(\epsilon + q)^2}{1 + \epsilon^2}, \tag{25}$$

which is called after U. Fano, who first introduced a full mathematical description of the autoionization process [47]. Here, q is the asymmetry parameter, which is proportional to the probability ratio of the two ionization pathways. In addition, the q-parameter can be connected to a temporal phase shift of the dipole moment, $\Delta\varphi_D$ [69] (Figure 6c):

$$q(\Delta\varphi_D) = -\cot(\frac{\Delta\varphi_D}{2}). \tag{26}$$

It has been shown [69], that an intense IR laser pulse can additionally induce energy-shifts of the weakly XUV-excited electronic states in helium and therefore phase-shift the dipole moment in time, such that the Fano lines can be modified in their asymmetry and made Lorentzian-like—or the other way around in case of the singly excited states. The same mechanism can be used with an intense XUV pulse to couple two states and thereby shift the dipole phase (Figure 6e)

and modify the absorption line shape symmetry (Figure 6f). While this was shown for the $2s2p$ autoionizing state in helium [4], the state-coupling mechanism is general and can be used in any two-level system. This is investigated in detail in the two publications in Sections 4.1 and 4.2. In total, this concept illustrates how absorption spectroscopy can be used to measure the underlying light-matter-interaction. For the weak and linear regime, the $OD(\omega)$ is independent of the laser peak intensity I_0, because both $|E_{\text{in}}|^2$ and $|E_{\text{gen}}|^2$ (see Equations (10) and (23)) scale linearly with I_0. The absorption features, especially the resonance position ω_R, are determined by the electronic structure of the excited atom under study and can be used as spectral absorption fingerprints to identify atomic or ionic species. This will be used in the identification of oxygen fragments in the experiment presented in Section 4.3. The modifications of the electronic structure can also be detected in absorption spectroscopy for intense enough pulses by means of absorption changes, allowing to reconstruct the temporal dipole response [70], but the underlying state-population *dynamics* cannot be resolved. For the case of a single pulse, a convolutional neural network can be employed for the population reconstruction, which will be introduced in Section 2.4 and discussed in the publication in Section 4.2. Alternatively, a combination of two pulses in a *pump-probe* scheme with controllable time delay between the pulses can be used in *time-resolved absorption spectroscopy*. This is used in the third publication in Section 4.3.

Propagation Effects in High Gas Densities

The discussion above relies on the assumption of a sufficiently low gas density, such that the generated light does not interact again with the medium. This assumption is well justified in many typical XUV/x-ray absorption experiments, because of two reasons:

(i) From a scientific perspective, the investigated XUV/x-ray-interaction is meant to be studied without propagation effects to investigate quantum dynamics of independent atoms.

(ii) From a technical perspective, XUV/x-ray-based experiments require (ultra-high-)vacuum setups to prevent the XUV/x-ray light to be absorbed by air, and high target-gas densities are challenging under these conditions. Yet, the propagation of XUV and x-ray pulses in high gas densities is a promising field of research [63, 68, 71–79].

To investigate the XUV/x-ray propagation in dense gas clouds theoretically, the coupled Schrödinger- and Maxwell-equations need to be solved numerically, which is out of the scope for this thesis. The reader is referred to [63, 76–79] for more information. First experiments in dense gaseous media have been performed, utilizing target pressures of tens to hundreds of mbar and propagation distances of several mm up to 1 cm [68, 71–75]. To further increase the capabilities of XUV and x-ray propagation in high-density gases, an experimental setup was build as part of this thesis project (Section 3.2) allowing for absorption measurements with target pressures up to 6 bar and variable propagation lengths ranging from 2 mm to 8 mm. First results are discussed in Chapter 5.

2.4. Convolutional Neural Networks

With the theoretical background presented up to this point, the electronic excitations within an atom and the resulting absorption profiles can be calculated—setting the foundation for the publication in Section 4.1. Yet, the electron dynamics, especially in the case of Rabi oscillations, cannot be directly reconstructed from the absorption spectra. If the underlying equations are tried to be inverted, one finds that spectral phases are lost in absorption measurements, combined with the problem that at least two complex coefficients need to be determined from the dipole moment. This does not necessarily mean, that a correlation between OD and populations does not exist nor that an arbitrary function could not approximate an inversion. Finding such inversion approximation motivates the usage of sophisticated problem-solving numerical methods, known as *artificial intelligence (AI)*. A short introduction of the field is given in the following:
The AI sub-field of *machine learning* aims to construct a function by iterative optimization of its parameters. This 'learning' procedure is called *deep*, if many layers of nested functions are utilized to express a preferably arbitrary function. This process goes hand-in-hand with a large amount of *training* data to find the optimal values for the many parameters involved. If the learned function can also be used on previously unseen *test* data, the machine learning algorithm is able to *generalize* efficiently and would be an ideal tool for the above introduced task of predicting electron populations from absorption spectra. One of the most used archetype of machine learning are *neural networks*. They are build in a layered way from many (linear) units, the *neurons*, and (non-linear) activations to create a network. Absorption spectra are highly-correlated along the spectral axis, i.e. spectral intensities depend on their neighboring intensities. This is conceptually similar to images of objects, which are spatially correlated to create the features of a given object. In such cases, *convolutional* neural networks (CNNs) have proven to be highly effective to learn and classify images of objects, such as animals or handwritten digits. Hence, a CNN for the reconstruction of electron populations from absorption spectra is used in the second publication in Section 4.2.
In the following, some of the key machine learning concepts, on which the CNN in Section 4.2 is based on, will be explained briefly following [80]. The complete structure of this particular CNN is shown in Figure 7a. A general introduction into the broad field of deep learning and neural networks can be found in [80, 81]. It should be noted anyway, that neural networks are typically so complex and the field is developing rapidly, such that there is rarely a single, precise ML solution to any given task. Instead, a lot of detailed engineering as well as empirical and heuristic approaches are involved for finding a state-of-the-art optimal—or simply appropriate—network.

2.4.1. Single Neuron

The main building block of every neural network are single computational units, so called *neurons*, which are modeled after their biological equivalent. They take a pair of input (X) and output (Y) variables (which can be scalar, vectors or matrices) to learn a function f to predict $\hat{Y} = f(X)$, by

minimizing the loss L between predicted $\hat{Y}$ and target Y. The loss is utilized to perform the actual learning of the network—as shown later on. The function f is typically a linear combination of input elements $x_i \in X$ with weights w_i—which can be expressed as vector multiplication—followed up by a non-linear activation function Φ:

$$\hat{Y} = \Phi\left(\sum_i w_i \cdot x_i + b\right). \tag{27}$$

Here, b is the bias, which is added as an offset to the weighted input sum, before the activation. It is necessary, because any neural network or machine learning program makes implicit assumptions about the functions it tries to model due to its own structure. These assumptions can be regarded as bias (as for human behavior). It represents an additional learnable parameter of the network and can be added to the vectors or matrices of weights, and thus will not be further mentioned explicitly. A scheme of a single neuron is shown in Figure 7b. The choice of the activation function will be discussed below. Since a single neuron is not sufficient to model complex functions, larger networks are necessary.

2.4.2. Architecture of a Convolutional Neural Network

For a neural network, the individual neurons are ordered within layers, which in turn can be stacked one after another. Within a layer, the functionality stays the same, while different layers can have different purposes. In the case of a one-dimensional input array X (layer r) of length d_r and one-dimensional output vector Y (layer $r+1$) of length d_{r+1}, the weights of the layer $r+1$ can be ordered in an $d_r \times d_{r+1}$ matrix W with elements w_{ij}. Further, the vector-multiplication in Equation (27) needs to be replaced by the multiplication of matrix W with vector X to calculate the output array Y. It is important to note, that a non-linear activation is necessary to achieve benefits from the multi-layering, because several sequential linear-only layers can be reduced to a single linear layer [80, 81]. Here, only the *Rectified Linear Unit (ReLU)* function will be considered as activation, which is defined as:

$$\text{ReLU}\,(x) = \begin{cases} x, & x \geq 0 \\ 0, & x < 0 \end{cases}. \tag{28}$$

For non-scalar variables, the function is applied element-wise. While other activation functions exist and have been used in the past, the ReLU function is utilized in almost all state-of-the-art convolutional networks, if the input data does not demand otherwise, and hence in the publication in Section 4.2 as well. This choice of the activation function is mainly governed by how efficient the whole network can learn, while it does not change its overall capability significantly. In contrast, the choice of the weights w (defining the function f), allows to define the specific functionality of an individual layer, which determines what overall task the whole network is capable of achieving. For example, a *convolutional* layer is defined through the usage of *filters*, which have a certain

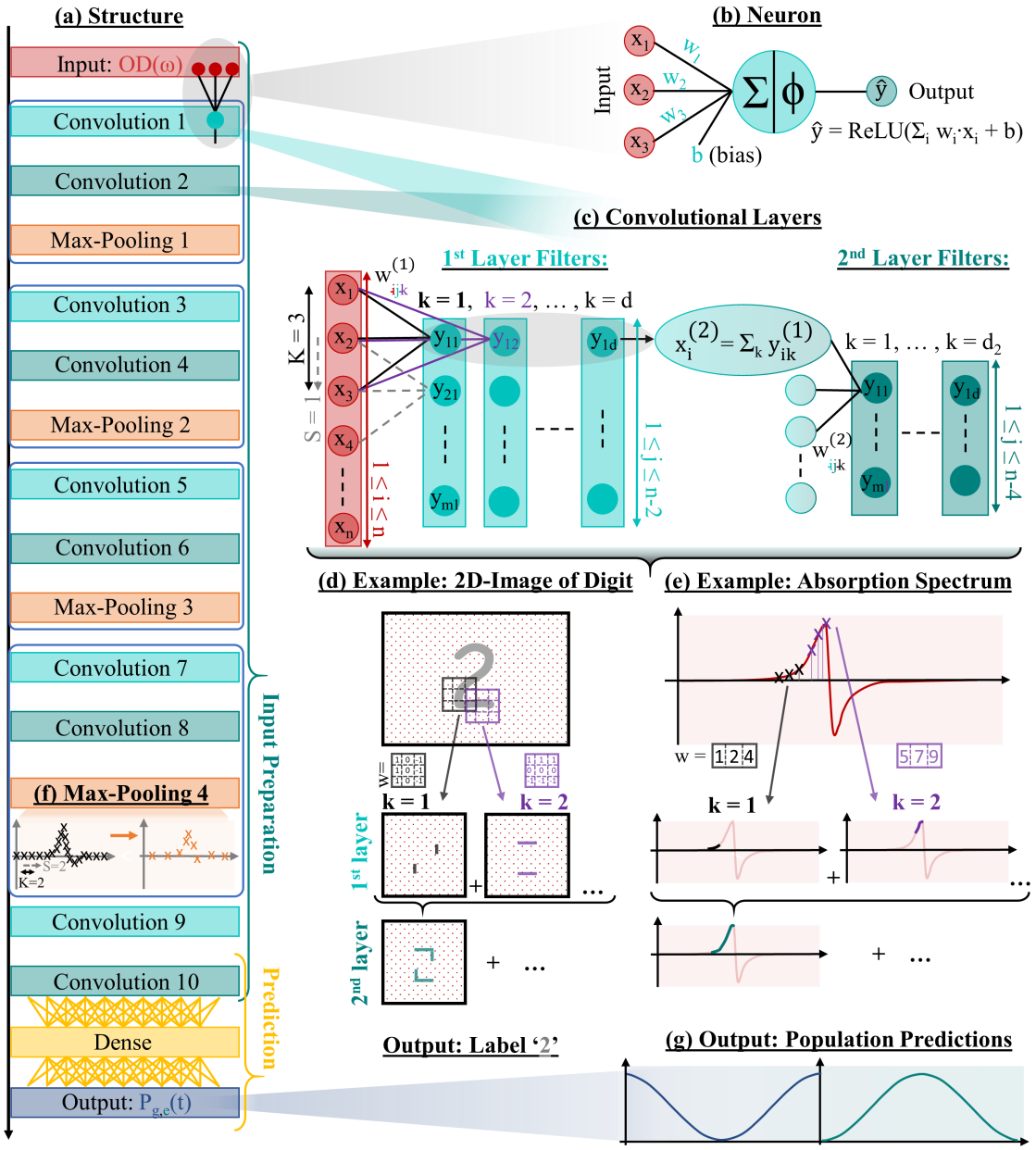

Figure 7.: Overview of different elements within a convolutional neural network. **(a)** Structure of the CNN used in Section 4.2. **(b)** Illustration how a single neuron calculates its output. **(c)** Illustration of convolutional layers. The first convolutional layer of the network (containing several filters) operates on the one-dimensional input layer, while the second (and all subsequent) layers operate on two-dimensional inputs, for which the different input filters are summed up. **(d)** Example of how the first two layers of another CNN can identify edges and corners in an image of the digit '2'. **(e)** Analogue, features of an absorption line can be identified with convolutional filters in the here shown network. **(f)** Illustration of a max-pooling layer. **(g)** Lastly, the CNN reconstructs or predicts electron-state populations.

size K (*kernel*) and their filter shape is given by their weights w_i ($1 \leq i \leq K$). The single output of a convolutional filter applied at a fixed position within an input array is calculated as for the neuron (see Equation (27)). In addition, the filter is then moved across the input layer with step size S (*stride*). Within this thesis, only the case S=1 is used, resulting in an output array with size n-K-1 (n is the input array size). The same filter weights are used while moving the filter across the whole input array. While optimizing the weights (as discussed later), the neural network learns which relevant structures the input data contains. Output elements with large values indicate positions, where the input data is structured in a similar way as the filter shape. Further, different filters can be defined within a single convolutional layer by different sets of weights. If d_f filters are used in a single layer, the output will be of shape $d_f \times (n - K + 1)$. The *expressive power* of a convolutional network, i.e. the capability to recognize complex input shapes and model arbitrary functions, comes from applying several convolutional filters sequentially. For example, a second convolutional layer (with the same kernel as the one above) is able to identify larger structures of size 2K-1 (known as *receptive field*) by combining the filters of the previous layer. It therefore sums over the d_f-dimensional axis of the previous layer output. More formally, if the p-th filter in the q-th layer of a network has the weights: $w_{ik}^{(p,q)}$ ($1 \leq i \leq n$; $1 \leq k \leq d_f^{(q)}$) and the input: $h_{ik}^{(q)}$, the convolution will have the output:

$$h_{ip}^{(q+1)} = \sum_{r=1}^{K} \sum_{k=1}^{d_f^{(q)}} w_{rk}^{(p,q)} h_{i+r-(K/2-1)}^{(q)}, \quad \forall\ i, p. \tag{29}$$

This convolutional operation is visualized in Figure 7c for the first two convolutional layers of the network utilizing filters with $K = 3$, $S = 1$, $d_f = d$.

A well-known example for the task of a convolutional network is the classification of hand-written digits as illustrated in Figure 7d. The mathematical framework would need to be extended for the two-dimensional inputs, which is out of the scope of this thesis. The reader is referred to [80, 81] for more information about multi-dimensional convolutions. Here, only the functionality is illustrated for visualization purposes. In the first layer, the convolutional filters learn to detect horizontal and vertical *edges* such that the second layer learns to identify *corner*-like features. In an similar manner, a convolutional network can learn the spectral features of a resonant absorption profile, as shown in Figure 7e.

For later layers, more filters are used in parallel per layer, because the structures become larger and more complex. Further, to cover both small and large spatial/spectral features with the neural network, filters of small kernel sizes (here = 3) and many subsequent layers are used. To accelerate the growth of the receptive field, i.e. enabling the network to recognize larger input structures faster, *max-pooling* layers are used after each couple of convolutional layers. They take an input of size K and give out its maximum element. With a stride greater than one, this allows for the above mentioned faster reduction of the receptive field. The max-pooling operation is illustrated for K=2 and S=2 in Figure 7f. It also introduces further non-linearity into the

network, which is helpful with its overall prediction capability. All convolutional, ReLU and max-pooling layers together can be regarded as input preparation, or *feature extraction*, allowing the CNN to recognize certain patterns. The extracted features are passed to a *dense* layer in the final step to predict the desired quantities, like a digit label or electron populations. For that purpose, all inputs of the dense-layer are connected to all neurons in the dense layer, and in turn, all of theses dense neurons are fully-connected to all the elements of the output layer. This introduces a large amount of parameters within the prediction step to allow for a highly non-linear and arbitrary function to be approximated. In case of the digit classification, the output layer contains a logistic regression as activation function, returning the digit label with the highest probability. In the case of the CNN with absorption spectra as input, a linear activation is used to reconstruct the time-dependent populations of the electronic states (Figure 7g).

2.4.3. Learning via Back-Propagation

While the CNN structure is typically chosen by the user to aim for specific pattern detection, only the autonomous learning, or *training*, process enables correct CNN predictions. This is achieved via optimization of the network's parameters: The loss L of a training data set is minimized by variation of the network's parameters. To quantify the loss, for regression problems the often implemented *mean square error (MSE)* of the prediction $\hat{Y}$ of data point o with regards to the actual output Y is utilized throughout this thesis:

$$L_o = \frac{1}{N} \sum_{j=1}^{N} |\hat{Y_j} - Y_j|^2 \tag{30}$$

The loss of the whole training data set is defined as the sum over all losses of its data points: $L = \sum_o L_o$. The CNN is trained optimally (in theory) when the following procedure is used until convergence of the loss function:

(i) parameters (weights) are randomly initialized,

(ii) predictions and loss are calculated for the given set of parameters,

(iii) weights are changed along the negative gradient of the loss function ∇L (*gradient descent*):

$$w_{ik}^{(p,q)} - \alpha \nabla L \rightarrow w_{ik}^{(p,q)}, \quad \forall\ i,k,p,q, \tag{31}$$

where α is the learning rate which will be discussed later,

(iv) steps (ii) and (iii) are repeated until convergence.

Yet, calculating the gradient of the highly complex, nested functions of a deep CNN is analytically unfeasible. The key idea is therefore to approximate the actual loss piece-wise, which makes

the training task practically implementable. To this end, the total element-wise derivatives of the gradient ∇L can be expressed with help of the *chain rule* of differential calculus utilizing the layered structure of the CNN: The derivative of a function $f(g_1(x), ..., g_N(x))$ depending on multiple input functions $g_i(x)$ is hereby given by:

$$\frac{\partial f(g_1(x), ..., g_N(x))}{\partial x} = \sum_i^N \underbrace{\frac{\partial f(g_1(x),...,g_N(x))}{\partial g_i(x)}}_{\text{outer derivative}} \underbrace{\frac{\partial g_i(x)}{\partial x}}_{\text{inner derivative}} . \tag{32}$$

Equation (32) can be utilized iteratively on the inner derivatives, because the functions $g_i(h_j(x))$ will depend on a own set of function h_j of the previous layer, unless the input layer is reached. In this manner, the loss can be calculated as a function of all layers and corresponding weights starting from the output layer—which is therefore called *back-propagation*. In general, the analytical forms of all inner and outer derivatives at any layer can be derived from the layer structure. Importantly, while performing the back-propagation, the outer derivatives $\frac{\partial f}{\partial g_i}$ can immediately be evaluated and stored numerically, because all input functions g_i have already been evaluated during the *forward-propagation* phase (step (ii) above). Hence, the analytical closed form of the total loss function does not need to be known and computations are significantly reduced to a subset of parameters by only evaluating the outer derivatives per layer. In the case of the CNN, this means the partial derivatives of convolutional operations, ReLU activations, max-pooling and dense layers need to be known. For the convolutional and dense layers, multi-dimensional arrays are reshaped into one-dimensional vector inputs x_i and outputs y_j. The weights of the corresponding layer are given in form of a matrix with elements w_{ij} and the derivative $\frac{\partial y}{\partial x}$ is given through the transposed matrix:

$$\frac{\partial y_j}{\partial x_i} = \left[w^T\right]_{ij} . \tag{33}$$

Further, the vector version of the chain rule hereby replaces scalar multiplications with matrix multiplications. The reader is referred to [80] for more details. For the (element-wise) ReLU activation the derivative is zero for non-negative input and 1 otherwise. The derivative of a max-pooling layer is zero in all cases, but for the maximal input, where it returns that maximum value.

While the previous concepts describe how individual iterations over the complete data set (*epochs*) of the weights optimization are carried out, the complete gradient descent over all iterations comes with its own convergence and calculation time problems. First, the computation of the loss over thousands or millions of input data points still takes too much time and resources. For practical reasons, the procedure above is calculated for small randomly-chosen sub-parts, or *mini-batches*, of the input data allowing for a good trade-off between speed and stability in minimizing the overall loss. Since the gradients resulting from the random mini-batches introduce a stochastic deviation from the actual gradient of the whole data set, this procedure is called

stochastic gradient descent. Furthermore, frequent problems in (stochastic) gradient descent are local minima or saddle points of the loss and too fast, slow or oscillating parameter updates. Many of them are connected to the choice of the learning rate α in Equation (31), which determines how fast one moves within the multi-dimensional loss landscape. Therefore, the learning rate is typically updated for (i) different iterations and (ii) for different direction components of the gradient:

(i) A common approach for iteration-based updates is *momentum*-based learning, which memorizes previous update steps to create an analogue to a classical-mechanical momentum and allows to avoid local minima among other benefits. It effectively changes the amplitude of the gradient step. For example, the *Nesterov Momentum* replaces the parameter updates in Equation (31) with a two-fold update step:

$$\beta v - \alpha \nabla L(w + \beta v) \to v, \qquad w + v \to w, \tag{34}$$

where $\beta \in (0, 1)$ is the momentum parameter, which needs to be chosen together with α before training.

(ii) In deep networks, the locally steepest gradient update does not necessary point into the direction of the global minimum. Further, not all parameter directions have equal partial derivative magnitudes—in fact, they can be order of magnitudes different. In such a scenario, the gradient descent could oscillate within several dimensions with each iteration, but barely make progress in other directions. Therefore, *parameter-specific learning rates* can be used, which effectively changes the direction of the gradient for an overall more consistent update progress. For example, *RMSProp* applies an exponentially-decaying averaging over the history of each (squared) gradient component (n), which is used as damping factor of the individual parameter update:

$$\rho A_n + (1 - \rho) \left(\tfrac{\partial L}{\partial w_n} \right)^2 \to A_n, \qquad w_n - \frac{\alpha}{\sqrt{A_n}} \frac{\partial L}{\partial w_n} \to w_n, \tag{35}$$

with $\rho \in (0, 1)$.

Furthermore, the two approaches of momentum and parameter-specific learning can be combined. A frequently used gradient-descent optimizer, which does so, is the *ADAM* algorithm. While it utilizes the RMSProp exactly as defined in Equation (35), it in addition also uses a exponentially-smoothed momentum update. For more (mathematical) details, the reader is referred to [80, 82]. The Adam optimizer is used within the CNN of the publication in Section 4.2.
The loss should decrease with the iteration count for a successful training of the CNN. In that case, a *validation* sub-set of the input data can be used to verify, the CNN predicts the output of previously unseen data reasonably well with respect to the training phase. This helps ensuring that the CNN does not *overfit* the training data, i.e. optimizing its weights too narrowly on the given input such that the predictions for the validation set are not accurate. In that case, the

validation learning curve—loss as function of iteration/epoch—would start increasing for later iterations, whereas the training learning curve does not. This would mean the network looses its ability to generalize in favor of memorizing training data. Adapting the CNN structure and amount of parameters can help solving the issue. Such behavior was not found for the CNN used in the publication in Section 4.2 and will thus not be discussed further.
Eventually, if the CNN is setup, trained and validated properly, it can be used on any unseen test data of the same type as the training data. In case for simulated electron population dynamics and corresponding absorption lines, the results are presented in Section 4.2. To use the CNN on experimental data as well, the training data would need to be changed to a mixture of the simulation and experimental data, for which the populations can be estimated without the CNN—for example in the weak-field limit using perturbation theory as in Equation (10) (see Section 2.2.2). This approach will be elaborated in more detail in the discussion in Chapter 5.

2.5. Electrons in Molecules

After the excursion into neural networks in the previous section, here the quantum-mechanical basis of molecules is revisited. Thematically, it can be seen as extension of Section 2.2—the electronic structure of atoms—yet it further leads to the foundation of chemical properties and reactions. To understand how atoms are bound within molecules and how molecular electronic structure looks like, the following introduction summarizes the main concepts, which can be found elaborated in more depth in text books like [45, 83].
As for atoms, the kinetic energy of all electrons $\hat{T}_e$ and—now all—nuclei as well as the sum of all Coulomb potentials $\hat{V}_C$ between each two particles, $\hat{V}_{\text{tot}}$, need to be considered for the Hamiltonian:

$$\hat{H} = \hat{T}_N + \hat{T}_e + \hat{V}_{\text{tot}} \tag{36}$$

While the Coulomb force $F_C = -\nabla V_C$ is equal for both nuclei and electrons, the electron mass m_e is much smaller than the nuclear mass m_N, thus the resulting momenta are much lower for nuclei than for electrons. As a result, the nuclear (kinetic) energy is expected to be smaller than the electronic one, hence the nuclei move slower than the electrons. This can be quantified with following considerations: Estimating the electron kinetic energy from the atomic size and using the uncertainty principle and the Viral theorem [45] leads to an order of $\leq$10 eV, which translates to photon energies in the VIS and UV spectral regime. Considering harmonic vibrations for the nuclei leads to a factor of $\sqrt{\frac{m_e}{M_N}} \sim 10^{-2}$ for the vibrational energies $\sim$0.1 eV (near-IR regime). Assuming a rigid rotator for the nuclear angular momentum leads to a factor of $\frac{m_e}{M_N} \sim 10^{-3}$ to 10^{-5} for the rotational energies $\leq$ meV (far-IR to microwave regime). Energies translating to the XUV or x-ray regime often lead to ionization followed up by dissociation, since too much energy is deposited into the molecular system to remain neutral or stable. This illustrates, why the following discussion will mainly be focused on the electronic structure to, ultimately, understand the interaction of XUV light with the oxygen molecule.

2.5.1. Born Oppenheimer Approximation

To translate the considerations above into equations, typically center-of-(nuclear) mass (COM) coordinates are introduced for the individual electrons $\vec{r}_i$ and nuclei $\vec{R}_i$, where for convenience $\vec{r}$ and $\vec{R}$ are taken to represent the entity of all electronic and nuclear coordinates, respectively. The spatial part of the total molecular wavefunction $\Psi(R, r)$ can then be expressed in the basis of nuclear, $F(\vec{R})$, and electronic wavefunctions $\phi(\vec{r})$:

$$\Psi(R, r) = \sum_q F_q(R)\phi_q(r) \tag{37}$$

This leads to coupled differential equations when the Hamiltonian in Equation (36) is inserted in the SEQ (Equation (6)). As introduced above, the central idea is to separate electronic and

nuclear motion by treating the nuclei as fixed in space, while solving for the electronic motion. This is known as *adiabatic* or *Born Oppenheimer (BO) approximation*. Formally, this applies assuming:

(i) $|\phi_q\rangle$ does not depend on the nuclear coordinate, $\frac{\partial \phi_q(R)}{\partial R} \approx 0$, and

(ii) no coupling between electronic states due to nuclear orbital angular momentum $\hat{N}$ exists.

The BO approximation leads to the decoupling of the differential equations of the TDSE. For that purpose, first the electronic TDSE for a given R needs to be solved, resulting in the electronic wavefunctions and energies $E_q(R)$, before the electronic energies can be used as R-dependent potential for the nuclear motion.

2.5.2. Symmetry Properties

Besides the BO approximation, the symmetry of the molecule is crucial to describe its properties, especially the total electronic wavefunction, which needs to be determined first in the BO approximation. In general, group theory can be employed to describe molecular symmetries [84]. Here, only homonuclear diatomic molecules with cylindrical symmetry (in group theory denoted as: $D_{\infty h}$) will be considered, because the O_2 molecule is the target of interest. Because homonuclear diatomic molecules as O_2 have cylindrical instead of spherical symmetry, the electronic Hamiltonian $\hat{H}_e = \hat{T}_e + \hat{V}_{\text{tot}}$ does not have common eigenstates with the total electronic angular momentum $\hat{L}^2$. Yet, $\hat{L}_z$ has common eigenstates with $\hat{H}_e$, where z is the direction of the inter-nuclear axis. Therefore, the angular momentum projection: $\Lambda = |M_L|$ (with M_L eigenvalues of $\hat{L}_z$) are considered to describe molecular eigenstates instead of the total angular momentum L for atoms. They are labeled: $\Lambda = \{0, 1, 2, ...\} \rightarrow \{\Sigma, \Pi, \Delta ...\}$ for the total (multi-)electronic states and with respective lowercase letters for single-electron orbitals. Further, two symmetry transformations are relevant for homonuclear diatomic molecules:

(I) The reflection of all electronic coordinates with respect to the origin $\vec{O}$ in the COM-system. The parity operator, $\hat{P}$: $\vec{r} \rightarrow -\vec{r}$, does exactly so, as in the atomic case, and in addition has common eigenstates with L_z. If the wavefunctions do not flip sign under $\hat{P}$, they are labeled as *gerade (g)* states, whereas the ones which do flip sign are called *ungerade (u)* states.

(II) The reflections in all planes containing the internuclear axis $\vec{z}$, e.g. $\hat{A}_y$: $y \rightarrow -y$, have always common eigenfunctions with $\hat{H}_e$, and also with $\hat{L}_z$ for $\Lambda = 0$ (i.e. Σ-states). As for the parity operator, applying $\hat{A}_y^2$ twice, leads to identity and only eigenvalues of ± 1 exist for $\hat{A}_y$. The states symmetric under $\hat{A}_y$ (with positive eigenvalue) are labeled $\Sigma_{g,u}^+$ and distinguishable in energy from the ones anti-symmetric under $\hat{A}_y$, labeled $\Sigma_{g,u}^-$.

In general, the total electronic configuration in molecules is labeled as ${}^{2S+1}\Lambda_{g,u}^{\pm}$, where the $\pm$ label is omitted for $\Lambda \neq 0$ states, which are doubly degenerate in energy with respect to the $\hat{A}_y$ operator. Here, the term $2S + 1$ is the spin multiplicity (neglecting spin-orbit coupling),

where $S = |\hat{S}|$ is the total electronic spin defined as for multi-electron atoms (Section 2.2.1). The total electronic wavefunction must be anti-symmetric, such that symmetric spin wavefunctions can only be paired with anti-symmetric spatial wavefunctions and vice versa. In the following, the multi-electron states are constructed as linear combinations from different (spatial) basis functions, but always such that they obey the here presented symmetry properties.

2.5.3. Multi-Electron Molecular Orbitals

It is remarkable, how much of the total molecular structure can already be understood just considering symmetry properties and the large mass ratio between electrons and nuclei. To actually solve the TDSE (in the BO approximation), one needs to construct molecular many-electronic orbitals, similar as for multi-electron atoms, but in addition also taking into account several nuclei. For doing so, it is helpful to first consider the simplest molecule, $H_2{}^+$, and the simplest multi-electron molecule, H_2. The single-electron molecular orbitals (MOs) are build by a *linear combination of atomic orbitals (LCAO)* and employing the variational method. Multi-electron MOs for H_2 are constructed on the basis of the single-electron MOs again with the variational method. This approach gives straightforward insight into the *covalent* part (electron(s) shared between nuclei) and *ionic* part (electron(s) exchanged between nuclei) of molecular bonds. While heteronuclear molecules can form ionic bonds because of different atomic elctronegativities, homonuclear molecules are typically convalently bound. Alternatively, one can consider multi-electron atomic orbitals (AOs) as in Section 2.2.1 first, and build multi-electron MOs from there. Breaking down the TDSE, naturally leads to solving the so-called *Coulomb integral*, i.e. the spatial charge density overlap between the nuclei. Comparing the charge density overlap of a MO to the charge densities of the individual AOs it is made of, leads to an intuitive understanding of molecular bonding. The MO is *bonding*, i.e. keeping the molecule together, when its internuclear charge density is higher than of the individual AOs. If the MO charge density is lower than of the two AOs, the MO leads to *dissociation* of the molecule, and the electronic configuration called *anti-bonding*.

In general, and especially for the O_2 molecule, the first approach, known as *Hund-Mulliken method* of constructing multi-electron MOs, is used. The idea of charge density overlap and bonding can be applied anyhow and one finds, that only the outer-most valence electron wavefunctions have enough spatial overlap between each other, such that the charge density can significantly change when forming a MO. Therefore, typically only valence electrons contribute to the formation of molecular bonds. In the case of the O_2 molecule, mainly the outer-most atomic $2p$ orbitals are involved in the formation of molecular bonds, while the inner-shell $2s$ and even more so the $1s$ core orbitals keep atomic character [85] and thus are localized within the molecule. Especially, the $2s$ and $2p$ energy spacing is large enough, that no hybridization takes place. As in the atomic case, the Hartree-Fock method followed up by the Configuration Interaction method can be employed to determine the molecular orbitals and energies more precisely [86].

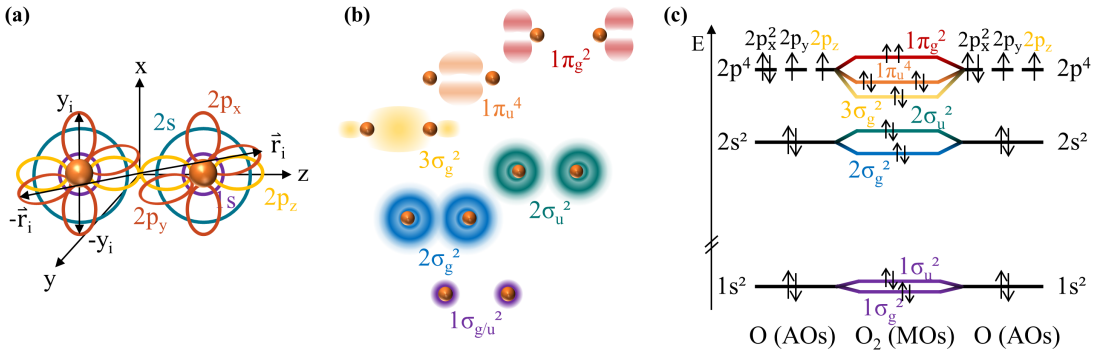

Figure 8.: Electronic Molecular Orbitals and Energy Levels of the O_2 ground state. **(a)** Atomic electron orbitals of two oxygen atoms involved the molecular formation. The COM coordinates system as well as the two transformation operators $\hat{A}_y(y_i) = -y_i$ and $\hat{P}(\vec{r}_i) = -\vec{r}_i$ are shown. **(b)** Molecular orbitals formed in the O_2 molecule. The lower three orbitals formed from the $1s$ and $2s$ atomic orbitals stay rather localized, whereas the upper three formed from the $2p$ atomic states lead to the delocalized molecular orbitals. **(c)** The energy level scheme shows which atomic oxygen orbitals transform into which molecular O_2 orbitals.

These approaches can also be applied to hetero-nuclear and larger molecules, where the localization of the inner-shell- and core-electrons leads to the site-specificity mentioned in Chapter 1. Figure 8 illustrates how MOs are formed in O_2. The atomic oxygen orbitals are shown for both nuclei in Figure 8a. Utilizing the shape of the atomic orbitals by means of the spherical harmonics, one can construct the molecular orbitals as shown in Figure 8b. A detailed explanation of this orbital construction can be found in [84]. The formation of MO energy levels from the AO and their energy order is shown in Figure 8c. Notably, all binding orbitals, which are gerade for σ orbitals and ungerade for π orbitals are energetically lower lying than the respective anti-bonding orbitals. Typically, the lowest lying λ orbital is numbered as $n = 1$ and n is successively increased for higher lying orbitals of the same λ family. Yet, the energy order between different λ orbitals is not always the same. It can be determined empirically [84], that O_2 is the lightest molecule with $1\pi_u$ higher lying than $3\sigma_g$. Filling the orbitals of O_2 starting from the bottom, leads to all $n\sigma_{g,u}$ with $n = \{1, 2, 3\}$ and the $1\pi_u$ subshell being completely filled. Since for filled subshells $S = 0$ and $\Lambda = 0$ holds, only the two outer-most anti-bonding $1\pi_g$ electrons contribute to the total configuration. This leads to a triplet ground state configuration, O_2 ($X^3\Sigma_g^-$), with both valence $1\pi_g$ electron spins aligned. As a result, the O_2 ground state is paramagnetic. Here, the ground state is labeled as X and most exciting states with same multiplicity are usually labeled $A, B, C, ...$, whereas the states with different multiplicity are labeled $a, b, c, ...$, and historically later identified states are labeled with numbers.

2.5.4. Nuclear Motion

With the above method, the electronic energies $E_q(R)$ can be determined as a function of R, which are used as potentials to describe the nuclear motion. The resulting nuclear TDSE can be divided into an angular part, depending on the two rotational angles only, and a radial part depending only on the internuclear distance R. For bound states, the first part leads to angular wavefunctions and rotational eigenenergies, and the second one to radial wavefunctions and vibrational eigenenergies with quantum number v. The respective equations are typically solved under the assumption of a rigid rotator and harmonic vibrations, respectively, and further corrections can be applied. The reader is referred to textbooks like [45, 83, 84] for more information. If the electronic energy potentials do not support bound states, the molecule dissociates. As in the atomic case, coupling of angular momenta, including couplings to the nuclear angular momentum, cannot be resolved in the presented experiments (Chapter 4) and will not be considered further. For oxygen, as for all homonuclear diatomic molecules, no rotational or vibrational transitions are allowed within the same electronic state because of their symmetry. In total, molecular energy states are mainly governed by the electronic energies with ∼eV energy spacing, which are split due to vibrational levels on the order of ∼0.1 eV, which are further split in rotational states on the order of ∼meV. The last splitting is also neglectable small and therefore rotational states will not be considered further. The full quantum-mechanical treatment leads to very similar results about these three energy scales as the very first estimations at the beginning of the section.

2.5.5. Potential-Energy Curves and XUV-Excitation/Ionization

The XUV photon energies used in the experiment in Chapter 4 lead mainly to the ionization of the O_2 molecule. The calculation of the energy states in $O_2{}^+$ follows exactly what has been discussed for neutral O_2 and can be found in [86–88]. The relevant potential-energy curves (PECs), $E_q(R)$, are shown in Figure 9. As for atoms, electronically-excited states in the neutral molecule (e.g. the $2\sigma_u \rightarrow ({}^4\Sigma_u^-)\ n\ s\sigma_g/d\pi_g$ Rydberg series [89] shown in Figure 9) need to be excited resonantly and obey molecular dipole transition rules [45, 83, 84]. In contrast, all photon energies above an ionization threshold can lead to ionization. With increasing energy, more ionic states can be excited in parallel with different probabilities. These probabilities can be estimated with the *Franck-Condon principle*: The overlap of the wavefunctions between which a transition takes place is evaluated at the equilibrium distance of the initially lower-lying state while assuming the dipole operator $\hat{D}$ is independent of R. In general, symmetry properties can help determine which transitions are allowed [90]. In the case of the oxygen molecule, the lowest-lying, dipole-allowed states of the singly-ionized molecule have also been measured experimentally [91]. These states:

$$1)\ X\ {}^2\Pi_g,\ 2)\ a\ {}^4\Pi_u,\ 3)\ A\ {}^2\Pi_u,\ 4)\ b\ {}^4\Sigma_g^-,\ 5)\ B\ {}^2\Sigma_g^-,\ 6)\ 3\ {}^2\Pi_u,\ 7)\ c\ {}^4\Sigma_u^-$$

result from ionization of the the:

$$1)\ 1\pi_g,\ 2,3,6)\ 1\pi_u\ ,\ 4,5)\ 3\sigma_g,\ 7)\ 2\sigma_u$$

orbital of the neutral molecule, respectively [87]. From this list, only the ionic c $^4\Sigma_u^-$ state results from ionizing a localized inner-shell electron, while the others arise from valence-electron ionization. Several of these states lead to the dissociation of the molecule via different mechanisms, but the most significant contributions to O^+ fragment yields have been determined in [92] to come from the B $^2\Sigma_g^-$, 3 $^2\Pi_u$ and c $^4\Sigma_u^-$ state. In all dissociation cases, the electronic configurations of the fragments must match the atomic configurations, thus only several dissociation limits exist to which the excited molecular states dissociate into. They are summarized in Table 2.2.

Table 2.2.: First five dissociation limits of $O_2{}^+$ as reported in [92]

Dissociation Limit	**Atomic Fragments**	**Potential Energy**
(I)	$O(^3P) + O^+(^4S^o)$	18.7 eV
(II)	$O(^1D) + O^+(^4S^o)$	20.7 eV
(III)	$O(^3P) + O^+(^2D^o)$	22.1 eV
(IV)	$O(^1S) + O^+(^4S^o)$	22.9 eV
(V)	$O(^3P) + O^+(^2P^o)$	23.8 eV

The ionic ground state and most ionic excited states have energy minima around the Franck-Condon region, supporting bound vibrational states. The vibrational levels are below the respective dissociation limit, and therefore cannot dissociate into their own adiabatic limit, but only via coupling to other electronic states. Alternatively, for the 3 $^2\Pi_u$ state and photon energies larger than the respective dissociation limit, excitation into a repulsive curve leads to a direct dissociation. The difference between the potential energy in the FC region and the energy of the dissociation limit is translated into the *kinetic energy release (KER)* of the fragments, which splits equally between the two fragments. For the $O_2{}^+$ ($c\ ^4\Sigma_u^-$) state, the two vibrational levels, $v = 0, 1$, are also above the dissociation limit, which thus can *tunnel-dissociate* through the potential-energy well into the $O^+(^4S)$+$O(^1D)$ limit. The involved quantum-tunneling process is based on a non-vanishing probability of the nuclear wavefunction outside of the electronic potential barrier. The formation of this potential-barrier arises due to nearby electronic states of the same $^4\Sigma_u^-$ symmetry [88]. These states are not allowed to cross, which is known as *Neumann-Wigner non-crossing rule*, and their avoided crossings leads to the potential barrier of the c $^4\Sigma_u^-$ state. This illustrates, that the diabatic states (green dashes in Figure 9) under the BO approximation, need correction do obtain the actual adiabatic states (pink lines in Figure 9). Furthermore, the $^{2,4,6}\Sigma_g^+$ states [93, 94] overlap with the c $^4\Sigma_u^-$ state, which can undergo the *non-adiabatic* process of *internal conversion* due to spin-orbit couplings and change into a $^{2,4,6}\Sigma_g^+$ state. Conceptually, this process is similar to autoionization, as the electronic configuration changes without emission of a photon. The molecule than follows the repulsive PECs of the $^{2,4,6}\Sigma_g^+$ states and thereby *pre-dissociates* into the $O^+(^4S)$+$O(^3P)$ limit.

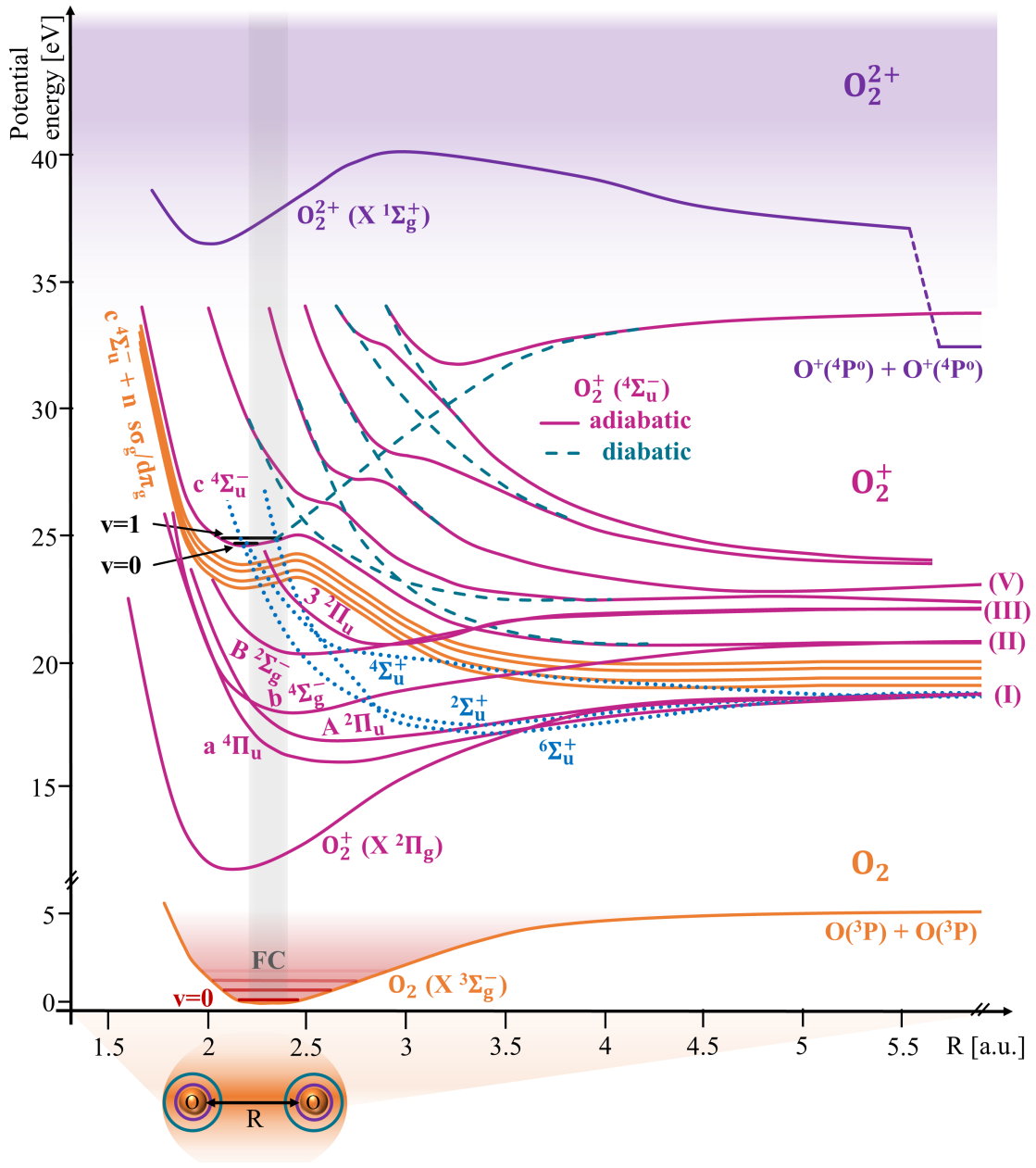

Figure 9.: Potential-energy curves (PECs) selection of molecular oxygen [88, 89, 92–95]. The neutral ground state (X $^3\Sigma_g^-$, orange) supports tens of vibrational states (red), of which mainly the lowest, v=0, is occupied at room temperature [96]. The Frack-Condon region is shaded in gray. Lowest PECs of $O_2{}^+$ are shown in pink, up to the c $^4\Sigma_u^-$ state—which supports two vibrational levels (black: v=0,1) [88], because the family of diabatic $^4\Sigma_u^-$ states (green dashes) avoids curve-crossing resulting in the adiabatic curves (pink) [88]. The c $^4\Sigma_u^-$ state can tunnel-dissociate though the resulting barrier, or alternatively pre-dissociate via the $^{2,4,6}\Sigma_u^+$ states (blue dots) [93, 94]. Relevant dissociation limits are labeled at $R \to \infty$ and given in Table 2.2. A relevant subset of the ($^4\Sigma_u^-$) n $s\sigma_g/d\pi_g$ O_2 Rydberg series (orange) [89] is shown around 24 eV. The $O_2{}^{2+}$ ground state, X $^1\Sigma_g^+$, is given in violet [95].

In total, the $O_2{}^+$ ($c\ {}^4\Sigma_u^-,\ v = 0$) state can dissociate via two coupled pathways, of which one is governed by nuclear tunneling and the other by electronic couplings—representing an interesting candidate to investigate coupled electronic-nuclear dissociations. The dissociation time of the $O_2{}^+$ ($c\ {}^4\Sigma_u^-,\ v = 0$) state has been measured for the first time within the third publication (Section 4.3). Further results are discussed is Section 5.2.

3. Technical Background: Experimental Setups

The previous two chapters have introduced the conceptual, scientific and theoretical background of this thesis. As a result, the probabilistic quantum nature of atoms and molecules in combination with the high photon energies of XUV and x-ray light leading to simultaneous reaction pathways, often demands a multidimensional data recording to reconstruct (and eventually control) the underlying processes from a scientific perspective. Yet, the interaction of XUV/x-ray light with atoms and molecules also represents its own technical challenge. The most important technical details of the following two setups will be introduced within this chapter:

(3.1) The FL26 beamline at FLASH combines both FEL and HHG laser pulses as well as an absorption spectroscopy setup and a reaction microscope to measure complimentary and multidimensional data sets for the dissociation of oxygen molecules (see Section 4.3, Chapter 5). While most of the various components of this beamline have been constructed previously and are reported in [8, 97–101], the data acquisition of the HHG spectra is a central contribution of this thesis project and will be explained in more detail.

(3.2) This setup is streamlined to achieve high target-gas pressures for stimulated resonant inelastic x-ray scattering in neon atoms in an absorption spectroscopy measurement at the SQS endstation of EuXFEL (see Chapter 5). The design and construction of the target-delivery and differential-pressure setup is a major contribution of this thesis project.

In general, an experimental setup for the measurement of XUV-/x-ray-induced dynamics in matter typically consists of various components, which need to work in interplay with each other. Because of the XUV and x-ray pulse sources, such experiments need to take place under high vacuum conditions (i.e. gas pressures $\leq 10^{-7}$ mbar) for the XUV/x-ray light not to be absorbed due to photo-ionization of the air molecules. This also implies, that the target-gas supply, electronics—detectors and controllers—and optics among others need to be designed accordingly. For example, target gases cannot be encapsulated, since the XUV pulses are absorbed by any material or, alternatively, the intense x-ray pulses drill through any wall, see Section 3.2. Experiments are therefore performed in 'cells' with transmission holes for the laser pulses and hence under constant input and output gas flow. Due to the technical and scientific complexity, experimental setups typically tend to start small aiming for a specific task (as in Section 3.2) and then often grow over time to enable further investigations (as in Section 3.1).

3.1. Absorption Beamline for FEL–Pump—HHG–Probe Experiments at FLASH

The experimental data for the dissociation of oxygen molecules (Section 4.3) and absorption line modifications in helium atoms (see Chapter 5) were obtained at the experimental setup, the *FL26 beamline*, at FLASH2. This beamline evolved over time, which will be briefly summarized below with focus on the latest updates relevant for the experiments in the publication in Section 4.3. A scheme of the current configuration used in these experiments is shown in Figure 10.

The FEL is the central tool for the XUV-driven experiments. Its working principle and pulse parameters are introduced in Section 2.1.2. For the data acquisition discussed below, the burst-mode operation of the FEL needs to be considered: Pulse trains, or *bunches*, are produced with the 10 Hz repetition rate of the RF pulses and individual pulses within such a bunch have a 10 µs spacing due to the repetition rate of the UV pulses. A fast shutter at the beginning of the beamline allows to block every second FEL bunch, which is used for static HHG references of the target O_2 absorption spectrum. Further, two filter wheels allow for different attenuation settings and hence FEL pulse energies. For the oxygen measurements (Section 4.3) only the the full FEL pulse energies of ∼10.7 µJ (∼8.4 µJ) at 27.7 eV (24 eV) of photon energy are used, whereas for the measurement in helium, the 100 nm and 400 nm thick aluminum filters transmit roughly 80 % and 40 % of the ∼15 µJ FEL pulse energy at 21.1 eV photon energy.

The OPCPA (optical parametric chirped-pulse amplification) IR laser system with the IR pulse pattern being synchronized in time with the FEL pulse pattern is reported in [97]. An optical time-delay stage allows to delay the IR pulses with respect to the FEL pulses. The µm step size and tens of cm travel range translates to femtosecond precision on a nanosecond range. While in principle the central wavelength and pulse duration of the IR pulses can be tuned, a set value of $\lambda_{IR} = 800$ nm and $\tau_{IR} \approx 15$ fs was used for the experiment in Section 4.3. The IR laser pulses are focused into a target cell for HHG, where 100 mbar of Krypton are used for the experiment in Section 4.3. A 100 nm aluminum filter allows to block the driving IR afterwards while letting through 80 % of the XUV light, but can also be omitted to include the driving IR pulse within the experiment. The HHG pulses are intrinsically synchronized with the IR pulses and of shorter duration. More details about HHG setup and the incoupling of the HHG into the FEL beampath can be found in [98, 99].

The first detector part of the FL26 beamline is based on a *reaction microscope (REMI)*, which allows to measure individual ions and electrons in coincidence [100]. In short, electromagnetic fields guide the charged particles to microchannel plate (MCP) detectors, where their spatial distribution and time-of-flight (TOF) is recorded, which can be converted to the 3D momentum vector and thereby also the kinetic energy. The general working principle of a REMI and the particular FL26 REMI are explained in detail in [66, 100, 102], and will not be elaborated in more detail here. In case only FEL pulses are used, a split-and-delay unit (SDU) allows for FEL pump–probe experiments. Instead using the FEL in combination with the HHG pulses, the two

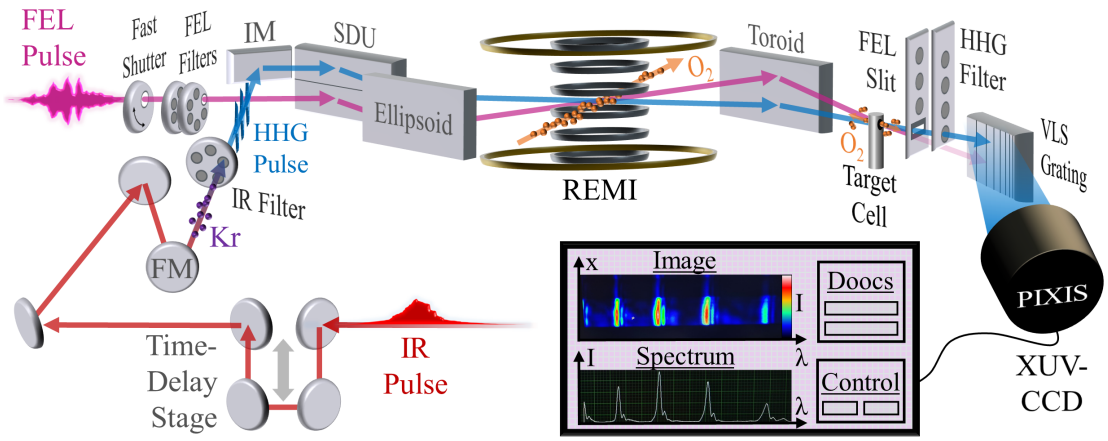

Figure 10.: Scheme of FEL–pump—HHG-probe experimental setup at the FL26 beamline at FLASH2 as discussed in the text. FM = focusing mirror; IM = incoupling mirror.

flat mirrors of the SDU are used for separately steering the two pulses. In general, all optics need to be used under grazing incidence angles, typically $\leq 8°$, to reflect the XUV/x-ray pulses. Both FEL and HHG pulses are focused into the REMI with an ellipsoidal mirror. The supersonic target jet produces very low target densities in the interaction region, such that the pulses are nearly unaltered after passing through the jet. Ion or electron detection counts depend strongly on the utilized photon number per pulse. Since the FEL pulses have orders of magnitude larger pulse energies and hence amount of photons than the HHG pulses, nearly all counts in the REMI come from the FEL pulses, when both pulses are used in parallel. Yet, for HHG only pulses, the REMI can be adjusted to measure photo-ions as well, as shown in [99].
The second detection part is an absorption spectroscopy beamline with an XUV spectrometer behind the REMI, which was initially setup to measure single-shot FEL spectra as diagnostic tool for the two-photon ionization of helium in the REMI [8]. The details about the absorption beamline are reported in [8, 101]. Besides the FEL spectral characterization, it has already been designed for parallel absorption measurements utilizing a toroidal mirror to refocus FEL (and HHG) pulses into a second interaction region. There, a target cell with two 200 µm holes along the beam axis for transmission of the XUV pulses and 2 mm length allows for sufficient target-gas pressures for absorption measurements. The continuous and constant gas inlet (at the bottom of the cell) compensates the leakage flow through the 200 µm holes and allows for constant target pressures during the entire measurement. The pressures are chosen to optimize the signal-to-noise ratio (SNR) as trade-off between resonant signal and off-resonant absorption, which lowers the overall measured XUV flux. In the experiments, $p(O_2) \approx 9$ mbar and $p(He) \approx 30$ mbar are chosen (Section 4.3, Chapter 5). The cell is connected to a manipulator, enabling three-dimensional placement and rotation around the vertical axis of the cell for alignment to the XUV beams. In particular, the vertical movement perpendicular to the beam propagation allows

for the usage of a phosphor screen, or a fast photo-diode in the focus region. The *spatial* overlap in the interaction region can be adjusted with the phosphor screen—converting the XUV light into visible light—filmed by a long-distance microscope camera (Navitar 6000, Imaging Source). The HHG beam is first aligned onto the spectrometer, and the FEL beam is than steered to match the focus position. Lastly, the target cell is moved back into the common focus. For the first experiments, both FEL and HHG pulses are focused at the same propagation distance, which leads to an average HHG focus diameter ($\sim$50 µm) an order of magnitude larger than the average FEL focus ($\sim$5 µm). This implies, that most of the HHG probes the static target gas (without the FEL pumping), such that the resulting absorption features are relatively small in intensity. This is compensated partly by the large FEL pulse energies and thereby peak intensities, which also leads to non-vanishing probabilities of two-photon absorption or the formation of plasma in the target gas cloud—which will be discussed further in Chapter 5. To avoid such effects in the future, a configuration with the FEL beam being slightly out of focus in the target region and preferably of same size as the HHG focus could be employed. Also, with the given focal sizes, the average time for an oxygen atom or molecule to leave the focus—due to thermal motion at room temperature—can be estimated to be on the order of 100 ns. Thus, a pair of FEL and HHG pulses have the (desired) high probability to interact with the same atoms or molecules within the focus on femto- to picosecond time scales. In contrast, the subsequent pulses of an FEL bunch—arriving 10 µs later—interact with a refreshed gas cloud and hence initiate independent experiments.

Further, the *temporal* overlap between the FEL and HHG pulses is found step-wise. While the rough timing between the pulses is on a few millisecond scale due to the RF-based synchronization system, the REMI can be used to detect the time-of-flight of ions generated by the FEL and (unfiltered) IR pulses, respectively. Thereby, the timing between two pulses can be determined with a nanosecond uncertainty. This procedure worked for the first experiments (Section 4.3), but is tedious to be employed, because it strongly depends on the IR REMI-focus intensity, which is otherwise irrelevant for all-XUV absorption experiments. Instead, a fast photo-diode can be used in the second interaction region instead of the target cell and read-out with a fast oscilloscope. The common IR and HHG focus is already optimized with the toroidal mirror. This procedure has been implemented in a more recent experiment and worked comparably faster and more robust than using the REMI. Again, this leads to a nanosecond scale for the estimation of the timing between FEL and IR (and thereby HHG) pulses. Eventually, the optical stage of the IR can be used within a $\sim$4 nanosecond range and with a few femtoseconds step size to find the temporal overlap between FEL and HHG pulses in the second interaction focus by measuring time-resolved absorption spectra of an even faster ionization event. For the experiment in the publication in Section 4.3, the ionization of argon atoms and the formation of Ar^+ Rydberg resonances at $\sim$28 eV [103] are measured with the XUV spectrometer described below.

Behind the absorption cell, two arrays of filters and slits can be utilized to separate pump and probe pulses and, in case of HHG measurements, minimize the stray light of the orders-

of-magnitude more intense FEL pulses. A variable line space (VLS) concave grating (Hitachi 001-0639) utilizing the interaction region as entrance point can be used for both XUV pulses. For a high repetition-rate read-out of individual FEL spectra a fluorescence screen and a gotthard detector [104] are used [8]. For the measurement of the HHG spectra, a slower but XUV-sensitive charge-coupled device (CCD) camera (PIXIS 400B) is used. It enables the measurement of the lower HHG intensities but needs longer integration times (at least a millisecond). Thus, a 'single' HHG spectrum always needs to be measured as an average over the HHG bunch arriving every 100 ms. In case of the oxygen experiments in Section 4.3, the FEL and HHG bunches contain 38 pulses each and hence, a HHG spectral measurement averages over 38 individual pulses. Yet, for both FEL and HHG bunches the amounts of pulses per bunch can be tuned, such that single pulse per bunch setups and measurements are possible. As discussed in Chapter 5, the experimental time resolution is limited by the temporal jitter (and drifts) between the two pulse sources. The jitter can be minimized by using single pulses per bunch in trade-off for a lower repetition rate—translating to lower SNR when the recording time is constant. The spectral resolution is dominated by the grating properties and is around 30 meV for photon energies of 30 eV. Hence, the following effects cannot be resolved properly—and do not need to be considered in detail for cases (i) and (iii):

(i) the fine-structure splitting of < 10 meV in O^+—as introduced in Section 2.2.1,

(ii) the long-lived absorption lines decaying via spontaneous emission, e.g. the He $1snp$ series (Section 2.2.2), where the 1 ns to 100 ns [105] lifetimes translate to 1 µeV to 100 µeV spectral linewidths, and

(iii) the macroscopic Doppler-broadening, δE, of absorption lines. For example for oxygen atoms, due to thermal motion at room temperature: $\delta E \approx 0.1$ meV to 1 meV, or with a few eV kinetic energy after dissociation (see Section 2.5): $\delta E \approx 1$ meV to 10 meV.

The limitations of (ii) are discussed with corresponding experimental findings in Chapter 5. The spectrometer is calibrated with additional measurements of helium and argon resonance lines and respective literature values [46, 103]. Further, the PIXIS CCD-camera allows for spatially resolved measurements (with 20 µm pixels and 8 mm size) perpendicular to the spectral dispersion axis, which will also be further discussed in Chapter 5.

Data Acquisition

The *data acquisition* runs in parallel from several sites: While the spectrometer and REMI have own computers, software and memory for the absorption and fragment data, the FEL and IR/HHG pulse parameters are recorded from DESY site. The complete data set thus consists of all the different recordings, which need to be brought together. While the later data analysis can in principle access the different data banks, this is not recommended during the experiment—as data is not always written or accessible in real time, yet the running of the experiment demands

control over certain parameters inbetween recordings. For the first FEL and HHG combined experiments (Section 4.3), this is achieved by centralizing some major parts of the experimental control at the spectrometer computer. This was achieved within this thesis project by utilizing LabView-based software, adapted from previous setups [106]. The key concepts used in the data acquisition are summarized in the following and may help guide future users:

(I) The *bunch ID* tags every FEL bunch with a 10-digit identifier and all data and metadata are stored with a bunch ID. Hence, it is essential for combining the different data banks. Yet a covariance analysis of correlated parameters of different recordings might need to be employed (e.g. FEL pulse energy and integrated FEL spectrum), because systematic shifts, often of ± 1 or ± 2, can appear.

(II) The *PIXIS control* program goes through the following steps, once all experimental parameters—especially time delay, FEL pulse and photon energy—are set:

  (i) waiting for external trigger, which is synchronized with the 10 Hz repetition rate of the FEL bunches, but slightly early.

  (ii) reading (previous) bunch ID.

  (iii) measuring HHG spectrum with 10 ms integration time, which is sufficient to ensure that the complete bunch is within the recording time. The averaged spectrum is typically read by using a two-dimensional region of interest (ROI) of the camera chip, which is employed during the hardware readout and immediate binning into an one-dimensional spectrum to enable fast enough readouts.

  (iv) reading a subset of relevant pulse parameters to be stored with the absorption spectra. See step (III).

  (v) reading (actual) bunch ID. If the difference to the previous bunch ID in step (ii) is more than one, a (communication) problem must have occurred and several bunches could have been in measured within the same file. Since actual spectra and references are measured back to back, these shots are sorted out in post analysis.

  (vi) repeating steps (i)-(v) according to number of frames chosen, in most cases 100 frames.

  (vii) saving data into files.

(III) *Doocs* is the DESY/FLASH-internal software for communication and readout. A doocs Labview program handles the live communication for the parameters to be set at the FEL and optical laser system—see step (IV)—while reading relevant parameters like the time delay or the FEL pulse and photon energy. The parameters are directly stored with the recorded absorption data from step (II).

(IV) The *experimental control* LabView program takes care of the overall sequencing of tasks and is used to record step-wise scans of time delays between the FEL and HHG pulses (or alternatively: scans of FEL photon energies) while recording HHG spectra at each step.

In contrast, the REMI only takes data of the fragments produced by the FEL pulses, and hence is not effected by the time delay between FEL and HHG, nor by the FEL fast shutter—it simply measures low background noise instead of fragment counts every other shot when the FEL shutter is closed. Hence, the REMI is operated independent of the spectrometer and collects continuously data while saving Bunch IDs on its own for later data analysis.
In the future, a centralized experimental control and data acquisition could be considered beneficial. Further, it should be highlighted that the goal of the experiment was to combine FEL and HHG pulses for time-resolved absorption measurements, and hence live analysis was mainly carried out on the absorption spectra. As discussed in Chapter 5, the post-analysis of oxygen ions measured with the REMI is helpful for understanding and validating the results of the publication in Section 4.3. This will also illustrate, how a combined approach of REMI and absorption measurements could enable even more diverse scientific opportunities.

3.2. High Target-Pressure Experimental Setup at EuXFEL

For non-linear absorption processes and *spatial* or *spectral* reshaping of XUV/x-ray pulses, high densities of the interacting gas are considered beneficial, if not necessary, as the reshaping is connected to propagation effects within the target gas cloud. For example, the turning of an absorption line into an emission line—as discussed in Section 4.2, Chapter 5—can be regarded as spectral reshaping. Alternatively, the process of *resonant inelastic x-ray scattering (RIXS)* (introduced in Section 2.2.2) generates a new spectral feature and can be used as non-linear (and background-free) x-ray probe of atoms or molecules. Stimulated RIXS in neon atoms has been first measured in transient absorption at incoming photon energies of 870 eV and target-gas pressures of $\sim$0.67 bar in [75]. The process has a low interaction probability—given by the Kramers–Heisenberg formula [60]—and hence demands high photon numbers, which are provided by the XFEL pulses, as well as high target densities. The later also enables a stimulated RIXS signal, which is initially generated by spontaneous emission at the beginning of the gas cloud to be amplified via stimulated emission while propagating through the target. Therefore, the RIXS in neon atoms is re-investigated at an order of magnitude higher target pressure ([107] and discussion Chapter 5) with the setup presented in the following. The target-delivery setup was designed and constructed as a part of this thesis project and installed at the *SQS endstation* of the EuXFEL facility in combination with a soft x-ray spectrometer provided by the group of Prof. Jan-Erik Rubensson (Uppsala University). A scheme of the complete experiment is shown in Figure 11a and an overview of the target-delivery setup is given in Figure 11b. The project and collaboration has been initiated and lead by Prof. Linda Young (Argonne National Lab) and the RIXS results in neon atoms are discussed in detail in the doctoral thesis of Dr. Kai Li [107].

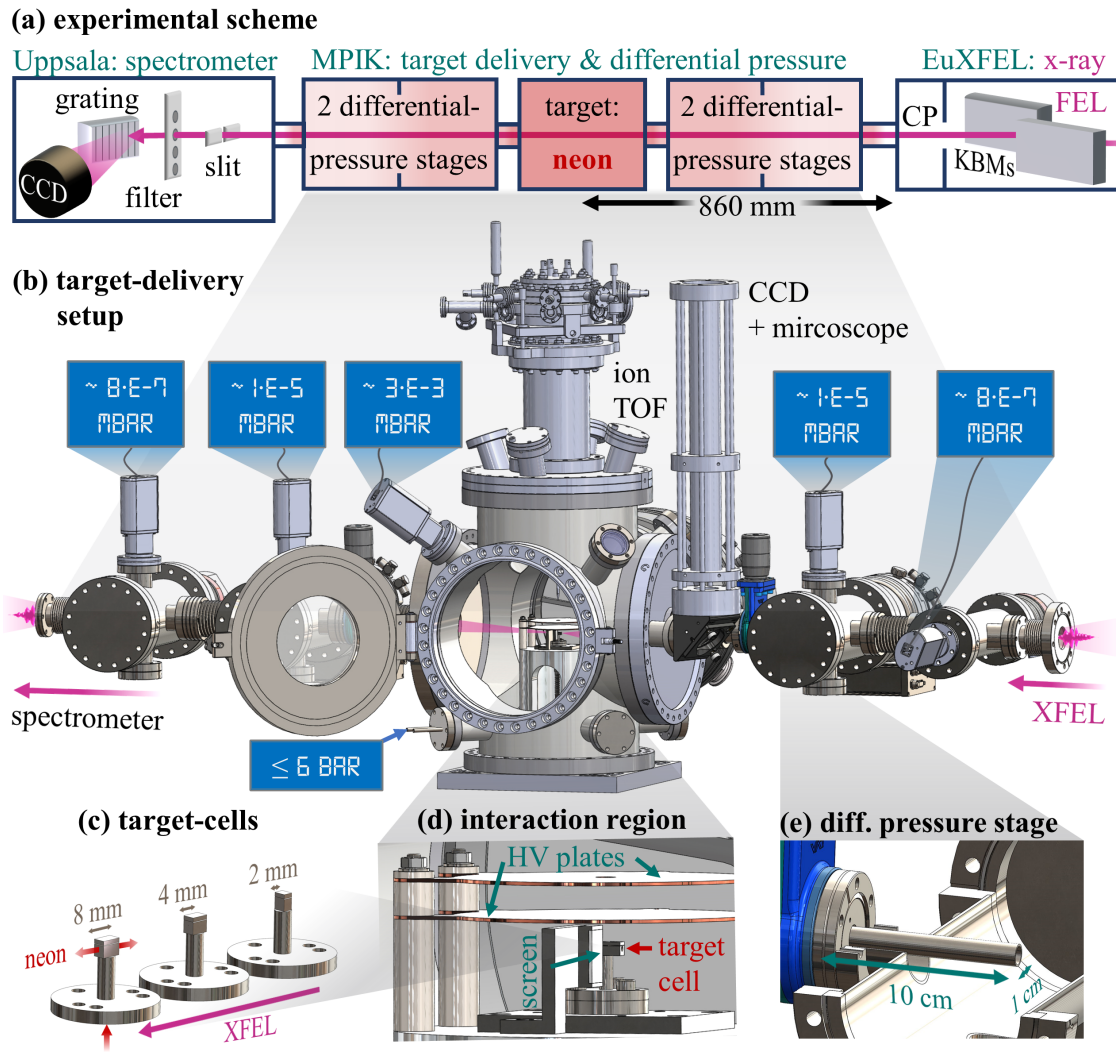

Figure 11.: **(a)** Scheme of the RIXS in neon (red) measured in transient-absorption geometry at the SQS endstation of the EuXFEL facility. XFEL pulses (violet) propagate from right to left. CP = connection port; KBMs = Kirkpatrick–Baez mirrors. **(b)** Overview of the high target-pressure delivery and differential-pumping setup. Chamber pressures for 6 bar of neon backing pressure are shown in white and blue. **(c)** Exchangeable target cells with variable length. Neon gas (red) is supplied via an inlet at the bottom and flows out via the XFEL-drilled holes. **(d)** Beside the target cells, a phosphor screen, or the center of two high-voltage (HV) plates for ion TOF measurements can be moved into the XFEL focus. **(e)** Differential-pressure stages within the vacuum chambers allow for an reduction of pressure by orders of magnitude along the setup.

The target-delivery setup has been build with the following properties of the EuXFEL facility and SQS endstation in mind: The x-ray FEL (XFEL) pulses are focused with a pair of Kirkpatrick–Baez (KB) mirrors [108] down to focal diameters of 1 µm to 2 µm. The focal distance from the connection port (a CF63 flange) is 860 mm, hence the target-delivery and differential-pressure setup needs to be compact to meet this constrain. Further, a SQS Newport stand is used for three-dimensional translational movement of the target chamber with µm precision. In contrast to the FL26 beamline in the previous section, the whole target chamber is moved with a fixed target-cell position to place the target in the XFEL focus. The setup does not contain any filters before the target, because the XFEL pulse energy can be controlled by a gas attenuator.
The key idea of the target-delivery setup is a steep pressure gradient between the interaction region—with high target pressures inside the cells to enable propagation effects—and the surrounding chamber—with high vacuum conditions to not absorb or attenuation the XFEL pulses. To this end, a target-cell design similar as presented in the previous section is used, but without pre-drilled holes (Figure 11b). Instead, the XFEL pulses are used to drill through the 200 µm thick steel cell walls and hence create their own holes. In principle, this allows for hole sizes as small as the focal diameter of 1 µm to 2 µm. Yet, due to XFEL pointing jitters and potential plasma effects, these holes grow over time. After one week of experiment, the hole size is roughly estimated under a microscope to be on the order of 20 µm to 50 µm. This hole size is crucial, because it determines the gas flow out of the target cell and thereby the pressure in the surrounding vacuum chamber—the reader is referred to [109] for more details. The maximum pressure inside the target cell is limited by the maximal pressure within the surrounding chamber which still can be pumped out by the turbo-molecular pump (Pfeiffer HiPace 2300). During the test phase, this maximal chamber pressure was estimated to be $5 \cdot 10^{-3}$ mbar for a neon gas backing pressure of 2 bar when cells with the smallest possible mechanically pre-drilled holes with a 100 µm diameter are used [110]. The target-gas backing pressure is controlled by a pressure regulator (Festo VPPM) in the range of 1 bar to 10 bar, which can be further reduced with a needle valve to a few tens of mbar. During the experiment, backing pressures up to 6 bar are utilized leading to a chamber pressure of $2.6 \cdot 10^{-3}$ mbar. The chamber pressure p_{ch} can be estimated under the assumption of viscous flow through thin apertures (the holes in each side of the cell) [109, 110]:

$$p_{\mathrm{ch}} = C \cdot d^2 \cdot p_{\mathrm{tar}}, \tag{38}$$

where p_{tar} is the pressure within the target cell, and d is the diameter of the cell holes. C is a constant depending on the pump capacity and the (assumed linear) ratio between backing and target-cell pressure. With help of Equation (38), the results of the test measurement with 100 µm holes, and the pressures recorded during the experiment, the XFEL-drilled hole size can be determined as ∼40 µm—agreeing with the microscope estimation given above. For initial alignment at the EuXFEL, a cell with pre-drilled holes with 200 µm diameters is used. Further, the cells can be exchanged and different cell lengths of 2 mm, 4 mm and 8 mm can be utilized for investigating propagation-length-dependent effects as shown in (Figure 11b). In the first

experiments discussed in [107] and Chapter 5, a fixed cell with a length of 2 mm is used.
For initially finding and optimizing the XFEL focus, the two following options are implemented in the target chamber as shown in Figure 11c: (i) A horizontal movement of the target chamber by 7.5 mm brings a phosphor screen in the (therefore highly attenuated) XFEL focus, which is recorded with a long-distance microscope and CCD camera—as in the FLASH setup in Section 3.1—allowing for visual feedback. (ii) Instead, moving the target chamber down by 1.5 cm brings the center of two high-voltage (HV) plates into the XFEL focus. The HV plates provide an ion-extraction field for a TOF measurement of the XFEL-generated neon ions. The upper HV plate has an ion-extraction hole with a 5 mm diameter aligned to the TOF detector entrance. The ion TOF detector further accelerates the ions before measuring their mass-to-charge ratio. The detector is provided from and operated by the SQS beamline team. The target chamber has a second gas inlet, which fills the complete chamber with neon gas at a pressure of $8 \cdot 10^{-8}$ mbar for the ion TOF measurement. Minimizing the XFEL focus size with the KB mirrors leads to the highest XFEL peak intensities, which is found by maximizing the count rate of the highest ion charge, Ne^{8+}, detected with the TOF measurement.
The residual setup is used for differential pumping enabling high-vacuum conditions towards the XFEL connection port and the x-ray spectrometer. It consists of four vacuum chambers each with a turbo-molecular pump, where Pfeiffer HiPace 700 pumps are used for the two inner chambers—next to the target chamber—and HiPace 300 pumps for the outer chambers. The pressures in all chambers are monitored with separate Pfeiffer PBR 260 gauges in the range of $1 \cdot 10^{-9}$ mbar to 1000 mbar. Each chamber entrance contains a differential-pumping stage as shown in Figure 11d. The stages are made of 10 cm long tubes with an inner diameters of 1 cm. As a result, the pressures within the two inner chambers are reduced by two orders of magnitude ($\leq 1 \cdot 10^{-5}$ mbar) and the outer-chamber pressures are reduced by another order of magnitude (10^{-7} mbar to 10^{-6} mbar). More detailed theoretical considerations about gas flow and pressure reduction can be found in [109], while a first experimental characterization of the setup is reported in [110]. The vacuum chambers are connected to each other—and the first chamber to the EuXFEL connection port—via bendable bellows, which allows for (i) the initial alignment of the differential-pumping chambers with respect to the XFEL beam, and (ii) movement of the target chamber (on the Newport stages) with respect to the residual setup.
The x-ray spectrometer is placed ∼1.9 m behind the XFEL focus to reduce the XFEL peak intensity and hence avoid damaging the entrance slit. The spectrometer is made of a commercial Scienta XES 350, which provides an adjustable entrance slit and a spherical grating under grazing incidence [111], filter arrays and a x-ray-sensitive CCD camera (Andor Newton). The EuXFEL can be operated in a similar burst mode as FLASH, but here single pulses (per bunch) are used to record two-dimensional images of individual FEL spectra with a 10 Hz repetition rate. This setup allows for spectral measurements with a high resolution of 200 meV at 850 eV for the RIXS experiments in neon [107]. The data acquisition as well as the overall experimental-setup control is integrated into the centralized EuXFEL software system and operated by the SQS team.

4. Main Results: Publications

The several backgrounds introduced within the previous chapters lay the foundation of the scientific results—the here presented three publications—of this cumulative dissertation. Their common ground is understanding ultrafast quantum-dynamics of atoms and molecules based on XUV-electron interaction by connecting time-and-energy–domain perspectives. Therefore, they employ *energy-resolved* absorption spectroscopy to identify underlying processes in combination with a variable excitation energy. The first publication (Section 4.1) *simulates* the temporal electron dynamics by numerically solving the Schrödinger equation, but then shifts to the spectral domain to understand their absorption imprint. In contrast, the goal of the second publication (Section 4.2) is to directly *reconstruct* the temporal population dynamics of coupled electronic states in atoms with help of a convolutional neural network. Ultimately, the third publication (Section 4.3) explicitly *time-resolves* a molecular dissociation processes by using a pair of time-delayed XUV pulses. The three publications are thereby ordered simultaneously by an increasing degree of quantum-dynamical complexity and capability to investigate temporal quantum processes. Their central massages and connections to other parts of this thesis can be summarized as follows:

4.1 Explaining simulated state-couplings and absorption changes with energy/phase-shifts.
Background: Sections 2.1 to 2.3. Further results: Sections 4.2 and 5.1.

4.2 Demonstrating a CNN can reconstruct electron populations from absorption changes.
Background: Sections 2.1 to 2.4. Further results: Sections 4.1 and 5.1.

4.3 Demonstrating a FEL-pump–HHG-probe experiment resolving molecular dissociation.
Background: Sections 2.1, 2.3, 2.5 and 3.1. Further results: Section 5.2.

The publications are presented separately in this chapter, while the connections between them illustrated with further results are discussed in detail in Chapter 5. In particular, the back-action of the atoms and molecules on the driving XUV/x-ray pulses is a crucial aspect of light-matter–interaction. In fact, it gives rise to the absorption signals used in all three publications, which come from a single-particle perspective of the interaction. Yet, the propagation of XUV/x-ray pulses through a dense gas cloud can result in further spectral, temporal and spatial reshaping of the driving pulse. This represents a scientific field on its own, and has been a central part of this thesis project. It is not mentioned in the publications, but several aspects concerning propagation effects are summarized in Sections 2.3 and 3.2, and first results are discussed in Section 5.1.

4.1. Bound-State Electron Dynamics Driven by Near-Resonantly Detuned Intense and Ultrashort Pulsed XUV Fields

The theoretical background provided in Section 2.2.1 explains the intrinsic, i.e. unperturbed, electronic structure of atoms and molecules. It lays the foundation for the identification of elements due to their unique absorption fingerprints: *Resonant electronic transitions* between two bound states (Section 2.2.2). The weak-field interaction of light with electrons in an atom is thus photon-energy–dependent, which can be measured when *spectrally resolving* the interacting light, e.g. with absorption spectroscopy (Section 2.3). But the electronic structure can also be perturbed, e.g. by shifting or splitting the electronic energies [61] with coherent, (nearly) monochromatic lasers with sufficient *intensity* (Section 2.2.3). Yet, the interaction with an intense laser *pulse* in the impulsive limit, i.e. when the pulse is significantly shorter in time than the excited-state lifetime, yields different results. First experiments with intense infrared laser pulses have demonstrated, how this leads to changes of the absorption line-*shapes* [69]. The central idea is that *transient* energy shifts—i.e. shifts during the pulse duration—lead to a phase-shift of the corresponding dipole moment (Figure 6). Yet, this was not connected to bound-state transitions, and was described as a pure phase shift for the involved electronic states disregarding state-populations. In contrast, subsequent experiments with intense XUV FEL pulses have demonstrated that the strong-coupling of electronic states includes significant population transfer and leads to absorption line-shape changes as well [4].

The publication shown within this section is based on first ideas and theoretical framework [112, 113] utilized to explain the experimental findings in [4]: Combining the transient energy shifts with dressed-state energies as in [61], and translating them to phase shifts of the state coefficients and resulting dipole moment as in [69]. A simple analytical formulation allows to compare this idea with full-simulation results for a two-level system. It can be regarded as the key conceptual aspect of the work, although deviations between analytical and numerical treatment arise, which will be discussed further in Section 5.1. However, these first results regarding XUV-driven line-shape changes influenced further combined experimental and theoretical work on the subject [2, 5–7]. In particular, induced temporal dynamics of the electron populations are not discussed explicitly in the first publication, but will be investigated in the follow-up work presented in the second publication in the next section.

applied sciences

MDPI

Article

Bound-State Electron Dynamics Driven by Near-Resonantly Detuned Intense and Ultrashort Pulsed XUV Fields

Alexander Magunia *, Lennart Aufleger, Thomas Ding, Patrick Rupprecht, Marc Rebholz, Christian Ott * and Thomas Pfeifer *

Max-Planck-Institute for Nuclear Physics, Saupfercheckweg 1, 69117 Heidelberg, Germany; lennart.aufleger@mpi-hd.mpg.de (L.A.); thomas.ding@mpi-hd.mpg.de (T.D.); patrick.rupprecht@mpi-hd.mpg.de (P.R.); marc.rebholz@mpi-hd.mpg.de (M.R.)

* Correspondence: alexander.magunia@mpi-hd.mpg.de (A.M.); christian.ott@mpi-hd.mpg.de (C.O.); thomas.pfeifer@mpi-hd.mpg.de (T.P.)

Received: 30 July 2020; Accepted: 31 August 2020; Published: 4 September 2020

Abstract: We report on numerical results revealing line-shape asymmetry changes of electronic transitions in atoms near-resonantly driven by intense extreme-ultraviolet (XUV) electric fields by monitoring their transient absorption spectrum after transmission through a moderately dense atomic medium. Our numerical model utilizes ultrashort broadband XUV laser pulses varied in their intensity (10^{14}–10^{15} W/cm^2) and detuning nearly out of resonance for a quantitative evaluation of the absorption line-shape asymmetry. It will be shown how transient energy shifts of the bound electronic states can be linked to these asymmetry changes in the case of an ultrashort XUV driving pulse temporally shorter than the lifetime of the resonant excitation, and how the asymmetry can be controlled by the near-resonant detuning of the XUV pulse. In the case of a two-level system, the numerical model is compared to an analytical calculation, which helps to uncover the underlying mechanism for the detuning- and intensity-induced line-shape modification and links it to the generalized Rabi frequency. To further apply the numerical model to recent experimental results of the near-resonant dressing of the 2s2p doubly excited state in helium by an ultrashort XUV free-electron laser pulse we extend the two-level model with an ionization continuum, thereby enabling the description of transmission-type (Fraunhofer-like) transient absorption of a strongly laser-coupled autoionizing state.

Keywords: atomic physics; ultrashort physics; bound-bound electronic transitions; strong-field couplings; transient-absorption spectroscopy; line shape manipulation; free-electron-laser; numerical calculations

1. Introduction

The manipulation of electronic states in atoms with intense electromagnetic fields has been studied theoretically for several decades [1,2]. One of the many investigated cases has been the existence of an excited state energetically embedded in an ionization continuum, nowadays known as an autoionizing Fano state [3], for which resonant couplings with strong fields have been studied in detail [3,4]. Also, transient-absorption spectroscopy experiments have been carried out more recently with sensitivity to strong-coupling dynamics of Fano resonances in rare gas atoms [5–9]. These experiments employ broadband extreme-ultraviolet (XUV) attosecond pulses in combination with time-delayed intense femtosecond laser pulses in the near-infra red (NIR) spectral regime. Characteristic absorption lines are observed in the XUV-pulse spectrum after transmission through a moderately dense cloud of atoms or molecules. Hereby, measuring the transient absorption signal allows one to access the real-time dynamics of the XUV-excited system when it is driven by the NIR laser pulse [10] while

retaining state-specific spectroscopic resolution. With the advent of XUV and x-ray free-electron-lasers (FELs) [11,12], new possibilities opened up for ultrafast nonlinear light-matter interaction at high photon energy and intensity [13–15]. Regarding transient absorption spectroscopy with intense XUV-FEL pulses, signatures of strongly driven XUV resonant transitions have been observed [16,17]. Hereby, the intense XUV-FEL laser pulses may strongly couple the ground state directly to a highly excited state of an atom. Predicting the ionization yield and photoelectron emission fur such a transition in helium, XUV-FEL absorption spectroscopy at high intensity has been studied theoretically [18–20]. In this work, we computationally model intense-field XUV absorption spectroscopy by directly observing the intense XUV light after its transmission through a resonant medium and use it to explain and predict line-shape asymmetry changes of resonant transitions strongly coupled by XUV light. To properly account for the broad spectral bandwidth of the ultrashort pulses, we solve the underlying few-level system of resonant couplings numerically and further compare it to an analytical approximation [1,2] for monochromatic fields as a function of the detuning in terms of the generalized Rabi frequency. Our numerical findings for the autoionizing 2s2p doubly excited state in helium further support recent experimental results that have been obtained with intense XUV-FEL pulses [16].

2. Methods

First, we consider a two-level system for our numerical model, for which the Hamiltonian H_{2lvl} is described as a matrix with two states at energy $E_g = 0$ eV and $E_e = 60.15$ eV, for the ground and the excited state, respectively, which are coupled in dipole approximation by the dipole matrix element $d_{ge} = d_{eg} = -0.035$ a.u. (a.u. = atomic units; which are used throughout this work unless stated otherwise). The parameters are chosen to match the relative energy separation and dipole coupling strength between the $1s^2$ ground state and the 2s2p doubly excited state in helium [21]. Hereby at first, we explicitly neglect the configuration interaction with the ionization continuum of the 2s2p doubly excited state, but still take its finite autoionization lifetime into account by means of the excited-state decay parameter $h\Gamma_e = 37$ meV. Going one step further, we consider a second model, where we account for the configuration interaction between the excited state and the one-electron ionization continuum by extending our first model to a three-level system with Hamiltonian H_{3lvl}, which additionally includes an energetically broad quasi-continuum state that serves as a short-lived ionization-loss channel for the system. The parameters of this quasi-continuum state are set to energy $E_c = 32.654$ eV, decay width $h\Gamma_c = 39.728$ eV, dipole matrix element $d_{gc} = d_{cg} = 0.675298$ a.u. for its dipole coupling to the ground state and configuration interaction $V_{CI} = 0.0373209$ a.u. for the inter-channel coupling between the quasi-continuum state and the 2s2p state. In this three-level system, the excited-state parameters are slightly altered to the excited-state energy $E_e = 60.122$ eV and to the dipole matrix element $d_{ge} = -0.0493158$ a.u. for dipole coupling to the ground state, while the previously introduced direct decay of the excited state can be omitted ($h\Gamma_e = 0$ eV), since its autoionization is now explicitly taken into account through V_{CI}. The numerical parameters of this three-level system have been chosen such that the weak-field transient absorption profile of the $1s^2$–2s2p transition agrees with the reported literature values [21], most importantly now also including its asymmetric line shape. See also Figure 1b for a simplified energy-level scheme of the system. The XUV laser pulse is treated as a classical electric field $E(t)$ with a Gaussian envelope of duration $T_{FWHM} = 3$ fs (intensity full width at half maximum). To summarize, the Hamiltonian matrices H_{3lvl} and H_{2lvl} for the three- and two-level system, respectively, are given by:

$$H_{3lvl} = \begin{pmatrix} E_g & d_{ge}\,E(t) & d_{gc}\,E(t) \\ d_{ge}\,E(t) & E_e & V_{CI} \\ d_{gc}\,E(t) & V_{CI} & E_c + i\,\Gamma_c/2 \end{pmatrix}, \text{ and } H_{2lvl} = \begin{pmatrix} E_g & d_{ge}\,E(t) \\ d_{ge}\,E(t) & E_e + i\,\Gamma_e/2 \end{pmatrix}, \quad (1)$$

with the numerical parameters as defined above. The time-dependent Schrödinger equation $i\hbar\frac{\partial}{\partial t}|\Psi(t)\rangle = H(t)|\Psi(t)\rangle$ is solved on a discrete time grid (time steps $\Delta t = 0.1$ a.u. $= 2.42$ as) through numerical diagonalization of the Hamiltonian at each time step. The state vector of

the system, $\left|\Psi(t)\right\rangle^{(2lvl)} = \left[c_g(t), c_e(t)\right]^T$ or $\left|\Psi(t)\right\rangle^{(3lvl)} = \left[c_g(t), c_e(t), c_c(t)\right]^T$, is expressed through the complex-valued coefficients c_i (i = g, e, c). For the initial state, only the ground state is populated ($c_g(t=0) = 1$). The coefficients are propagated in time within the diagonalized Hilbert space by multiplication with a pure phase factor, $e^{-iE_i\Delta t/\hbar}$, containing the eigenvalues E_i $\left[i = 1, 2, \left(3\text{only when } c_c \text{ is included}\right)\right]$ of the diagonalized Hamiltonian. The complex time-dependent dipole moment $d^+(t)$ of the system rotating with positive frequencies (containing terms $\propto e^{i\omega t}$) is given by:

$$d^+(t) = d_{ge}\, c_g(t) c_e^*(t) + d_{gc}\, c_g(t)\, c_c^*(t), \tag{2}$$

with the previously defined dipole matrix elements d_{ge} and d_{gc}. The second term in Equation (2) does not contribute for the two-level system. The optical density (OD) of transient absorption is calculated with the frequency spectrum of the time-dependent dipole moment $d(\omega) = FT\left\{d^+(t)\right\}$ obtained after Fourier transformation and is given by taking the negative decadic logarithm of the ratio between transmitted (numerator) and incoming (denominator) spectral intensity:

$$OD(\omega) = -\log_{10}\left(\frac{\left|E(\omega) + i\,\eta{\cdot}d(\omega)\right|^2}{\left|E(\omega)\right|^2}\right). \tag{3}$$

here, $E(\omega)$ is the frequency spectrum of the incoming laser pulse and $\eta = 10^{-4}$ is a constant connected to the macroscopic particle density of the target medium. Its numerical value is arbitrary and here chosen small enough to avoid macroscopic propagation effects. Equation (3) contains the term $\left|E(\omega) + i\,\eta{\cdot}d(\omega)\right|^2$, which is an interferometric superposition of the polarization response ($P = \eta{\cdot}d$ [22]) and the driving field following Maxwell's equations, which is at the heart of transient absorption spectroscopy (see Figure 1a). The resulting optical density (Figure 1d,e) is, thus, directly sensitive to the relative phase between the driving field and the dipole response [8] manifesting in an absorption profile, which can be parametrized by a generalized Fano line shape. To quantify the asymmetry of the resonant absorption lines we hence fit the OD with a Fano profile:

$$OD(\omega) = A\frac{(\varepsilon(\omega) + q)^2}{(1 + \varepsilon^2(\omega))} + B,\ \varepsilon(\omega) = \frac{\hbar\omega - E_r}{\Gamma_r/2}, \tag{4}$$

where q is the Fano asymmetry parameter, $\varepsilon(\omega)$ is the relative photon energy depending on the resonance position E_r, its spectral width Γ_r and the photon energy $\hbar\omega$. A and B are fitting parameters for the amplitude and offset, respectively. In the case of the weak-field two-level system, the absorption profile is unperturbed and assumes a Lorentzian shape (Figure 1d), which is the limiting case of a Fano profile for $q \to \pm\infty$. When the third quasi-continuum state for the 2s2p resonance in helium is included in the weak-field case, the q parameter equals −2.75 [23]. With strong laser fields and in the "impulsive limit" [8,24,25], i.e., when the pulse duration (here: 3 fs) is short compared to the resonance lifetime (here: $\tau = 1/\Gamma_r = 17$ fs), the absorption profile asymmetry, which is captured by the q parameter, can be modified. For the transmission-geometry transient absorption, this change is related to a phase shift $\Delta\varphi_D$ of the time-dependent dipole moment with respect to the weak-field response of the system [8] and is given by:

$$q\,(\Delta\varphi_D) = -\cot\left(\frac{\Delta\varphi_D}{2}\right) \Leftrightarrow\ \Delta\varphi_D = 2\arg(q - i). \tag{5}$$

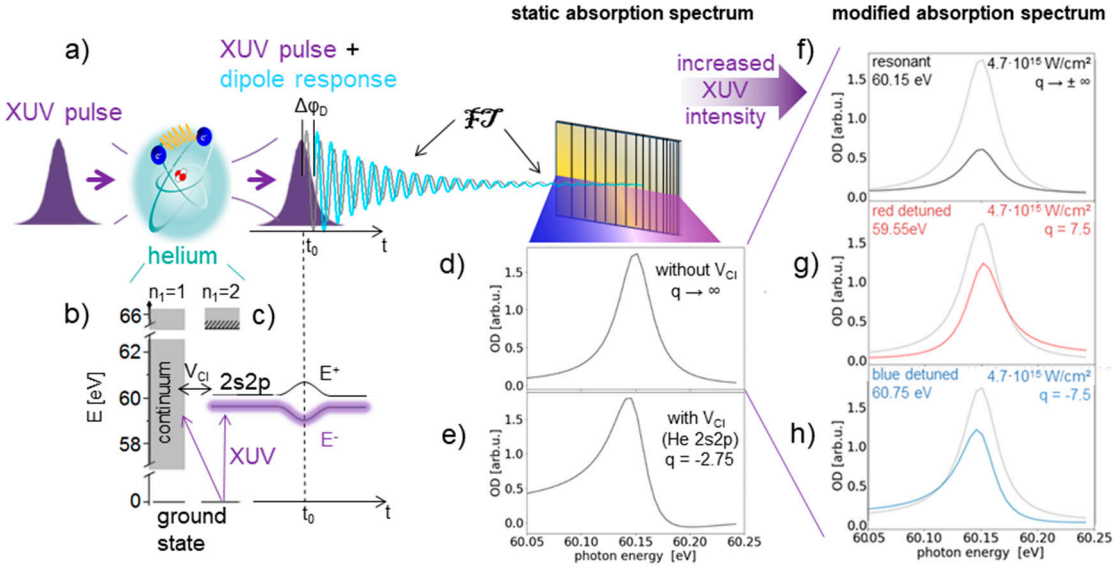

Figure 1. (**a**) the interaction of an ultrashort extreme-ultraviolet (XUV) pulse (violet) with an atom, e.g., helium, leads to the emission of a dipole response (blue) interfering with the driving XUV pulse. (**b**) simplified energy level scheme of helium. With a photon energy of 60.15 eV the helium atom can be either singly ionized or excited into a doubly excited state, which autoionizes due to its configuration interaction V_{CI} with the ionization continuum. Corresponding absorption spectra are shown in (**d**,**e**). If the configuration interaction is disregarded, the absorption profile is Lorentzian (**d**), whereas the inclusion of the configuration interaction leads to a Fano absorption line shape (**e**). (**c**) dressed states are generated in the presence of an intense XUV pulse. The states' energy separation increases with increasing XUV laser intensity and depends on the detuning [1,2], therefore their energy shift follows the Gaussian pulse envelope in time (compare to a), here illustrated for a red-detuned case. This leads to a temporal dipole phase shift $\Delta\varphi_D$ with respect to the weak-field response (grey in a) [8]. (**f**)–(**h**) manipulated absorption profiles of the two-level system (without configuration interaction) initiated by the strong coupling with an XUV pulse of different detunings. (**f**) the peak intensity of a resonant laser pulse is increased to 4.7×10^{15} W/cm^2 leading to a decreased amplitude of the resonance, but leaving the line shape unchanged ($q \to \pm\infty$). (**g**,**h**) the additional detuning of the laser pulse to central photon energies $\hbar\omega_c$ of 59.55 eV or 60.75 eV, leads to modified now asymmetric absorption line shapes with a positive or negative q -parameter, respectively.

3. Results and Discussion

3.1. Two-Level System

In Figure 1f–h, modified absorption profiles of a two-level system driven by Gaussian laser pulses of 3 fs duration with high peak intensity $I_0 = 4.7 \times 10^{15}$ W/cm^2 and with detunings $\Delta/E_e = 0$ (Figure 1f, resonant), $\Delta/E_e = -0.01$ (Figure 1g, red detuned) and $\Delta/E_e = +0.01$ (Figure 1h, blue detuned) are shown in comparison to the unperturbed absorption profile (grey). Hereby the detuning is defined as

$$\Delta = \hbar\omega_c - E_r, \tag{6}$$

where $\hbar\omega_c$ is the central photon energy of the XUV pulse. It should be noted that the corresponding spectral bandwidth of the XUV laser pulse amounts to ~0.6 eV (intensity full width at half maximum), which corresponds to $\lesssim$1% of the central photon energy. The detuning is thus changed only within the spectral bandwidth of the XUV pulse which leads to near-resonant couplings at all detunings. To further investigate the mechanism behind the modified line shapes, we now systematically vary the XUV intensity and detuning. In Figure 2c we plot the fit results of the q parameter for the two-level resonance under the influence of an XUV pulse with peak intensities ranging from $I_0 \approx 0.1 \times 10^{15}$ W/cm^2 to $I_0 \approx 4.7 \times 10^{15}$ W/cm^2 and detunings ranging from $\Delta = -0.65$ eV to

$\Delta = +0.65$ eV. For low intensities, the resonance is unperturbed and forms a Lorentzian shape, where the fit yields $q \to \pm\infty$. The divergence of q for a Lorentzian line shape is better quantified with the corresponding dipole phase shift $\Delta\varphi_D$ (see Equation (5)), which is shown in Figure 2b. Instead of the divergent q parameter, the phase shift is now smoothly changing around zero for low intensities. The three horizontal lineouts for detunings of −0.6 eV (red), 0 eV (black) and +0.6 eV (blue) are shown in Figure 2a and the three vertical lineouts for peak intensities of 0.1×10^{15} W/cm^2 (violet), 2.4×10^{15} W/cm^2 (orange) and 4.7×10^{15} W/cm^2 (black) are depicted in Figure 2d.

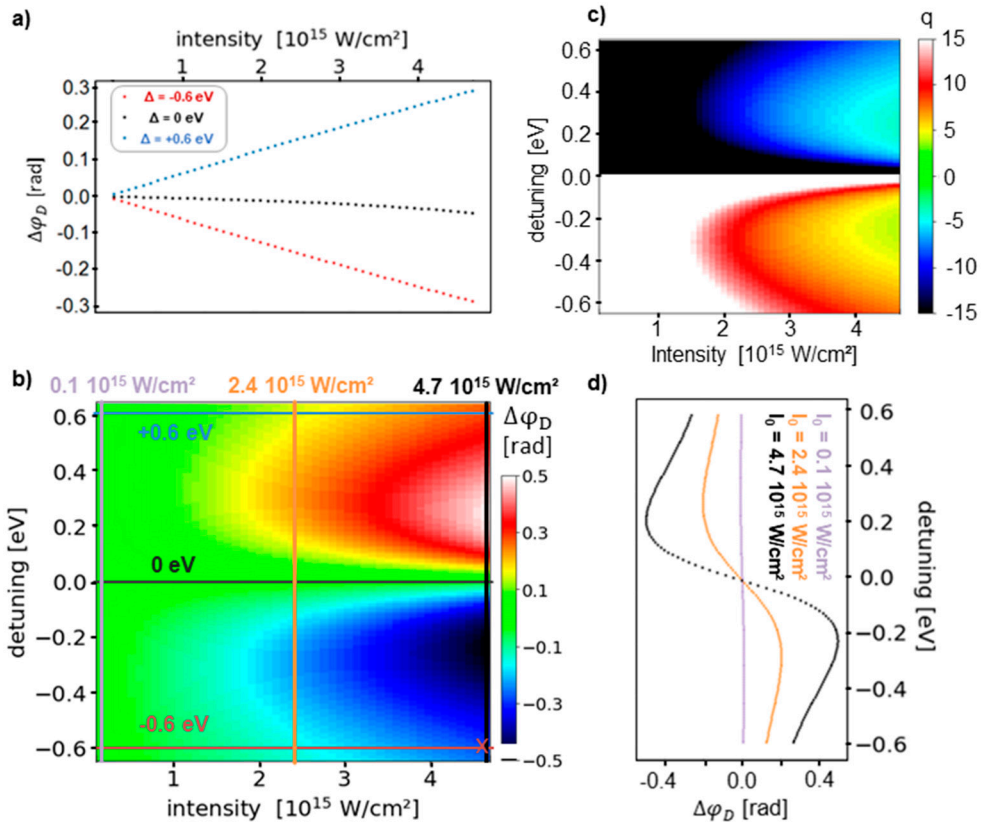

Figure 2. Results for the two-level system obtained by fitting a generalized Fano line shape (Equation (4)) to the simulated optical density. (**b**) dipole phase shift $\Delta\varphi_D$ obtained after applying Equation (5) to the direct fit results of q shown in (**c**) as a function of detuning and intensity, with corresponding (**a**) horizontal lineouts as a function of intensity for different detunings and (**d**) vertical lineouts as a function of detuning for different intensities. (**c**) the fitted q -parameter as a function of detuning and intensity.

We conclude from these results, that the dipole phase shift changes monotonically with the laser intensity (decreasing for red detuning and increasing for blue detuning), is equal in amplitude but flipped in sign if the detuning is flipped in sign and approximately vanishes for resonant driving pulses.

3.2. Analytical Approximation

In the following, we will relate these findings to the well-known description of a strongly coupled two-level system in the generalized Rabi formalism [1,2]. To understand the connection between the splitting and shifting of the involved energy levels to the modified absorption profile, we propose the comparison to the following analytical approximation: In the presence of the intense XUV pulse, the excited state of the system is split into two states $E^{\pm}$, which are the eigenstates of the laser-dressed two-level system, and which are energetically shifted with increasing field strength. For a temporally Gaussian-shaped XUV pulse envelope, the dressed states also shift energetically along a Gaussian curve in time (see Figure 1c). Hereby, one dressed state emerges directly from the atomic excited

state, whereas the other one is created from the ground state with the absorption of an XUV photon. It depends on the detuning Δ of the XUV pulse, which of the two bare states transforms into the energetically upshifted state E^+, and which transforms into the downshifted state E^- of the dressed two-level system. For a red-detuned XUV pulse, i.e., when the central photon energy of the pulse is smaller than the resonance transition energy, the excited state translates into E^+, whereas for a blue-detuned XUV pulse it translates into E^-. After the interaction with the XUV pulse, both bare states have collected a phase shift:

$$\Delta\varphi_{g,e} = \int \Delta E_{g,e}(t)\, dt, \tag{7}$$

due to the energy difference between the laser- dressed and bare states with respect to the weak-field coupling. The energy shifts are thus given by:

$$\Delta E_g(t) = \begin{cases} E^-(t) - E_{g+\omega}\,, \Delta\ < 0 \\ E^+(t) - E_{g+\omega}\,, \Delta\ > 0 \end{cases}, \ \Delta E_e(t) = \begin{cases} E^+(t) - E_e\,, \Delta\ < 0 \\ E^-(t) - E_e\,, \Delta\ > 0 \end{cases}, \tag{8}$$

where $E_{g+\omega} = E_g + \hbar\omega_c$ stands for the ground state energy plus the XUV photon energy. With the dipole phase $\varphi_D = \arg\left(c_g c_e^*\right)$ according to Equation (2), this directly translates into a phase shift of the resulting dipole emission:

$$\Delta\varphi_D = \Delta\varphi_g - \Delta\varphi_e. \tag{9}$$

For a monochromatic driving field of constant electric-field amplitude E_o, we can use the generalized Rabi formulas and obtain

$$E^\pm = E_e + \frac{\Delta}{2} \pm \frac{1}{2}\sqrt{\Delta^2 + |\hbar\Omega|^2} \tag{10}$$

for the energies of the laser-dressed states with the Rabi frequency $\Omega = d_{ge}E_o/\hbar$. We assume a rectangular pulse profile of duration $T = 2.82$ fs for the XUV pulse so that the dipole phase shift can now be analytically written as:

$$\Delta\varphi_D = \frac{\left(\Delta E_g - \Delta E_e\right)}{\hbar}T = \frac{1}{\hbar}\begin{cases} \left(-\Delta - \sqrt{\Delta^2 + |\Omega|^2}\right)T\,, \Delta\ < 0 \\ \left(-\Delta + \sqrt{\Delta^2 + |\Omega|^2}\right)T\,, \Delta\ > 0 \end{cases}. \tag{11}$$

We note, that this approximation is only valid in the impulsive limit ($T \ll 1/\Gamma_r$). The choice of $T = 2.82$ fs was made to match the integrated intensity –the fluence– of the rectangular pulse with the one of the $T = 3$ fs Gaussian pulse used previously. This analytical calculation of the dipole phase shift already explains some of the previously obtained trends (see Figure 3a): The dipole phase shift increases monotonically with peak intensity and assumes opposite sign for positive/negative detuning. However, we now observe a sharp jump from a maximal to a minimal phase shift across $\Delta = 0$ instead of a smooth transition through $\Delta\varphi_D = 0$ (compare with Figure 2b). This discontinuity in fact arises from the initial assumption of monochromatic light fields and thus well-defined detunings. Note that for zero detuning Equation (11) does not apply and thus the dipole phase shift is set to zero in this illustration. For temporally short and, thus, spectrally broad pulses, all spectral components of the pulse, i.e., photons with a detuning within the spectral pulse band width, contribute to this energy- and phase-shifting mechanism at the same time. Therefore, the resulting dipole phase shift is expected not to be determined by the central photon energy of the driving pulse alone, but rather by the average over its spectrum. In Figure 3b, we convolute (result shown in violet) the analytical expectation (shown in blue) of the detuning-dependent dipole phase shift for lowest intensities, $I_0 = 0.1 \times 10^{15}$ W/cm^2, with the spectrum of the 3 fs Gaussian driving pulse, which is also a Gaussian profile with an intensity FWHM of 0.61 eV (shown in red) and compare it to the numerical results from Figure 2d (shown

in black). Additionally, we scale the magnitude of the convoluted dipole phase shift with a factor of ~0.53 for a better qualitative comparison to the numerical results. One possible interpretation for this rescaling with a factor of approximately one half could be that the "effective" phase shift of the dipole emission is mainly induced by the trailing edge of the pulse, while its leading edge is mainly responsible for the excitation of the system. Since the dipole phase shift (see Equation (11)) is of equal magnitude but changes sign for positive/negative detuning, it evaluates to zero after convolution for a resonant driving pulse. In Figure 3c,d, we plot the detuning-dependent dipole phase shift from Figure 3a in the same manner as in Figure 3b, but for higher peak intensities, $I_0 = 2.4 \times 10^{15}$ W/cm^2 and $I_0 = 4.7 \times 10^{15}$ W/cm^2, respectively. For the result of this convolution, we find excellent agreement of the analytically calculated and convoluted phase shifts with the numerically obtained phase shifts, when we set the FWHM of the Gaussian convolution function to 0.45 eV and 0.3 eV and rescale the convoluted dipole phase shifts by ~0.64 and ~0.65, respectively. The finding of an intensity-dependent FWHM of the convolution function indicates a nonlinear process, which needs further investigation. Yet, this agreement shows how detuning-dependent line-shape asymmetry changes from impulsive dressing at high intensity can be captured and approximated within an analytical framework of the well-known Autler–Townes energy-level splitting of a strongly coupled two-level system using the generalized Rabi formalism.

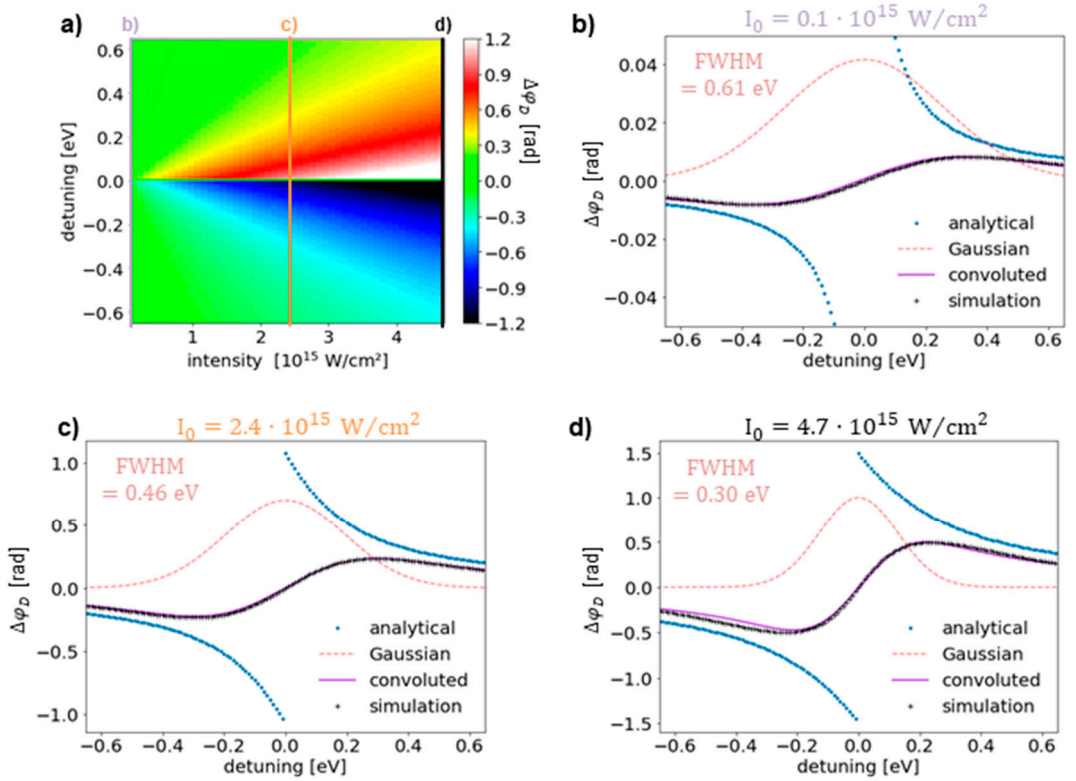

Figure 3. (**a**) dipole phase shifts $\Delta\varphi_D$ calculated analytically with Equation (11). A jump from positive to negative dipole phase shifts at zero detuning is clearly present as well as the monotonic increase (decrease) of $\Delta\varphi_D$ for blue (red) detuned pulses. (**b**–**d**) lineouts of the dipole phase shift (of Figure 3a), blue) are convoluted along the detuning axis (violet) with an intensity-dependent Gaussian profile (depicted at the resonance position, red) and compared to the numerical results (Figure 2d), black). (**b**) for the lowest intensity, $I_0 = 0.1 \times 10^{15}$ W/cm^2, the Gaussian convolution function with a FWHM = 0.61 eV corresponds to the spectrum of the 3 fs Gaussian driving pulse. (**c**,**d**) for higher intensities, $I_0 = 2.4 \times 10^{15}$ W/cm^2 and $I_0 = 4.7 \times 10^{15}$ W/cm^2, respectively, a decreasing FWHM of the Gaussian convolution function provides the best fit of the convoluted analytically calculated dipole phase shifts to the corresponding numerical results.

3.3. Autoionizing 2s2p Resonance in Helium

Pertaining to previous experimental results obtained at the Free-Electron Laser in Hamburg (FLASH) [16], we focus in the following on the impact of the detuning for the impulsive dressing of the 2s2p doubly excited state in helium, where the excited state couples to an ionization continuum. By repeating the numerical simulations for the autoionizing state (see H_{3lvl} in Equation (1)) for the same peak intensity and detuning values as used for the two-level system, the dipole phase shift and q parameter are again obtained from the same Fano fitting procedure as in the two-level case and are depicted in Figure 4. The literature asymmetry parameter $q = -2.75$ is reproduced for the lowest pulse intensity (see Figure 4b) and corresponds to an intrinsic dipole phase shift of $\varphi_0 \approx 0.7$ rad. To quantify only the field-induced dipole phase shift $\Delta\varphi'_D$, we subtract this offset phase: $\Delta\varphi'_D = \Delta\varphi_D - \varphi_0$ for Figure 4a. With increasing pulse intensity, we observe the three following features in the dipole phase shifts: (i) there is no dipole phase shift and hence no modification of the absorption line shape approximately for $\Delta \approx -0.2$ eV, which weakly depends on the laser intensity (violet line in Figure 4a, (ii) the dipole phase shift is negative for $\Delta \lesssim -0.2$ eV and positive for $\Delta \gtrsim -0.2$ eV and (iii) the magnitude of the dipole phase shift increases with the pulse peak intensity. Features (ii) and (iii) are very similar to the previous results of the two-level system, indicating that similar energy and phase shifts take place when the coupling to an ionization channel is explicitly included in contrast to the previous simple decay of an isolated state. However, now we observe a significant offset detuning $\Delta \approx -0.2$ eV for which the measurable line-shape asymmetry is approximately unchanged for increasing laser intensity. Furthermore, the magnitude of the positive and negative dipole phase shift around this offset are also different in strength. We give a first qualitative explanation of these new observations through the initial (i.e., weak-field) asymmetric Fano line shape by invoking a similar idea as for the analytical and convoluted calculations of the two-level system: For the given q-parameter of −2.75, the weak-field absorption cross section of the 2s2p resonance has a peak at photon energies smaller than the resonance position and a minimum for higher photon energies (see Figure 1e). Hence, the spectral components of a resonant driving XUV pulse with lower photon energies are more likely to be absorbed and, thus, their contributions to the dipole phase shift are expected to be more pronounced than the contribution of the higher photon energy components of the pulse. The dipole phase shift, thereby, is not cancelled out for a resonantly tuned XUV pulse as is the case for a weak-field Lorentzian resonance, but rather it is cancelled out for a slightly red detuned pulse, which is in qualitative agreement with the finding of an unchanged line-shape asymmetry around $\Delta \approx -0.2$ eV in Figure 4a. The observed trend, thus, seems to be a direct consequence of the configuration interaction and channel interference of a Fano resonance. We would like to note that the detuning offset ($\Delta \approx -0.2$ eV) for this specific case may depend on the exact description of the internal configuration interaction between the excited state and the ionization continuum. Since we utilize a quasi-continuum state here, we do not expect this value to be quantitatively precise. Nevertheless, the exact model choice of the coupled configurations is not expected to change our main finding of an asymmetric line-shape modification as a function of detuning for the impulsive dressing of an autoionizing state.

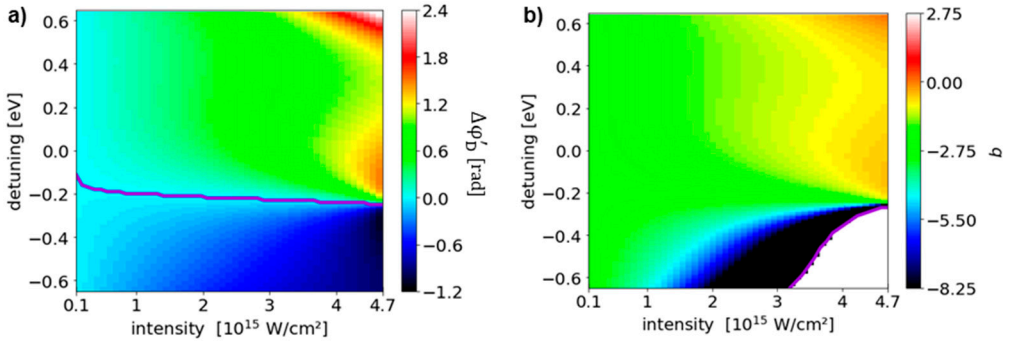

Figure 4. (**a**) dipole phase shift $\Delta\varphi'_D$ and (**b**) q parameter of the autoionizing 2s2p resonance in helium under variation of the driving pulse peak intensity and detuning. The dipole phase shift of the autoionizing resonance is comparable to the case of the two-level system, but an asymmetry along the detuning axis arises from the weak-field asymmetric Fano absorption profile. More details are given in the text. In (**a**), the superimposed violet line indicates an unchanged dipole phase, $\Delta\varphi'_D \approx 0$ rad, whereas in (**b**), the jump around $q \to \pm\infty$, corresponding to a Lorentzian profile, is also marked in violet in the parameter region $I_0 = (3 \ldots 4.7) \times 10^{15}$ W/cm^2 and $\Delta = (-0.65 \ldots -0.2)$ eV.

Further, a jump from $q \to -\infty$ to $q \to +\infty$ is clearly visible at the borderline between black and white colors in Figure 4b in the region of higher intensities between $I_0 > 3 \times 10^{15}$ W/cm^2 and $I_0 = 4.7 \times 10^{15}$ W/cm^2 and red detunings between $\Delta = -0.65$ eV and $\Delta < -0.2$ eV, which is highlighted with another superimposed violet line. Thus, the weak-field Fano line shape can be turned into a Lorentzian shape with the correct choice of XUV pulse intensity and detuning. This agrees qualitatively with previous experimental findings for the modification of the helium 2s2p resonance at an XUV-FEL facility [16]. There we regard the strong coupling by the FEL pulse to be mainly driven by a few temporally short coherence spikes within the much longer average FEL pulse duration. The temporal duration of these coherence spikes relates to the average FEL spectral bandwidth and amounts to a few femtoseconds [17], which approximately corresponds to the Gaussian pulse duration (T = 3 fs) used in this work. A more quantitative investigation of the impact of the average FEL pulse duration on the observed line-shape asymmetry will be subject of a forthcoming work [26].

4. Conclusions

In summary, we have utilized a numerical two- and three-level system to investigate the influence of the near-resonant detuning on the resonant absorption line shape for a strongly coupled XUV transition to an excited or autoionizing state in the impulsive limit, respectively. We used the relation between the Fano q asymmetry parameter and the dipole phase shift [8] and linked the observed phase shift to energy level shifts of a strongly coupled resonant transition. We could therefore explain how the near-resonant detuning of a strong XUV driving pulse can change and control the observed absorption line shape. We verified this assumption with a comparison to an analytical approximation based on the generalized Rabi formalism which yields a very good agreement. With the help of this analytical approximation we concluded that the broadband spectrum of the XUV pulse cannot be neglected, which is inherently connected to its ultrashort temporal duration in the limit of impulsive dressing of resonant transitions. Spectrally averaging over the detuning-dependent shift of the analytical approximation agrees well with the numerical results. Our numerical model also reveals line-shape asymmetry changes for the autoionizing 2s2p resonance in helium driven directly from the $1s^2$ ground state. Hereby, the line-shape modification and dipole phase shift induced by the intense XUV pulse reveals different trends for different detunings in an asymmetric manner. This asymmetry can be qualitatively explained by the weak-field limit of an initially asymmetric absorption profile. Notably, for a detuning around −0.2 eV the resonance line shape approximately keeps its weak-field asymmetry. We have shown in agreement with previous experimental results [16], that an intense and slightly red detuned XUV pulse may modify the absorption line shape of the weak-field Fano resonance to

a Lorentzian-like shape at high XUV intensity, with sensitivity to impulsively induced energy level shifts. Since our approach can be straightforwardly extended to any core-excited electron resonances in atomic targets, we expect these results to be of great interest for any spectroscopy and imaging experiments that are based on intense and short XUV and x-ray pulses generated from FEL facilities, where the average (X)FEL spectral bandwidth may become (much) broader than the natural spectral bandwidth of the coupled transition.

Author Contributions: Conceptualization, A.M. and T.P.; methodology, A.M., T.D. and L.A.; software, A.M. and L.A.; validation, A.M., L.A., T.D., P.R., M.R., C.O. and T.P.; formal analysis, A.M., L.A., T.D., P.R., M.R., C.O. and T.P.; investigation, C.O. and T.P.; data curation, A.M. and L.A.; writing—original draft preparation, A.M.; writing—review and editing, L.A., T.D., P.R., M.R., C.O. and T.P.; visualization, A.M. and C.O.; supervision, C.O. and T.P.; project administration, C.O. and T.P.; All authors have read and agreed to the published version of the manuscript.

Funding: This research received funding from the European Research Council (ERC) (X-MuSiC-616783).

Conflicts of Interest: The authors declare no conflict of interest.

References

1. Rabi, I.I. Space Quantization in a Gyrating Magnetic Field. *Phys. Rev.* **1937**, *51*, 652–654. [CrossRef]
2. Autler, S.H.; Townes, C.H. Stark Effect in Rapidly Varying Fields. *Phys. Rev.* **1955**, *100*, 703–722. [CrossRef]
3. Fano, U. Effects of Configuration Interaction on Intensities and Phase Shifts. *Phys. Rev.* **1961**, *124*, 1866–1878. [CrossRef]
4. Lambropoulos, P.; Zoller, P. Autoionizing states in strong laser fields. *Phys. Rev. A* **1981**, *24*, 379–397. [CrossRef]
5. Wang, H.; Chini, M.; Chen, S.; Zhang, C.-H.; He, F.; Cheng, Y.; Wu, Y.; Thumm, U.; Chang, Z.; Macdonald, J.R. Attosecond Time-Resolved Autoionization of Argon. *Phys. Rev. Lett.* **2010**, *105*, 143002. [CrossRef]
6. Loh, Z.H.; Greene, C.H.; Leone, S.R. Femtosecond induced transparency and absorption in the extreme ultraviolet by coherent coupling of the He 2s2p (1Po) and 2p2 (1Se) double excitation states with 800 nm light. *Chem. Phys.* **2008**, *350*, 7–13. [CrossRef]
7. Ott, C.; Kaldun, A.; Argenti, L.; Raith, P.; Meyer, K.; Laux, M.; Zhang, Y.; Blättermann, A.; Hagstotz, S.; Ding, T.; et al. Reconstruction and control of a time-dependent two-electron wave packet. *Nature* **2014**, *516*, 374–378. [CrossRef]
8. Ott, C.; Kaldun, A.; Raith, P.; Meyer, K.; Laux, M.; Evers, J.; Keitel, C.H.; Greene, C.H.; Pfeifer, T. Lorentz Meets Fano in Spectral Line Shapes: A Universal Phase and Its Laser Control. *Science* **2013**, *340*, 716–720. [CrossRef]
9. Reduzzi, M.; Chu, W.-C.; Feng, C.; Dubrouil, A.; Hummert, J.; Calegari, F.; Frassetto, F.; Poletto, L.; Kornilov, O.; Nisoli, M.; et al. Observation of autoionization dynamics and sub-cycle quantum beating in electronic molecular wave packets. *J. Phys. B At. Mol. Opt. Phys.* **2016**, *49*, 065102. [CrossRef]
10. Stooß, V.; Cavaletto, S.M.; Donsa, S.; Blättermann, A.; Birk, P.; Keitel, C.H.; Březinová, I.; Burgdörfer, J.; Ott, C.; Pfeifer, T. Real-Time Reconstruction of the Strong-Field-Driven Dipole Response. *Phys. Rev. Lett.* **2018**, *121*, 173005. [CrossRef]
11. Ackermann, W.; Asova, G.; Ayvazyan, V.; Azima, A.; Baboi, N.; Bähr, J.; Balandin, V.; Beutner, B.; Brandt, A.; Bolzmann, A.; et al. Operation of a free-electron laser from the extreme ultraviolet to the water window. *Nat. Photonics* **2007**, *1*, 336–342. [CrossRef]
12. Emma, P.; Akre, R.; Arthur, J.; Bionta, R.; Bostedt, C.; Bozek, J.; Brachmann, A.; Bucksbaum, P.; Coffee, R.; Decker, F.-J.; et al. First lasing and operation of an ångstrom-wavelength free-electron laser. *Nat. Photonics* **2010**, *4*. [CrossRef]
13. Young, L.; Kanter, E.P.; Krässig, B.; Li, Y.; March, A.M.; Pratt, S.T.; Santra, R.; Southworth, S.H.; Rohringer, N.; DiMauro, L.F.; et al. Femtosecond electronic response of atoms to ultra-intense X-rays. *Nature* **2010**, *466*, 56–61. [CrossRef] [PubMed]
14. Kanter, E.P.; Krässig, B.; Li, Y.; March, A.M.; Ho, P.; Rohringer, N.; Santra, R.; Southworth, S.H.; Dimauro, L.F.; Doumy, G.; et al. Unveiling and Driving Hidden Resonances with High-Fluence, High-Intensity X-Ray Pulses. *Phys. Rev. Lett.* **2011**, *107*, 23301. [CrossRef] [PubMed]
15. Sorokin, A.A.; Bobashev, S.V.; Feigl, T.; Tiedtke, K.; Wabnitz, H.; Richter, M. Photoelectric Effect at Ultrahigh Intensities. *Phys. Rev. Lett.* **2007**, *99*, 213002. [CrossRef] [PubMed]

16. Ott, C.; Aufleger, L.; Ding, T.; Rebholz, M.; Magunia, A.; Hartmann, M.; Stooß, V.; Wachs, D.; Birk, P.; Borisova, G.D.; et al. Strong-Field Extreme-Ultraviolet Dressing of Atomic Double Excitation. *Phys. Rev. Lett.* **2019**, *123*, 163–201. [CrossRef]
17. Ding, T.; Rebholz, M.; Aufleger, L.; Hartmann, M.; Meyer, K.; Stooß, V.; Magunia, A.; Wachs, D.; Birk, P.; Mi, Y.; et al. Nonlinear Coherence Effects in Transient-Absorption Ion Spectroscopy with Stochastic Extreme-Ultraviolet Free-Electron Laser Pulses. *Phys. Rev. Lett.* **2019**, *123*, 103001. [CrossRef]
18. Artemyev, A.N.; Cederbaum, L.S.; Demekhin, P. V Impact of intense laser pulses on the autoionization dynamics of the $2s2p$ doubly excited state of He. *Phys. Rev. A* **2017**, *96*, 33410. [CrossRef]
19. Mouloudakis, G.; Lambropoulos, P. Autoionizing states driven by stochastic electromagnetic fields. *J. Phys. B At. Mol. Opt. Phys.* **2018**, *51*, 01LT01. [CrossRef]
20. Mouloudakis, G.; Lambropoulos, P. Effects of field fluctuations on driven autoionizing resonances. *Eur. Phys. J. D* **2018**, *72*, 226. [CrossRef]
21. Domke, M.; Schulz, K.; Remmers, G.; Kaindl, G.; Wintgen, D. High-resolution study of 1 P o double-excitation states in helium. *Phys. Rev. A* **1996**, *53*, 1424–1438. [CrossRef] [PubMed]
22. Wu, M.; Chen, S.; Camp, S.; Schafer, K.J.; Gaarde, M.B. Theory of strong-field attosecond transient absorption. *J. Phys. B At. Mol. Opt. Phys.* **2016**, *49*, 062003. [CrossRef]
23. Rost, J.M.; Schulz, K.; Domke, M.; Kaindl, G. Resonance parameters of photo doubly excited helium. *J. Phys. B At. Mol. Opt. Phys.* **1997**, *30*, 4663. [CrossRef]
24. Kaldun, A.; Blättermann, A.; Stooß, V.; Donsa, S.; Wei, H.; Pazourek, R.; Nagele, S.; Ott, C.; Lin, C.D.; Burgdörfer, J.; et al. Observing the ultrafast buildup of a Fano resonance in the time domain. *Science* **2016**, *354*, 738–741. [CrossRef] [PubMed]
25. Kaldun, A.; Ott, C.; Blättermann, A.; Laux, M.; Meyer, K.; Ding, T.; Fischer, A.; Pfeifer, T. Extracting Phase and Amplitude Modifications of Laser-Coupled Fano Resonances. *Phys. Rev. Lett.* **2014**, *112*. [CrossRef]
26. Aufleger, L.; Friebel, P.; Rupprecht, P.; Magunia, A.; Ding, T.; Rebholz, M.; Hartmann, M.; Stooß, V.; Ott, C.; Pfeifer, T. Pulse length effects on autoionizing states under the influence of strong SASE XUV fields. *J. Phys. B*. (under review).

4.2. Electronic Population Reconstruction from Strong-Field-Modified Absorption Spectra with a Convolutional Neural Network

The previous publication has theoretically investigated XUV-driven absorption-line modifications and connected them to strong-field couplings of the electronic states. The resulting energy shifts of the electronic states are used to explain the simulated—and experimentally demonstrated [4]—line-shape changes. While these spectral changes are connected to temporal dipole phase shifts, and the dipole response can be reconstructed [70], the underlying *time-dependent* electron state-population dynamics cannot be accessed. This *inversion problem* is addressed in the publication shown in this section by utilizing a machine-learning–based approach: A *convolutional neural network (CNN)*. Although the foundations of CNNs (Section 2.4) are thematically (and mathematically) the least-related theoretical topic with respect to the central quantum-dynamical theme of this thesis, they are conceptually connected nevertheless: The energy-resolved, i.e. spectral, absorption measurement allows to identify the highly-correlated spectral features of a resonance line. The usage of a single XUV pulse shorter in time than the resonance life time, which thereby is spectrally broader than the resonance width, allows to measure the absorption line in one shot—capturing all of its potential modifications. The intrinsic relation between time- and energy-dependent observables arises from the Fourier-transformation and corresponding uncertainty principle (Equation (3)), which is fundamental to quantum dynamics. As the coupling/superposition of states leads to both Rabi-oscillations in the time domain, as well as energy shifts—and for short pulses to line-shape changes—in the spectral domain, the CNN used in the publication is capable of learning such relations and a corresponding inversion function. The publication utilizes a large data set based on varying the number of electronic states involved, driving-pulse peak intensity/field strength and photon energy/detuning to train the CNN. By utilizing an extended parameter range with respect to the previous publication (Section 4.1), it also includes further physical phenomena, which will be briefly mentioned within the publication, but the focus is on employing the CNN. In contrast, the findings of absorption-to-emission-line inversion and intensity-dependent population control in electron wave-packets connect on a (quantum-)physical base with further results of this thesis and will be discussed in Chapter 5.
As a CNN can *reconstruct time-resolved* quantities based on an *energy-resolved measurement*, it could potentially be employed in several quantum-dynamical experiments, which often require such an spectral analysis of data. In fact, an increasing number of experimental approaches, as for example presented with the setup in Section 3.1, are based on collecting multidimensional and complimentary (spectral) data sets to allow identification and understanding of underlying (temporal) processes. In the publication, pure simulation-based data is considered. Ideas for using CNNs on ultrafast quantum-dynamics experiments will be mentioned throughout Chapter 5. Alternatively, the scheme of pump-probe experiments as used in the third publication (Section 4.3) enables *direct time-resolved* measurements with ultrafast pulses.

optics

MDPI

Article

Electronic Population Reconstruction from Strong-Field-Modified Absorption Spectra with a Convolutional Neural Network

Daniel Richter [1,2,†], Alexander Magunia [1,2,*,†], Marc Rebholz [1], Christian Ott [1,*] and Thomas Pfeifer [1,*]

[1] Max-Planck-Institut für Kernphysik, Saupfercheckweg 1, 69117 Heidelberg, Germany; daniel.richter@mpi-hd.mpg.de (D.R.)
[2] Fakultät für Physik und Astronomie, Ruprecht-Karls-Universität Heidelberg, Im Neuenheimer Feld 226, 69120 Heidelberg, Germany
* Correspondence: alexander.magunia@mpi-hd.mpg.de (A.M.); christian.ott@mpi-hd.mpg.de (C.O.); thomas.pfeifer@mpi-hd.mpg.de (T.P.)
† These authors contributed equally to this work.

Abstract: We simulate ultrafast electronic transitions in an atom and corresponding absorption line changes with a numerical, few-level model, similar to previous work. In addition, a convolutional neural network (CNN) is employed for the first time to predict electronic state populations based on the simulated modifications of the absorption lines. We utilize a two-level and four-level system, as well as a variety of laser-pulse peak intensities and detunings, to account for different common scenarios of light–matter interaction. As a first step towards the use of CNNs for experimental absorption data in the future, we apply two different noise levels to the simulated input absorption data.

Keywords: atomic physics; ultrafast science; electronic population transfer; free-electron laser; transient absorption spectroscopy; extreme ultraviolet light; convolutional neural network

check for updates

Citation: Richter, D.; Magunia, A.; Rebholz, M.; Ott, C.; Pfeifer, T. Electronic Population Reconstruction from Strong-Field-Modified Absorption Spectra with a Convolutional Neural Network. *Optics* **2024**, *5*, 88–100. https://doi.org/10.3390/opt5010007

Academic Editor: Yuriy Garbovskiy

Received: 19 December 2023
Revised: 25 January 2024
Accepted: 15 February 2024
Published: 26 February 2024

1. Introduction

The development of attosecond laser sources [1–3] not only allows for capturing electronic motion in atoms, molecules and solids on their natural time scales, but it has also expanded the spectral regime of ultrafast pulses into the ultraviolet (UV) and extreme-ultraviolet (XUV) ranges. Besides the pioneering work on high-order harmonic generation (HHG) from near-infrared optical pulses [1–3], free-electron lasers can also generate XUV laser pulses [4], which are, since recently, also available with attosecond pulse durations [5,6]. One of the crucial benefits of FEL pulses is their high peak intensity, which allows for all-XUV pump–probe experiments [7] and strong-field effects in the XUV range on ultrashort time scales, such as Rabi cycling [8] or absorption line shape modifications [9–12]. Although properties such as the temporal dipole moment can be reconstructed under certain circumstances [13], the (intra-pulse) time-dependent state populations have not yet been directly reconstructed. This kind of inversion problem is common in a broad variety of quantum-based experiments, where phase information is typically lost and inversions are non-trivial, if possible at all. Still, electronic state populations and coherences are crucial for understanding effects such as Rabi cycling [8] or X-ray lasing [14] in atoms or charge transfer in molecules [15–17].

In contrast, machine learning (ML) in general and especially neural networks [18] as a subtype of ML based on multilayers of interconnected 'neurons' are well-known methods for pattern recognition and solving inversion problems. While nowadays utilized in broad areas and diverse applications, ML has recently also been used in ultrafast science, for example, in laser pulse reconstructions [19–24], high-order harmonic generation [25], noise reduction [26] and molecular- [27–30] or electronic-structure reconstruction methods [31–33]. In these applications, neural networks [19–23,25,27,28,30,33], and especially

convolutional neural networks (CNNs) [23,27,28,30,33], based on convolutional operations on spectral data, are utilized frequently. A common technique is to train the CNNs on simulated or modeled datasets [21,23–25,27,28,30,33] and (potentially) use them on experimental data afterwards. Besides large-scale quantum simulations and experimental approaches, ML can provide new insights for data analysis and reconstruction problems, with the goal of ultimately enhancing the understanding of the underlying quantum processes. Most recently, the first steps towards reconstructing time-resolved molecular dynamics have been demonstrated [28].

In this work, we simulate strong-field-induced line shape modifications with a numerical, few-level system, similar to previous work [9–12]. Furthermore, we implement a CNN, which reconstructs the electronic populations during the driving pulse from the simulated strong-field-modified absorption spectra of a two-level system. To allow the CNN to predict populations from experimental data in the future, we also introduce different noise levels into the absorption spectra before training the CNN. To extend our model towards more complex electron dynamics involving several states, we additionally apply the CNN to a four-level system, where a coherent wavepacket of three excited states is initiated.

2. Materials and Methods

2.1. Few-Level Systems for Simulations of Absorption Line Shape Changes

To simulate strong-field light–matter interaction and the resulting absorption changes, we consider a few-level system and solve the Schrödinger equation numerically, as described in detail in our previous work [11]. First, we describe a generic two-electronic-state system in an atom interacting with a laser pulse, cf. Figure 1a,b, with a Hamiltonian as follows:

$$H_{2lvl} = \begin{pmatrix} E_g & d_{ge}\varepsilon(t) \\ d_{ge}\varepsilon(t) & E_e - ih\Gamma_e/2 \end{pmatrix} \quad (1)$$

The diagonal matrix elements contain the eigenstate energies of the ground (g) and excited (e) state, E_g = 0 a.u and E_e = 0.2932 a.u., and the inverse lifetime of the excited state, Γ_e = 0.002 a.u. (a.u. denotes atomic units). The i represents the imaginary unit, whereas the h is the Planck constant. The off-diagonal matrix elements describe the dipole coupling between the two states, where we choose $d_{ge} = d_{eg}$ = 1 a.u. as the dipole constant and $\varepsilon(t)$ is the electric field of the laser pulse. We use a Gaussian pulse defined in the spectral domain $\tilde{\varepsilon}(\omega)$, with a spectral width of σ = 0.02314 a.u., corresponding to a 2.5 fs pulse duration, and centered at the resonance transition of the two states. To additionally produce a detuned dataset, we shift the excited-state energy by 0.0568 a.u towards lower photon energies without changing the laser pulse parameters. The time-dependent Schrödinger equation is solved for each time step t between −2.5 fs and 2.5 fs relative to the pulse peak intensity in steps of 0.025 fs. The two resulting time-dependent populations, $P_{g,e}(t) = |c_{g,e}(t)|^2$, of the bare states are shown in Figure 1c,d for the resonant and detuned pulses, respectively. $c_{g,e}$ are the coefficients of the general quantum state of the system, $|\Psi(t)\rangle = \left[c_g(t), c_e(t)\right]^T$, in the basis of the two bare states. With the help of the state coefficients, we can calculate the dipole response of the two-level system, $d(t) = d_{ge} \cdot c_g(t) c_e \times (t)$ + c.c., see Figure 1e, and its Fourier transform, $\tilde{d}(\omega)$. In the case of strong coupling dynamics, the resulting energy-level shifts lead to a phase shift of the temporal dipole response since the laser pulse is (much) shorter than the lifetime of the excited state [34]. This leads to line shape changes in the optical density, $OD(\omega)$, which we calculate from the in- and outgoing fields:

$$OD(\omega) = -\log_{10}\left(\frac{\left|\tilde{\varepsilon}(\omega) + i\eta \cdot \tilde{d}(\omega)\right|^2}{\left|\tilde{\varepsilon}(\omega)\right|^2}\right) \quad (2)$$

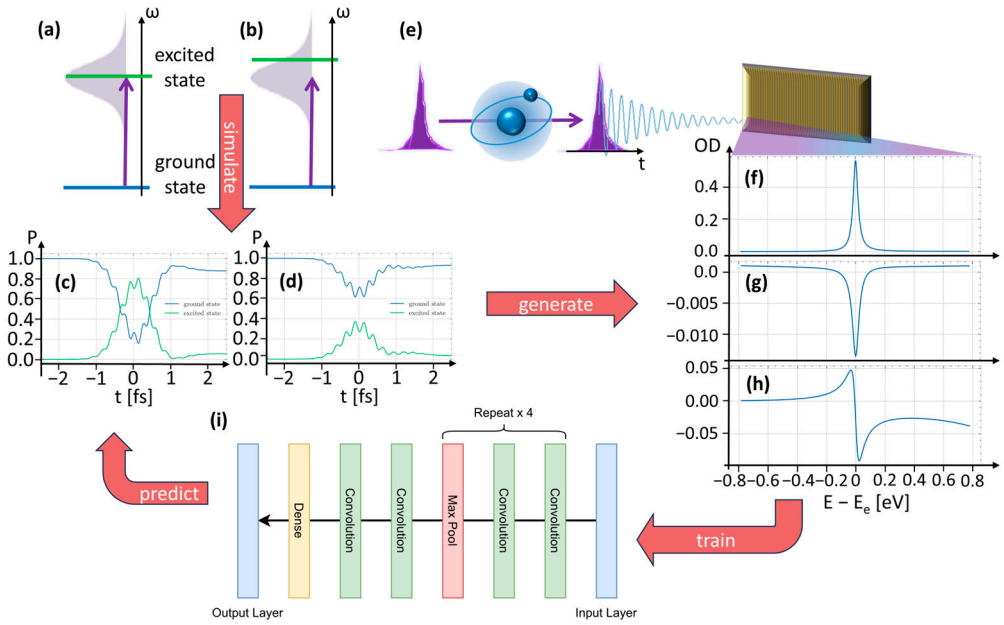

Figure 1. Conceptual overview of the population reconstruction from absorption changes in a two-level system. (**a**,**b**) A laser pulse (violet) excites a two-level system from its electronic ground (blue) state to an excited state (green)—either resonantly (**a**) or with a small detuning (**b**). (**c**) Time-dependent populations of the ground (blue) and excited state (green) for the resonant excitation are simulated with the numerical model. (**d**) Same as (**c**) but for the detuned case. (**e**) The excitation of the two-level system leads to a dipole response (blue) interfering with the incoming laser pulse (violet). (**f**–**h**) A spectroscopic measurement of these signals leads to a resonance line in the optical density for a weak (ε_0 = 0.7 a.u.) and resonant pulse (**f**), a strongly coupling (ε_0 = 6.1 a.u.) and resonant pulse (**g**) or a strongly coupling (ε_0 = 6.1 a.u.) and detuned pulse (**h**). The natural line shape (**f**) is modified due to the strong driving fields (**g**,**h**), which we use to train the CNN (**i**) to predict the state populations of the two states (**c**,**d**).

Here, $\eta = 10^{-4}$ is a numerical constant, proportional to the particle density in an absorption experiment. We illustrate the change in the resonance line shape in $\mathrm{OD}(\omega)$ from the weak-field case in Figure 1f to the strongly driven case for resonant and detuned pulses, shown in Figure 1g,h, respectively. $\mathrm{OD}(\omega)$ is the input for the CNN, see Figure 1i, which is used to reconstruct the populations, as described in the next section.

Regarding the four-level system, we replace the Hamiltonian with a 4×4 matrix containing the four eigen-energies of the ground state and the three excited states (e1, e2 e3): E_g = 0 a.u, E_{e1} = 0.2676 a.u., E_{e2} = 0.2932 a.u. and E_{e3} = 0.315 a.u. For all three excited states, we use the same inverse lifetime and dipole constant as for the two-level system. No dipole couplings are allowed between any two excited states by setting all other off-diagonal matrix elements to zero. The laser pulse is defined as above and resonant with the second excited state, thus also being equally red- and blue-detuned as the two other excited states.

2.2. Convolutional Neutral Network for State Population Reconstruction

2.2.1. Convolutional Neural Network Architecture

The inputs for the CNN are the OD spectra sampled with 300 data points symmetrically around the resonance position. The output variables of the CNN are the electron populations, each sampled on a time grid centered around a pulse between −2.5 fs and 2.5 fs with 200 points. For the two-level system, this results in a prediction of 2×200 output variables based on 300 input variables. To achieve such a high-dimensional output (relative to the input), the CNN architecture is constructed with several layers, in total containing 279,932 trainable parameters. The CNN layer-by-layer structure, which is constructed in a similar way as the methodologies in [30,33] describe, is depicted in Figure 2. The

CNN architecture is characterized by five blocks, each comprising two convolutional layers with a convolution window of size = 3 (kernel) and stride = 1, which is the step size by which the convolutional window moves across the input data. After each convolutional operation within the network, the convolutional layers are followed up by the Rectified Linear Unit (ReLU) activation function, defined as ReLU(x) = max(0, x). The convolutional operations are calculated without padding, resulting in an array size shrinkage of 2 after each layer. In each block, the two convolutional layers are followed up by a max-pooling layer with a kernel size = 2 and stride = 2. The inclusion of max-pooling layers segments the arrays into pooling regions of size 2, resulting in a further reduction in array dimensions by half after each block. To allow for more complex patterns to be captured by the CNN, the number of filters in each convolutional layer is doubled between consecutive blocks, ranging from 8 filters in the initial block to 128 filters in the last block. For the final block, the max-pooling layer is replaced by a densely, i.e., fully connected layer (with ReLU activation) consisting of 100 neurons. The final output layer is also a dense layer (with linear activation) with an output size of 2×200—quantifying the two time-dependent populations of the two-level system.

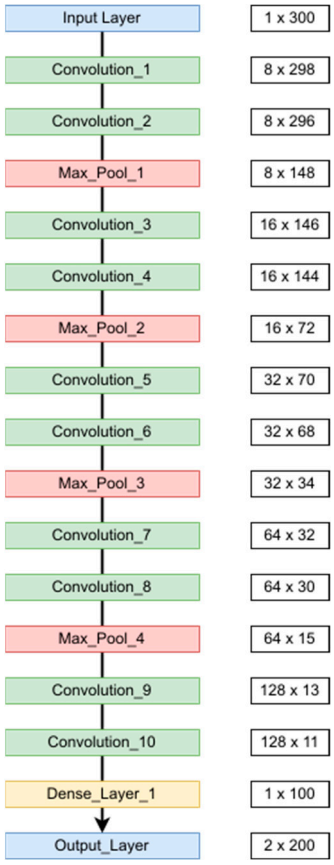

Figure 2. Overview of the convolutional neural network structure (for the two-level system). On the left, the sequence of layers is shown. On the right, the (output) array sizes for each layer are given.

2.2.2. Training Dataset Properties

For the training phase, we generated a comprehensive dataset consisting of 10,000 samples through repeated simulations of the two-level model by randomly sampling the peak field strength of the driving laser pulse, ε_0, on a logarithmic scale, ranging from 0.1 a.u. to 10 a.u. The random sampling improves consistency, promotes comparability and serves to minimize randomness as a confounding factor during the training process. This dataset combines the resonant and detuned cases introduced in Section 2.1. We allocate subsets of 6400 of these samples for training, 1600 for validation during training and 2000 for subsequent testing. Exactly

one half of all (sub)sets are calculated with the resonant and detuned settings, respectively. Furthermore, we generate two more datasets by introducing two Gaussian noise levels into the OD spectra. The two noise levels, 1% and 3%, are given as the standard deviation of Gaussian sampled noise. We chose these noise levels based on our experimental observations, for example, detecting absorption changes at a 2% level clearly above a smaller noise level in [35]. For the four-level system, as described in Section 2.1, we use nearly the same architecture as for the two-level system. Since the output variables, i.e., the state populations, are twice as large as before, 4×200, we also increase the resolution of the OD to 350 points to maintain comparable predictive resolution. This results in a total network size of 358,732 trainable parameters for the four-level system.

2.2.3. Training Process

To train the CNN, we utilize the Adam optimizer [36], a widely known optimization algorithm used for training deep neural networks. Both the selection of the optimizer and an initial learning rate of 10^{-3} are grounded in a heuristic approach, given that the Adam optimizer inherently adapts the learning rate during training. For the established regression task, the mean-squared error (MSE) is used as the loss function. This metric quantifies the average squared difference between predicted and actual values, thereby providing a measure of the CNN's proficiency in capturing the deviations between simulated and reconstructed populations.

$$\mathrm{MSE}(y, \hat{y}) = \frac{1}{n_{\mathrm{samples}}} \sum_{i=1}^{n_{\mathrm{samples}}} (y_i - \hat{y}_i)^2 \tag{3}$$

Here, $\hat{y}_i$ are the (simulated) input values and y_i are the values predicted by the CNN. The sample size, n_{samples}, sums over all data points, including all populations, time steps and laser field strengths. By training the CNN on datasets of different sizes and quantifying the losses with the MSE, as shown in Figure 3a, we observe the loss to be converged for the scenarios with 1% and 3% noise when our utilized training size of 6400 is reached. The loss function for the set without noise still decreases within the reported number of samples, as expected for a noise-free scenario, since the machine precision was not reached. Our goal is a CNN which, ultimately, can predict populations from (noisy) experimental data; thus, we did not increase the data size for the noise-free scenario. Further, we also use the Mean Absolute Error (MAE) as an additional metric, given as follows:

$$\mathrm{MAE}(y, \hat{y}) = \frac{1}{n_{\mathrm{samples}}} \sum_{i=1}^{n_{\mathrm{samples}}} |y_i - \hat{y}_i| \tag{4}$$

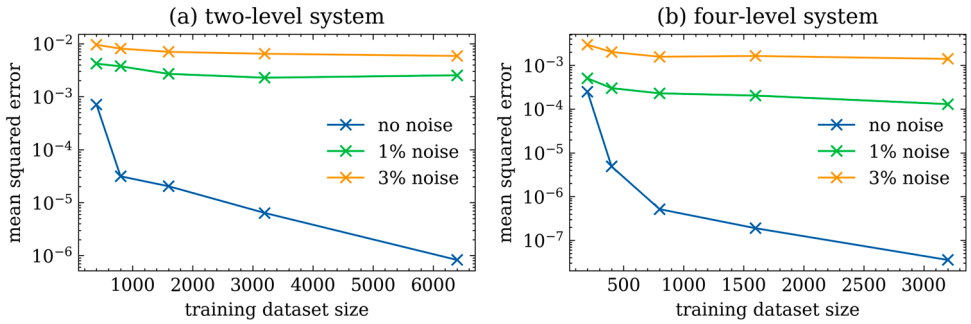

Figure 3. Loss (MSE) as a function of training dataset size for (**a**) the two-level system and (**b**) the four-level system. In both panels, the models trained on data without noise are shown in blue, the 1% noise cases are shown in green and the 3% noise cases are shown in orange.

This choice is grounded in the constraint of our model outputs within the range of zero to one for the populations. Consequently, interpreting the Mean Absolute Error allows for an intuitive understanding of our CNN's performance because it quantifies the average error over all data points, which can also be read as a percentage, i.e., MAE = 0.01 can be read as an average error of 1% over all data points. We train the two- and four-level CNNs for 5000 epochs each, with early stopping after 1000 epochs if the loss function has already converged. For each epoch, we randomly divide the training set into 100 batches of size 64, on which the CNN is trained iteratively to circumvent the expansive full training dataset size of 6400. After training, only the best-performing model is saved and selected for subsequent testing. As for the two-level case, we evaluate our model with the MSE for different training data sizes, as shown in Figure 3b. For the two cases containing noise, the loss converges for our data size of 3200, whereas the noise-free case has not reached convergence yet.

3. Results

3.1. Line Shape Changes and Population Reconstruction for the Two-Level System

In this section, we first show the results of the simulated absorption spectra (Figure 4) and discuss them with respect to previous findings [11,12]. Afterwards, the results of our novel approach to reconst the time-dependent electronic state populations from the absorption spectra are presented and discussed (Figures 5 and 6). In Figure 4a, the field-strength-dependent absorption is changing continuously in amplitude while staying Lorentzian, thus symmetric. As shown in our previous work [11,12], dipole phase shifts cancel out for exactly resonant driving pulses, hence explaining the symmetric line shape. For electric field strengths of 3.3 a.u. and 6.3 a.u., the resonant OD switches sign due to π-phase jumps in the Rabi cycle of the population coefficients [12]. In contrast, the detuned pulses can change the asymmetry of the resonance line by inducing dipole phase shifts [11,12], as shown in Figure 4b, hence making it Fano-like shaped [37]. For electric field strengths around 5 a.u. to 6 a.u., Fano-like line shapes emerge, which exhibit negative OD. A more detailed discussion of these line shape changes and how they are connected to the electronic state energies and coefficients can be found in [11,12].

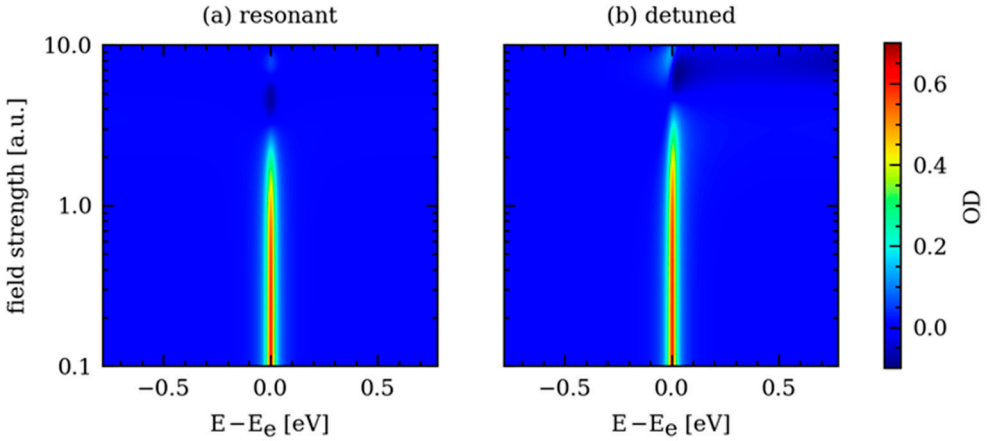

Figure 4. Field-strength-dependent OD(ω, ε_0) for (**a**) resonant and (**b**) detuned driving pulses of the two-level system. The field strength axis is logarithmic to cover the two orders of magnitude of field strength changes. For the resonant case (**a**), the line shape stays symmetric. In contrast, the line shape becomes asymmetric for the detuned case (**b**), as discussed in more detail in the text.

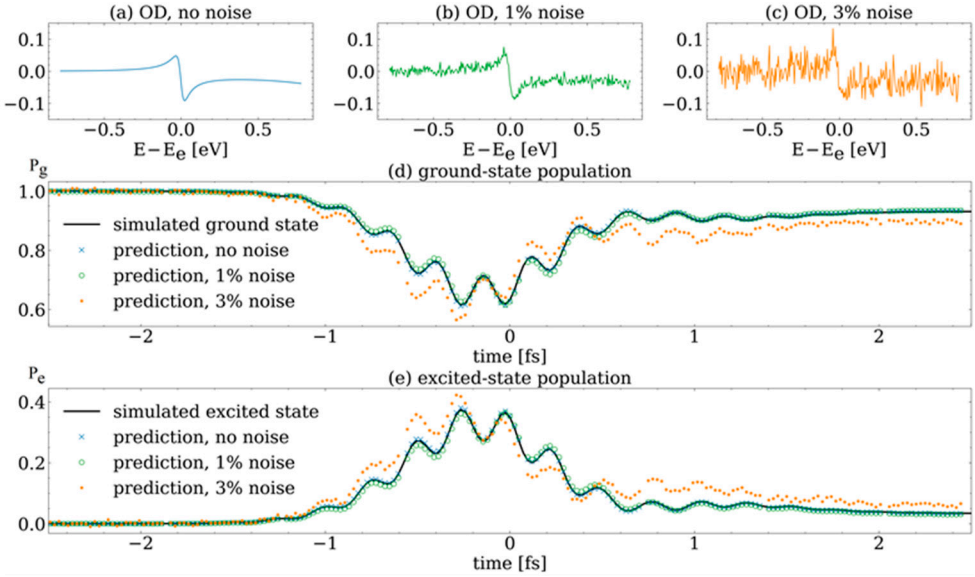

Figure 5. Population reconstructions for different noise levels. The same absorption lineout for a detuned driving pulse with a peak field strength of ε_0 = 6.1 a.u. is shown for different noise levels: (**a**) no noise, (**b**) 1% noise and (**c**) 3% noise. Simulated populations (black line) are compared to the CNN reconstructions (blue for no noise, green for 1% noise and orange for 3% noise) of the excited (**d**) and ground states (**e**).

In Figure 5, we illustrate that the CNN is capable of reconstructing the populations of the ground (Figure 5d) and excited states (Figure 5e), including the three different noise levels, for a single field strength of ε_0 = 6.1 a.u. of a detuned driving pulse. The OD spectrum is shown in Figure 5a without noise, with a 1% noise level in Figure 5b and a 3% noise level in Figure 5c. For both states—the ground state in Figure 5d and the excited state in Figure 5e—the reconstructed populations for the noise-free case (blue) are in near-perfect agreement with the simulated populations (black). Even when introducing 1% noise into the OD, the CNN reconstructs the state populations excellently (shown in green). In contrast, when the noise level is increased to 3%, only the slow overall shapes of the reconstructed populations (orange) can be predicted reasonably well, whereas the faster dynamics are not accurate anymore. To prove that the CNN can reconstruct the electronic populations in general for the complete dataset, we compare the simulated population (Figure 5a,b) of the excited state to the reconstructed population (Figure 5c,d) as a function of the field strength of the driving pulse in Figure 6. We look at the excited state population only because the sum of the ground state and excited state populations is equal to one for all time steps without the presence of further loss channels. For the CNN reconstruction, we chose the 1% noise level in the OD based on the results obtained for a single electric field strength, as discussed in Figure 5. For the resonant driving pulse, the population is reconstructed excellently for most field strengths in Figure 6c compared to the simulated population in Figure 6a. Only for field strengths from 6.1 a.u. to 6.6 a.u. does the reconstruction differ from the simulation, as discussed below. In the detuned case, the population is reconstructed accurately for most field strengths in Figure 6d compared to Figure 6b. For field strengths of 4.5 a.u. to 4.6 a.u., the reconstruction is significantly different from the simulation. Looking at the corresponding input ODs in Figure 4a,b reveals that for a field strength of 3.3 a.u. and 6.5 a.u. in the resonant case (a) and 4.5 a.u. in the detuned case (b), the ODs are near flat and close to zero. Due to this ambiguity, the CNN cannot distinguish between the three cases where the OD vanishes, which is why the training and reconstruction with the CNN fail in these specific cases.

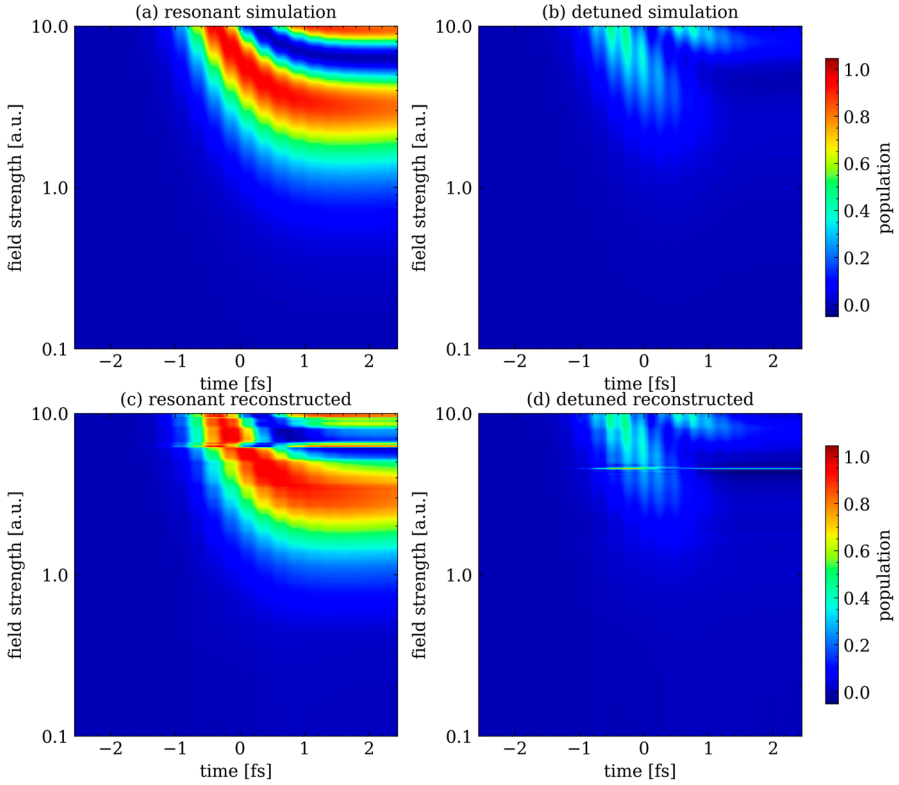

Figure 6. Field-strength-dependent simulated populations of the excited state for (**a**) resonant and (**b**) detuned driving pulses and respective CNN reconstructions (**c**,**d**) for the 1% noise level on the ODs. In all panels, the populations are close to zero for low field strengths ($\varepsilon_0 \leq 1$). For higher field strengths (1 a.u. $< \varepsilon_0$), the population is first significantly increased and further begins to oscillate up and down when 7 a.u. $< \varepsilon_0$. As is well known from Rabi oscillations [38], the population transfer is significantly reduced for detuned pulses; thus, the maximum excited state population for the detuned case (**b**,**d**) of $P_e{}^{max} \approx 0.5$ is smaller than for the resonant case (**a**,**c**), where $P_e{}^{max} = 1$. We do not use the rotating wave approximation; thus, the populations oscillate with $2\omega_r$ [38] during the interaction with the pulse, which is twice the frequency of the resonance transition.

For a quantitative comparison of the reconstructed with the simulated populations, the MSEs (Equation (3)) and MAEs (Equation (4)) are presented in Table 1 for all three noise levels. As expected from the above findings, the errors increase with the noise. All error values are a few percent or less, thus confirming the excellent agreement between the reconstructed and simulated populations for most field strengths, with the exceptions mentioned above. This demonstrates that the CNN is capable of reconstructing the populations of two electronic states based on absorption line changes in all cases where the absorption signal is larger than the noise.

Table 1. MSE and MAE of the population reconstruction for the two-level system.

Error	No Noise	1% Noise	3% Noise
MSE	5.7×10^{-7}	3.4×10^{-3}	5.5×10^{-3}
MAE	4.1×10^{-4}	1.5×10^{-2}	3.3×10^{-2}

3.2. Line Shape Changes and Population Reconstruction for the Four-Level System

To investigate how more complex electronic population dynamics can be reconstructed with our CNN, we simulate a four-level system, as described in Section 2.1.

The driving pulse, resonant with the central excited state, excites a coherent wavepacket across the three states, where the energy spacing between the excited states is smaller than

the spectral bandwidth of the pulse. The resulting absorption spectra for three different field strengths are shown in Figure 7. With an increasing field strength of the pulse, the amplitudes of all three resonances are reduced because of a reduction in the ground state population. As in the two-level system, the resonant excited state stays symmetric, whereas the line shapes of the two other excited states become more asymmetric with increased field strength. As shown in [11], for equal red and blue detuning of the driving pulse, their line shapes become Fano-like with mirrored asymmetries. Small deviations from this asymmetry come from numerical errors due to the discrete spectral grid. The corresponding population dynamics of the four states are shown in Figure 8. The CNN can reconstruct all four state populations for all three field strengths when no noise is added to the OD, compared to the simulated populations (depicted with black markers; see Figure 8a,d,g). Adding noise levels of 1% and 3%, the populations can be reconstructed as well, but only for low and intermediate field strengths; see Figure 8b,c,e,f. For the highest field strength and a 1% noise level, shown in Figure 8h, the reconstructed populations show similar slower dynamics as the simulated populations, but the local minima and maxima of the population transfer are decreased in amplitude when compared to the simulations. When increasing the noise to 3% for the highest field strength, as shown in Figure 8i, many of the predicted population dynamics are not correct with regard to the simulated populations: the fast oscillations are missing, the number of Rabi cycles is reduced and after the pulse is over (t > 1 fs), the populations of the detuned states, e1 (green) and e2 (red), are larger than the resonant excited state population (orange), which is in contrast to the simulated populations. Yet these deviations can only be found for the highest field strengths in the 3% noise case. Overall, the CNN reconstructs the four electronic state populations mostly accurately, as quantified by the mean errors in Table 2. The mean errors are obtained by averaging over the populations of all field strengths; thus, the deviations for the highest field strengths contribute only marginally. As in the two-level system, the errors increase by an order(s) of magnitude when the noise level is increased. Comparing the overall performance to the two-level system and the error values in Table 1, the CNN reconstructs the four-level populations slightly better than for the two-level system, which might be due to the higher amount of information provided in the OD spectra.

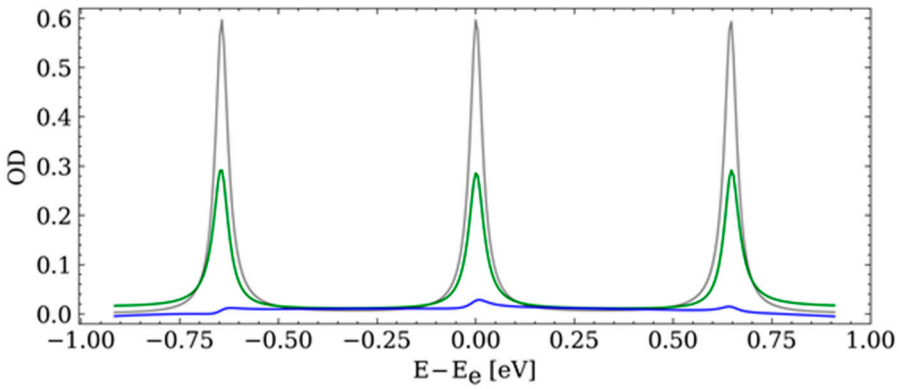

Figure 7. Absorption of the four-level system for different field strengths. The OD is shown for a weak field strength, ε_0 = 0.1 a.u. (grey), an intermediate field strength, ε_0 = 1.2 a.u. (green) and a high field-strength, ε_0 = 9.1 a.u. (blue), of the driving pulse. For the high field strength, the OD is multiplied by a factor of 4 for better visibility.

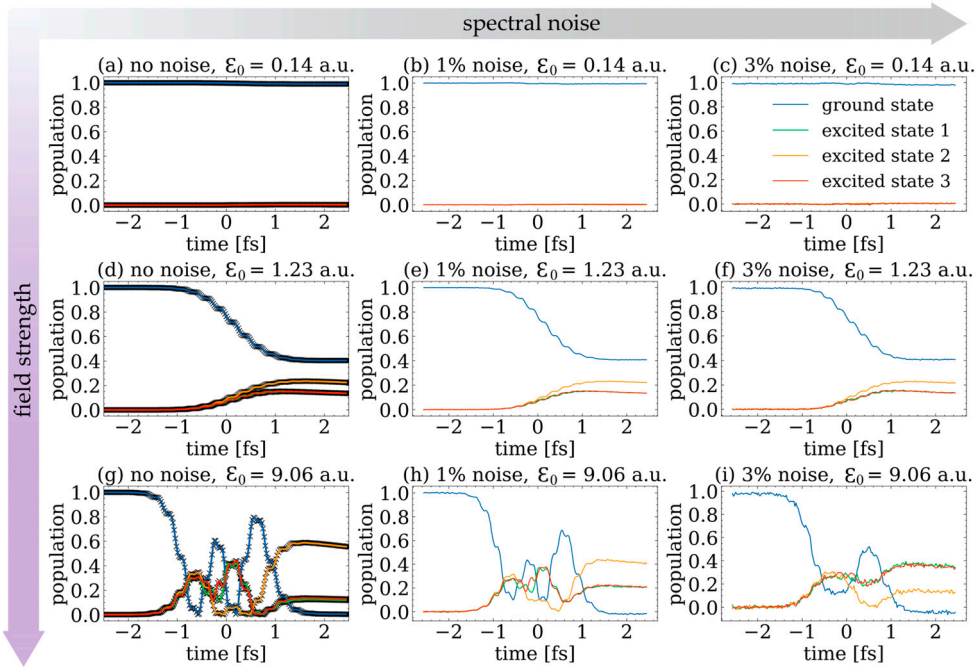

Figure 8. CNN-reconstructed populations of the ground (blue), first excited (green), second excited (orange) and third excited states (red) in the four-level system for (**a**–**c**) low (ε_0 = 0.14 a.u.), (**d**–**f**) intermediate (ε_0 = 1.23 a.u.) and (**g**–**i**) high field strengths (ε_0 = 9.06 a.u.) of the pulse, as well as for (**a**,**d**,**g**) no noise, (**b**,**e**,**h**) 1% and (**c**,**f**,**i**) 3% noise. In (**a**,**d**,**g**), the simulated populations are shown with black markers. Similar to the two-level case, the populations stay nearly unchanged for low field strengths but are significantly transferred for higher field strengths and undergo several Rabi oscillations (and faster $2\omega_r$ oscillations) for the highest field strength. In all panels, the populations of the two detuned excited states, e1 (green) and e2 (red), are nearly the same, whereas the population of the resonant excited state, e2 (orange), shows clearly different temporal behavior.

Table 2. MSE and MAE of the population reconstruction for the four-level system.

Error	No Noise	1% Noise	3% Noise
MSE	3.6×10^{-8}	1.7×10^{-4}	1.3×10^{-3}
MAE	1.2×10^{-4}	4.4×10^{-3}	1.4×10^{-2}

4. Conclusions and Outlook

In summary, we have shown that a CNN can be used to reconstruct time-dependent electronic state populations from simulated OD spectra for two different scenarios of laser pulse excitations: the excitation of an individual electronic state (in the two-level system) as well as launching an electronic wave packet consisting of three excited states (in the four-level system). We have demonstrated this for driving pulse electric-field strengths spanning across two orders of magnitude—continuously tuning from the weak-field to the strong-coupling case. For the two-level system, we have further shown that reconstruction is possible for (two) different cases of pulse detunings. Furthermore, by including two different noise levels in the input spectra, we have found that a 1% noise level does not change the CNN reconstructions significantly, whereas an increase to a 3% noise level leads to the CNN predictions deviating more significantly from the input populations for the highest driving pulse field strengths. With regards to the pulse intensities and dipole couplings chosen here, we thus identify the 3% noise level as an upper limit. In the future, for utilizing the CNN for experimental strong-field-driven absorption spectra, we suggest a dataset combining theoretical simulations and experimental weak-field absorption measurements—where the populations are nearly unchanged and could be calculated with perturbation

theory—which is conceptually similar to previous works [21,23–25,27,28,30,33]. In the XUV spectral regime, strong coupling experiments have been performed with self-amplified spontaneous emission (SASE) [4]-based FEL pulses in an autoionizing state [9]. In these cases, not only the peak intensity but also the spectral structure, central photon energy and pulse duration vary from shot to shot. The models and datasets discussed here should thus be expanded to higher dimensions by also training the CNN on this extended parameter space. To that end, the measurements should account for these different input parameters instead of averaging over them to provide large enough datasets. As a possible benefit of this, the CNN might be capable of learning and predicting FEL pulse parameters in parallel with the populations or could be combined with other neural networks (NNs) trained for FEL pulses [20,24] to achieve this. Alternatively, using more stable and coherent seeded FEL pulses [39], the simulation and CNN presented here could already be sufficient to predict the electronic state populations, but such experiments have not been performed yet. Furthermore, combinations with noise reduction NNs [26] might be helpful for even more precise predictions. As an outlook, our simulated two-level dynamics reveal absorption changes that in principle allow for a novel method of light amplification (when the OD becomes negative), even without population inversion (cf. Figure 5). In previous work, light amplification was achieved by population inversion [14], stimulated Raman scattering [40,41], phase shifts through mechanical displacement [42] or by including additional states/ionization continua or light fields in the case of amplification without population inversion [34,43–52]. In most cases, the electron populations play a key role. Thus, we expect that our approach of a few-level-based simulation and CNN will also help in the future to investigate different light amplification mechanisms. In addition, the population dynamics of the coherent wavepacket excitation in the four-level system illustrate how intra-pulse electronic population transfer leads to absorption changes when more than a single resonance in an atom is involved. Going one step further by exciting or ionizing (several) electronic states in molecules could ultimately lead to ultrafast charge transfer dynamics [15,17,53], where we expect a CNN to provide predictions of electronic populations during the pulse duration—which might influence subsequent charge transfer and even slower molecular structural dynamics—perhaps in combination with corresponding CNNs [27–30]. Overall, strong-field-modified absorption spectra can be used to investigate electronic dynamics in atoms and molecules, which—in turn—can also be used to shape and modify the driving pulses themselves, such as their amplification in selected spectral regions. In the future, we expect ML in general and CNNs in particular to provide new insights into the ultrafast interplay of UV, XUV and X-ray laser pulses with atoms or molecules.

Author Contributions: Conceptualization: D.R., A.M. and T.P.; methodology: D.R., A.M. and M.R.; software: D.R.; investigation: D.R., A.M. and M.R.; resources: C.O. and T.P.; writing—original draft preparation: D.R. and A.M.; writing—review and editing: C.O. and T.P.; visualization: D.R. and A.M.; supervision: T.P.; project administration: A.M., M.R. and T.P. All authors have read and agreed to the published version of the manuscript.

Funding: We acknowledge support by the Deutsche Forschungsgemeinschaft (DFG, German Research Foundation) under Germany's Excellence Strategy EXC2181/1-390900948 (the Heidelberg STRUCTURES Excellence Cluster).

Institutional Review Board Statement: Not applicable.

Informed Consent Statement: Not applicable.

Data Availability Statement: Data are contained within the article.

Conflicts of Interest: The authors declare no conflicts of interest.

References

1. Hentschel, M.; Kienberger, R.; Spielmann, C.; Reider, G.A.; Milosevic, N.; Brabec, T.; Corkum, P.; Heinzmann, U.; Drescher, M.; Krausz, F. Attosecond Metrology. *Nature* **2001**, *414*, 509–513. [CrossRef]

2. Lewenstein, M.; Balcou, P.; Ivanov, M.Y.; L'Huillier, A.; Corkum, P.B. Theory of High-Harmonic Generation by Low-Frequency Laser Fields. *Phys. Rev. A* **1994**, *49*, 2117. [CrossRef]
3. Paul, P.M.; Toma, E.S.; Breger, P.; Mullot, G.; Augé, F.; Balcou, P.; Muller, H.G.; Agostini, P. Observation of a Train of Attosecond Pulses from High Harmonic Generation. *Science* **2001**, *292*, 1689–1692. [CrossRef] [PubMed]
4. Ackermann, W.; Asova, G.; Ayvazyan, V.; Azima, A.; Baboi, N.; Bähr, J.; Balandin, V.; Beutner, B.; Brandt, A.; Bolzmann, A.; et al. Operation of a Free-Electron Laser from the Extreme Ultraviolet to the Water Window. *Nat. Photonics* **2007**, *1*, 336–342. [CrossRef]
5. Duris, J.; Li, S.; Driver, T.; Champenois, E.G.; MacArthur, J.P.; Lutman, A.A.; Zhang, Z.; Rosenberger, P.; Aldrich, J.W.; Coffee, R.; et al. Tunable Isolated Attosecond X-Ray Pulses with Gigawatt Peak Power from a Free-Electron Laser. *Nat. Photonics* **2019**, *14*, 30–36. [CrossRef]
6. Maroju, P.K.; Grazioli, C.; Di Fraia, M.; Moioli, M.; Ertel, D.; Ahmadi, H.; Plekan, O.; Finetti, P.; Allaria, E.; Giannessi, L.; et al. Attosecond Pulse Shaping Using a Seeded Free-Electron Laser. *Nature* **2020**, *578*, 386–391. [CrossRef]
7. Tzallas, P.; Skantzakis, E.; Nikolopoulos, L.A.A.; Tsakiris, G.D.; Charalambidis, D. Extreme-Ultraviolet Pump–Probe Studies of One-Femtosecond-Scale Electron Dynamics. *Nat. Phys.* **2011**, *7*, 781–784. [CrossRef]
8. Nandi, S.; Olofsson, E.; Bertolino, M.; Carlström, S.; Zapata, F.; Busto, D.; Callegari, C.; Di Fraia, M.; Eng-Johnsson, P.; Feifel, R.; et al. Observation of Rabi Dynamics with a Short-Wavelength Free-Electron Laser. *Nature* **2022**, *608*, 488–493. [CrossRef]
9. Ott, C.; Aufleger, L.; Ding, T.; Rebholz, M.; Magunia, A.; Hartmann, M.; Stooß, V.; Wachs, D.; Birk, P.; Borisova, G.D.; et al. Strong-Field Extreme-Ultraviolet Dressing of Atomic Double Excitation. *Phys. Rev. Lett.* **2019**, *123*, 163–201. [CrossRef]
10. Aufleger, L.; Friebel, P.; Rupprecht, P.; Magunia, A.; Ding, T.; Rebholz, M.; Hartmann, M.; Ott, C.; Pfeifer, T. Line-Shape Broadening of an Autoionizing State in Helium at High XUV Intensity. *New J. Phys.* **2022**, *24*, 013014. [CrossRef]
11. Magunia, A.; Aufleger, L.; Ding, T.; Rupprecht, P.; Rebholz, M.; Ott, C.; Pfeifer, T. Bound-State Electron Dynamics Driven by Near-Resonantly Detuned Intense and Ultrashort Pulsed XUV Fields. *Appl. Sci.* **2020**, *10*, 6153. [CrossRef]
12. He, Y.; Shi, H.; Xue, N.; Magunia, A.; Sun, S.; Ding, J.; Hu, B.; Liu, Z. Direct Manipulation of Atomic Excitation with Intense Extreme-Ultraviolet Laser Fields. *Phys. Rev. A* **2022**, *105*, 043113. [CrossRef]
13. Stooß, V.; Cavaletto, S.M.; Donsa, S.; Blättermann, A.; Birk, P.; Keitel, C.H.; Březinová, I.; Burgdörfer, J.; Ott, C.; Pfeifer, T. Real-Time Reconstruction of the Strong-Field-Driven Dipole Response. *Phys. Rev. Lett.* **2018**, *121*, 173005. [CrossRef]
14. Rohringer, N.; Ryan, D.; London, R.A.; Purvis, M.; Albert, F.; Dunn, J.; Bozek, J.D.; Bostedt, C.; Graf, A.; Hill, R.; et al. Atomic Inner-Shell X-Ray Laser at 1.46 Nanometres Pumped by an X-Ray Free-Electron Laser. *Nature* **2012**, *481*, 488–491. [CrossRef]
15. Calegari, F.; Ayuso, D.; Trabattoni, A.; Belshaw, L.; De Camillis, S.; Anumula, S.; Frassetto, F.; Poletto, L.; Palacios, A.; Decleva, P.; et al. Ultrafast Electron Dynamics in Phenylalanine Initiated by Attosecond Pulses. *Science* **2014**, *346*, 336–339. [CrossRef]
16. Mayer, D.; Lever, F.; Picconi, D.; Metje, J.; Alisauskas, S.; Calegari, F.; Düsterer, S.; Ehlert, C.; Feifel, R.; Niebuhr, M.; et al. Following Excited-State Chemical Shifts in Molecular Ultrafast x-Ray Photoelectron Spectroscopy. *Nat. Commun.* **2022**, *13*, 198. [CrossRef]
17. Al-Haddad, A.; Oberli, S.; González-Vázquez, J.; Bucher, M.; Doumy, G.; Ho, P.; Krzywinski, J.; Lane, T.J.; Lutman, A.; Marinelli, A.; et al. Observation of Site-Selective Chemical Bond Changes via Ultrafast Chemical Shifts. *Nat. Commun.* **2022**, *13*, 7170. [CrossRef]
18. Cheng, B.; Titterington, D.M. Neural Networks: A Review from a Statistical Perspective. *Stat. Sci.* **1994**, *9*, 2–30. [CrossRef]
19. Salmela, L.; Tsipinakis, N.; Foi, A.; Billet, C.; Dudley, J.M.; Genty, G. Predicting Ultrafast Nonlinear Dynamics in Fibre Optics with a Recurrent Neural Network. *Nat. Mach. Intell.* **2021**, *3*, 344–354. [CrossRef]
20. Sanchez-Gonzalez, A.; Micaelli, P.; Olivier, C.; Barillot, T.R.; Ilchen, M.; Lutman, A.A.; Marinelli, A.; Maxwell, T.; Achner, A.; Agåker, M.; et al. Accurate Prediction of X-Ray Pulse Properties from a Free-Electron Laser Using Machine Learning. *Nat. Commun.* **2017**, *8*, 15461. [CrossRef] [PubMed]
21. Kleinert, S.; Morgner, U.; Tajalli, A.; Nagy, T. Rapid Phase Retrieval of Ultrashort Pulses from Dispersion Scan Traces Using Deep Neural Networks. *Opt. Lett.* **2019**, *44*, 979–982. [CrossRef]
22. DeLong, K.W.; Ladera, C.L.; Fittinghoff, D.N.; Krumbügel, M.A.; Trebino, R.; Sweetser, J.N. Direct Ultrashort-Pulse Intensity and Phase Retrieval by Frequency-Resolved Optical Gating and a Computational Neural Network. *Opt. Lett.* **1996**, *21*, 143–145. [CrossRef]
23. Zahavy, T.; Dikopoltsev, A.; Cohen, O.; Mannor, S.; Segev, M. Deep Learning Reconstruction of Ultrashort Pulses. *Optica* **2018**, *5*, 666–673. [CrossRef]
24. Breckwoldt, N.; Son, S.-K.; Mazza, T.; Rörig, A.; Boll, R.; Meyer, M.; LaForge, A.C.; Mishra, D.; Berrah, N.; Santra, R. Machine-Learning Calibration of Intense x-Ray Free-Electron-Laser Pulses Using Bayesian Optimization. *Phys. Rev. Res.* **2023**, *5*, 023114. [CrossRef]
25. Gherman, A.M.M.; Kovács, K.; Cristea, M.V.; Toşa, V. Artificial Neural Network Trained to Predict High-Harmonic Flux. *Appl. Sci.* **2018**, *8*, 2106. [CrossRef]
26. Gutberlet, T.; Chang, H.-T.; Zayko, S.; Sivis, M.; Ropers, C. High-Sensitivity Extreme-Ultraviolet Transient Absorption Spectroscopy Enabled by Machine Learning. *Opt. Express* **2023**, *31*, 39757–39764. [CrossRef]
27. Shvetsov-Shilovski, N.I.; Lein, M. Deep Learning for Retrieval of the Internuclear Distance in a Molecule from Interference Patterns in Photoelectron Momentum Distributions. *Phys. Rev. A* **2022**, *105*, L021102. [CrossRef]
28. Liu, X.; Amini, K.; Sanchez, A.; Belsa, B.; Steinle, T.; Biegert, J. Machine Learning for Laser-Induced Electron Diffraction Imaging of Molecular Structures. *Commun. Chem.* **2021**, *4*, 154. [CrossRef]

29. Rupp, M.; Tkatchenko, A.; Müller, K.R.; Von Lilienfeld, O.A. Fast and Accurate Modeling of Molecular Atomization Energies with Machine Learning. *Phys. Rev. Lett.* **2012**, *108*, 058301. [CrossRef]
30. Shvetsov-Shilovski, N.I.; Lein, M. Transfer Learning, Alternative Approaches, and Visualization of a Convolutional Neural Network for Retrieval of the Internuclear Distance in a Molecule from Photoelectron Momentum Distributions. *Phys. Rev. A* **2023**, *107*, 033106. [CrossRef]
31. Brockherde, F.; Vogt, L.; Li, L.; Tuckerman, M.E.; Burke, K.; Müller, K.-R. By-Passing the Kohn-Sham Equations with Machine Learning. *Nat. Commun.* **2016**, *8*, 872. [CrossRef]
32. Snyder, J.C.; Rupp, M.; Hansen, K.; Müller, K.R.; Burke, K. Finding Density Functionals with Machine Learning. *Phys. Rev. Lett.* **2012**, *108*, 253002. [CrossRef]
33. Mills, K.; Spanner, M.; Tamblyn, I. Deep Learning and the Schrödinger Equation. *Phys. Rev. A* **2017**, *96*, 042113. [CrossRef]
34. Ott, C.; Kaldun, A.; Raith, P.; Meyer, K.; Laux, M.; Evers, J.; Keitel, C.-H.; Greene, C.-H.; Pfeifer, T. Lorentz Meets Fano in Spectral Line Shapes: A Universal Phase and Its Laser Control. *Science* **2013**, *340*, 716–720. [CrossRef]
35. Rupprecht, P.; Aufleger, L.; Heinze, S.; Magunia, A.; Ding, T.; Rebholz, M.; Amberg, S.; Mollov, N.; Henrich, F.; Haverkort, M.W.; et al. Resolving Vibrations in a Polyatomic Molecule with Femtometer Precision via X-Ray Spectroscopy. *Phys. Rev. A* **2023**, *108*, 032816. [CrossRef]
36. Kingma, D.P.; Lei Ba, J. Adam: A method for stochastic optimization. *arXiv* **2017**, arXiv:1412.6980.
37. Fano, U. Effects of Configuration Interaction on Intensities and Phase Shifts. *Phys. Rev.* **1961**, *124*, 1866–1878. [CrossRef]
38. Rabi, I.I. Space Quantization in a Gyrating Magnetic Field. *Phys. Rev.* **1937**, *51*, 652–654. [CrossRef]
39. Allaria, E.; Appio, R.; Badano, L.; Barletta, W.A.; Bassanese, S.; Biedron, S.G.; Borga, A.; Busetto, E.; Castronovo, D.; Cinquegrana, P.; et al. Highly Coherent and Stable Pulses from the FERMI Seeded Free-Electron Laser in the Extreme Ultraviolet. *Nat. Photonics* **2012**, *6*, 699–704. [CrossRef]
40. Weninger, C.; Purvis, M.; Ryan, D.; London, R.A.; Bozek, J.D.; Bostedt, C.; Graf, A.; Brown, G.; Rocca, J.J.; Rohringer, N. Stimulated Electronic X-Ray Raman Scattering. *Phys. Rev. Lett.* **2013**, *111*, 233902. [CrossRef]
41. Li, K.; Labeye, M.; Ho, P.J.; Gaarde, M.B.; Young, L. Resonant Propagation of x Rays from the Linear to the Nonlinear Regime. *Phys. Rev. A* **2020**, *102*, 053113. [CrossRef]
42. Heeg, K.P.; Kaldun, A.; Strohm, C.; Reiser, P.; Ott, C.; Subramanian, R.; Lentrodt, D.; Haber, J.; Wille, H.C.; Goerttler, S.; et al. Spectral Narrowing of X-Ray Pulses for Precision Spectroscopy with Nuclear Resonances. *Science* **2017**, *357*, 375–378. [CrossRef]
43. Gao, J.; Guo, C.; Guo, X.; Jin, G.; Wang, P.; Zhao, J.; Zhang, H.; Jiang, Y.; Wang, D.; Jiang, D. Observation of Light Amplification without Population Inversion in Sodium. *Opt. Commun.* **1992**, *93*, 323–327. [CrossRef]
44. Grynberg, G.; Pinard, M.; Mandel, P. Amplification without Population Inversion in a V Three-Level System: A Physical Interpretation. *Phys. Rev. A* **1996**, *54*, 776. [CrossRef]
45. Van Der Veer, W.E.; Van Diest, R.J.J.; Dönszelmann, A.; Van Linden Van Den Heuvell, H.B. Experimental Demonstration of Light Amplification without Population Inversion. *Phys. Rev. Lett.* **1993**, *70*, 3243. [CrossRef]
46. Zibrov, A.S.; Lukin, M.D.; Nikonov, D.E.; Hollberg, L.; Scully, M.O.; Velichansky, V.L.; Robinson, H.G. Experimental Demonstration of Laser Oscillation without Population Inversion via Quantum Interference in Rb. *Phys. Rev. Lett.* **1995**, *75*, 1499. [CrossRef]
47. Wen, P.Y.; Kockum, A.F.; Ian, H.; Chen, J.C.; Nori, F.; Hoi, I.C. Reflective Amplification without Population Inversion from a Strongly Driven Superconducting Qubit. *Phys. Rev. Lett.* **2018**, *120*, 063603. [CrossRef]
48. Kocharovskaia, O.A.; Khanin, I.I. Coherent Amplification of an Ultrashort Pulse in a Three-Level Medium without Population Inversion. *Pisma V Zhurnal Eksperimentalnoi I Teor. Fiz.* **1988**, *48*, 581–584.
49. Kocharovskaya, O. Amplification and Lasing without Inversion. *Phys. Rep.* **1992**, *219*, 175–190. [CrossRef]
50. Kocharovskaya, O.; Mandel, P. Amplification without Inversion: The Double-Λ Scheme. *Phys. Rev. A* **1990**, *42*, 523. [CrossRef]
51. Lyras, A.; Tang, X.; Lambropoulos, P.; Zhang, J. Radiation Amplification through Autoionizing Resonances without Population Inversion. *Phys. Rev. A* **1989**, *40*, 4131. [CrossRef] [PubMed]
52. Arkhipkin, V.G.; Heller, Y.I. Radiation Amplification without Population Inversion at Transitions to Autoionizing States. *Phys. Lett. A* **1983**, *98*, 12–14. [CrossRef]
53. Sansone, G.; Kelkensberg, F.; Pérez-Torres, J.F.; Morales, F.; Kling, M.F.; Siu, W.; Ghafur, O.; Johnsson, P.; Swoboda, M.; Benedetti, E.; et al. Electron Localization Following Attosecond Molecular Photoionization. *Nature* **2010**, *465*, 763–766. [CrossRef] [PubMed]

4.3. Time-Resolving State-Specific Molecular Dissociation with XUV Broadband Absorption Spectroscopy

While the first two publications are thematically similar, the third and final results section investigates a different aspect of XUV-induced quantum dynamics: *Ultrafast photochemical reactions*. This implies studying molecular instead of atomic targets, for which the theoretical foundation is provided in Section 2.5. Nuclear dynamics—in the sense of relative nuclear movement in space—play an important role in chemical reactions, and are non-existent in atoms—although processes inside the atomic nuclei exist. The interplay of electronic and nuclear dynamics of a molecule is a central aspect of photochemical reactions. For example, photo-exciting a single electron inside a molecule can lead to the subsequent dissociation of the whole molecule. This also illustrates the dynamical, i.e. time-dependent, character of chemical reactions. The exact type of reaction—i.e. which electronic state is excited inside the molecule, and which fragments are formed—is *energy-dependent* as for atoms. On a coarse energy-scale, using XUV/x-ray pulses allows to excite localized inner-shell- and core-electrons, and on a finer scale, state- and site-specific excitation and resulting molecular dissociation is initiated by tuning the pulses to absorption resonances. As the high XUV/x-ray photon energies are transferred to an excited molecule, the dissociation typically takes place on ultrafast time scales, 10^{-15} s to 10^{-12} s. Eventually, the time scale of nuclear dynamics can become as fast as electronic time scales, especially in combination with low electronic correlations and slow internal electronic processes. Therefore, *coupled electronic-nuclear dynamics* is an important aspect of XUV/x-ray-photochemical reactions.

The publication presented in the following makes explicit use of *time-resolving* dissociation dynamics by utilizing a pair of ultrashort XUV pulses, instead of reconstructing time-dependent properties, e.g. electron populations, from the absorption spectra of a single XUV pulse, as in the previous section. The *real-time* evolution of a dynamical processes is unresolved by measuring time-integrated spectra. Yet, the spectral measurements allow for high energy resolution. In combination with broadband HHG probe pulses in a transient absorption experiment, it provides high spectral resolution (< 100 meV) in a large energy range (10 eV to 100 eV) enabling *electronic-state–sensitivity* of several potential reaction products simultaneously. Further, tuning XUV-FEL pump pulses with <1 eV precision over >10 eV ranges allows additionally for *excitation-energy–resolving* molecular dissociation pathways. Repeating spectral measurements with a *controlled time-delay* between FEL and HHG pulses leads to ultrafast time resolutions ($\sim$100 fs) while retaining both pump- and probe-energy–resolutions. The results presented in the publication make use of the well-known FEL-pump energy and femtosecond resolution to measure a coupled electronic-nuclear dissociation processes of a specific electronic state in $O_2{}^+$ on picosecond time scales by identifying electronic-states of neutral and ionic fragments with the HHG probe pulses. Further results on femtosecond time scales with varying FEL photon energies and additionally resolving the kinetic energy release of ionic fragments will be presented in Section 5.2.

PHYSICAL SCIENCES

Time-resolving state-specific molecular dissociation with XUV broadband absorption spectroscopy

Alexander Magunia[1,2]*, Marc Rebholz[1], Elisa Appi[3]†, Christina C. Papadopoulou[4], Hannes Lindenblatt[1,2], Florian Trost[1,2], Severin Meister[1,2], Thomas Ding[1], Michael Straub[1,2]‡, Gergana D. Borisova[1,2], Junhee Lee[1,2], Rui Jin[1], Alexander von der Dellen[1], Christian Kaiser[1], Markus Braune[4], Stefan Düsterer[4], Skirmantas Ališauskas[4], Tino Lang[4], Christoph Heyl[4,5,6], Bastian Manschwetus[4], Sören Grunewald[4], Ulrike Frühling[4], Ayhan Tajalli[4], Ammar Bin Wahid[7], Laura Silletti[7], Francesca Calegari[7,8], Philip Mosel[3], Uwe Morgner[3], Milutin Kovacev[3], Uwe Thumm[9], Ingmar Hartl[4], Rolf Treusch[4], Robert Moshammer[1], Christian Ott[1]*, Thomas Pfeifer[1]*

The electronic and nuclear dynamics inside molecules are essential for chemical reactions, where different pathways typically unfold on ultrafast timescales. Extreme ultraviolet (XUV) light pulses generated by free-electron lasers (FELs) allow atomic-site and electronic-state selectivity, triggering specific molecular dynamics while providing femtosecond resolution. Yet, time-resolved experiments are either blind to neutral fragments or limited by the spectral bandwidth of FEL pulses. Here, we combine a broadband XUV probe pulse from high-order harmonic generation with an FEL pump pulse to observe dissociation pathways leading to fragments in different quantum states. We temporally resolve the dissociation of a specific O_2^+ state into two competing channels by measuring the resonances of ionic and neutral fragments. This scheme can be applied to investigate convoluted dynamics in larger molecules relevant to diverse science fields.

INTRODUCTION

The measurement of (neutral) fragments and radicals, or chemical shifts within intact molecules, allows us to track molecular dissociation or intramolecular excitation and charge flow (*1*, *2*) on ultrafast timescales (*3*). The understanding of processes in chemically reactive environments, for example, atmospheric or biological processes (*4*–*11*), is facilitated by their sensitivity to electronic structure and atomic sites (*5*–*7*) and the capabilities of time-resolved experiments (*12*). The oxygen molecule is a key component in such environments and its photodissociation is thus an active area of research (*13*–*16*). Tunable extreme ultraviolet (XUV) free-electron lasers (FELs) (*17*) provide a unique tool to trigger electronic or molecular dynamics (*18*) by preparing specific initial states, but mostly lack the spectral bandwidth to detect all relevant resonances and fragments at the same time (*14*, *19*). In contrast, high-order harmonic generation (HHG) pulses (*20*) can be used as XUV broadband probes in transient absorption spectroscopy (*21*) to simultaneously detect several neutral and ionic fragments and chemical shifts within a molecule, but up to now have only been used in combination with pump pulses at lower (optical) frequencies (*22*), and thereby lose the benefit of a state- and/or site-specific excitation.

Here, we combine the benefits of the FEL pump and HHG probe pulses in all-XUV transient absorption spectroscopy to specifically address and clock the fragmentation of the $O_2^+(c^4\Sigma_u^-\ v=0)$ state by fragment-tunneling through a nuclear potential energy well and predissociation. Theoretical estimates for the timescale of this process are unsettled (*23*–*27*) because of the high sensitivity of the underlying tunneling process on the energy barrier, with no direct time-resolved measurement so far. We thus perform this experiment also as a benchmark to illustrate how our experimental approach can be used to track tunneling and predissociation and, in general, dissociation dynamics of ionic and neutral fragments, including their final quantum state, on ultrafast timescales, which can be straightforwardly applied to more complex molecules (*28*). Understanding tunneling processes of charge carriers—on its own or in competition with other charge flow dynamics—can be relevant in many research areas and applications, from the production of attosecond pulses via HHG (*29*–*31*), to properties of transistors (*32*), semiconductors (*33*) or two-dimensional materials (*34*), as well as in chemical reactions (*4*, *5*, *7*, *35*) and charge transfer in proteins.

RESULTS

In the experiment (illustrated in Fig. 1A), we use an FEL pulse at 27.7-eV central photon energy and ~0.3-eV bandwidth, which is well above the resonance energy of 24.6 eV of the excited molecular $O_2^+(c^4\Sigma_u^-\ v=0)$ state relative to the ground state of the neutral O_2 molecule (for simplicity, we will refer to this specific state of O_2^+ as "excited molecular state" below). This ensures that the whole FEL

[1]Max-Planck-Institut für Kernphysik, Saupfercheckweg 1, 69117 Heidelberg, Germany. [2]Ruprecht-Karls-Universität Heidelberg, Grabengasse 1, 69117 Heidelberg, Germany. [3]Leibniz University Hannover, Welfengarten 1, 30167 Hannover, Germany. [4]Deutsches Elektronen-Synchrotron (DESY), Notkestraße 85, 22607 Hamburg, Germany. [5]Helmholtz Institute Jena, Fröbelstieg 3, 07743 Jena, Germany. [6]GSI Helmholtzzentrum für Schwerionenforschung, Planckstraße 1, 64291 Darmstadt, Germany. [7]Center for Free-Electron Laser Science (CFEL), Deutsches Elektronen-Synchrotron (DESY), Notkestr. 85, 22607 Hamburg, Germany. [8]Physics Department, Universität Hamburg, Luruper Chaussee 149, 22761 Hamburg, Germany. [9]J. R. Macdonald Laboratory, Kansas State University, Manhattan, KS 66506,USA.
*Corresponding author. Email: alexander.magunia@mpi-hd.mpg.de (A.M.); christian.ott@mpi-hd.mpg.de (C.O.); thomas.pfeifer@mpi-hd.mpg.de (T.P.)
†Present address: Lund University, Stora Algatan 4, SE-221 00 Lund, Sweden.
‡Present address: University of Geneva, 24 Quai Ernest-Ansermet, 1211 Geneva 4, Switzerland.

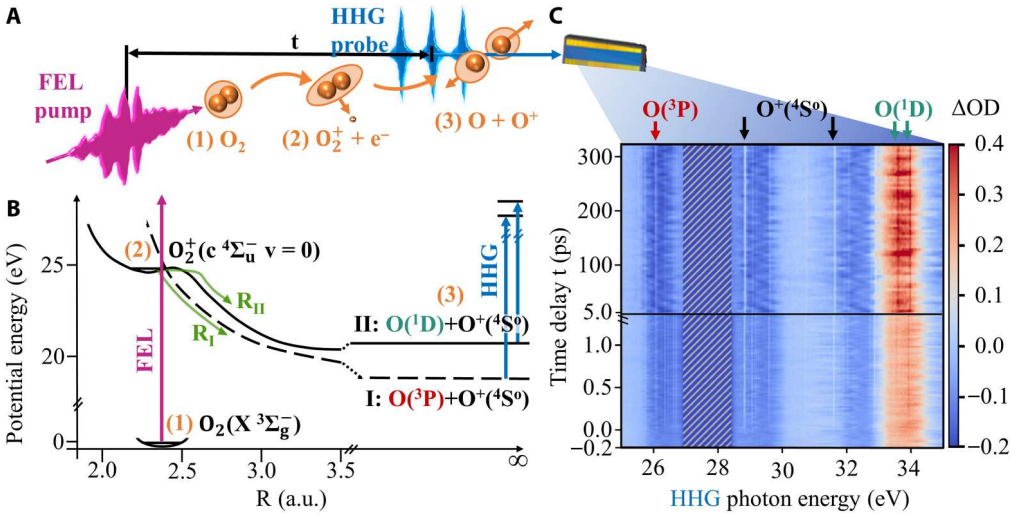

Fig. 1. Overview of the measurement concept and absorption data. (**A**) Experimental scheme. The FEL pulse excites the oxygen molecule from its ground (1) to the excited state in the molecular ion (2), from where it dissociates. After a delay time *t*, the HHG pulse (train) probes the resulting fragments (3), allowing to identify fragments resulting from the targeted c $^4\Sigma_u^-$ state. (**B**) Scheme of relevant potential-energy curves of oxygen based on (*36*). The excited state can couple to another state (dashed line) and thereby predissociate into the (I) dissociation channel (lower green arrow). In addition, being confined by a potential-energy barrier, tunneling through that barrier into the (II) dissociation channel (upper green arrow) is possible. (**C**) Time-resolved differential absorbance $\Delta OD(t, E_{\mathrm{HHG-ph.}})$ for 27.7 eV FEL photon energy. For positive time delays, the FEL pulse arrives first. The data are compiled from a femtosecond and a picosecond scale measurement, the change of the time-delay axis is indicated with the black horizontal line. The sharp absorption features, arising on a timescale of femtoseconds (lower half) and changing their intensity over hundreds of picoseconds (upper half), are identified as different resonant electronic transitions in various fragments. The sharp resonances relevant to the dissociation process are marked in red for $O(^3P)$, black for $O^+(^4S^o)$, and cyan arrows for $O(^1D)$ fragments. Broader features are due to the residual HHG spectral structure (cf. Fig. 3). The area around 27.7 eV is overlaid with gray stripes because the residual FEL stray light is more intense than the harmonics and thus precludes a meaningful measurement of HHG spectra in this spectral region. a.u., atomic units.

spectrum contributes to the molecular excitation process, where the residual energy is taken away by the emitted electron. The excited molecular state can predissociate via nonadiabatic couplings to other states into the first dissociation channel of oxygen: $O(^3P)$ + $O^+(^4S^o)$ (*36*), or dissociate via tunneling into the second dissociation channel: $O(^1D)$ + $O^+(^4S^o)$ (*36*) (Fig. 1B). The broadband ($\Delta\omega$ ~ 20 eV) HHG probe pulse—after transmission through the sample—allows to detect the difference in spectral absorption ΔOD caused by emerging fragments in different states (more details can be found in Materials and Methods). By scanning the time delay t between the HHG and FEL pulses, first with 20-fs steps for delays <1.5 ps and afterward with coarser 5-ps steps, we stepwise record a time-dependent differential absorbance $\Delta OD(t, E_{\mathrm{HHG-ph.}})$ (see Fig. 1C). The spectrally sharp absorption features originate from resonant transitions within the neutral and ionic fragments produced in various excited atomic states after the dissociation of the excited molecular state. We are able to identify resonances that are attributed to the first dissociation channel with $O(^3P)$ at 26.1 eV (*37*) (red labeled) as well as to the second dissociation channel with $O(^1D)$ at 32.9 and 33.9 eV (*38*) (cyan), whereas $O^+(^4S^o)$ at 28.8 and 31.6 eV (*39*, *40*) (black) appears in both channels. The rise in amplitude of the resonances along the time-delay axis (Fig. 1C) is a measure of the time-resolved abundance of the corresponding fragment.

In the following, we extract the dissociation times of the two channels I and II by using a rate-equation model: The population in the excited molecular state $N_0(t)$ dissociates into the first dissociation channel with population $N_{\mathrm{I}}(t)$ and rate R_{I} or, alternatively, into the second channel with population $N_{\mathrm{II}}(t)$ and rate R_{II}. Solving the differential equations (see Materials and Methods) leads to the following exponential solutions of the population dynamics of the fragments

$$N_{O+(4S)}(t) = N_{\mathrm{I}}(t) + N_{\mathrm{II}}(t) = 1 - \exp[-(R_{\mathrm{I}} + R_{\mathrm{II}})t] \quad (1.1)$$

$$N_{O(1D)}(t) = N_{\mathrm{II}}(t) = R_{\mathrm{II}}/(R_{\mathrm{I}} + R_{\mathrm{II}})\ \{1 - \exp[-(R_{\mathrm{I}} + R_{\mathrm{II}})t]\} \quad (1.2)$$

$$N_{O(3P)}(t) = N_{\mathrm{I}}(t) = R_{\mathrm{I}}/(R_{\mathrm{I}} + R_{\mathrm{II}})\ \{1 - \exp[-(R_{\mathrm{I}} + R_{\mathrm{II}})t]\} \quad (1.3)$$

As a result, all three fragments appear with the same exponential time constant

$$\tau_{\mathrm{d}} = 1/(R_{\mathrm{I}} + R_{\mathrm{II}}) \quad (2)$$

through dissociation of the excited molecular state, which we thereby define as the dissociation time. In contrast, the amplitudes and hence probabilities of the three fragments in Eqs. 1.1 to 1.3 are different. To verify whether this is the process that leads to the observed experimental features, we fit lineouts of the measured resonance lines *r* for a given fragment *f* at a specific HHG photon energy interval centered at E_r with exponential functions $A_f(E_r)(1 - \exp[-t/\tau_f)]$ (see Materials and Methods).

Figure 2 shows the lineouts of the $\Delta OD(t)$ for these resonances along the time-delay axis, together with corresponding exponential fits. Off-resonant backgrounds have been subtracted for each lineout as discussed in Materials and Methods. The sharp rises in

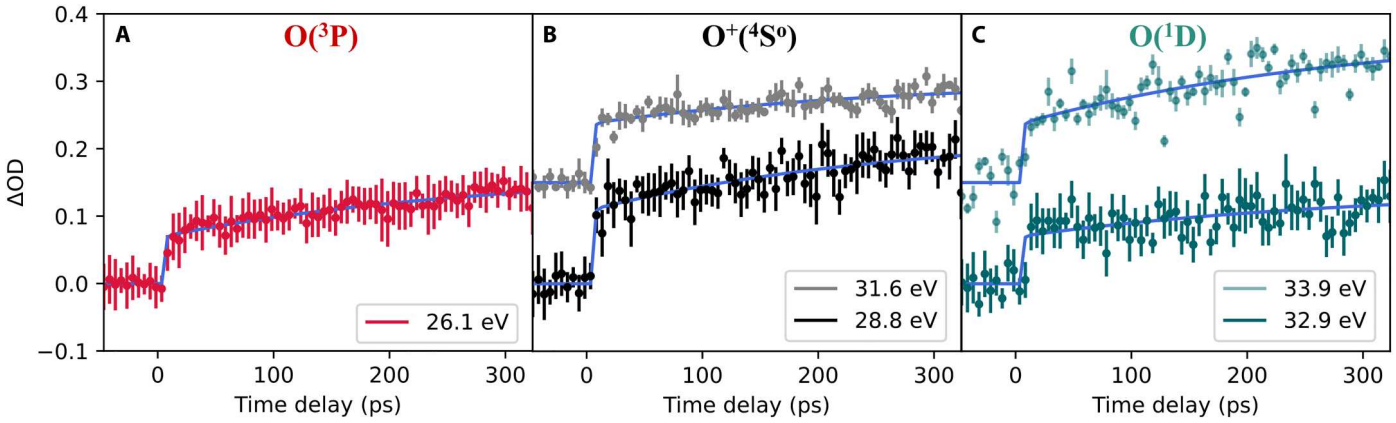

Fig. 2. Time-resolved, background-corrected resonant Δ*OD*(*t*) lineouts (dots with error bars) and corresponding fits (blue lines). Lineouts and fits are shown for (**A**) O(^{3}P), (**B**) O$^+$(^{4}S^o) and (**C**) O(^{1}D) fragments. In (B) and (C), two resonances at different HHG photon energies (see legends) are presented with different colors. These are fitted with a global fit to extract a single dissociation time constant per fragment, but with different amplitudes, due to different cross sections. The resonances shown in fainter colors are shifted upward by 0.15 along the Δ*OD* axis for better. visibility. Error bars represent the SD of data points after averaging over 400 individually calculated Δ*OD*s for every time step and resonance lineout.

Δ*OD* for all resonance lineouts around time zero is a combined effect of all faster (femtosecond to single picosecond) dissociation processes, which cannot be resolved on the coarser 5-ps delay step scale in this measurement (cf. Materials and Methods). Notably, the $O_2^+(c^4\Sigma_u^-)$ state supports a second, higher-lying vibrational level, $v = 1$, which dissociates via tunneling much faster than the $v = 0$ level, since it faces a lower potential-energy barrier. The $v = 1$ tunneling dissociation is expected to take place on a femtosecond timescale (*24*, *25*), which is not resolved in the present experiment. In addition, these processes can be attributed to $O_2^+(B^2\Sigma_g^-)$ dissociation into the first dissociation channel (*41*), and two pump-photon processes and respective O^++O^+ dissociation (*14*), which are all known to dissociate faster than our 5-ps resolution. For all resonance lines, we find this fitted timescale to be $\tau_{fast} \lesssim 1$ ps. In view of the orders-of-magnitude slower dissociation process of the here-targeted $O_2^+(c^4\Sigma_u^-\ v = 0)$ excited molecular state, the subpicosecond resolution is not required for its scrutiny. The resulting fit parameters, dissociation times $\tau_{f,slow}$ and resonance amplitudes A_r, are shown in Table 1.

The three independently fitted values of $\tau_{f,slow}$ agree well within their error bars and support the model of the dissociation process from a single reservoir, the excited molecular state, into two channels, the two dissociation limits, with different probabilities but the same time constant, as described with the rate-equation model above. Averaging over the three individual $\tau_{f,slow}$ from Table 1, we extract the tunneling and predissociation time of the excited molecular state as $\bar{\tau} = 280 \pm 160$ ps. This value lies within the range of theoretical estimations, which span from a few picoseconds to 10 ns (*23*–*27*). Furthermore, measurements of the spectral linewidth of the $O_2^+(c^4\Sigma_u^-\ v = 0)$ state (*27*, *42*) have estimated a lower limit for the dissociation time of a few picoseconds, but their spectral resolution would not have allowed to infer a lifetime of 280 ps, especially because potential rotational broadening was not resolved. Thus, our time domain–based result is compared with their spectral domain–based findings a more direct assignment of the dissociation time. The ratio of the two rates R_{II}/R_I equals the ratio of the probabilities P_{II}/P_I of the excited molecular state for dissociation into the first or second dissociation channel, which is known from previous studies (*36*) to be $P_{II}/P_I = 1.5$. With the help of this ratio and the dissociation time $\bar{\tau}$, we determine the individual rates of dissociation into the two channels I and II: $R_I = 1.4 \pm 0.8$ ns^{-1}, $R_{II} = 2.1 \pm 1.2$ ns^{-1}. More details are provided in Materials and Methods. To the best of our knowledge, this provides the first direct time-resolved measurement of the dissociation time and the individual rates. Comparable experiments (*16*, *43*) are complementary to our results, studying the neutral Rydberg series converging to the $O_2^+(c^4\Sigma_u^-)$ ionic state, which in parallel to predissociation also autoionizes on a faster timescale, but not the $O_2^+(c^4\Sigma_u^-)$ state itself.

Table 1. Fit parameters quantifying the tunneling and predissociation dynamics of the $O_2^+(c^4\Sigma_u^-\ v = 0)$ state. A_r is the amplitude of the relative optical density Δ*OD* of resonance *r* of a given fragment *f* at large time delays. $\tau_{f,slow}$ designates the exponential rise time at which fragment *f* appears via tunneling [O(^{1}D) and O$^+$(^{4}S^o)] and predissociation [O(^{3}P) and O$^+$(^{4}S^o)]. arb.u., arbitrary units.

Fragment *f*	O(^{3}P)	O$^+$(^{4}S^o)	O(^{1}D)
$\tau_{f,slow}$ (ps)	280 ± 120	290 ± 170	280 ± 200
A_r (arb.u.)	$A_{26.1eV}$ = 0.097 ± 0.022	$A_{28.8eV}$ = 0.119 ± 0.037 $A_{31.6eV}$ = 0.067 ± 0.022	$A_{32.9eV}$ = 0.067 ± 0.028 $A_{33.9eV}$ = 0.138 ± 0.052

DISCUSSION

These results illustrate how state-specific ultrafast molecular dynamics can be extracted with spectrally and temporally resolved FEL pump–HHG probe transient absorption spectroscopy. In particular, the use of HHG probe pulses at an FEL facility with a spectral bandwidth much (>10 times) broader than the average FEL pulse bandwidths is essential to detect both neutral and ionized fragments. Thereby, we gain insight into the state-specific molecular breakup including experimentally distinguishing both

competing dissociation channels and determine its dissociation time, which is strongly influenced by the interplay of the parallel tunneling and predissociation channel. In the future, this scheme can be applied to molecular systems, allowing both precision tests of state-of-the-art quantum dynamics theory in small molecules (*44*–*46*) as well as time-resolving state-specific molecular dynamics in more complex systems with a broad dynamic range from nanoseconds to femtoseconds. It will be possible to experimentally address questions about intermediate states or electronic changes faster than or in interplay with structural dynamics (*47*). Furthermore, electronic charge transfer within intact neutral molecules can be investigated, extending previous studies (*2*, *48*, *49*) to a higher (XUV) photon energy or to neutral and more complex systems covering several atomic sites, respectively. Our approach provides a complementary method to charged-particle–based detection schemes, which, in addition, can be operated in parallel in the same experimental setup using a reaction microscope (REMI) (*50*). It suggests further avenues for unraveling and manipulating element-selective ultrafast molecular dynamics and the coherent control of atoms and molecules (*51*) with XUV/x-ray multipulse sequences, involving the unique combination of tunable and intense (*52*, *53*) FEL pump pulses and spectrally broad HHG-based probe pulses. Extensions of the here-demonstrated technique hold promise to promote diverse fields of science. For example, in radiation chemistry, where chemically active fragments and radicals interact with the environment, precise knowledge of the involved electronic configurations of all product states is relevant for understanding complex interactions and chemical cycles. Similarly, biochemical reactions with charged and neutral fragments are research areas that may benefit from the transient-absorption technique that we examined and benchmarked here for a prototypical small molecule.

MATERIALS AND METHODS

Experimental setup

This experiment was performed at the FL26 beamline of the free-electron laser FLASH, DESY, Hamburg. The REMI permanent end station, described in more detail in (*50*, *54*, *55*), has recently been upgraded by adding an absorption setup with an XUV spectrometer, which allows us to detect XUV spectra with a resolution of ~30 meV (*56*). In addition, a beamline for HHG driven by the output of the FLASH2 pump-probe OPCPA (optical parametric chirped-pulse amplification) laser system has been integrated into the FL26 beamline (*57*–*59*). By using the master timing system of the FLASH facility, the OPCPA system is synchronized with the FEL and produces the same pulse pattern. The optical delay stage of the driving laser system can introduce up to 4 ns of time delay between the HHG and FEL pulses with femtosecond precision, allowing to study the dynamics of processes over a wide time range. After suppression of the remaining driving radiation by a 100-nm-thick Al filter, the HHG pulses are coupled into the FLASH2 beamline by means of a motorized hyperboloidal mirror, described in more detail in (*57*, *58*). From this point, the HHG beam propagates parallel to the FEL beam, shifted upward by around 7.5 mm. We focus the FEL and HHG beams with an ellipsoidal mirror into the REMI (*50*) and further downstream we refocus both beams with a toroidal mirror into the interaction region. There, we spatially overlap them by adjusting the HHG in-coupling mirror with the help of a phosphorus screen imaged by a charge-coupled device (CCD) camera.

For the here presented experiment, the FEL pulses are spectrally centered at 27.7 eV and have a time duration of 100 fs (full width at half maximum, FWHM), as estimated by an electron-bunch duration measurement before the beamtime. The pulse energy of the FEL pulses was measured to be 37.3 ± 4.1 μJ before the FL26 beamline. Taking the beamline transmission of 29% into account, we estimate an FEL pulse energy of 10.7 ± 1.2 μJ at the oxygen target. The HHG pulses are generated by focusing the OPCPA driving pulses with ~15-fs duration (FWHM) and 780-nm central wavelength into a gas cell filled with 100 mbar of Kr. The pulse duration of the HHG pulses was not measured directly but is expected to be shorter than the driving pulse duration due to the nonlinear nature of HHG production. The HHG pulse energy was estimated at ~100 pJ at the generation point. Taking into account the combined transmission of a 100-nm-thick aluminum filter and the in-coupling mirror, as well as the residual beamline transmission, we estimate 18 pJ at the oxygen target. Figure 3 shows averaged reference spectra of the HHG pulses and FEL pulses (as stray light) recorded during the time-delay scan shown in Results. In the interaction region of the transient-absorption setup, a cell of 3-mm length with 200-μm holes on both sides along the beam axis is filled with oxygen at 8 mbar backing pressure and placed in the overlapping focus of both beams. The focal diameter of the FEL beam at the target interaction was not directly measured in this experiment, but previous measurements at this beamline resulted in a focal diameter of 5 to 10 μm (*56*). Behind the interaction region, the FEL beam is spatially separated from the HHG beam allowing it to block the FEL beam with an aluminum plate. We minimize the remaining FEL stray light with an additional 100-nm-thick aluminum filter to avoid saturation of the CCD detector, simultaneously attenuating the measured HHG beam only by ~80%. However, this still leaves us with a spectral region around the central FEL photon energy of 27.7 eV, where we cannot record HHG spectra (see Fig. 1C). We disperse the HHG pulses with a Hitachi variable line-space grating and record the resulting XUV spectra with a PIXIS XUV-sensitive CCD camera. Both HHG and FEL are produced in the FLASH pulse train mode consisting of pulse trains with a 10-Hz repetition rate, which contain 38 pulses with a spacing of 10 μs. We find the temporal overlap between FEL and HHG pulses by measuring the transient absorption spectra of argon, where the ionization and thereby creation of ionic resonances in the HHG spectra takes place orders of magnitude faster (in subfemtoseconds) than the experimental temporal jitter (tens of femtoseconds). We record the HHG spectra with 10-Hz and 10-ms exposure time, thereby integrating over the pulse train of 38 HHG spectra.

Recording of Δ*OD* and extraction of resonance lineouts

Using the FL26 beamline fast shutter, we can block every second FEL pulse train, thereby alternating between measuring absorption spectra $I(E_{\mathrm{HHG-ph.}})$ and static (unpumped) molecular oxygen reference spectra $I_0(E_{\mathrm{HHG-ph.}})$ at 5 Hz. We average over all $I(E_{\mathrm{HHG-ph.}})$ and $I_0(E_{\mathrm{HHG-ph.}})$ for a given time delay, respectively, and calculate

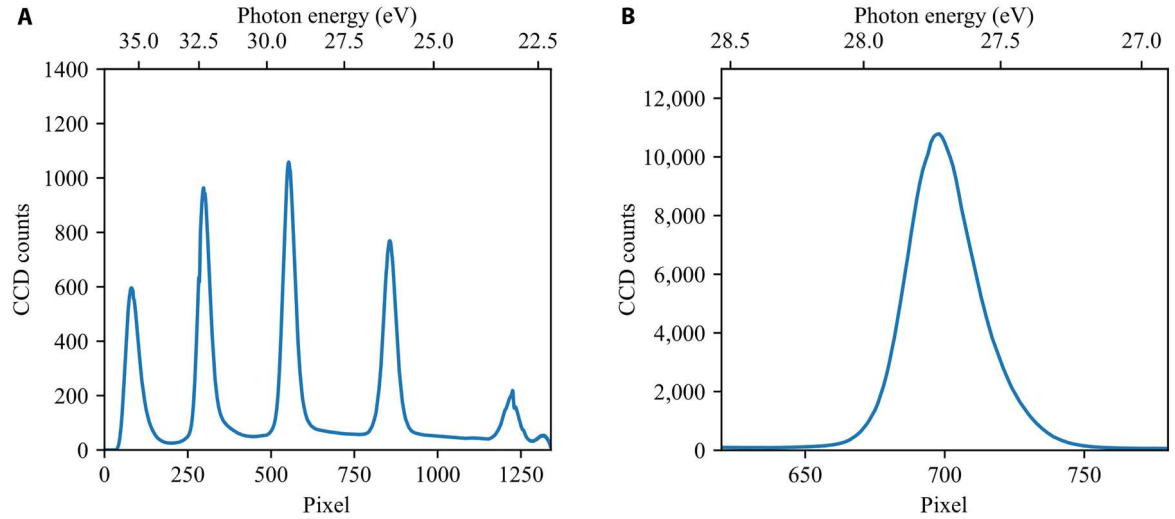

Fig. 3. HHG and FEL reference spectra. (**A**) Average of all HHG reference spectra of static molecular oxygen absorption recorded during the time-delay scan without the FEL pump pulse. (**B**) Average of all FEL reference spectra recorded during the time-delay scan as stray light. The static molecular oxygen absorption is nonresonant and flat in this confined spectral regime, thus mainly decreasing the overall FEL intensity without major spectral changes.

the $\Delta OD(E_{\mathrm{HHG-ph.}})$ via

$$\Delta OD(E_{\mathrm{HHG-ph.}}) = -\log_{10}\left[\frac{\bar{I}(E_{\mathrm{HHG-ph.}})}{\bar{I}_0(E_{\mathrm{HHG-ph.}})}\right] \quad (3)$$

By using the delay stage for the HHG-driving IR pulse, we scan the time delay t between the HHG and FEL pulses from −200 to 1400 fs in steps of 20 fs and additionally from −46.5 to 323.5 ps in steps of 5 ps. In this way, we record the time-dependent ΔOD (t, $E_{\mathrm{HHG\text{-}ph.}}$) with the two time-delay scales in Fig. 1C). We record 1000 frames at a given time-delay position for the scan with femtosecond resolution and with 400 frames for the picosecond scan. By comparing ΔOD spectra of late time delays with early delays, we identify spectral regions of resonant transitions in the fragments and define all other spectral regions as off-resonant backgrounds. For every resonance, we average over 1 to 4 pixels, both for the resonance itself as well as for a nearby off-resonant spectral region, spanning ~10 to 40 meV. By subtracting the nearby off-resonant lineout from the resonant one, we ensure to account for the resonant effects of the fragments without off-resonant residual absorption changes. These lineouts along the time-delay axis (of the picosecond-resolution scan) are shown in Fig. 2. Fitting two off-resonant lineouts with a complementary error function, $\mathrm{erfc}[(t\text{-}t_0)/\sigma]$, we find the temporal resolution to be around 300 fs [cf. the "Fitting procedure of resonant lineouts $\Delta OD(t, E_r)$" section], which gives an estimate of the combined effects of (i) both individual FEL and HHG pulse durations and (ii) the temporal jitter and drifts between the pulses. Potential electronic configuration changes during fragmentation, which would lead to shifts in the measured resonance positions, are expected to be on the same order of magnitude or faster (*14*) and thus cannot be resolved in this experiment. In addition, the position t_0 of the complementary error function allows for an in situ determination of the temporal overlap of FEL and HHG pulses.

Differential rate–equation model

The dissociation process of the excited molecular state given in Results is governed by the following set of differential rate equations

$$\frac{dN_0(t)}{dt} = -R_{\mathrm{I}}N_0(t) - R_{\mathrm{II}}N_0(t); \frac{dN_{\mathrm{I}}(t)}{dt} = R_{\mathrm{I}}N_0(t);$$
$$\frac{dN_{\mathrm{II}}(t)}{dt} = R_{\mathrm{II}}N_0(t); N_0(t=0) = 1 \quad (4)$$

Their exponential solutions and the resulting exponential dynamics of the individual fragments are given in Results.

Fitting procedure of resonant lineouts $\Delta OD(t, E_r)$

For all three fragments f, all resonances r are fitted simultaneously with the following equation

$$\Delta OD(t, E_r) = \exp\left[-\frac{(t-t_0)^2}{2\sigma^2}\right] * \left[\theta(t, t_0)\left(A_{f,\mathrm{slow}}(E_r)\left\{1 - \exp\left[-\frac{(t-t_0)}{\tau_{f,\mathrm{slow}}}\right]\right\} + A_{f,\mathrm{fast}}(E_r)\left\{1 - \exp\left[-\frac{(t-t_0)}{\tau_{f,\mathrm{fast}}}\right]\right\}\right)\right] + b(E_r) \quad (5)$$

where the two amplitudes $A_{f,d}$ (d = slow, fast) are energy-dependent contributions of the different dynamics d leading to the same fragment and the two $\tau_{f,d}$ are the time constants of the corresponding dynamics; $b(E_r)$ is a time-independent offset; t_0 is the temporal overlap position; $\theta(t, t_0)$ is a Heaviside function, and $\exp\left[-\frac{(t-t_0)^2}{2\sigma^2}\right] * (\ldots)$ represents the convolution of the molecular dynamics with the temporal instrument response function, here chosen to be a Gaussian function with SD σ. The t_0 and σ parameters are determined by independent fits to off-resonant regions of the ΔOD, as described in the "Recording of ΔOD and extraction of resonance lineouts" section. The second exponential function indexed with "fast" is necessary to describe the sharp rises in ΔOD for all resonance lineouts

around time zero as described in Results. For all resonance lines, we find this timescale to be $\tau_{fast} \lesssim 1$ ps, which can be extracted by a similar fitting procedure from the femtosecond-scale measurement more precisely as $\tau_{fast} \lesssim 300 \pm 100$ fs. It is negligible for the much slower dissociation of the $O_2^+(c^4\Sigma_u^-\ v=0)$ state.

Extracting the dissociation rates R_I and R_{II}

With the help of the dissociation time $\bar{\tau}$ of the $O_2^+(c^4\Sigma_u^-\ v=0)$ state, the ratio of the rates (*36*) $R_{II}/R_I = 1.5$, and Eq. 2, the individual rates R_I and R_{II} can be estimated as follows

$$R_I = 1/\bar{\tau} - R_{II} = 1.4 \pm 0.8\ ns^{-1} \quad (6)$$

$$R_{II} = 1/\bar{\tau} - R_I = 2.1 \pm 1.2\ ns^{-1} \quad (7)$$

REFERENCES AND NOTES

1. D. Mayer, F. Lever, D. Picconi, J. Metje, S. Alisauskas, F. Calegari, S. Düsterer, C. Ehlert, R. Feifel, M. Niebuhr, B. Manschwetus, M. Kuhlmann, T. Mazza, M. S. Robinson, R. J. Squibb, A. Trabattoni, M. Wallner, P. Saalfrank, T. J. A. Wolf, M. Gühr, Following excited-state chemical shifts in molecular ultrafast x-ray photoelectron spectroscopy. *Nat. Commun.* **13**, 1356 (2022).
2. A. Al-Haddad, S. Oberli, J. González-Vázquez, M. Bucher, G. Doumy, P. Ho, J. Krzywinski, T. J. Lane, A. Lutman, A. Marinelli, T. J. Maxwell, S. Moeller, S. T. Pratt, D. Ray, R. Shepard, S. H. Southworth, Á. Vázquez-Mayagoitia, P. Walter, L. Young, A. Picón, C. Bostedt, Observation of site-selective chemical bond changes via ultrafast chemical shifts. *Nat. Commun.* **13**, 7170 (2022).
3. O. Geßner, A. M. D. Lee, J. P. Shaffer, H. Reisler, S. V. Levchenko, A. I. Krylov, J. G. Underwood, H. Shi, A. L. L. East, D. M. Wardlaw, E. T. H. Chrysostom, C. C. Hayden, A. Stolow, Femtosecond multidimensional imaging of a molecular dissociation. *Science* **311**, 219–222 (2006).
4. P. R. Schreiner, Quantum mechanical tunneling is essential to understanding chemical reactivity. *Trends Chem.* **2**, 980–989 (2020).
5. R. J. McMahon, Chemical reactions involving quantum tunneling. *Science* **299**, 833–834 (2003).
6. P. S. Zuev, R. S. Sheridan, T. V. Albu, D. G. Truhlar, D. A. Hrovat, W. T. Borden, Carbon tunneling from a single quantum state. *Science* **299**, 867–870 (2003).
7. T. L. Nguyen, B. C. Xue, R. E. Weston, J. R. Barker, J. F. Stanton, Reaction of HO with CO: Tunneling is indeed important. *J. Phys. Chem. Lett.* **3**, 1549–1553 (2012).
8. D. Gatteschi, R. Sessoli, R. Sessoli, D. Gatteschi, Quantum Tunneling of Magnetization and Related Phenomena in Molecular Materials. *Angew. Chem. Int. Ed.* **42**, 268–297 (2003).
9. H. B. Gray, J. R. Winkler, Long-distance electron tunneling in proteins: A new challenge for time-resolved spectroscopy1. *Q. Rev. Biophys.* **36**, 341–372 (2003).
10. Y. A. Berlin, A. L. Burin, M. A. Ratner, Elementary steps for charge transport in DNA: Thermal activation vs. tunneling. *Chem. Phys.* **275**, 61–74 (2002).
11. E. M. Boon, J. K. Barton, Charge transport in DNA. *Curr. Opin. Struct. Biol.* **12**, 320–329 (2002).
12. M. Magrakvelidze, O. Herrwerth, Y. H. Jiang, A. Rudenko, M. Kurka, L. Foucar, K. U. Kühnel, M. Kübel, N. G. Johnson, C. D. Schröter, S. Düsterer, R. Treusch, M. Lezius, I. Ben-Itzhak, R. Moshammer, J. Ullrich, M. F. Kling, U. Thumm, Tracing nuclear-wave-packet dynamics in singly and doubly charged states of N_2 and O_2 with XUV-pump-XUV-probe experiments. *Phys. Rev. A* **86**, 013415 (2012).
13. A. S. Sandhu, E. Gagnon, R. Santra, V. Sharma, W. Li, P. Ho, P. Ranitovic, C. L. Cocke, M. M. Murnane, H. C. Kapteyn, Observing the creation of electronic Feshbach resonances in soft X-ray-induced O2 dissociation. *Science* **322**, 1081–1085 (2008).
14. M. Rebholz, T. Ding, L. Aufleger, M. Hartmann, K. Meyer, V. Stooß, A. Magunia, D. Wachs, P. Birk, Y. Mi, G. D. Borisova, C. Da Costa Castanheira, P. Rupprecht, M. Magrakvelidze, U. Thumm, S. Roling, M. Butz, H. Zacharias, S. Düsterer, R. Treusch, G. Brenner, C. Ott, T. Pfeifer, XUV-Initiated Dissociation Dynamics of Molecular Oxygen (O_2). *J. Phys. Chem. A.* **125**, 10138–10143 (2021).
15. A. Plunkett, N. Harkema, R. R. Lucchese, C. W. Mccurdy, A. Sandhu, Ultrafast Rydberg-state dissociation in oxygen: Identifying the role of multielectron excitations. *Phys. Rev. A* **99**, 063403 (2019).
16. H. Timmers, N. Shivaram, A. Sandhu, Ultrafast dynamics of neutral superexcited oxygen: A direct measurement of the competition between autoionization and predissociation. *Phys. Rev. Lett.* **109**, 173001 (2012).
17. W. Ackermann, G. Asova, V. Ayvazyan, A. Azima, N. Baboi, J. Bähr, V. Balandin, B. Beutner, A. Brandt, A. Bolzmann, R. Brinkmann, O. I. Brovko, M. Castellano, P. Castro, L. Catani, E. Chiadroni, S. Choroba, A. Cianchi, J. T. Costello, D. Cubaynes, J. Dardis, W. Decking, H. Delsim-Hashemi, A. Delserieys, G. Di Pirro, M. Dohlus, S. Düsterer, A. Eckhardt, H. T. Edwards, B. Faatz, J. Feldhaus, K. Flöttmann, J. Frisch, L. Fröhlich, T. Garvey, U. Gensch, C. Gerth, M. Görler, N. Golubeva, H. J. Grabosch, M. Grecki, O. Grimm, K. Hacker, U. Hahn, J. H. Han, K. Honkavaara, T. Hott, M. Hüning, Y. Ivanisenko, E. Jaeschke, W. Jalmuzna, T. Jezynski, R. Kammering, V. Katalev, K. Kavanagh, E. T. Kennedy, S. Khodyachykh, K. Klose, V. Kocharyan, M. Körfer, M. Kollewe, W. Koprek, S. Korepanov, D. Kostin, M. Krassilnikov, G. Kube, M. Kuhlmann, C. L. S. Lewis, L. Lilje, T. Limberg, D. Lipka, F. Löhl, H. Luna, M. Luong, M. Martins, M. Meyer, P. Michelato, V. Miltchev, W. D. Möller, L. Monaco, W. F. O. Müller, O. Napieralski, O. Napoly, P. Nicolosi, D. Nölle, T. Núez, A. Oppelt, C. Pagani, R. Paparella, N. Pchalek, J. Pedregosa-Gutierrez, B. Petersen, B. Petrosyan, G. Petrosyan, L. Petrosyan, J. Pflüger, E. Plönjes, L. Poletto, K. Pozniak, E. Prat, D. Proch, P. Pucyk, P. Radcliffe, H. Redlin, K. Rehlich, M. Richter, M. Roehrs, J. Roensch, R. Romaniuk, M. Ross, J. Rossbach, V. Rybnikov, M. Sachwitz, E. L. Saldin, W. Sandner, H. Schlarb, B. Schmidt, M. Schmitz, P. Schmüser, J. R. Schneider, E. A. Schneidmiller, S. Schnepp, S. Schreiber, M. Seidel, D. Sertore, A. V. Shabunov, C. Simon, S. Simrock, E. Sombrowski, A. A. Sorokin, P. Spanknebel, R. Spesyvtsev, L. Staykov, B. Steffen, F. Stephan, F. Stulle, H. Thom, K. Tiedtke, M. Tischer, S. Toleikis, R. Treusch, D. Trines, I. Tsakov, E. Vogel, T. Weiland, H. Weise, M. Wellhöfer, M. Wendt, I. Will, A. Winter, K. Wittenburg, W. Wurth, P. Yeates, M. V. Yurkov, I. Zagorodnov, K. Zapfe, Operation of a free-electron laser from the extreme ultraviolet to the water window. *Nat. Photonics* **1**, 336–342 (2007).
18. L. Fang, T. Osipov, B. F. Murphy, A. Rudenko, D. Rolles, V. S. Petrovic, C. Bostedt, J. D. Bozek, P. H. Bucksbaum, N. Berrah, Probing ultrafast electronic and molecular dynamics with free-electron lasers. *J. Phys. B: At. Mol. Opt. Phys.* **47**, 124006 (2014).
19. M. Rebholz, T. Ding, V. Despré, L. Aufleger, M. Hartmann, K. Meyer, V. Stooß, A. Magunia, D. Wachs, P. Birk, Y. Mi, G. D. Borisova, C. D. C. Castanheira, P. Rupprecht, G. Schmid, K. Schnorr, C. D. Schröter, R. Moshammer, Z. H. Loh, A. R. Attar, S. R. Leone, T. Gaumnitz, H. J. Wörner, S. Roling, M. Butz, H. Zacharias, S. Düsterer, R. Treusch, G. Brenner, J. Vester, A. I. Kuleff, C. Ott, T. Pfeifer, All-xuv pump-probe transient absorption spectroscopy of the structural molecular dynamics of Di-iodomethane. *Phys. Rev. X.* **11**, 031001 (2021).
20. F. Krausz, M. Ivanov, Attosecond physics. *Rev. Mod. Phys.* **81**, 163–234 (2009).
21. R. Geneaux, H. J. B. Marroux, A. Guggenmos, D. M. Neumark, S. R. Leone, Transient absorption spectroscopy using high harmonic generation: A review of ultrafast X-ray dynamics in molecules and solids. *Philos. Trans. A Math. Phys. Eng. Sci.* **377**, 20170463 (2019).
22. E. Goulielmakis, Z. H. Loh, A. Wirth, R. Santra, N. Rohringer, V. S. Yakovlev, S. Zherebtsov, T. Pfeifer, A. M. Azzeer, M. F. Kling, S. R. Leone, F. Krausz, Real-time observation of valence electron motion. *Nature* **466**, 739–743 (2010).
23. A. Ehresmann, L. Werner, S. Klumpp, H. Schmoranzer, P. V. Demekhin, B. M. Lagutin, V. L. Sukhorukov, S. Mickat, S. Kammer, B. Zimmermann, K.-H. Schartner, De-excitation dynamics of Rydberg states in O_2: II. Vibrational and rotational structure of $2\sigma_u^{-1}(c\ ^4\Sigma_u^-)(ns/nd)\sigma_g\ ^3\Sigma_u^-(v = 0, 1)$ states. *J. Phys. B: At. Mol. Opt. Phys.* **37**, 4405–4422 (2004).
24. P. V. Demekhin, D. V. Omel'yanenko, B. M. Lagutin, V. L. Sukhorukov, L. Werner, A. Ehresmann, K. H. Schartner, H. Schmoranzer, Investigation of photoionization and photodissociation of an oxygen molecule by the method of coupled differential equations. *Opt. Spectrosc.* **102**, 318–329 (2007).
25. H. Liebel, A. Ehresmann, H. Schmoranzer, P. V. Demekhin, B. M. Lagutin, V. L. Sukhorukov, De-excitation dynamics of Rydberg states in O_2: I. Total cross sections for O I fluorescence emission following predissociation of $2\sigma_u^{-1}(c^4\Sigma_u^-)n\sigma g\ ^3\Sigma_u^-$ states. *J. Phys. B: At. Mol. Opt. Phys.* **35**, 895 (2002).
26. K. Tanaka, M. Yoshimine, A theoretical study of the predissociation of the $c\ ^4\Sigma_u^-$ state of O_2^+. *J. Chem. Phys.* **70**, 1626–1633 (1979).
27. Y. Hikosaka, P. Lablanquie, M. Ahmad, R. I. Hall, J. G. Lambourne, F. Penent, J. H. D. Eland, Competition between autoionization and dissociation in the $[O_+^2(B\ ^2\Sigma_g^-)]nl$ and $[O_2^+(c\ ^4\Sigma_u^-)]nl$ Rydberg states investigated by photon-induced dissociation to neutral fragments. *J. Phys. B: At. Mol. Opt. Phys.* **36**, 4311 (2003).
28. N. Berrah, A. Sanchez-Gonzalez, Z. Jurek, R. Obaid, H. Xiong, R. J. Squibb, T. Osipov, A. Lutman, L. Fang, T. Barillot, J. D. Bozek, J. Cryan, T. J. A. Wolf, D. Rolles, R. Coffee, K. Schnorr, S. Augustin, H. Fukuzawa, K. Motomura, N. Niebuhr, L. J. Frasinski, R. Feifel, C. P. Schulz, K. Toyota, S. K. Son, K. Ueda, T. Pfeifer, J. P. Marangos, R. Santra, Femtosecond-resolved observation of the fragmentation of buckminsterfullerene following X-ray multiphoton ionization. *Nat. Phys.* **15**, 1279–1283 (2019).
29. M. Lewenstein, P. Balcou, M. Y. Ivanov, A. L'Huillier, P. B. Corkum, Theory of high-harmonic generation by low-frequency laser fields. *Phys. Rev. A* **49**, 2117–2132 (1994).
30. P. B. Corkum, Plasma perspective on strong field multiphoton ionization. *Phys. Rev. Lett.* **71**, 1994–1997 (1993).

31. P. M. Paul, E. S. Toma, P. Breger, G. Mullot, F. Augé, P. Balcou, H. G. Muller, P. Agostini, Observation of a train of attosecond pulses from high harmonic generation. *Science* **292**, 1689–1692 (2001).
32. P. F. Wang, K. Hilsenbeck, T. Nirschl, M. Oswald, C. Stepper, M. Weis, D. Schmitt-Landsiedel, W. Hansch, Complementary tunneling transistor for low power application. *Solid State Electron.* **48**, 2281–2286 (2004).
33. E. O. Kane, Zener tunneling in semiconductors. *J. Phys. Chem. Solid* **12**, 181–188 (1960).
34. L. Britnell, R. V. Gorbachev, R. Jalil, B. D. Belle, F. Schedin, A. Mishchenko, T. Georgiou, M. I. Katsnelson, L. Eaves, S. V. Morozov, N. M. R. Peres, J. Leist, A. K. Geim, K. S. Novoselov, L. A. Ponomarenko, Field-effect tunneling transistor based on vertical graphene heterostructures. *Science* **335**, 947–950 (2012).
35. B. C. Stipe, M. A. Rezaei, W. Ho, S. Gao, M. Persson, B. I. Lundqvist, Single-molecule dissociation by tunneling electrons. *Phys. Rev. Lett.* **78**, 4410–4413 (1997).
36. M. Richard-Viard, O. Dutuit, M. Ait-Kaci, P. M. Guyon, Isotope effect in the predissociation of the $c^4\Sigma_u$-state of O_2^+. *J. Phys. B: At. Mol. Opt. Phys.* **20**, 2247–2254 (1987).
37. G. C. Angel, J. A. R. Samson, Total photoionization cross sections of atomic oxygen from threshold to 44.3 Å. *Phys. Rev. A Gen. Phys.* **38**, 5578–5585 (1988).
38. K. L. Bell, P. G. Burke, A. Hibbert, A. E. Kingston, Photoionisation of the $2p^4 {}^3P,{}^1D,{}^1S$ states of atomic oxygen. *J. Phys. B: At. Mol. Opt. Phys.* **22**, 3197–3204 (1989).
39. K. L. Bell, A. Hibbert, R. P. Stafford, B. M. McLaughlin, Accurate transition probabilities for some spectral lines of singly ionized oxygen. *Phys. Scr.* **50**, 343–353 (1994).
40. B. Edlén, "Wellenlängen und termsysteme zu den atomspektren der elemente lithium, beryllium, bor, kohlenstoff, stickstoff und sauerstoff," thesis, Department of Physics, Lund University (1934).
41. M. Evans, S. Stimson, C. Y. Ng, C. W. Hsu, G. K. Jarvis, Rotationally resolved pulsed field ionization photoelectron study of $O_2^+(B\ {}^2\Sigma_g^-, {}^2\Sigma_u^-; v^+=0–7)$ at 20.2–21.3 eV. *J. Chem. Phys.* **110**, 315–327 (1998).
42. M. Evans, S. Stimson, C. Y. Ng, C. W. Hsu, High-resolution pulsed field ionization photoelectron study of O2: Predissociation lifetimes and high-n Rydberg lifetimes converging to $O_2^+(c\ {}^4\Sigma_u^-, v^+=0,1)$. *J. Chem. Phys.* **109**, 1285–1292 (1998).
43. Y.-C. Lin, A. P. Fidler, A. Sandhu, R. R. Lucchese, C. W. Mccurdy, S. R. L. Abe, D. M. Neumark, Coupled nuclear–electronic decay dynamics of O_2 inner valence excited states revealed by attosecond XUV wave-mixing spectroscopy. *Faraday Disc.* **228**, 537–554 (2021).
44. P. M. Abanador, U. Thumm, Characterization of light-induced potentials in the strong-field dissociation of O_2^+. *Phys. Rev. A* **102**, 053114 (2020).
45. P. Cörlin, A. Fischer, M. Schönwald, A. Sperl, T. Mizuno, U. Thumm, T. Pfeifer, R. Moshammer, Probing calculated O_2^+ potential-energy curves with an XUV-IR pump-probe experiment. *Phys. Rev. A* **91**, 043415 (2015).
46. M. Magrakvelidze, A. Kramer, K. Bartschat, U. Thumm, Complementary imaging of the nuclear dynamics in laser-excited diatomic molecular ions in the time and frequency domains. *J. Phys. B: At. Mol. Opt. Phys.* **47**, 124003 (2014).
47. F. Calegari, D. Ayuso, A. Trabattoni, L. Belshaw, S. De Camillis, S. Anumula, F. Frassetto, L. Poletto, A. Palacios, P. Decleva, J. B. Greenwood, F. Martín, M. Nisoli, Ultrafast electron dynamics in phenylalanine initiated by attosecond pulses. *Science* **346**, 336–339 (2014).
48. Y. Kobayashi, K. F. Chang, T. Zeng, D. M. Neumark, S. R. Leone, Direct mapping of curve-crossing dynamics in IBr by attosecond transient absorption spectroscopy. *Science* **365**, 79–83 (2019).
49. G. Sansone, F. Kelkensberg, J. F. Pérez-Torres, F. Morales, M. F. Kling, W. Siu, O. Ghafur, P. Johnsson, M. Swoboda, E. Benedetti, F. Ferrari, F. Lépine, J. L. Sanz-Vicario, S. Zherebtsov, I. Znakovskaya, A. L'Huillier, M. Y. Ivanov, M. Nisoli, F. Martín, M. J. J. Vrakking, Electron localization following attosecond molecular photoionization. *Nature* **465**, 763–766 (2010).
50. G. Schmid, K. Schnorr, S. Augustin, S. Meister, H. Lindenblatt, F. Trost, Y. Liu, M. Braune, R. Treusch, C. D. Schröter, T. Pfeifer, R. Moshammer, Reaction microscope endstation at FLASH2. *J. Synchrotron Radiat.* **26**, 854–867 (2019).
51. S. Mukamel, Y. Tanimura, P. Hamm, Coherent multidimensional optical spectroscopy. *Acc. Chem. Res.* **42**, 1207–1209 (2009).
52. L. Young, E. P. Kanter, B. Krässig, Y. Li, A. M. March, S. T. Pratt, R. Santra, S. H. Southworth, N. Rohringer, L. F. Dimauro, G. Doumy, C. A. Roedig, N. Berrah, L. Fang, M. Hoener, P. H. Bucksbaum, J. P. Cryan, S. Ghimire, J. M. Glownia, D. A. Reis, J. D. Bozek, C. Bostedt, M. Messerschmidt, Femtosecond electronic response of atoms to ultra-intense X-rays. *Nature* **466**, 56–61 (2010).
53. M. Hoener, L. Fang, O. Kornilov, O. Gessner, S. T. Pratt, M. Gühr, E. P. Kanter, C. Blaga, C. Bostedt, J. D. Bozek, P. H. Bucksbaum, C. Buth, M. Chen, R. Coffee, J. Cryan, L. Dimauro, M. Glownia, E. Hosler, E. Kukk, S. R. Leone, B. McFarland, M. Messerschmidt, B. Murphy, V. Petrovic, D. Rolles, N. Berrah, Ultraintense x-ray induced ionization, dissociation, and frustrated absorption in molecular nitrogen. *Phys. Rev. Lett.* **104**, 253002 (2010).
54. J. Ullrich, R. Moshammer, A. Dorn, R. Dörner, L. P. H. Schmidt, H. Schmidt-Böcking, Recoil-ion and electron momentum spectroscopy: Reaction-microscopes. *Rep. Prog. Phys.* **66**, 1463–1545 (2003).
55. R. Dörner, V. Mergel, O. Jagutzki, L. Spielberger, J. Ullrich, R. Moshammer, H. Schmidt-Böcking, Cold target recoil ion momentum spectroscopy: A 'momentum microscope' to view atomic collision dynamics. *Phys. Rep.* **330**, 95–192 (2000).
56. M. Straub, T. Ding, M. Rebholz, G. D. Borisova, A. Magunia, H. Lindenblatt, S. Meister, F. Trost, Y. Wang, S. Palutke, M. Braune, S. Düsterer, R. Treusch, C. H. Greene, R. Moshammer, T. Pfeifer, C. Ott, Differential measurement of electron ejection after two-photon two-electron excitation of helium. *Phys. Rev. Lett.* **129**, 183204 (2022).
57. E. Appi, C. C. Papadopoulou, J. L. Mapa, N. Wesavkar, C. Jusko, P. Mosel, S. Ališauskas, T. Lang, C. M. Heyl, B. Manschwetus, M. Brachmanski, M. Braune, H. Lindenblatt, F. Trost, S. Meister, P. Schoch, R. Treusch, R. Moshammer, I. Hartl, U. Morgner, M. Kovacev, A synchronized VUV light source based on high-order harmonic generation at FLASH. *Sci. Rep.* **10**, 6867 (2020).
58. E. Appi, C. C. Papadopoulou, J. L. Mapa, C. Jusko, P. Mosel, A. Schoenberg, J. Stock, T. Feigl, S. Ališauskas, T. Lang, C. M. Heyl, B. Manschwetus, M. Brachmanski, M. Braune, H. Lindenblatt, F. Trost, S. Meister, P. Schoch, A. Trabattoni, F. Calegari, R. Treusch, R. Moshammer, I. Hartl, U. Morgner, M. Kovacev, Synchronized beamline at FLASH2 based on high-order harmonic generation for two-color dynamics studies. *Rev. Sci. Instrum.* **92**, 123004 (2021).
59. T. Lang, S. Alisauskas, U. Große-Wortmann, T. Hülsenbusch, B. Manschwetus, C. Mohr, J. Müller, F. Peters, N. Schirmel, S. Schulz, A. Swiderski, J. Zheng, I. Hartl, Versatile OPCPA pump-probe laser system for the FLASH2 XUV FEL beamline at DESY, in *2019 Conference on Lasers and Electro-Optics Europe and European Quantum Electronics Conference*, Munich Germany, 23 to 27 June 2019 (OSA Technical Digest (Optica Publishing Group, 2019).

Acknowledgments: We acknowledge DESY (Hamburg, Germany), a member of the Helmholtz Association HGF, for the provision of experimental facilities. Parts of this research were carried out at FLASH, and we want to acknowledge the work of the scientific and technical team. Beamtime was allocated for proposal F-20200759. **Funding:** This work was supported by the Deutsche Forschungsgemeinschaft (DFG, German Research Foundation), Germany's Excellence Strategy EXC2181/1 390900948 (the Heidelberg STRUCTURES Excellence Cluster) (to T.P.); European Research Council (grant no. X-MuSiC 616783) (to T.P.); Deutsche Forschungsgemeinschaft (DFG, German Research Foundation), Germany's Excellence Strategy EXC 2122 (PhoenixD - 390833453, EXC-2123, Quantum Frontiers 390837967) (to M.K.); Deutsche Forschungsgemeinschaft (DFG, German Research Foundation), Germany's Excellence Strategy Cluster of Excellence Advanced Imaging of Matter – AIM (to F.C.); Helmholtz Association (HIRS-0018) (to C.C.P., M.B., S.D., S.A., T.L., C.H., B.M., S.G., U.F., A.T., I.H., and R.T.); Chemical Sciences, Geosciences, and Biosciences Division, Office of Basic Energy Sciences, Office of Science, U.S. Department of Energy, award no. DEFG02-86ER13491 (strong field dynamics of small molecules) (to U.T.); and NSF grant no. PHY 2110633 (numerical model development) (to U.T.). **Author contributions:** Experimental setup, transient absorption spectroscopy beamline: M.R., T.D., M.S., A.v.d.D., and C.K. Experimental setup and operation, optical laser system: S.A., T.L., and I.H. Experimental setup and operation, high-order harmonic source: E.A., C.C.P., P.M., U.M., and M.K. Software setup for data collection: A.M., M.B., S.D., B.M., and S.G. Experimental investigation: A.M., M.R., E.A., C.C.P., H.L., F.T., S.M., M.S., G.D.B., J.L., M.B., S.D., S.A., T.L., C.H., B.M., U.F., A.T., A.B.W., L.S., F.C., R.T., R.M., C.O., and T.P. Data evaluation: A.M., M.R., J.L., U.T., R.J., R.M., C.O., and T.P. Writing: A.M., M.R., C.O., and T.P. **Competing interests:** The authors declare that they have no competing interests. **Data and materials availability:** All data needed to evaluate the conclusions in the paper are present in the paper.

Submitted 4 August 2023
Accepted 24 October 2023
Published 22 November 2023
10.1126/sciadv.adk1482

5. Discussion: Interconnecting Publications and Further Results

In the previous parts of this thesis a broad conceptual, theoretical and technical overview is provided as foundation for the various, partly independent results in the three publications of Chapter 4. Here, these results will be re-elaborated to highlight the connections between the different publications, which is supported by additional results and discussion of potential next scientific steps to combine their approaches. For that purpose, the overall scientific goal—as laid out in Chapter 1—should be kept in mind and hence will be restated: Investigating interaction of XUV and x-ray pulses with atoms and molecules within (dense) gases in a bottom-up approach, where absorption spectroscopy can be utilized to study neutral and ionic species, and intermediate states or superposition of electronic states. Following this bottom-up approach, the simplest system, atomic electron dynamics in a two-level system, has been investigated in the first two publications, in combination with studying an autoionizing state (Section 4.1) and a four-level system (Section 4.2). This sets the basis for considering the following extensions: (I) combining atoms within a dense gas to shift the understanding of light-matter interaction from a single-particle response towards macroscopic propagation effects, and (II) combining atoms within a molecule to investigate the electronic-state-dependent and coupled electronic-nuclear dynamics of molecules. For both cases, first the key aspects from the atomic simulations will be highlighted as potential goals, which is followed by a discussion of additional experimental results supporting the theoretical considerations. The central ideas for both topics are summarized briefly below and will be discussed in more detail in the respective sections:

(I) The first two publications theoretically investigate the detection and control of electron population transfer in atoms by means of absorption spectroscopy. The second publication builds on the numerical framework of the first one, but includes further physical phenomena such as generating resonant emission features, and the population reconstruction with a convolutional neural network. The generation of emission features has only been discussed briefly within the second publication, and will be further investigated within this chapter. The generation of an emission line within the driving pulse spectrum can be regarded as spectral reshaping of the driving pulse, for which typically a macroscopic propagation-based description is necessary. First experimental results for changing an absorption line to an emission line (in helium) with a single intense FEL pulse will be presented. The diffraction direction of this signal raises questions about the propagation dynamics through the gas

cloud—which are not included in the single-atom–response theoretical framework of the two publications. Thus, these findings connect to the technical achievement of enabling high target-density experiments presented in Section 3.2. As an outlook, first results of the high target-density experiments with high peak-intensity pulses allowing for non-linear excitation processes and spatial-spectral reshaping of the x-ray pulses via stimulated RIXS in neon atoms near the K-edge will be presented. A detailed discussion of this recent results of stimulated RIXS in neon can be found in [107].

(II) The second publication investigates—among other aspects—the electron populations dynamics on ultrafast times scales in a coherent electronic superposition of a four-level system. While changing the XUV photon energy to initiate different excitation processes is a well-established concept, the idea of tuning the XUV driving-pulse intensity to manipulate the electron populations in an atomic electron-wavepacket has also been introduced in the publication. This potential population-control concept will be discussed in more detail. If the excitation pulse and hence the electron-population transfer is faster than the nuclear dynamics in a molecule, the concept should be transferable to molecular electron-excitations as well. The (un-)coupling of electronic and nuclear dynamics is therefore a crucial aspect when considering ultrafast photochemical reactions, even more so for a potential coherent control of such reactions. The third publication (Section 4.3) investigates and time-resolves such coupled electronic-nuclear dissociation pathways of ionic molecular oxygen in a benchmark experiment. Further investigations of neutral O_2 and ionic $O_2{}^+$ dissociation pathways need both femtosecond time scales as well as variation of the excitation energy. Corresponding results will be presented and discussed in detail.

5.1. From Electron Populations in Atoms towards Spectral Reshaping and Propagation Effects

Theoretical Study Connecting Rabi-Cycles to Absorption-Line Changes

The experimental work of Ott et al [4] motivated the investigation of XUV-driven line-shape changes in connection with a significant population transfer. This study has been carried out at FLASH on an autoionizing—thus initially Fano-shaped—doubly-excited state in helium. The first publication of this thesis (Section 4.1) is motivated by these results and explores line shape-changes for strongly-coupled two-level systems and autoionizing states. It lays the foundation for everything that follows within this section, and therefore details and limitations not explained in the publication will be explained first before discussing the connections to the second publication and related experimental results. For both, a two-level system and an autoionizing state, absorption line-shape changes can be modeled numerically, illustrating that the underlying mechanism does *not* rely on the quantum-interference within the autoionizing state. In fact, for the autoionizing state it is more difficult to understand precisely the quantitative nature of

the absorption-line changes. This is connected with the modeling of the ionization-continuum and not with the state-couplings and dipole-phase shifts—which are the relevant effects behind these line-shape changes—and thus autoionizing states will not be further investigated. Instead, for a two-level system the absorption changes can also be approximated with a combination of a dipole-phase shift, analytical expressions for the dressed-state energies, and a convolution of the dipole-phase shifts with the pulse spectrum (cf figure 3 in the first publication). As a result, the publication in Section 4.1 first predicted line-shape changes of XUV-coupled states, which are initially Lorentzian-shaped. The line-shape changes are explained *qualitatively* with pure *state-coefficient phase-changes*, $\Delta\varphi_{g,e} = \int \Delta E \, dt$, due to shifts of the dressed-state energies, ΔE (see Figure 4)—as in the benchmark work of strong IR-field-induced line-shape changes [69]. The state-phase shifts lead to a dipole-phase shift, $\Delta\varphi_D = \Delta\varphi_g$ - $\Delta\varphi_e$ as the states shift into opposite directions, resulting in a corresponding change of absorption line shape. But for increased driving-pulse peak intensities, two deviations from this description can be found:

(I) For moderate peak intensities and small detunings of the pulse with respect to the resonance energy, the analytical approximation in the first publication (Section 4.1) differs from the results of the full numerical calculations. In the publication this is compensated by reducing the width of the Gaussian pulse spectrum in the convolution with the dipole-phase shifts calculated for a monochromatic laser. In the analytical treatment it is implicitly assumed, that there is a one-to-one correspondence between the bare-atomic states and two dressed states. But as introduced in Section 2.2.3, the strong XUV field generates four dressed states in total. Previous studies with intense near-infrared (NIR) pulses have demonstrated, that the relative population of dressed states during transient state-couplings depends on the driving pulse properties [114–118], and all dressed states need to be considered for describing the evolution of the bare states. Similar findings can be derived from the photo-electron spectra of XUV-driven Rabi cycles in helium [25, 119]. Expressing the bare-atomic states of an XUV strong-coupled two-level system with all four dressed-state energies, a *quantitative* agreement of an analytical expression with the full numerical treatment of the absorption line-shape changes is demonstrated in [5].

(II) For sufficiently high intensities of resonant driving pulses, full transient population transfer within a Rabi cycle (Figure 5) can be achieved. This has been reported for XUV-excited states in helium [25] by employing seeded FEL pulses [42], and measuring photo-electron spectra. It motivates a detailed investigation of the absorption changes at (i) high peak intensities, and (ii) in connection with population transfer Rabi-cycles. Such a study is performed within the second publication (Section 4.2), building on the numerical framework of the first publication. It incorporates high driving intensities, which lead to the inversion from an absorption to an emission line. It will be shown, how this arises from full Rabi population cycles, which can be reconstructed with a convolutional neural network (CNN). The usage of the CNN and further applications are discussed at the end of this section.

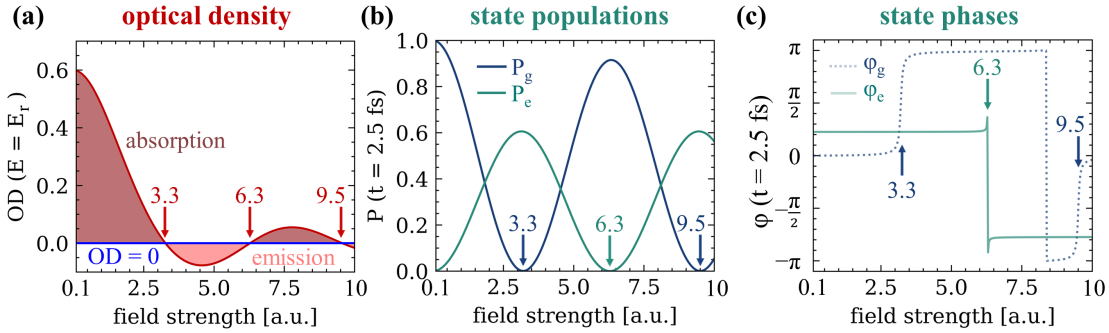

Figure 12.: **(a)** Resonant OD amplitude, ground- (blue) and excited-state (green) **(b)** populations, and **(c)** phases—all as function of the driving-pulse electric-field strength. The OD zero-crossings at field strengths of 3.3 a.u., 6.3 a.u. and 9.5 a.u. indicate inversion from absorption to emission or vice versa and correspond to the state-population minima, and π-jumps of the state-coefficient phases. In (c), the 2π-jump of the ground-state phase at a field strength of $\sim$8.4 a.u. comes from the 2π-phase periodicity and does not contain physical meaning.

In the following, the connection between the absorption line ($OD > 0$) turning into an emission line ($OD < 0$) and the corresponding Rabi-cycles of the state populations will be elaborated in more detail. As shown in figure 4a of the second publication (Section 4.2), the OD of a resonance line oscillates between positive and negative values with increasing field-strength of the resonant driving pulse. A lineout of the OD amplitude at the resonance energy is shown in Figure 12a as function of the driving-pulse field strength. For field strengths between 0.1 a.u. and 3.3 a.u., and in the range from 6.3 a.u. to 9.5 a.u., the OD is positive and hence corresponding to an absorption line. For field strengths between 3.3 a.u. and 6.3 a.u., and higher than 9.5 a.u., the OD is negative, which corresponds to an emission line. The zero-crossings of the OD at 3.3 a.u., 6.3 a.u. and 9.5 a.u. in Figure 12a can be explained with the electronic-state populations at late times, i.e. after the interaction with the driving pulse. The simulated excited-state population as function of time and field-strength is shown in figure 6a of the second publication (Section 4.2). Here, lineouts of the simulated ground- and excited-state populations at the latest time step, t = 2.5 fs, are shown as function of the driving-pulse field strength in Figure 12b. For field strengths of 3.3 a.u. and 9.5 a.u., the ground-state population exhibits a minimum with $P_g = 0$, and the excited-state population has a maximum, and vice versa for a field strength of 6.3 a.u.. The zero-crossings of the OD are thus directly correlated to the maxima/minima of the populations. The populations $P_{g,e}$ become zero, whenever the corresponding state coefficients $c_{g,e}$ change their sign, which is equivalent to a π-phase jump. This can be verified by looking at the phases of the state coefficients—as shown in Figure 12c as a function of the driving-pulse field strength. For field strengths of 3.3 a.u. and 9.5 a.u., only the ground-state phase makes a π-phase jump, whereas in the case of a field strength of 6.3 a.u., the phase jump occurs only for the excited state. When one of the coefficients makes a π-phase jump, the phase of the resulting (complex)

dipole $d_{ge} = c_g \cdot c_e^*$ does the same. In that case, the dipole moment changes from destructive to constructive interference with the incoming field (or vice versa), and the OD changes its sign, too. The connection between dipole phases and absorption lines is illustrated in Figure 6 in Section 2.3 as well as in both publications in Sections 4.1 and 4.2. Thus, whenever an $n \cdot \pi$ ($n \in \mathbb{N}$) driving pulse is utilized, which has an integrated field strength—or pulse area as defined in Section 2.2.3, $\Theta = \int dt\ E(t)$—leading to n-times full population transfers, the state coefficients alternately exhibit in total $n\pi$-phase jumps. For odd n, the ground-state phase undergoes the last phase jump, whereas the excited-state phase jumps (an additional time) whenever an even n is reached. Hence, crossing 3.3 a.u. corresponding to n=1, the ground-state phase jumps by π, changing the OD from an absorption to an emission line for higher field-strengths. For field strengths $>$ 6.3 a.u., where n=2 is reached, both states undergo a π-phase jump, changing the OD back to an absorption line, and for $>$ 9.5 a.u. (n=3), the OD is changed to an emission line again, as the ground-state phase makes its second jump.
Although the *zero-crossings* of the OD correspond to *full population transfers*, the field-strength range for which the OD is *negative*, e.g. 3.3 a.u. to 6.3 a.u. (see Figure 12a), is not related to *population inversion*, as the populations are inverted for a field strength range from 3.3 a.u. to 4.5 a.u., but not so for 4.5 a.u. to 6.3 a.u. (cf. Figure 12b). This does not contradict expectations from classical, rate-equation-based considerations about stimulated emission in classical lasing, because classically the coherent state-coupling and corresponding Rabi oscillations are not taken into account.

Experimental Absorption-to-Emission-Line Inversion in Helium Atoms

Such an effect has not been observed previously in case of a coupled two-level system driven by a single pulse. A conceptually related idea is the work of [120], where a hard x-ray FEL pulse is used to excite the nuclear transition of the the Mössbauer-isotope ^{57}Fe at 14.4 keV. A mechanical displacement of the target induces a π-phase shift of the re-emitted light, thereby increasing the resonant spectral intensity of the driving pulse. This idea is based on *classical wave interference* of the incoming and re-emitted hard x-ray light. In contrast, the findings discussed above and in the publications, induce a π-phase shift on a *quantum level* by XUV-induced strongly-coupled states, yet also leading to wave interference and an inversion from an absorption to an emission resonance line. Further similar studies on quantum-level induced light amplification in the field of *x-ray quantum optics* utilize either three electronic states or two laser pulses, or work with autoionizing states [69, 121–130].
These theoretical predictions lead to the question, whether the strong-coupling-based absorption to emission-line inversion can be measured experimentally. As the first evidence of XUV-induced Rabi oscillations has been reported in singly-excited helium, an experiment was performed in helium at FLASH with the absorption setup presented in Section 3.1. To this end, FEL pulses centered at 21.1 eV, near-resonant to the $1s2p$ (^{1}P) resonance, are used with two aluminum filter thicknesses, 100 nm and 400 nm, transmitting 80 % and 40 % of the ∼15 µJ FEL pulse energy.

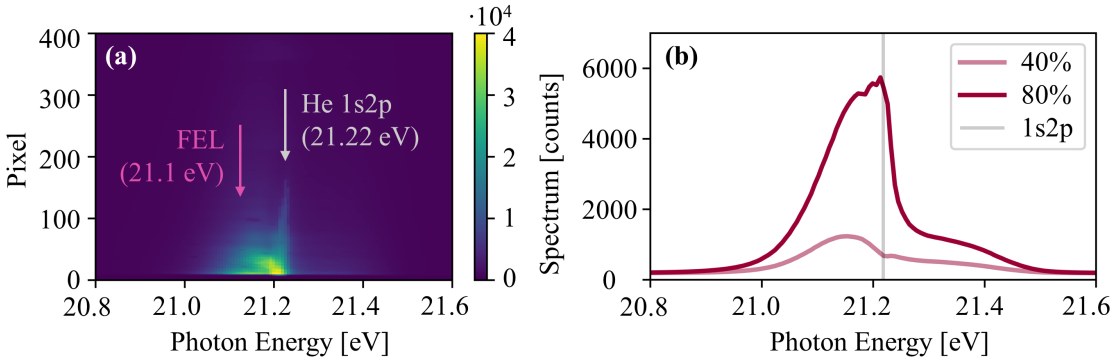

Figure 13.: **(a)** Spatially-resolved FEL transmission spectrum at the singly-excited $1s2p$ helium line. A pixel corresponds to 20 µm. The FEL is centered beneath Pixel 0. **(b)** In the spatially-integrated spectrum the $1s2p$ resonance changes from a local absorption minimum to an (emission) peak with increasing FEL intensity. The light-red spectrum corresponds to lower FEL intensities (40 % transmission), whereas the dark-red spectrum corresponds to higher FEL intensities (80 % transmission).

The data was recorded during a combined FEL-HHG experiment, and the XUV-sensitive CCD camera was aligned to the center of the HHG spectra. Therefore, only the lower spatial half of the camera is illuminated with FEL (stray) light. This issue will be further discussed below. In Figure 13a, the spectrally- and spatially-resolved FEL transmission spectrum (highlighted with a violet arrow) for the 80 % filter-transmission setting is shown. The data is recorded with a 10 s exposure time, and with a single pulse per bunch arriving every 0.1 s, which is repeated 17 times and hence the resulting spectrum is averaged over 1700 FEL pulses. A peak is visible in the spectrum at the $1s2p$ (^{1}P) resonance position, which is marked with a gray arrow in Figure 13a. The spatially-integrated spectrum is shown in Figure 13b in dark red and compared to the spatially-averaged spectrum for the 40 % filter-transmission setting (light red). Again, the $1s2p$ resonance position is given in gray. At this resonance energy, for the higher FEL pulse energy (80 % transmission), a potential emission peak is apparent, whereas for the lower FEL pulse energy (40 % transmission), a small absorption dip is visible. As discussed in Section 3.1, the spectral linewidth of the $1s2p$ ^{1}P resonance, $\Gamma \approx 7.5\,\mu\text{eV}$ [105], is much smaller than the spectral resolution of ∼30 meV, yet due to the high peak cross section of the resonance, a residual but broader absorption feature remains evident in the transmitted spectrum.

This measurement supports the initial idea of changing an absorption into an emission line with increasing pulse energy/peak intensity of the pulses. It demonstrates the spectral reshaping character, as more spectral intensity on resonance is generated in the transmitted spectrum. In the future, reusing such reshaped pulses at a secondary target could be beneficial for allowing higher resonant excitation probabilities of the same XUV-excited electronic state, while off-resonant spectral pulse components and the overall pulse energy become (slightly) smaller, thus suppressing for example competing two-photon ionization channels or valence ionization in case of core-excited

states. It is conceptually similar to the spectral-narrowing of hard x-ray pulses enabling high probabilities of nuclear transitions [120] discussed above. Yet, the practical feasibility of this ideas need to be evaluated more carefully in the future. Further, from an experimental/technical point of view, repeating the measurement with higher target-gas pressures could allow for an amplification of the emission feature—at least linearly scaling with atom number density. As evident in Figure 13a, the emission feature seems to extent vertically towards higher pixel than the residual FEL spectrum, indicating a larger diffraction angle. Assuming diffraction in the target gas, the 20 µm pixel size at the camera distance of 820 mm from the target position corresponds to a diffraction angle of 0.0014°. Measuring the FEL spectra in the FEL-beam propagation direction could therefore be helpful to disentangle light coming from the direct forward propagation, from diffuse stray light, and from diffracted light due to the interaction with the helium gas. Such measurements should also be combined with a theoretical framework of coupling the Schrödinger and Maxwell equations [63, 76–79] for a full propagation treatment as introduced in Section 2.3.

Experimental X-ray Propagation in Dense Neon Gas

Going one step further, it is possible to achieve propagation-based (initially-)exponential light amplification along the propagation distance (before gain saturation). In fact, this is the central principle of most lasers, and in particular has been used for the first demonstration of an x-ray atomic laser in neon gas pumped by an XFEL [74]. While x-ray lasing occurs in Ne^+ ions and produces narrow-band radiation limited by the core-hole lifetime, a similar process can take place within neutral neon atoms by the excitation of a $1s$ electron into the $3p$ state with 867 eV photon energy, and decay from a $2p$ electron into the $1s$ hole emitting a photon at 849 eV, as first demonstrated in [75]. This leads to the non-sequential two-photon process introduced as resonant inelastic x-ray scattering (RIXS) in Section 2.2.2. The RIXS signal is generated by the complete XFEL spectrum, which is much broader (∼5 eV to 10 eV) than the excited-state spectral width (∼0.3 eV) as discussed in [107]. Since a core-electron excitation is necessary to allow another electron to decay into this core hole, RIXS in only possible for x-ray photon energies and allows for novel studies of atoms and molecules [131]. As the RIXS probability is small, the propagation through a dense gas cloud allows for amplification of the RIXS signal in the XFEL propagation direction. This *stimulated* amplified RIXS is also referred to as 'stimulated resonant electronic x-ray Raman scattering' (SRXRS) and has been measured in transient-absorption geometry. To this end, the experimental setup introduced in Section 3.2 is utilized to measure the stimulated RIXS with an order-of-magnitude higher gas pressures (6 bar) and XFEL pulse energies (6 mJ) than the original work (0.7 bar and 0.3 mJ) [75]. An extensive analysis of the (saturated) amplification of the RIXS signal with variable input parameters as target-gas pressure, XFEL pulse energy and XFEL photon energy among others are provided in [107]. For illustration purposes, a measured RIXS spectrum at 6 bar of neon gas pressure, 6 mJ of XFEL pulse energy and 867 eV photon energy is provided in Figure 14 demonstrating the capabilities of the experimental setup in Section 3.2. Figure 14a shows a spatially- and spectrally-resolved spectrum.

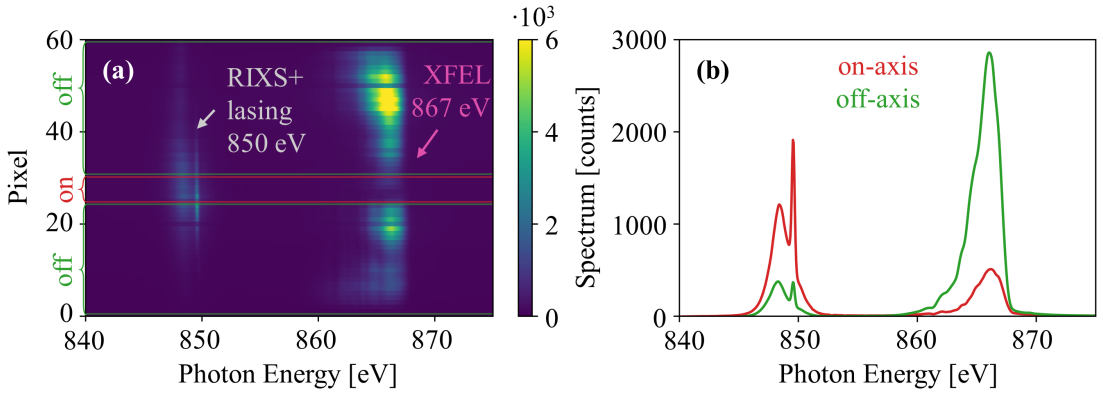

Figure 14.: **(a)** Spatially-resolved EuXFEL transmission spectrum near the neon K-edge (870 eV) with RIXS and Ne^+-lasing signals at 850 eV. **(b)** Spatially-averaged spectra for central on-axis (red), and off-axis regions (green). Results are elaborated in depth in [107].

The XFEL spectrum is only visible below 867 eV, because higher photon energies are absorbed by the $1s \rightarrow np$ Rydberg series and due to $1s$-photoionization above the K-edge of the dense neon cloud. The XFEL is aligned directly towards to the camera, and the center of the spatial axis, which is marked with red lines around pixel = 30 as 'on-axis' region. There, the center of the XFEL spatial intensity distribution is determined from reference measurements without neon gas. Yet, the XFEL spectrum is nearly vanishing in this spatial region in Figure 14a. However, at ∼850 eV the RIXS and x-ray lasing signals are clearly visible in the 'on-axis' spatial region and decrease towards the spatial edges of the detector. This is further illustrated with spectrally-averaged lineouts for the 'on-axis' and 'off-axis' region, respectively, shown in Figure 14b. While the 'off-axis' RIXS signal is nearly an order of magnitude smaller than the transmitted XFEL spectrum, the on-axis RIXS signal is around three times larger than the transmitted XFEL spectrum. This does not imply that the RIXS signal is larger than the incoming XFEL spectrum, as a lot of the XFEL pulse is absorbed or scattered during the propagation through the neon gas. Figure 14a also demonstrates the combined spectral-spatial reshaping of the incoming XFEL pulse by means of an amplified stimulated RIXS signal. In the future, spatially separating the amplified RIXS signal from the residual transmitted XFEL spectrum could provide a way to generate a two-color pump-probe scheme.

Further Opportunities Using Convolutional Neural Networks

In total, this illustrates that understanding the electronic-state populations in non-linear XUV and x-ray excitations as Rabi oscillations in coupled states or two-photon transitions in RIXS is a crucial aspect for investigating absorption spectra and potential reshaping or propagation effects. While the electron transfer and state populations can be simulated to predict the XUV/x-ray spectra, the reverse, i.e. reconstructing electronic-state populations from spectra, is in general not possible. Yet, in case of the strongly-coupled states and modified absorption lines, the

convolutional neural network (CNN) presented in the second publication (Section 4.2) is capable of reconstructing the simulated populations. The important aspect here is, that the unperturbed electronic structure gives rise to the *static* absorption lines, but the population transfer has to be connected to absorption *changes*, which can be learned by the CNN. As most non-linear excitations are intensity-dependent and lead to absorption features unavailable to the linear weak-field regime, the CNN could—in principle—be modified to predict electron-state populations in several different XUV/x-ray interaction cases, for example the RIXS in neon as well. To this end, the simulated training data needs to be adapted accordingly. To further use the CNN on experimental data, the combination of simulated training data over the full parameter range and measured training data for a subset, where the target population is known, is necessary. Therefore, measurements with sufficiently weak pulse intensities will lead to the static absorption, for which the populations are nearly unchanged and can be calculated with perturbation theory—as introduced in Equation (10) in Section 2.2.2.

The propagation of the XUV/r-ray pulses through a dense gas cloud can be modeled with a coupled Schrödinger- and Maxwell-equation approach as mentioned above, which thereby leads to different electronic-state populations along the propagation distance. At the same time, the driving pulse becomes increasingly more modified in spectral and *temporal* domain, which is theoretically predicted for the resonant x-ray propagation in dense neon gas in [79]. A first measurement campaign in dense neon clouds using angular laser-streaking [132, 133] to measure temporally-reshaped XFEL pulses has been performed at the Linac Coherent Light Source (LCLS) at Stanford University with attosecond *XLEAP* pulses [21] and data is evaluated by the group of Dr. James Cryan (LCLS). In the future, it could be tested whether a CNN can be used for predicting propagation-length-dependent populations or temporal pulse reshaping as well.

Furthermore, still ongoing analysis of potential absorption line-shape changes of the $3p$ resonance in neon during the same experiment has been part of this thesis project, and could clarify the feasibility of attosecond-scale x-ray-driven state-coupling of core-excited states in competition with valence ionization. Related to this subject are Rabi-cycles in helium *ions* with XUV-FEL pulses energetically above the ionization threshold of neutral helium [134]. There, the initial ionization is not a competitive process, but rather used to generate an entanglement between photo-electron and Rabi-cycles in the parent ion [134]. Applying the above discussion of absorption-to-emission-line inversion to this case, tuning the intensity of a Rabi-cycle-driving pulse to the point, where the corresponding absorption line vanishes, could be utilized as in-situ characterization of a full electron-population transfer regardless of additional ionization or propagation effects. In the future, a CNN could be utilized for analyzing such processes and perhaps predicting the ion-electron-entanglement by analyzing the ionic resonance in absorption spectra, complementary to investigating the photo-electrons as in [134].

5.2. From Electron Wavepackets in Atoms towards Disentangling and Manipulating Molecular Dynamics

The discussion in the previous section is focused on non-linear electronic excitations with ultrashort XUV/x-ray pulses in atoms and resulting propagation effects in dense gas clouds. Extending such excitations to electrons in molecules, would allow to transition towards probing and, eventually, controlling *ultrafast photochemical reactions*. Some of the key aspects and open question of this research field are summarized in a recent review about the topic [135]:

(I) coupling of electronic to nuclear dynamics,

(II) importance of electronic and vibronic coherences,

(III) quantum-state control for influencing the photochemical reaction outcome.

To this end, this section will first discuss the coherent excitation of electron wavepackets in connection with state-population control using the driving-pulse intensity as adjustment parameter—which is theoretically predicted in an atom in the second publication (Section 4.2). Transferring this concept to molecules would connect to the open questions in (II) and (III) above and requires driving-pulse durations shorter than the nuclear dynamics. Otherwise, electronic and nuclear dynamics can become coupled, for example breaking electronic superposition due to vibronic motions or dissociation. The photoinduced molecular dissociation dynamics governed by the intermediate electronically-excited molecular state connects to the ideas (I) and (III) above—and is addressed with the molecular-oxygen dissociation measurements presented in the third publication (Section 4.3). Hence, the second part of this section will present photon-energy–dependent molecular excitations and coupled electronic-nuclear dissociation dynamics. Further results expanding the findings in the third publication to femtosecond-scale dissociation times and different FEL photon energies will be discussed together with their implications and technical challenges.

Theoretical Study of Population Transfer in Atomic Electron Wavepackets

A coherent excitation of an electronic wavepacket in an atom from the ground state into three excited states is investigated in the second part—section 3.2—of the second publication (Section 4.2). In figure 7 of the publication, intensity-dependent examples of the OD for this four-level system are shown, whereas the time-dependent populations of the four states are given in figure 8. An intensity-dependent population transfer is already visible there, but will be elaborated here in more detail.

The model describing this system contains equal dipole moments of $d = 1$ a.u. between the ground state and all three excited states, which are equally spaced in energy. An energy scheme of the four-level system is shown in Figure 15a. The Gaussian driving-pulse duration of 2.5 fs enables transient energy and phase shifts as well as population transfers significantly faster than the life times

of the excited states ($\Gamma = 0.002$ a.u. $= 54.4$ meV translating to $\tau = 76$ fs). The pulse is centered spectrally at the second excited state, and therefore has an equal amount of spectral intensity at the energy positions of the first and third excited state, which is significantly smaller than the spectral intensity at the second excited-state resonance. For weak driving-pulse field-strengths, the second excited state is therefore always higher populated than the two neighboring excited states (cf. Equation (10)). For higher pulse field strengths, a coherent, non-trivial state-coupling and transient population transfer takes place, which is presented in the publication (Section 4.2). The final electronic-state populations for the complete data set utilized in the simulations of the publication are shown in Figure 15b as function of the peak driving-pulse field strength. As for Figure 12b in Section 5.1 of this discussion chapter, the final populations are evaluated at the last simulation time step, t = 2.5 fs, and therefore include the complete, time-integrated interaction with the driving pulse of fixed duration. As expected for the lowest field strengths, 0.1 a.u. to 2 a.u., the ground-state population is strictly decreasing, the three excited-state populations are monotonically increasing, while the second excited state is always higher populated than the other two excited states in Figure 15b. At a field strength of 2.3 a.u., a case is reached, which is conceptually similar to a π-pulse as discussed for the two-level system in Section 2.2.3 and Section 5.1: The ground-state population goes to zero, and the population is fully transferred to the three excited-states. The sum of all excited-state populations, $P_e = P_{e_1} + P_{e_2} + P_{e_3} = 81\,\%$, with $P_{e_1,e_3} = 24\,\%$, $P_{e_2} = 33\,\%$, does not reach 100 % because coherent population is inherently lost due to the spontaneous lifetimes used in the model. For higher field strengths, the population transfer becomes more complicated and cannot be compared nor described with the Rabi-oscillations of the two-level system. In a mechanical analogy, the field-strength-dependent populations might be thought of as the spatial displacements (the populations) of a four-mass chain or pendulum (the four states) connected via a central mass (the ground state) and different spring constants ($d_{ge} \cdot E_0$) exhibiting chaotic oscillatory motion.

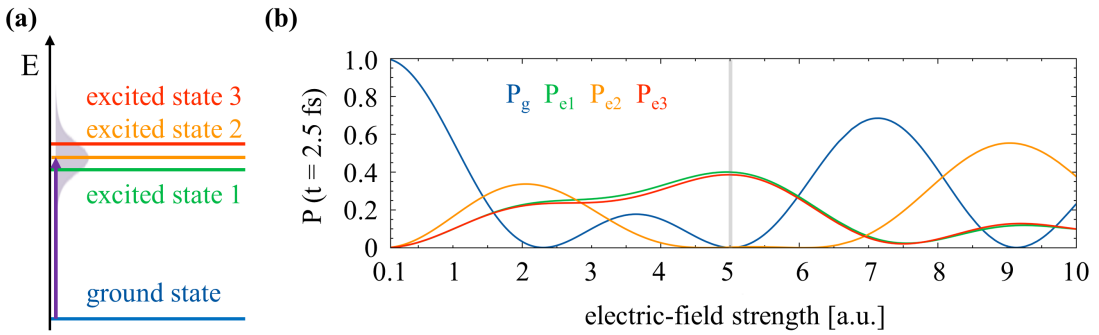

Figure 15.: **(a)** Four-level energy scheme as used in the second publication (Section 4.2). Colors match the choices of the publication. **(b)** Populations of the four levels as function of driving-pulse electric-field strength. The case of a 5 a.u. field strength discussed in the text is highlighted with a vertical gray line.

Yet, certain insights can be gained by looking into the details: For a field strength of 5 a.u., a case is reached where both the ground-state and second excited-state populations are close to zero and the other two excited states are maximally populated with $P_{e_1,e_3} = 40\,\%$. This illustrates, how the two off-resonant excited states (e_1, e_3) can be elected to be solely populated within the coherent superposition of an electronic-wavepacket excitation, although they are less favorable to be excited with respect to the resonant excited state (e_2) in the weak-field regime. In contrast, choosing a field strength of 9.1 a.u., an electronic-state superposition can be achieved, where the resonant excited-state has the largest relative population, $P_{e_2} = 53\,\%$, with respect to the off-resonant excited-state populations, $P_{e_1,e_3} = 12\,\%$, while the ground-state population remains close to zero. The relative contrast between P_{e_2} and P_{e_1,e_3} is even larger than for the case at 2.3 a.u. discussed above.
The symmetry of the electronic system and the pulse spectrum does not allow to separate the populations of the first and third excited state (small deviations in Figure 15 come from numerical uncertainties). If the driving pulse would be spectrally centered detuned with respect to the second excited state, such that its spectral intensity is different at all three resonance positions, a single state could be elected to be maximally—or potentially even solely—populated. Further, in more realistic scenarios, where (i) the energy spacing between the excited states is not symmetric, (ii) the dipole moments between the ground and excited states are not all equal, or (iii) the pulse spectrum is not perfectly symmetric, achieving a high contrast of a single excited-state population with respect to all other states excited by the same pulse should be even more likely.
This theoretical idea of preparing *initial* (with respect to subsequent dynamics) state populations in a coherent superposition of electronic states (at the end of the pulse) could be beneficial for time-resolved and state-selective pump-probe experiments, when the pump-pulse spectrum is too broad to only overlap with individual resonances, but cannot be chosen more narrow ro retain ultrafast temporal resolution due to the Fourier-transformation limit. While this *field-strength–dependent population-preparation* mechanism has not been explicitly shown within the second publication (Section 4.2), it is nevertheless contained within the population simulations and thereby inherently utilized for the training and correct predictions of the CNN. Therefore, the absorption line-shape changes in the four-level system are sufficient to also reconstruct this population-preparation mechanism. Experimental feasibility strongly depends on competing (ionization) channels, which need to be evaluated for particular atomic targets of interest in the future. Here, the general possibility is demonstrated in a generic model.

Towards Manipulating Electron-Population Transfer in Molecules

When transferring this idea to electronic-wavepacket excitations in molecules, a coherent electronic superposition can only be maintained before nuclear motion starts taking place and couples to the electronic dynamics. This aspect is both, a central feature of, as well as a challenge for investigating molecular dynamics. In the following, possibilities of enabling non-linear electronic excitations will be discussed first, before coupled electronic-nuclear dynamics are investigated.

As the population-selective mechanism above is based on the integrated electronic population transfer over the complete duration of the driving pulse, the driving pulse has to contain three characteristics in parallel: (i) The pulse duration has to be shorter than the time scales of the nuclear dynamics, while (ii) maintaining sufficient pulse areas, and (iii) coherence to enable Rabi-cycling. (i) The usage of the shortest available XFEL pulses with sub-femtosecond durations with tens to hundreds µeV of pulse energy produced at LCLS [21] could be employed for molecular systems with fast nuclear dynamics (10 fs). Recently, such pulses have been utilized to excite electronic superpositions in NO molecules in an impulsive RIXS scheme [136], i.e. enabling non-linear population transfer faster than the electronic-state lifetimes. This also further illustrates novel possibilities with the RIXS process discussed in the previous section. However, even larger pulse energies are likely to be necessary for full Rabi-population transfers. (ii) Alternately for slower nuclear dynamics, EuXFEL pulses with 1 fs to 30 fs durations and mJ-level pulse energies, as introduced in Sections 2.1.2 and 3.2 as well as used in the previous section, are more likely to deliver sufficient integrated pulse areas, but could only be employed for specific targets with slow nuclear motion. (iii) In case these SASE-based FEL sources are not sufficiently coherent, seeded-FEL sources have already demonstrated Rabi-cycling in atomic helium, but only with pulse durations $\geq$ 50 fs [25, 134].

In total, the experimental demonstration of the intensity-dependent population preparation in an molecular electronic wavepacket could be technically challenging, but not impossible with state-of-the-art XFEL pulse parameters. In contrast, a different concept to the same subject of selective electron-wavepacket excitations in molecules—but with valence electrons—utilizing intense and spectrally-modulated IR pulses is presented in [118]. There, instead of avoiding nuclear dynamics by sufficiently short pulses, the IR pulses are shaped to match and compensate the effects of the vibrational motion on the electronic dipole on single femtosecond times scales. It thereby enables population control of laser-dressed states and charge oscillations in potassium dimers. This experiment exemplifies the benefits of ultrafast pulse shaping and the necessity of understanding coupled electronic-nuclear dynamics at the same time. Further, it illustrates the intriguing aspect of electronic-charge transfer, which can only take place in molecules, and here is coupled to its vibrational motions. Coming back to the XUV and x-ray regime, arbitrary pulse shapers as used in the NIR-pulse experiment above are not (yet) available, but first ideas of pulse reshaping through non-linear interactions and dense gas clouds are discussed in Section 5.1. Further, the photo-ionization of localized electrons utilizing the x-ray site-selectivity in poly-atomic molecules can lead to electron-correlation–driven charge transfer much faster than nuclear motion [137]. In contrast, the coupling of electronic and nuclear dynamics can take place in specific cases of ionic molecular states, for example when low electron correlations lead to slower electronic processes. Further, excitations to (high) Rydberg-states in a neutral molecule can lead to rather slow electron dynamics as well, as the Rydberg-electrons have a larger orbit size and smaller overlap with the electrons of the ionic core. In this case, the coupling of electronic and nuclear dynamics becomes likely.

Experiments: Femtosecond-Scale Coupled Electronic-Nuclear Dynamics in O_2

This connects directly to the experiments in molecular oxygen shown in the third publication in Section 4.3. There, the dissociation of a specific electronic state in the molecular ion, $O_2{}^+$ (c $^4\Sigma_u^-$), is investigated. The two parallel dissociation pathways of this state, based on nuclear tunneling and electronic non-adiabatic spin-orbit coupling leading to pre-dissociation, are found to take place with the same 280 ps time scale. The nuclear-tunneling-dissociation pathway (II) is more favorable than the electronic pre-dissociation (I), as the corresponding rate $R_{II} = 2.1\,\mathrm{ns}^{-1}$ is larger than $R_I = 1.4\,\mathrm{ns}^{-1}$ as determined in the publication. As the spin-orbit coupling rate is proportional to the overlap of the two wavefunctions of the two interacting electronic states involved in the pre-dissociation [94], assuming a low overlap of the two electronic states can explain the low pre-dissociation rate R_I and slow electronic internal conversion dynamics.
Further, two corresponding and energetically-overlapping Rydberg series, ($^4\Sigma_u^-$) $n\ s\sigma_g/d\pi_g$, exist in the energy range 20.9 eV to 24.6 eV (see Section 2.5). Their dissociation dynamics are different from the dissociation of the ionic state, because the Rydberg states can also autoionize into the B $^2\Sigma_g^-$ state of the molecular ion, which then dissociates [138]. The autoionization time mainly depends on the principal quantum number n of the electronic Rydberg state: $\tau_n \sim n^3$ [139], whereas the competing pathway of tunneling dissociation depends on the vibrational quantum number v as for the ionic state. Coupling between vibrational and electronic states for the autoionization were suggested in [138]. This coupled electronic-nuclear dissociation mechanism in a *neutral* XUV-excited molecule is a promising candidate for corresponding benchmark measurements, but only time-resolved measurements for the $3s\sigma_g$ state in [138] and near-overlapping $5s\sigma_g/4d\pi_g$, $6s\sigma_g/5d\pi_g$ states in [139] are reported. The ∼5 fs autoionization time of the $3s\sigma_g$ state in [138] is expected to be too fast to be measured with combined FEL-HHG measurements, but the autoionization lifetime of 90 fs and 180 fs for the $5s\sigma_g/4d\pi_g$ and $6s\sigma_g/5d\pi_g$ states reported in [139] could in principle be resolvable. In addition, the tunneling-dissociation time of the lower vibrational state, v=0, of all Rydberg states is expected to be the same as for the v=0 state of the ionic c $^4\Sigma_u^-$ state, but [139] reported 1.1 ps for the v=0 dissociation time of the Rydberg states in contrast to the 280 ps found in the third publication (Section 4.3) for the ionic state. To further investigate these coupled electronic-nuclear dynamics of the molecular Rydberg states and compare them to the ionic state, the experimental scheme of FEL-pump and HHG-probe transient-absorption spectroscopy as introduced in Sections 3.1 and 4.3 can be used by tuning the FEL from 27.7 eV to 24 eV and repeating the measurements on femtosecond time scales. First results of such a measurement are shown in Figure 16. An illustration of the relevant potential-energy curves (PECs) close to the Frack-Condon (FC) region (see Figure 9) is presented in Figure 16a for two cases:

(I) With a FEL photon energy of 27.7 eV as in the third publication (Section 4.3), three ionic states and all their vibrational levels v: B $^2\Sigma_g^-$ (v=0–9) [92], 3 $^2\Pi_u$ (v=0–29) [91], and c $^4\Sigma_u^-$ (v=0,1) can be reached, which lead to significant fragment yields as introduced in Section 2.5. This will be discussed further below. The neutral Rydberg states, ($^4\Sigma_u^-$) $n\ s\sigma_g/d\pi_g$, cannot

be excited as the FEL photon energy is not resonant. Probing the same three fragments, $O(^3P)$, $O^+(^4S^o)$ and $O(^1D)$, with a time-delayed HHG pulse as in Section 4.3, leads to the resonant ΔOD lineouts shown in Figure 16b-d, which are extracted and colored in the same manner as in figure 2 of the third publication. Yet, they are recorded on the shorter time scale of -0.2 ps to 1.4 ps with 20 fs steps, which corresponds to the time-delay scan of the $\Delta OD(t, E_{\text{HHG-ph.}})$ shown in the lower half of figure 1C in the publication in Section 4.3.

(II) Alternatively, tuning the FEL photon energy to 24.0 eV, the FEL is resonant to the $5s\sigma_g$ (v=1), $6s\sigma_g$ (v=0) and $5d\pi_g$ (v=0) Rydberg states, respectively. The tails of the spectrum might excite further lower- and higher-lying Rydberg states with a small probability as well. In addition, the ionic B $^2\Sigma_g^-$ and 3 $^2\Pi_u$ states can be excited, but not the c $^4\Sigma_u^-$ ionic state, as the FEL photon energy is tuned below the two vibrational energies of this state. Repeating the same time-delay measurement with the HHG probe pulses as for the FEL photon energy of 27.7 eV, the ΔOD resonance lineouts for the same three fragments as above can be extracted and are presented in Figure 16e-g.

For analyzing the (background-corrected) data, first two averaged off-resonant regions of the time-dependent spectra, $\Delta OD(t, E_{\text{HHG-ph.}})$: 22.8 eV to 22.9 eV, and 25.1 eV to 25.2 eV, are fitted with a complementary error function, $\text{erfc}\left[(t - t_0)/\sigma\right]$, as describe in the third publication (Section 4.3). The decrease in ΔOD in these off-resonant regions is independent of the fragment formation—it does not further decrease after the initial step around t_0, whereas the resonant lineouts for the fragments do increase at later times—it is connected to the decrease of ground-state population of the neutral molecule, and hence depends only on the temporal overlap between the FEL and HHG pulses and corresponding temporal resolution. The FWHM of the error function therefore gives an in-situ estimation of the temporal resolution of the measurement independent of the dissociation time scales. In a second step, the temporal overlap and resolution are used while fitting the resonant (increasing) ΔOD lineouts shown in Figure 16 with exponentially rising functions, such that one time constant per fragment is extracted. This fitting procedure is shown in detail in equation 5 of the third publication (Section 4.3). The here presented fits are the precise estimation of the 'fast'-times-scale exponential fits used in the publication. The exponentially-fitted dissociation times for all three fragments and for both FEL photon energies as well as the two temporal resolutions for the two measurements are summarized in Table 5.1.

Table 5.1.: Fit results for FEL pulses at 27.7 eV and 24.0 eV: Resonance-fitted exponential dissociation times for the three oxygen fragments and off-resonant-fitted temporal resolutions.

FEL photon Energy	**$O(^3P)$**	**$O^+(^4S^o)$**	**$O(^1D)$**	**time resolution**
27.7 eV	(200 ± 30) fs	(60 ± 20) fs	(300 ± 50) fs	(320 ± 130) fs
24.0 eV	(80 ± 30) fs	(110 ± 20) fs	(210 ± 50) fs	(170 ± 80) fs

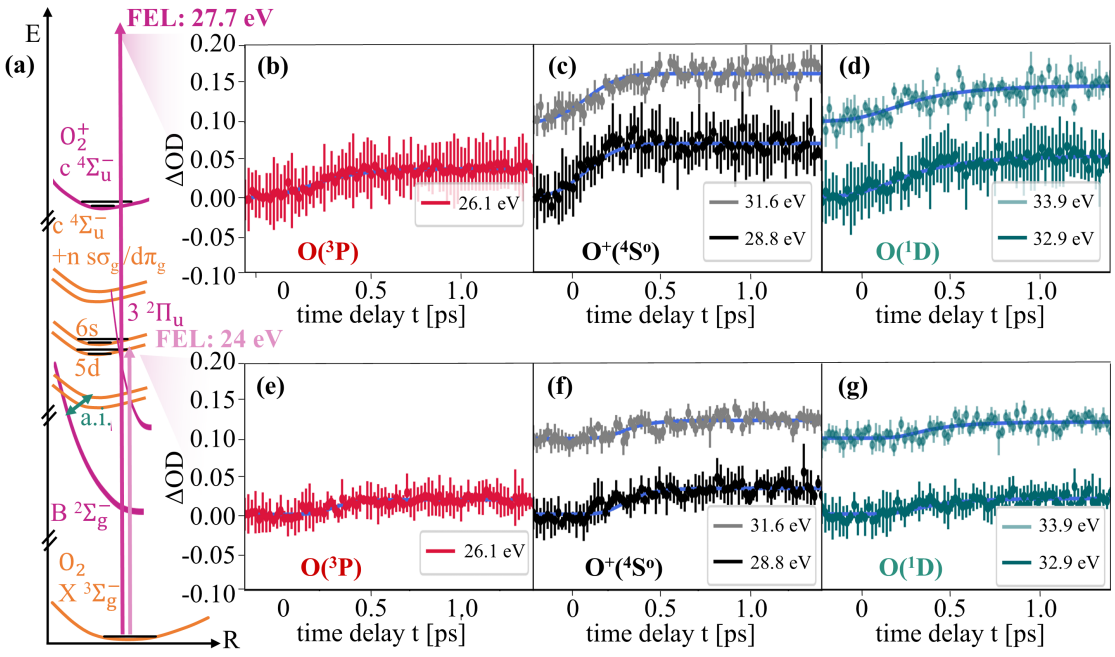

Figure 16.: **(a)** Relevant PECs in the FC region for the femtosecond-scale dissociation of O_2 for two FEL photon energies. Energy scales and positions are not accurate for better visibility. a.i. = autoionization. **(b)-(d)** Resonant ΔOD lineouts for O(^{3}P) (red), O$^+$(^{4}S^o) (black) and O(^{1}D) (green) fragments as a function of FEL-HHG time delay for $E_{\text{FEL-ph.}} = 27.7\,\text{eV}$. **(e)-(g)** Same time-dependent ΔOD lineouts as in (b)-(d) for $E_{\text{FEL-ph.}} = 24.0\,\text{eV}$

The temporal resolutions of the two time-resolved measurements, 170 fs to 320 fs, are on the order of the dissociation times, 60 fs to 300 fs, if not larger. Thus, a critical evaluation of the measurement needs to be cautious with regards to scientific implications. Several results can be extracted from the measurement nevertheless:

- All dissociation times are fitted with relative errors of 40 % or less, although the time resolutions are on the order of 80 % to 530 %. This can be explained by the fact, that the time resolution enters the fitting procedure as a fixed input, such that a residual increase for positive time delays can be fitted with a precision higher than the time resolution.

- However, several molecular states dissociate into the three different fragments via several pathways as introduced above. The fitted time scales therefore do not correspond to any concrete dissociation mechanisms and should rather be taken as a combined upper limit of the dissociation times of the different pathways. While fitting multiple exponential functions to the same ΔOD lineout is technically possible, the expected dissociation times are on the same order of magnitude, and the relative amplitudes are unknown, which would lead to a large cross-talk during the fitting, large relative errors and no meaningful results either.

- The $O(^1D)$ fragment is only generated within the second dissociation limit at 20.7 eV, together with a $O^+(^4S^o)$ fragment. The ionic B $^2\Sigma_g^-$ state has just a small probability of <10 % for two (v=4,5) out of its ten vibrational levels to pre-dissociate into this limit, while the rest dissociates into the first limit, $O(^3P)$, $O^+(^4S^o)$ at 18.7 eV, as found in [92]. Hence, only a negligible contribution of this state is expected for the $O(^1D)$ fragment in case of $E_{\text{FEL-ph.}} = 27.7$ eV. The 3 $^2\Pi_u$ state dissociation does not produce $O(^1D)$ fragments [92]. Under this assumption, tunneling dissociation of the $O_2{}^+$ (c $^4\Sigma_u^-$) v=1 state would be the only pathway leading to this fragment. As the v=1 state does not couple to the electronic states leading to the non-adiabatic pre-dissociation of the v=0 state [92, 94], the nuclear-tunneling is the only dissociation mechanism of the v=1 state. Its dissociation time could therefore be directly estimated with an upper limit of 300 fs as given in Table 5.1. Estimations for this dissociation time by measuring the spectral linewidth as in [140, 141] are ∼70 fs, and theoretical considerations give similar values of 50 fs to 100 fs [88, 142–144].

- Hence, for a correct evaluation and assignment of the underlying dynamics, the different dissociation times of all fragments need to be determined at the same time. As introduced in Section 3.1, the temporal resolution of the measurement can be significantly increased, when (i) shorter FEL pulse durations are used, e.g. 10 fs instead of here: 100 fs, (ii) respective arrival monitors for the FEL and IR/HHG pulses are applied, and (iii) post-analysis of single-pulse-per-bunch spectra are utilized. A detailed discussion of this approach based on the same FL26 beamline at FLASH2 and IR laser setup as used for the here presented experiment can be found in [145]. There, a reduction of temporal resolution from 130 fs down to 50 fs is reported, which could be sufficient to resolve the here investigated processes.

XUV-Photon-Energy–Resolved Measurements of O_2-Dissociation Products

The discussion above regarding the coupled electronic-nuclear dissociation dynamics of XUV-excited molecular oxygen is based on several previous theoretical and experimental results reported in publications such as [85–89, 91–95, 138–144]—but the list is far from complete for $O_2/O_2{}^+$ alone, and does not include other molecules. While this indicates a broad scientific interest in the topic of coupled electronic-nuclear dynamics over the course of several decades, it simultaneously illustrates its intrinsic complexity. In particular, identifying dissociation pathways for a given XUV photon energy by means of measuring kinetic energy release (KER) spectra of O^+ fragments is a central contribution for disentangling and, ultimately, understanding of the molecular dissociation pathways. The discussion above relies heavily on the findings for O^+-KER spectra reported in [92], where weak and tuneable XUV synchrotron radiation in combination with a photo-electron–photo-ion time-of-flight (TOF) coincidence method have been used. Such a detection scheme is also available via the reaction microscope (REMI) at the FL26 beamline, where the oxygen measurements are performed (see Section 3.1). In addition, the usage of XUV-FEL pulses instead of synchrotron radiation enables non-linear electronic excitations of the oxygen molecules, which

is both: (i) a challenge for interpreting the results for the linear excitation pathways, and (ii) a new avenue to investigate non-linear XUV photo-dissociation of molecules at the same time. Notably, the double-ionization of molecular oxygen can be reached with two-photon processes for the two FEL photon energies of 24 eV and 27.7 eV utilized above. Therefore, a comprehensive study of O^+-KER spectra measured with the FL26-REMI *in parallel* to the transient-absorption spectroscopy (TAS) measurements will be presented in the following.
The REMI collects data independent of the absorption spectra, which effectively is only generated by the FEL pulses, as the HHG pulses are orders of magnitude lower in pulse energy (see Section 3.1). Therefore and although the REMI measures oxygen fragments, it allows to understand the FEL-pumping step of the combined FEL-HHG measurements in more detail, while the time-dependent dissociation dynamics are probed with the delayed HHG pulses measured in the absorption setup. REMI data collection, processing, calibration and analysis was performed by colleagues in the group of PD Dr. Robert Moshammer, and in particular analysis for the O^+ fragments was performed with the help of Dr. Severin Meister and Dr. Hannes Lindenblatt. As part of this thesis project, evaluation of the corresponding REMI data in combination with the absorption spectra was carried out. A scan of the O^+-KER spectra as function of the FEL photon energy in the range from 20 eV to 30 eV is shown in Figure 17a. Lineouts of the KER spectra for the two FEL photon energies discussed above, 24.0 eV and 27.7 eV—averaged over a ±0.3 eV range of the FEL photon energy ($E_{\text{FEL-ph.}}$) covering the total FEL spectrum—are presented in Figure 17b and several features in the KER spectra can be identified. The following discussion of these findings is based on information provided in Figure 9 and Table 2.2, which come from previous results in [92].

- For $E_{\text{FEL-ph.}} \geq 20.3\,\text{eV}$, a KER peak at ∼0.8 eV—which equals (20.3 eV−18.7 eV)/2—is clearly visible. It is attributed to the pre-dissociation of the B $^2\Sigma_g^-$ state into $O^+(^4S^o)$ fragments belonging to the first dissociation limit at 18.7 eV [92]. The substructure arises from the vibrational levels of the B $^2\Sigma_g^-$ state.

- For $E_{\text{FEL-ph.}} \geq 20.8\,\text{eV}$, maybe a small KER peak near ∼0 eV is visible, which would be expected from pre-dissociation of the B $^2\Sigma_g^-$ ($v \geq 4$) states into the second dissociation limit, $O(^1D) + O^+(^4S^o)$, at 20.7 eV [92]. This supports the assumption above, that the contribution of the B $^2\Sigma_g^-$ state to the $O(^1D)$-fragment formation is negligible.

- For $E_{\text{FEL-ph.}} \geq 24.6\,\text{eV}$, two KER peaks at ∼2 eV and ∼3 eV appear. As only the v=0 c $^4\Sigma_u^-$ state pre-dissociates into $O^+(^4S^o)$ fragments belonging to the first dissociation limit (18.7 eV) [92], only a single corresponding KER peak at 3 eV is visible. In contrast, both v=0,1 c $^4\Sigma_u^-$ states tunnel-dissociate into $O^+(^4S^o)$ fragments of the second dissociation limit (20.7 eV) [92], such that the corresponding KER peak at 2 eV is split. This supports the findings of the third publication (Section 4.3) and the assignment of the 300 fs dissociation time of the $O(^1D)$ fragment (Table 5.1) to the tunnel-dissociation of the v=1 c $^4\Sigma_u^-$ state.

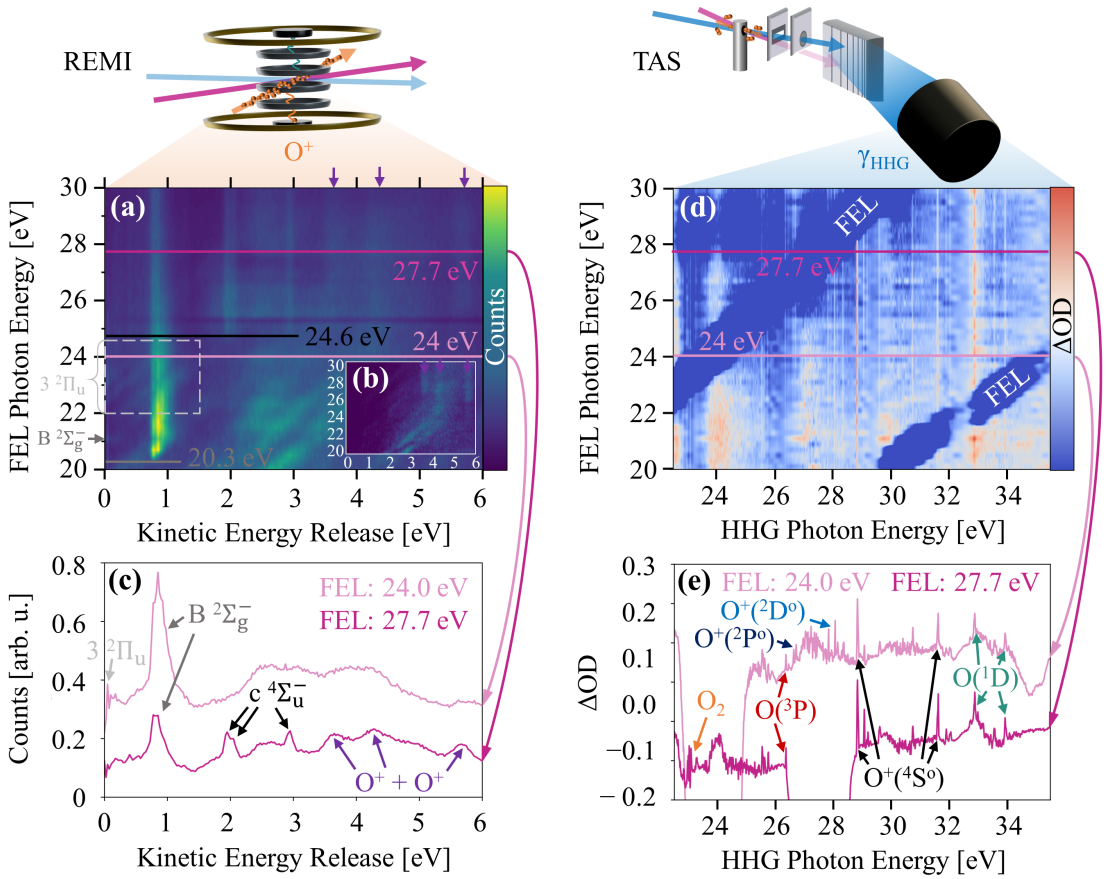

Figure 17.: Combined FEL-photon-energy–dependent REMI ((**a**)-(**c**)) and TAS ((**d**)-(**e**)) measurements. **(a)** KER spectra of O^+ fragments as function of FEL photon energy. Molecular ionc-state thresholds are given in gray and black. **(b)** Same KER spectra as in (a), but for O^++O^+–coincidences only. **(c)** KER lineouts for FEL photon energies of 27.7 eV and 24 eV. Peaks are labeled with molecular states from which the dissociation takes place. **(d)** ΔOD as function of FEL and HHG photon energies, whit a fixed time delay of ∼1 ps **(e)** ΔOD lineouts for the same FEL photon energies as in (c). Absorption resonances of neutral and ionic atomic fragments and the molecular ground state are highlighted with different colors.

- For 22 eV ≤ $E_{\text{FEL-ph.}}$ ≤ 24.5 eV, the KER features are not straightforward to identify:
  (i) A small KER peak at ∼0 eV is barely visible, which is attributed to the dissociation of the 3 $^2\Pi_u$ state into the third dissociation limit, $O(^3P)$ + $O^+(^2D^o)$, at 22.1 eV [92], where the residual photon energy is carried away by the photo-ionized electron.
  (ii) Broad and weak KER diagonals from 0 eV to 2 eV could arise from the excitation into the higher-lying repulsive curve of the 3 $^2\Pi_u$ state, where nearly no energy is shared with the photo-electron. The state can again dissociate directly into the third dissociation limit as above [92], or alternatively, undergo a diabatic transition into another $^2\Pi_u$ state and

dissociation into the fifth limit, $O(^3P)$ + $O^+(^2P^o)$, at 23.8 eV [92]. Resulting KERs of these two processes are not sharp in both energies and could match the weak experimental diagonals.
Further, excitation into the $(^4\Sigma_u^-)$ n $s\sigma_g/d\pi_g$ Rydberg series, subsequent autoionization into the B $^2\Sigma_g^-$ state and dissociation, should produce O^+ fragments with a few eV as well—which could overlap with the features from the $^2\Pi_u$ state or lead to the observed broad KER signals around 2 eV to 3 eV. It is unclear, how their signatures would appear in Figure 17a, as they have not been reported in [92]. Further evaluation is therefore necessary.

- Residual features in the KER-spectra cannot be explained with one-FEL-photon excitations and corresponding dissociation pathways. The most prominent of these features are:
(i) KER peaks at 3.7 eV, 4.3 eV and 5.6 eV for FEL photon energies (roughly) larger than 25 eV, and (ii) broad KER diagonals linearly increasing from 2 eV to 4 eV with the FEL photon energy in the range from 20 eV to 25 eV.
As *two-FEL-photon-transitions* would lead to excitations of $O_2{}^{2+}$ states, which dissociate into O^++O^+ limits, they could be detected by measuring O^++O^+–*coincidences*. This can be achieved with the REMI by filtering the O^+ momenta, as discussed in [100]. Applying these filters to the data in Figure 17a, results in the FEL-dependent KER spectra for the O^++O^+–coincidences are shown in Figure 17b. The unexplained KER features in (i) and (ii) are also evident in these coincidence spectra, and it is therefore concluded that they arise from the assumed two-FEL-photon transitions.

Overall, most of the features in the O^+ KER spectra measured with the REMI agree with previous results utilizing synchrotron radiation [92]. Additional findings can be attributed to two-photon transitions initiated by the FEL pulses, which cannot be initiated with synchrotrons. Yet, some open questions remain about the dissociation fragments of the Rydberg series, $(^4\Sigma_u^-)$ n $s\sigma_g/d\pi_g$, as no clear fragment identification and dissociation assignment can be made with the present data. Some of the complications for analyzing the dissociation of the Rydberg series with the O^+ KER spectra are partly attributed to the tunneling dissociation of the ns/d Rydberg states yielding two *neutral* fragments, $O^*(ns/d)$+$O(^1D)$, which cannot be detected with the REMI. Detecting neutral fragment yields as function of the FEL-pump photon energy would be necessary for further insights. Such a measurement can be achieved by utilizing the HHG probe pulses at fixed, late time delays in transient absorption measurements, while varying the FEL photon energy. This novel type of experiment was implemented at the FL26 beamline for the first time. Preliminary results for the same FEL photon energy range from 20 eV to 30 eV as for the REMI measurement, and with HHG pulses arriving at a fixed time delay of 0.9 ps after the FEL pulses, are presented in Figure 17d. ΔOD lineouts as function of the HHG photon energy for the two FEL photon energies of 24.0 eV and 27.7 eV—corresponding to the two time-resolved measurements in Figure 16—are shown in Figure 17e. A detail discussion of the preliminary results is challenging, because of the reasons given below. As for the time-resolved measurements,

several partly scientific, partly technical aspects can be extracted and will be discussed in the following to enable improvements to this novel technique in the future:

- The *FEL stray light* overlays significant parts of the HHG spectra, appearing as large negative values in the ΔOD (dark blue). As the FEL spectrum moves diagonally across the ΔOD plot with a slope ≈ 1, it is straightforward to identify. Further, a similar feature appears at HHG photon energies equal 1.5-times the FEL photon energies, which arises from the third harmonic of the FEL measured in the second-order diffraction of the grating.
- The FEL stray light further significantly affects the residual parts of the ΔOD spectra as it prevents a proper *background correction* of the HHG spectra before calculation of the ΔOD.
- The *FEL pulse energy* estimated with an upstream gas-monitor detector (GMD), varies from 21.5 µJ to 37.5 µJ for the FEL *photon* energy range from 20 eV to 30 eV. More pulse energy implies higher interaction probabilities with the oxygen molecules (microscopically) leading ultimately to more fragments (macroscopically) and higher signals in the ΔOD. Without a correct background subtraction, it is difficult to account for these effects in the given data set.
- A *small FEL focus* and hence large FEL peak intensity leading to two-photon-excitations reduces the abundance of neutral fragments. Further, the combination of most linewidths of the neutral fragments being narrow (1–2 pixel) with respect to the larger spectrometer resolution, 30 meV, leads to a reduced absorption dip in the transmitted spectrum and small ΔOD signal—as discussed for the helium resonance in Section 5.1.
- Overall, a *quantitative* evaluation of FEL-photon-energy–dependent neutral oxygen fragments is challenging with the present data. Minimizing the FEL stray light and adjusting the FEL focus could help to improve the relevant ΔOD signals in the future. Nevertheless, the novel concept of this measurement is demonstrated with the parallel identification of several *neutral and ionic* fragments. In addition to previous assignments, $O^+(^2P^o)/O^+(^2D^o)$ ions are also detected due to their absorption lines at $E_{\text{HHG-ph.}} \approx 26.5\,\text{eV}/28\,\text{eV}$. This supports related observations made with the REMI: the direct and electronically-coupled 3 $^2\Pi_u$ state dissociation pathways.
- Further, absorption lines of the neutral oxygen molecule are visible due to excitations into the $(^4\Sigma_u^-)$ $n\,s\sigma_g/d\pi_g$ Rydberg series with HHG photon energies around 23 eV. Nevertheless, no new resonance lines arising from dissociation of the molecular Rydberg states into atomic Rydberg atoms are evident—which should only appear at certain FEL photon energies in the range from 20.9 eV to 24.6 eV. As no literature on XUV-excited oxygen Rydberg atoms has been found, the spectral position of such absorption lines is therefore not clear. XUV-excitation of an electron within the ionic $O^+(^4S^o)$ core of the neutral $O^*(ns/d)$ Rydberg atom could have similar transition energies—within the spectrometer resolution—as the $O^+(^4S^o)$ ion itself, and hence could be spectrally not distinguishable.

Concluding Remarks on Time-and-Photon-Energy–Resolved Molecular Dissociations

This section has illustrated how the combined FEL+HHG and sequential REMI+TAS experimental setup can be used for complimentary and multidimensional measurements of ultrafast XUV-photochemical reactions. The capability of the FEL to be tuned to different photon energies with high precision ($\sim$0.3 eV) allows for pumping various combinations and superpositions of molecular states, while an independent, broadband HHG pulse probes several dissociation fragments simultaneously. The combination of KER spectra and femto- to picosecond-scale resolved absorption spectra allows for unique insights into the dissociation mechanisms of XUV-excited molecules. Despite technical challenges during the proof-of-principle demonstration of this novel measurement technique, first results for coupled electronic-nuclear dynamics in molecular oxygen are obtained:

- The dissociation time and corresponding rates for the inner-shell-excited $O_2{}^+(c\ {}^4\Sigma_u^-)$ $v = 0$ state are measured for the first time in the third publication (Section 4.3). The coupled dissociation mechanism leading to a single dissociation time of (280 ± 160) ps has been predicted and used in similar previous work [138, 139], but is here demonstrated experimentally by measuring all relevant fragments and pathways simultaneously.
- Am estimation for the dissociation time of the $O_2{}^+(c\ {}^4\Sigma_u^-)$ $v = 1$ state, based on combined REMI and TAS results, is given. Further femtosecond-scale dissociation times indicating electronic-state–dependent parallel pathways can be extracted, but need further validation. This illustrates electronic- and vibrational-state dependent ultrafast photo-dissociation.
- Identification and assignment ionic dissociation pathways by means of O^+ KER spectra in an excitation range from 20 eV to 30 eV can be made verifying previous findings [92]. Novel two-photon-excitations into $O_2{}^{2+}$ and resulting ionic fragments can be identified with O^++O^+–coincidence measurements, which are further investigated as in [146].
- Identification of several neutral fragments for the 20 eV to 30 eV molecular-excitation range is achieved for the first time, but relative contributions from the different dissociation pathways cannot be extracted yet.

In the future, this experimental scheme could be extended by various means, connecting with ideas and concepts presented within the previous parts of this thesis:
Investigating poly-atomic molecules would enable the usage of the *XUV/x-ray-element selectivity* by exciting and probing inner-shell/core electrons localized at a specific atomic site of the molecule. This has been demonstrated with FEL-pump–FEL-probe experiments, for example in [13], but the novel scheme demonstrated here could potentially cover several atomic sites or fragments simultaneously by probing with the broadband HHG pulses instead.

In addition, the *high pulse energies and peak intensities* of the FEL pulses could enable further non-linear excitations, as two-photon-transitions have been already presented above. The XUV-induced line-shape changes in helium based on state-couplings and electron-population transfer have been measured at FLASH as well. Although the dissociation times for the $O_2(ns/d)$ Rydberg series could not be identified in this work, the autoionization times for the $6s/5d$ states are reported in [139]. In combination with our findings for the dissociation times of the vibrational states of the corresponding ionic c $^4\Sigma_u^-$ state—assuming similar time scales for the Rydberg states as in [138, 139]—the coupled electronic-nuclear dynamics are expected to be ≥ 100 fs. FEL pulses can be shorter in duration while retaining most of their pulse energy for this dissociation-time estimate. Therefore, the intensity-dependent population scheme introduced at the beginning of this section could potentially be tested experimentally with the $O_2(ns/d)$ Rydberg series, which could help disentangle dissociation pathways of the individual Rydberg states, e.g. differentiate between the nearly-overlapping $6s$ and $5d$ states. Absorption-line changes of this Rydberg series with short and intense IR pulses have been reported in [89].

Further lending ideas from the IR regime, impulsive Raman excitations of a vibrational mode in SF_6 molecules probed by modifications of x-ray inner-shell electronic transitions with HHG pulses has been demonstrated in [15]. Conceptually similar for electrons, the stimulated RIXS process discussed in the previous section, in particular the impulse stimulated RIXS process demonstrated in [136], can be used to excite electronic wavepackets in molecules, and their subsequent temporal evolution could be probed with another pulse. Yet it is likely that attosecond, x-ray instead of femtosecond, XUV FEL pulses are mandatory for such a scheme.

High-density experiments with *molecular targets* could enable new scientific avenues. The high neon-density RIXS-propagation experiments presented in Section 5.1 are based on the re-emitted or scattered photons *re-interacting* with the gas cloud, e.g. driving a stimulated amplification of the RIXS processes. Although far from the current state-of-art research, high molecular-gas densities should increase the probability of photo-electrons and fragments to re-interact with the molecular gas as well, enabling further investigations of chemical reactions.

In general, the less is know about a chemical reaction or dynamical process, the more helpful controllable parameters (FEL photon and pulse energy) and independent collection of as many information as possible (combined KER- and broadband-absorption-spectra) are expected to be. This is conceptually at the heart of *machine learning*: producing large data sets to extract underlying patters. Thus, as ultrafast and non-linear electronic excitations in molecules can produce modified absorption, photo-ion or photo-electron signals as in the case of atoms, the usage of a CNN to reconstruct and predict the underlying electronic populations and molecular structure and dynamics is expected to be possible as well. For example, reconstructing molecular structures from laser-induced electron diffraction imaging with a CNN is reported in [147].

6. Summary: Providing Four Answers

Overall, this doctoral thesis covers the subject of

'Time-and-Energy–Resolved Electron Dynamics in Atoms and Molecules with Intense Short-Wavelength Light'.

As the interaction of short-wavelength, i.e. XUV and x-ray, laser pulses with atoms and molecules is a rather recent and fundamental research field, it is approached in this thesis from a bottom-up perspective including four main avenues. They have been introduced in Chapter 1 by asking the following, rather-generally and openly phrased questions:

(I) How are absorption changes in an XUV pulse spectrum related to the perturbation of the electronic structure of the interacting atom?

(II) How can temporal electron dynamics in atoms be reconstructed from spectral absorption measurements?

(III) How can high gas-density experiments be performed to include propagation effects during the interaction of XUV/x-ray pulses with atoms and molecules?

(IV) How can a novel combination of XUV laser pulses be used to investigate and time-resolve a photochemical reaction?

As the questions are generally phrased, there is not a single comprehensive answer with respects to the multitude of on-going research activities. To combine the different theoretical, technical and scientific aspects and results of this thesis, the answers to these question will be given guided by the general underlying theme as laid out by the title, without disregarding different approaches to the same subject.
In this last chapter, all four questions will be answered with a comprehensive one-sentence statement about the research presented in this thesis, before further details are summarized for each topic, respectively.

How are absorption changes in an XUV pulse spectrum related to the perturbation of the electronic structure of the interacting atom?

The changes of an absorption line shape coherently driven by an intense XUV-FEL pulse arises from both the electronic population transfer and modification of the resulting dipole moment in time, as well as transient shifting and splitting of the electronic states in energy.

Combining (i) transient dressed-state energy shifts—as described for monochromatic lasers—with (ii) the relation between dipole-phase shifts and line-shape changes in the impulsive limit—as demonstrated with IR laser pulses—explains most of the induced absorption changes. This explanation is made in an energy-domain picture: Spectrally resolving the XUV light enables measuring line-shape changes in the first place. Further, variation of the central FEL photon energy leads to different line-shape changes. The interaction is therefore excitation-energy–resolved as well, but is convoluted with the spectrum of the driving pulse. Notably, scanning the FEL photon energy across the resonance, inverts the asymmetry of the line shape. This is connected to how the two bare electronic states translate into the dressed states during the interaction with the XUV pulse. The simplest explanation holds true for lower pulse intensities: Both bare states can be linked to a single dressed state, respectively, while the other two dressed states can be neglected. Whether the two relevant dressed-state energies are shifted closer to, or further away from each other during the pulse duration, depends on the spectral detuning of the pulse. As a result, the dipole phase at the end of the pulse shifts into opposite directions for opposite detunings, and the line-shape asymmetry is inverted when the detuning changes sign.
This also illustrates, that the time-integrated electric-field strength of the pulse determines the resulting absorption line changes. As many XUV-excited states decay rapidly via autoionization or Auger-Meitner decay, the durations of the driving pulses must be shorter than these decay times, which are on femto- to attosecond times scales. Achieving sufficiently large pulse areas therefore demands high peak intensities. However, high peak intensities can also lead to competing non-linear excitations or ionization with two-photon processes. In addition, autoionization and Auger-Meitner decay also imply the presence of competing (valence-)ionization processes. The study within this thesis focuses mainly on demonstrating and explaining XUV-driven line-shape changes in a two-level system without such competition, and with fixed pulse durations. An autoionizing resonance is also shown to undergo line-shape changes in agreement with previous experimental results [4]. Furthermore, for high pulse intensities not only external competing processes complicate the picture above, but the existence of the other two dressed states within the laser-dressed atom need to be considered as well. In that case, the two bare states split into two dressed states, respectively. Their relative populations depend on the driving pulse properties such as the detuning. Furthermore, the pulse intensity changes along the temporal profile, which effects the relative populations as well, and the resulting phase changes cannot be calculated analytically. However, these effects on the coherent electron dynamics are captured by numerical solutions of the employed few-level models, where limiting cases can be discussed analytically.

How can temporal electron dynamics in atoms be reconstructed from spectral absorption measurements?

While the quantum dynamics underlying measurement observables can often only be inferred indirectly, a convolutional neural network is capable of directly reconstructing the electronic population cycling from a modified absorption spectrum.

As the probabilistic nature of quantum particles is wave-like in space and time, the Fourier-transformation connects their time-and-energy–dependent behavior and observables. When both spectral amplitudes and phases are given, the time-dependent observable can be directly calculated from the spectral one, and vice versa. Yet, the spectrally measured optical density is not directly connected to a single electronic-state population. However, an absorption line is spectrally-correlated allowing a CNN to identify its shape, which is correlated with the temporal dipole moment and electronic-population transfer—as discussed by answering the first question. The full numerical simulations include all the time-dependent interactions such as the time-dependent pulse envelope, and the generation and the population of dressed states. As a result, the bare-state coefficients, dipole moment and absorption line can be accurately calculated, and the CNN is trained on these simulation results. However, this thesis only employs the CNN to predict from unseen, but nevertheless simulated absorption data. A demonstration of predicting electron populations from experimentally-measured absorption spectra has not been performed yet. Combining training sets of simulated data over a broad input-parameter range and experimental data for weak-field pulses and hence unchanged absorption lines is expected to yield prediction results for the experimental cases of high pulse intensities and modified absorption lines. An intriguing example is the theoretically-predicted, and in helium experimentally-observed absorption-to-emission–line inversion. In the simulations, the Rabi cycles of the populations are directly connected to the line inversion. In the future, the helium measurements can be further investigated in combination with simulations and a CNN.
However, the scrutiny of the CNN predictions is nevertheless difficult. It illustrates, that a major part of the CNN capabilities and limitations are given by the underlying theoretical framework. While a CNN prediction does not have to be the correct reconstruction of the underlying processes, in certain cases it might be the only option. The simulation and reconstruction of an electronic wavepacket consisting of four coupled states is an example, where an analytical expression cannot be provided. Their temporal populations dependent heavily on the input pulse parameters, resulting in complex, possibly chaotic dynamics, which needs further investigation. In such cases, the interaction with spectrally-fluctuating SASE-FEL pulses could perhaps only be reconstructed with a CNN. Nevertheless, for coherent pulses such as seeded FELs, the theoretical concept of intensity-dependent population-preparation of electronic wavepackets in atoms is demonstrated in this thesis, which is aimed to be tested with molecules in the future as well.

How can high gas-density experiments be performed to include propagation effects during the interaction of XUV/x-ray pulses with atoms and molecules?

The combination of a steep pressure gradient between a dense target-gas cloud and the surrounding vacuum environment, with high x-ray pulses energies, such that the pulses are not immediately absorbed entering the dense cloud, enables propagation-based studies.

This topic differs slightly from the other three, as mainly its technical aspect is considered in this thesis, which is the central contribution of this thesis project to the respective experiment. While most of the setup is designed as previous setups, looking into the details—as for the quantum-dynamical investigations—unravels its secrets: the replaceable target-gas cells, through which the XFEL pulses drills its own small holes. Since few-micrometer-sized entrance and exit holes cannot be mechanically drilled, the scientific experiment in dense neon gas was accompanied by an initial technical experiment during the beamtime, proving the self-drilling-hole approach is working well. For future experiments, the variability of cell lengths enabling different propagation lengths could be additionally employed. Further, optimizations of cell-wall thickness or material, as well as XFEL pointing stability may allow for even higher target-gas pressures. As alternative or in combination, a nested target-cell design with two-fold differential-pumping—similar to what is utilized for high-pressure high-order harmonic generation [26]—could be used.
The setup enables the measurement of stimulated resonant inelastic x-ray scattering (RIXS) in dense neon gas amplified along the propagation axis. While such a measurement has been demonstrated previously [75], here an order of magnitude higher target-gas pressure and XFEL pulse energy allowed to improve the stimulated RIXS amplification. To this end, the transient-absorption geometry is crucial to measure the stimulated RIXS in forward detection, and spectrally resolving the difference between absorbed and emitted/scattered photons. Further, the energy-resolved RIXS signal can be differentiated from the energetically-overlapping x-ray atomic lasing signal emitted by core-ionized Ne^+, as its spectral width is determined by the average XFEL spectral bandwidth, whereas the Ne^+ lasing is governed by the more narrow lasing-transition line-width. The measurement demonstrates spectral and spatial reshaping of the XFEL pulses, and additional temporal reshaping is expected from the theory work [79] by the project's main investigators. More recent measurements are currently under evaluation to experimentally demonstrate the attosecond temporal reshaping as well. While RIXS in atomic neon is based on single intermediate- and final-state transitions, the experiment work of [136] in NO molecules demonstrates impulsive stimulated RIXS employing superpositions of several intermediate and final electronic states. Thereby the RIXS allows for time-dependent electronic excitations in molecules, connecting the RIXS scheme to the theoretical considerations in the previous topic, as well as experimental findings regarding the next question.

How can a novel combination of XUV laser pulses be used to investigate and time-resolve a photochemical reaction?

An FEL laser pulse allows to photo-excite or -ionize electrons in molecules with a well-defined excitation energy, initiating electronic and nuclear dynamics, whereas a time-delayed broadband HHG pulse identifies most relevant reaction products by means of their absorption signatures.

Photo-excited molecules can dissociate via different pathways, which can vary drastically depending on the intermediate electronic excited-state—or even across vibrational states belonging to the same electronic state. While the nuclear degrees of freedom of a molecule are often responding to the initial electronic rearrangement after photo-excitation, a combination of fast nuclear, and slower electronic processes can lead to coupled nuclear-electronic dynamics. Time-resolving such ultrafast dissociations requires a pair of short pulses, which was first introduced in the XUV and x-ray regime by utilizing two FEL pulses. The only other—and historically preceding—ultrafast XUV/x-ray source of HHG pulses typically does not possess sufficiently high pulse energies for an HHG-pump–HHG-probe experiment, and therefore is often combined with IR laser pulses. The novel combination of FEL-pump–HHG probe pulses demonstrated within this thesis, enables to tune the excitation energy of the FEL pulses across different excited states in a neutral or ionic molecule, independent of the broadband HHG pulses detecting neutral and ionic fragments with sensitivity to their electronic states. This scheme is demonstrated with the coupled nuclear-electronic dissociation pathways of ionic oxygen molecules. The nuclear-tunneling in parallel to electronic coupling and pre-dissociation of the vibrational ground state (v=0) of a specific electronic state is verified by measuring the same dissociation time for all three fragments—of which two are neutral fragments of different electronic configurations—with the time-delayed HHG probe pulses. Further, the FEL photon-energy is scanned across multiple molecular electronic states while the HHG pulses are probing the resulting fragments at a fixed time delay of $\sim$1 ps. The investigation of the many absorption lines attributed to several neutral and ionic fragments is still ongoing. In addition, a complementary measurement is performed in parallel, by resolving the kinetic energy release of O^+ fragments. This measurement agrees well with previous findings, verifying that two vibrational states of the same electronic state can undergo different dissociation pathways, where only one vibrational state couples to other electronic states. In addition, first findings of two-FEL-photon–initiated dissociation into ionic-oxygen coincidences are presented, which will be further investigated [146]. Overall, the novel combination of time-resolved absorption spectra and kinetic-energy-release spectra suggests new avenues for studying non-linear XUV interactions with atoms and molecules. Further, the here presented results demonstrate the capability of XUV light to excite inner-shell electrons localized within the oxygen molecules. In the future, the XUV/x-ray element-specificity can be utilized by investigating poly-atomic and more complex molecules. The here-presented results are merely a subset of what can be learned about XUV-photochemistry, illustrating the richness and complexity of the subject, and the necessity of the related research, to which this doctoral thesis seeks to make a contribution.

Appendix

A. References

[1] Alexander Magunia et al. „Bound-State Electron Dynamics Driven by Near-Resonantly Detuned Intense and Ultrashort Pulsed XUV Fields“. In: *Applied Sciences* 10.18 (Sept. 2020), p. 6153. DOI: 10.3390/APP10186153 (cit. on p. viii).

[2] Daniel Richter, Alexander Magunia, Marc Rebholz, Christian Ott and Thomas Pfeifer. „Electronic Population Reconstruction from Strong-Field-Modified Absorption Spectra with a Convolutional Neural Network“. In: *Optics* 5.1 (2024), pp. 88–100. DOI: 10.3390/opt5010007 (cit. on pp. viii, 51).

[3] Alexander Magunia et al. „Time-resolving state-specific molecular dissociation with XUV broadband absorption spectroscopy“. In: *Science Advances* 9.47 (2023), eadk1482. DOI: 10.1126/sciadv.adk1482 (cit. on p. viii).

[4] Christian Ott et al. „Strong-Field Extreme-Ultraviolet Dressing of Atomic Double Excitation“. In: *Physical Review Letters* 123.16 (Oct. 2019). DOI: 10.1103/PhysRevLett.123.163201 (cit. on pp. viii, 3, 10, 23, 51, 63, 86, 109).

[5] Yu He et al. „Direct manipulation of atomic excitation with intense extreme-ultraviolet laser fields“. In: *Physical Review A* 105.4 (Apr. 2022), p. 043113. DOI: 10.1103/PhysRevA.105.043113 (cit. on pp. viii, 19, 51, 87).

[6] Lennart Aufleger et al. „Pulse length effects on autoionizing states under the influence of intense SASE XUV fields“. In: *Journal of Physics B: Atomic, Molecular and Optical Physics* 53.23 (Nov. 2020), p. 234002. DOI: 10.1088/1361-6455/ABBE2D (cit. on pp. viii, 10, 51).

[7] Lennart Aufleger et al. „Line-shape broadening of an autoionizing state in helium at high XUV intensity“. In: *New Journal of Physics* 24.1 (Jan. 2022), p. 013014. DOI: 10.1088/1367-2630/AC3B2E (cit. on pp. viii, 10, 51).

[8] Michael Straub et al. „Differential Measurement of Electron Ejection after Two-Photon Two-Electron Excitation of Helium“. In: *Physical Review Letters* 129.18 (Oct. 2022), p. 183204. DOI: 10.1103/PhysRevLett.129.183204 (cit. on pp. ix, 40, 42, 44).

[9] Thomas Ding et al. „Nonlinear Coherence Effects in Transient-Absorption Ion Spectroscopy with Stochastic Extreme-Ultraviolet Free-Electron Laser Pulses“. In: *Physical Review Letters* 123.10 (Sept. 2019), p. 103001. DOI: 10.1103/PhysRevLett.123.103001 (cit. on p. ix).

[10] Thomas Ding et al. „XUV pump–XUV probe transient absorption spectroscopy at FELs“. In: *Faraday Discussions* 228 (May 2021), pp. 519–536. DOI: 10.1039/D0FD00107D (cit. on p. ix).

[11] Thomas Ding et al. „Measuring the frequency chirp of extreme-ultraviolet free-electron laser pulses by transient absorption spectroscopy“. In: *Nature Communications* 12.643 (Jan. 2021). DOI: 10.1038/s41467-020-20846-1 (cit. on p. ix).

[12] Marc Rebholz et al. „XUV-Initiated Dissociation Dynamics of Molecular Oxygen (O_2)“. In: *Journal of Physical Chemistry A* 125.47 (Dec. 2021), pp. 10138–10143. DOI: DOI:10.1021/acs.jpca.1c06033 (cit. on pp. ix, 4).

[13] Marc Rebholz et al. „All-XUV Pump-Probe Transient Absorption Spectroscopy of the Structural Molecular Dynamics of Di-iodomethane“. In: *Physical Review X* 11.3 (Sept. 2021), p. 031001. DOI: 10.1103/PhysRevX.11.031001 (cit. on pp. ix, 4, 106).

[14] Patrick Rupprecht et al. „Laser Control of Electronic Exchange Interaction within a Molecule“. In: *Phys. Rev. Lett.* 128.15 (Apr. 2022), p. 153001. DOI: 10.1103/PhysRevLett.128.153001 (cit. on p. ix).

[15] Patrick Rupprecht et al. „Resolving vibrations in a polyatomic molecule with femtometer precision via x-ray spectroscopy“. In: *Phys. Rev. A* 108.3 (Sept. 2023), p. 032816. DOI: 10.1103/PhysRevA.108.032816 (cit. on pp. ix, 107).

[16] Patrick Rupprecht, Alexander Magunia, Lennart Aufleger, Christian Ott and Thomas Pfeifer. „Flexible experimental platform for dispersion-free temporal characterization of ultrashort pulses“. In: *Optics Express* 31.24 (Nov. 2023), pp. 39821–39831. DOI: 10.1364/OE.503731 (cit. on p. ix).

[17] M. Hentschel et al. „Attosecond metrology“. In: *Nature* 414.6863 (Nov. 2001), pp. 509–513. DOI: 10.1038/35107000 (cit. on pp. 2, 6, 7).

[18] M. Lewenstein, Ph. Balcou, M. Yu Ivanov, Anne L'Huillier and P. B. Corkum. „Theory of high-harmonic generation by low-frequency laser fields“. In: *Physical Review A* 49.3 (Mar. 1994), pp. 2117–2132. DOI: 10.1103/PhysRevA.49.2117 (cit. on pp. 2, 6, 7).

[19] P. M. Paul et al. „Observation of a train of attosecond pulses from high harmonic generation“. In: *Science* 292.5522 (June 2001), pp. 1689–1692. DOI: 10.1126/science.1059413 (cit. on pp. 2, 6).

[20] W. Ackermann et al. „Operation of a free-electron laser from the extreme ultraviolet to the water window“. In: *Nature Photonics* 1.6 (June 2007), pp. 336–342. DOI: 10.1038/nphoton.2007.76 (cit. on pp. 2, 8).

[21] Joseph Duris et al. „Tunable isolated attosecond X-ray pulses with gigawatt peak power from a free-electron laser“. In: *Nature Photonics* 14.1 (Dec. 2019), pp. 30–36. DOI: 10.1038/s41566-019-0549-5 (cit. on pp. 2, 93, 97).

[22] Praveen Kumar Maroju et al. „Attosecond pulse shaping using a seeded free-electron laser“. In: *Nature* 578.7795 (Feb. 2020), pp. 386–391. DOI: 10.1038/s41586-020-2005-6 (cit. on p. 2).

[23] J. B. Hearnshaw. *The analysis of starlight : two centuries of astronomical spectroscopy.* 2nd ed. Cambridge University Press, Mar. 2014 (cit. on p. 2).

[24] G. Kirchhoff. „Ueber die Fraunhofer'schen Linien“. In: *Annalen der Physik* 185.1 (Jan. 1860), pp. 148–150. DOI: 10.1002/ANDP.18601850115 (cit. on p. 2).

[25] Saikat Nandi et al. „Observation of Rabi dynamics with a short-wavelength free-electron laser“. In: *Nature* 608.7923 (Aug. 2022), pp. 488–493. DOI: 10.1038/s41586-022-04948-y (cit. on pp. 3, 87, 97).

[26] S. M. Teichmann, F. Silva, S. L. Cousin, M. Hemmer and J. Biegert. „0.5-keV Soft X-ray attosecond continua“. In: *Nature Communications* 7.1 (May 2016), pp. 1–6. DOI: 10.1038/ncomms11493 (cit. on pp. 4, 111).

[27] Ahmed H. Zewail. „Laser Femtochemistry“. In: *Science* 242.4886 (Dec. 1988), pp. 1645–1653. DOI: 10.1126/SCIENCE.242.4886.1645 (cit. on p. 6).

[28] P. B. Corkum. „Plasma perspective on strong field multiphoton ionization“. In: *Physical Review Letters* 71.13 (Sept. 1993), p. 1994. DOI: 10.1103/PhysRevLett.71.1994 (cit. on p. 6).

[29] E. Constant et al. „Optimizing High Harmonic Generation in Absorbing Gases: Model and Experiment“. In: *Phys. Rev. Lett.* 82.8 (Feb. 1999), pp. 1668–1671. DOI: 10.1103/PhysRevLett.82.1668 (cit. on p. 6).

[30] Ferenc Krausz and Misha Ivanov. „Attosecond physics“. In: *Rev. Mod. Phys.* 81.1 (Feb. 2009), pp. 163–234. DOI: 10.1103/RevModPhys.81.163 (cit. on p. 6).

[31] Thomas Gaumnitz et al. „Streaking of 43-attosecond soft-X-ray pulses generated by a passively CEP-stable mid-infrared driver“. In: *Opt. Express* 25.22 (Oct. 2017), pp. 27506–27518. DOI: 10.1364/OE.25.027506 (cit. on p. 7).

[32] Tenio Popmintchev et al. „Bright Coherent Ultrahigh Harmonics in the keV X-ray Regime from Mid-Infrared Femtosecond Lasers“. In: *Science* 336.6086 (2012), pp. 1287–1291. DOI: 10.1126/science.1218497 (cit. on p. 7).

[33] Philippe Balcou, Pascal Salières, Anne L'Huillier and Maciej Lewenstein. „Generalized phase-matching conditions for high harmonics: The role of field-gradient forces“. In: *Phys. Rev. A* 55.4 (Apr. 1997), pp. 3204–3210. DOI: 10.1103/PhysRevA.55.3204 (cit. on p. 8).

[34] Gennadii N Kulipanov. „Ginzburg's invention of undulators and their role in modern synchrotron radiation sources and free electron lasers“. In: *Physics-Uspekhi* 50.4 (Apr. 2007), pp. 368–376. DOI: 10.1070/PU2007v050n04ABEH006237 (cit. on p. 8).

[35] H. Motz. „Applications of the Radiation from Fast Electron Beams“. In: *Journal of Applied Physics* 22.5 (May 1951), pp. 527–535. DOI: 10.1063/1.1700002 (cit. on p. 8).

[36] H. Motz, W. Thon and R. N. Whitehurst. „Experiments on Radiation by Fast Electron Beams“. In: *Journal of Applied Physics* 24.7 (July 1953), pp. 826–833. DOI: 10.1063/1.1721389 (cit. on p. 8).

[37] Brian W.J. Mcneil and Neil R. Thompson. „X-ray free-electron lasers“. In: *Nature Photonics* 4.12 (Nov. 2010), pp. 814–821. DOI: 10.1038/nphoton.2010.239 (cit. on p. 8).

[38] David Attwood and Anne Sakdinawat. *X-Rays and Extreme Ultraviolet Radiation: Principles and Applications*. 2nd ed. Cambridge University Press, 2017. DOI: 10.1017/CBO9781107477629 (cit. on p. 8).

[39] Siegfried Schreiber and Bart Faatz. „The free-electron laser FLASH“. In: *High Power Laser Science and Engineering* 3 (2015), e20. DOI: 10.1017/hpl.2015.16 (cit. on p. 9).

[40] Thomas Tschentscher et al. „Photon Beam Transport and Scientific Instruments at the European XFEL“. In: *Applied Sciences* 7.6 (June 2017), p. 592. DOI: 10.3390/APP7060592 (cit. on p. 9).

[41] Stefan Düsterer et al. „Study of temporal, spectral, arrival time and energy fluctuations of SASE FEL pulses“. In: *Optics Express* 29.7 (Mar. 2021), pp. 10491–10508. DOI: 10.1364/OE.419977 (cit. on p. 10).

[42] E. Allaria et al. „Highly coherent and stable pulses from the FERMI seeded free-electron laser in the extreme ultraviolet“. In: *Nature Photonics* 6.10 (Sept. 2012), pp. 699–704. DOI: 10.1038/nphoton.2012.233 (cit. on pp. 10, 87).

[43] Thomas Pfeifer, Yuhai Jiang, Stefan Düsterer, Robert Moshammer and Joachim Ullrich. „Partial-coherence method to model experimental free-electron laser pulse statistics“. In: *Opt. Lett.* 35.20 (2010), pp. 3441–3443. DOI: 10.1364/OL.35.003441 (cit. on p. 10).

[44] Dipankar Bhattacharyya and Jyotirmoy Guha. *Quantum Optics and Quantum Computation*. 2053-2563. IOP Publishing, 2022. DOI: 10.1088/978-0-7503-2715-2 (cit. on p. 11).

[45] B. H. Bransden and C. J. Joachain. *Physics of Atoms Molecules*. Pearson, Apr. 2002 (cit. on pp. 11–13, 15, 16, 32, 36).

[46] Gordon Drake. „High Precision Calculations for Helium". In: *Springer Handbooks* (2006), pp. 199–219. DOI: 10.1007/978-0-387-26308-3_11 (cit. on pp. 12, 44).

[47] U. Fano. „Effects of Configuration Interaction on Intensities and Phase Shifts". In: *Phys. Rev.* 124.6 (1961), pp. 1866–1878. DOI: 10.1103/PhysRev.124.1866 (cit. on pp. 12, 22).

[48] R. P. Madden and K. Codling. „New Autoionizing Atomic Energy Levels in He, Ne, and Ar". In: *Phys. Rev. Lett.* 10.12 (June 1963), pp. 516–518. DOI: 10.1103/PhysRevLett.10.516 (cit. on p. 12).

[49] Jan M. Rost, K. Schulz, M. Domke and G. Kaindl. „Resonance parameters of photo doubly excited helium". In: *Journal of Physics B: Atomic, Molecular and Optical Physics* 30.21 (1997), p. 4663. DOI: 10.1088/0953-4075/30/21/010 (cit. on p. 12).

[50] Erwin Madelung, Karl Boehle and Siegfried Flügge. „Die mathematischen hilfsmittel des physikers". In: (1936) (cit. on p. 13).

[51] A Hibbert, E Biemont, M Godefroid and N Vaeck. „E1 transitions of astrophysical interest in neutral oxygen". In: *Journal of Physics B: Atomic, Molecular and Optical Physics* 24.18 (Sept. 1991), p. 3943. DOI: 10.1088/0953-4075/24/18/010 (cit. on p. 13).

[52] K. L. Bell, P. G. Burke, A. Hibbert and A. E. Kingston. „Photoionisation of the $2p^4$ ^3P, ^1D, ^1S states of atomic oxygen". In: *Journal of Physics B: Atomic, Molecular and Optical Physics* 22.20 (Oct. 1989), p. 3197. DOI: 10.1088/0953-4075/22/20/012 (cit. on p. 13).

[53] S. S. Tayal. „Resonant photoionization cross sections and branching ratios for atomic oxygen". In: *Phys. Rev. A* 65.3 (Feb. 2002), p. 032724. DOI: 10.1103/PhysRevA.65.032724 (cit. on p. 13).

[54] Charlotte Emma Moore. *Atomic energy levels as derived from the analyses of optical spectra*. Vol. 1. US Department of Commerce, National Bureau of Standards, 1949 (cit. on p. 13).

[55] G. C. Angel and James A. R. Samson. „Total photoionization cross sections of atomic oxygen from threshold to 44.3 Å". In: *Physical Review A* 38.11 (Dec. 1988), pp. 5578–5585. DOI: 10.1103/PhysRevA.38.5578 (cit. on p. 13).

[56] J. A. Fennelly and D. G. Torr. „Photoionization and photoabsorption cross sections of O, N_2, O_2, and N for aeronomic calculations". In: *Atomic Data and Nuclear Data Tables* 51.2 (July 1992), pp. 321–363. DOI: 10.1016/0092-640X(92)90004-2 (cit. on p. 13).

[57] Brendan M. Mclaughlin and Kate P. Kirby. „Photoabsorption of atomic oxygen in the vicinity of the K-edge". In: *Journal of Physics B: Atomic, Molecular and Optical Physics* 31.22 (Nov. 1998), p. 4991. DOI: 10.1088/0953-4075/31/22/010 (cit. on p. 13).

[58] Federica Frati, Myrtille O. J. Y. Hunault and Frank M. F. De Groot. „Oxygen K-edge X-ray Absorption Spectra". In: *Chemical Reviews* 120.9 (May 2020), pp. 4056–4110. DOI: 10.1021/ACS.CHEMREV.9B00439 (cit. on p. 13).

[59] Robert W Boyd. *Nonlinear optics*. Academic Press, 2008 (cit. on pp. 16, 20).

[60] W. P. Healy and R. G. Woolley. „On the derivation of the Kramers-Heisenberg dispersion formula from non-relativistic quantum electrodynamics". In: *Journal of Physics B: Atomic and Molecular Physics* 11.7 (Apr. 1978), p. 1131. DOI: 10.1088/0022-3700/11/7/013 (cit. on pp. 16, 46).

[61] S. H. Autler and C. H. Townes. „Stark Effect in Rapidly Varying Fields“. In: *Phys. Rev.* 100.2 (1955), pp. 703–722. DOI: 10.1103/PhysRev.100.703 (cit. on pp. 16, 18, 51).

[62] I. I. Rabi. „Space Quantization in a Gyrating Magnetic Field“. In: *Phys. Rev.* 51.8 (Apr. 1937), pp. 652–654. DOI: 10.1103/PhysRev.51.652 (cit. on pp. 16, 18).

[63] Mengxi Wu, Shaohao Chen, Seth Camp, Kenneth J. Schafer and Mette B. Gaarde. „Theory of strong-field attosecond transient absorption“. In: *Journal of Physics B: Atomic, Molecular and Optical Physics* 49.6 (Feb. 2016), p. 062003. DOI: 10.1088/0953-4075/49/6/062003 (cit. on pp. 16, 19, 23, 91).

[64] S. Guérin, F. Monti, J. M. Dupont and H. R. Jauslin. „On the relation between cavity-dressed states, Floquet states, RWA and semiclassical models“. In: *Journal of Physics A: Mathematical and General* 30.20 (Oct. 1997), p. 7193. DOI: 10.1088/0305-4470/30/20/020 (cit. on p. 16).

[65] B. R. Mollow. „Power Spectrum of Light Scattered by Two-Level Systems“. In: *Physical Review* 188.5 (Dec. 1969), pp. 1969–1975. DOI: 10.1103/PhysRev.188.1969 (cit. on p. 18).

[66] J. Ullrich et al. „Recoil-ion and electron momentum spectroscopy: reaction-microscopes“. In: *Reports on Progress in Physics* 66.9 (Aug. 2003), p. 1463. DOI: 10.1088/0034-4885/66/9/203 (cit. on pp. 20, 41).

[67] Henry N. Chapman et al. „Femtosecond diffractive imaging with a soft-X-ray free-electron laser“. In: *Nature Physics* 2.12 (Nov. 2006), pp. 839–843. DOI: 10.1038/nphys461 (cit. on p. 20).

[68] Adrian N. Pfeiffer et al. „Alternating absorption features during attosecond-pulse propagation in a laser-controlled gaseous medium“. In: *Physical Review A - Atomic, Molecular, and Optical Physics* 88.5 (Nov. 2013), p. 051402. DOI: 10.1103/PHYSREVA.88.051402 (cit. on pp. 21, 23).

[69] C Ott et al. „Lorentz Meets Fano in Spectral Line Shapes: A Universal Phase and Its Laser Control“. In: *Science* 340 (2013), pp. 716–720. DOI: 10.1126/science.1234407 (cit. on pp. 22, 51, 87, 89).

[70] V. Stooß et al. „Real-Time Reconstruction of the Strong-Field-Driven Dipole Response“. In: *Phys. Rev. Lett.* 121.17 (Oct. 2018), p. 173005. DOI: 10.1103/PhysRevLett.121.173005 (cit. on pp. 23, 63).

[71] Yu He, Christian Ott, Thomas Pfeifer and Mette B. Gaarde. „Local enhancement in transient absorption spectroscopy by gating the resonance in the time domain“. In: *Physical Review Research* 6.1 (Jan. 2024), p. 013103. DOI: 10.1103/PhysRevResearch.6.013103 (cit. on p. 23).

[72] Chen Ting Liao, Arvinder Sandhu, Seth Camp, Kenneth J. Schafer and Mette B. Gaarde. „Beyond the Single-Atom Response in Absorption Line Shapes: Probing a Dense, Laser-Dressed Helium Gas with Attosecond Pulse Trains“. In: *Physical Review Letters* 114.14 (Apr. 2015), p. 143002. DOI: 10.1103/PHYSREVLETT.114.143002 (cit. on p. 23).

[73] Chen Ting Liao, Arvinder Sandhu, Seth Camp, Kenneth J. Schafer and Mette B. Gaarde. „Attosecond transient absorption in dense gases: Exploring the interplay between resonant pulse propagation and laser-induced line-shape control“. In: *Physical Review A* 93.3 (Mar. 2016), p. 033405. DOI: 10.1103/PHYSREVA.93.033405 (cit. on p. 23).

[74] Nina Rohringer et al. „Atomic inner-shell X-ray laser at 1.46 nanometres pumped by an X-ray free-electron laser“. In: *Nature* 481 (2012), pp. 488–491. DOI: 10.1038/nature10721 (cit. on pp. 23, 91).

[75] Clemens Weninger et al. „Stimulated Electronic X-Ray Raman Scattering“. In: *Physical Review Letters* 111 (2013), p. 233902. DOI: 10.1103/PhysRevLett.111.233902 (cit. on pp. 23, 46, 91, 111).

[76] Yu He et al. „Watching the formation and reshaping of a Fano resonance in a macroscopic medium“. In: *Physical Review A* 103.4 (Apr. 2021), p. L041102. DOI: 10.1103/PHYSREVA.103.L041102 (cit. on pp. 23, 91).

[77] Yu He et al. „Resonant Perfect Absorption Yielded by Zero-Area Pulses“. In: *Physical Review Letters* 129.27 (Dec. 2022), p. 273201. DOI: 10.1103/PHYSREVLETT.129.273201 (cit. on pp. 23, 91).

[78] Mette B. Gaarde, Christian Buth, Jennifer L. Tate and Kenneth J. Schafer. „Transient absorption and reshaping of ultrafast XUV light by laser-dressed helium“. In: *Physical Review A - Atomic, Molecular, and Optical Physics* 83.1 (Jan. 2011), p. 013419. DOI: 10.1103/PHYSREVA.83.013419 (cit. on pp. 23, 91).

[79] Kai Li, Marie Labeye, Phay J. Ho, Mette B. Gaarde and Linda Young. „Resonant propagation of x rays from the linear to the nonlinear regime“. In: *Physical Review A* 102.5 (Nov. 2020), p. 053113. DOI: 10.1103/PhysRevA.102.053113 (cit. on pp. 23, 91, 93, 111).

[80] Charu C. Aggarwal. *Neural Networks and Deep Learning*. Springer International Publishing, 2023, pp. 1–529. DOI: 10.1007/978-3-031-29642-0 (cit. on pp. 24, 25, 27, 29, 30).

[81] Daniel Durstewitz. *Advanced Data Analysis in Neuroscience*. Springer International Publishing, 2017. DOI: 10.1007/978-3-319-59976-2 (cit. on pp. 24, 25, 27).

[82] Diederik P. Kingma and Jimmy Ba. *Adam: A Method for Stochastic Optimization*. 2017. arXiv: 1412.6980 [cs.LG] (cit. on p. 30).

[83] Ingolf V. Hertel and Claus-Peter Schulz. *Atoms, Molecules and Optical Physics 2*. Springer Berlin, Heidelberg, 2015. DOI: 10.1007/978-3-642-54313-5 (cit. on pp. 32, 36).

[84] Peter W. Atkins and Ronald S. Friedman. *Molecular quantum mechanics*. Oxford university press, 2011 (cit. on pp. 33, 35, 36).

[85] Paul H. Krupenie. „The Spectrum of Molecular Oxygen“. In: *Journal of Physical and Chemical Reference Data* 1.2 (Apr. 1972), pp. 423–534. DOI: 10.1063/1.3253101 (cit. on pp. 34, 101).

[86] Nelson H. F. Beebe, Erik W. Thulstrup and Andreas Andersen. „Configuration interaction calculations of low-lying electronic states of O_2, O_2^+, and O_2^{2+}“. In: *The Journal of Chemical Physics* 64.5 (Mar. 1976), pp. 2080–2093. DOI: 10.1063/1.432433 (cit. on pp. 34, 36, 101).

[87] Sonia Marggi Poullain, Markus Klinker, Jesús González-Vázquez and Fernando Martín. „Resonant photoionization of O_2 up to the fourth ionization threshold“. In: *Physical Chemistry Chemical Physics* 21.30 (July 2019), pp. 16497–16504. DOI: 10.1039/C9CP02150G (cit. on pp. 36, 37, 101).

[88] A Ehresmann et al. „De-excitation dynamics of Rydberg states in O_2: II. Vibrational and rotational structure of $2\sigma_u^{-1}(c\ ^4\Sigma_u^-)(ns/nd)\sigma_g\ ^3\Sigma_u^-(v = 0, 1)$ states“. In: *Journal of Physics B: Atomic, Molecular and Optical Physics* 37 (2004), pp. 4405–4422. DOI: 10.1088/0953-4075/37/22/002 (cit. on pp. 36–38, 101).

[89] Chen Ting Liao et al. „Probing autoionizing states of molecular oxygen with XUV transient absorption: Electronic-symmetry-dependent line shapes and laser-induced modifications“. In: *Physical Review A* 95.4 (Apr. 2017), p. 043427. DOI: 10.1103/PhysRevA.95.043427 (cit. on pp. 36, 38, 101, 107).

[90] Andreas Fischer. „Dissociative Photoionization of Molecular Hydrogen“. Doctoral Thesis. 2015. DOI: 10.11588/heidok.00018016 (cit. on p. 36).

[91] P. Baltzer, B. Wannberg, L. Karlsson, M. Carlsson Göthe and M. Larsson. „High-resolution inner-valence uv photoelectron spectra of the O_2 molecule and configuration-interaction calculations of $^2\Pi_u$ states betwwen 20 and 26 eV“. In: *Physical Review A* 45.7 (Apr. 1992), pp. 4374–4384. DOI: 10.1103/PhysRevA.45.4374 (cit. on pp. 36, 98, 101).

[92] M. Richard-Viard et al. „O_2^+ ions dissociation studied by threshold photoelectron–photoion coincidence method“. In: *The Journal of Chemical Physics* 82.9 (May 1985), pp. 4054–4063. DOI: 10.1063/1.448846 (cit. on pp. 37, 38, 98, 101–104, 106).

[93] M. Richard-Viard et al. „O_+^2 ions dissociation studied by threshold photoelectron–photoion coincidence method“. In: *The Journal of Chemical Physics* 82.9 (June 1998), pp. 4054–4063. DOI: 10.1063/1.448846 (cit. on pp. 37, 38, 101).

[94] M. Richard-Viard, O. Dutuit, M. Ait-Kaci and P. M. Guyon. „Isotope effect in the predissociation of the c $^4\Sigma_u^-$ state of O_2^+“. In: *Journal of Physics B: Atomic and Molecular Physics* 20.10 (May 1987), p. 2247. DOI: 10.1088/0022-3700/20/10/017 (cit. on pp. 37, 38, 98, 101).

[95] M. Magrakvelidze et al. „Tracing nuclear-wave-packet dynamics in singly and doubly charged states of N_2 and O_2 with XUV-pump-XUV-probe experiments“. In: *Physical Review A - Atomic, Molecular, and Optical Physics* 86.1 (July 2012), p. 013415. DOI: 10.1103/PhysRevA.86.013415 (cit. on pp. 38, 101).

[96] Daniil A. Andrienko and Iain D. Boyd. „Vibrational relaxation and dissociation of oxygen in molecule-atom collisions“. In: *45th AIAA Thermophysics Conference* (2015), pp. 1–19. DOI: 10.2514/6.2015-3251 (cit. on p. 38).

[97] T. Lang et al. „Versatile OPCPA Pump-Probe Laser System for the FLASH2 XUV FEL beamline at DESY“. In: OSA Technical Digest (Optica Publishing Group, 2019) (cit. on pp. 40, 41).

[98] Elisa Appi et al. „A synchronized VUV light source based on high-order harmonic generation at FLASH“. In: *Scientific Reports* 10.1 (Apr. 2020), p. 6867. DOI: 10.1038/s41598-020-63019-2 (cit. on pp. 40, 41).

[99] E. Appi et al. „Synchronized beamline at FLASH2 based on high-order harmonic generation for two-color dynamics studies“. In: *Review of Scientific Instruments* 92.12 (Dec. 2021), p. 123004. DOI: 10.1063/5.0063225 (cit. on pp. 40–42).

[100] Georg Schmid et al. „Reaction microscope endstation at FLASH2“. In: *Journal of Synchrotron Radiation* 26.3 (May 2019), pp. 854–867. DOI: 10.1107/S1600577519002236 (cit. on pp. 40, 41, 104).

[101] Michael Straub. „Multiphoton Ionization of Helium with Extreme Ultraviolet Light at the Free-Electron Laser in Hamburg“. Master Thesis. 2021 (cit. on pp. 40, 42).

[102] R. Dörner et al. „Cold Target Recoil Ion Momentum Spectroscopy: A ‘momentum microscope’ to view atomic collision dynamics“. In: *Physics Reports* 330 (2-3 June 2000), pp. 95–192. DOI: 10.1016/S0370-1573(99)00109-X (cit. on p. 41).

[103] S. L. Sorensen et al. „Argon 3s autoionization resonances“. In: *Phys. Rev. A* 50.2 (Aug. 1994), pp. 1218–1230. DOI: 10.1103/PhysRevA.50.1218 (cit. on pp. 43, 44).

[104] A. Mozzanica et al. „The GOTTHARD charge integrating readout detector: design and characterization“. In: *Journal of Instrumentation* 7.01 (Jan. 2012), p. C01019. DOI: 10.1088/1748-0221/7/01/C01019 (cit. on p. 44).

[105] Constantine E. Theodosiou. „Lifetimes of singly excited states in He I“. In: *Phys. Rev. A* 30.6 (Dec. 1984), pp. 2910–2921. DOI: 10.1103/PhysRevA.30.2910 (cit. on pp. 44, 90).

[106] Lennart Aufleger. „Nonlinear spectroscopy on an autoionizing two-electron resonance in intense, extreme ultraviolet fields at a free-electron laser“. Doctoral Thesis. 2022. DOI: 10.11588/heidok.00031209 (cit. on p. 45).

[107] Kai Li. „Nonlinear X-Ray Propagation Phenomena in Dense Gases“. Doctoral Thesis. 2023 (cit. on pp. 46, 49, 86, 91, 92).

[108] Paul Kirkpatrick and A. V. Baez. „Formation of Optical Images by X-Rays“. In: *J. Opt. Soc. Am.* 38.9 (Sept. 1948), pp. 766–774. DOI: 10.1364/JOSA.38.000766 (cit. on p. 48).

[109] John H. Moore, Christopher C. Davis, Michael A. Coplan and Sandra C. Greer. *Building Scientific Apparatus*. Cambridge University Press, 2009. DOI: 10.1017/CBO9780511609794 (cit. on pp. 48, 49).

[110] Leon Lindenberger. „Towards Ultra-Fast X-Ray Transient Absorption Spectroscopy in High Density Neon Gas: Gas Flow Model for Experimental Setup and Numerical Predictions“. Bachelor Thesis. 2021 (cit. on pp. 48, 49).

[111] J. Nordgren et al. „Soft x-ray emission spectroscopy using monochromatized synchrotron radiation“. In: *Review of Scientific Instruments* 60.7 (July 1989), pp. 1690–1696. DOI: 10.1063/1.1140929 (cit. on p. 49).

[112] Alexander Magunia. „Elektronen-Korrelation in Helium unter Einfluss intensiver XUV-Felder“. Bachelor Thesis. 2016 (cit. on p. 51).

[113] Alexander Magunia. „Doubly-Excited Helium Strongly Driven with Short and Long Wavelength Pulses“. Master Thesis. 2018 (cit. on p. 51).

[114] M. Wollenhaupt, A. Präkelt, C. Sarpe-Tudoran, D. Liese and T. Baumert. „Quantum control by selective population of dressed states using intense chirped femtosecond laser pulses“. In: *Applied Physics B: Lasers and Optics* 82 (2 SPEC. ISS. Feb. 2006), pp. 183–188. DOI: 10.1007/S00340-005-2066-0 (cit. on p. 87).

[115] Matthias Wollenhaupt, Tim Bayer, Nikolay V. Vitanov and Thomas Baumert. „Three-state selective population of dressed states via generalized spectral phase-step modulation“. In: *Phys. Rev. A* 81.5 (May 2010), p. 053422. DOI: 10.1103/PhysRevA.81.053422 (cit. on p. 87).

[116] Tim Bayer, Matthias Wollenhaupt and Thomas Baumert. „Strong-field control landscapes of coherent electronic excitation“. In: *Journal of Physics B: Atomic, Molecular and Optical Physics* 41.7 (Mar. 2008), p. 074007. DOI: 10.1088/0953-4075/41/7/074007 (cit. on p. 87).

[117] Matthias Wollenhaupt and Thomas Baumert. „Ultrafast laser control of electron dynamics in atoms, molecules and solids“. In: *Faraday Discuss.* 153 (2011), pp. 9–26. DOI: 10.1039/C1FD00109D (cit. on p. 87).

[118] Tim Bayer et al. „Charge Oscillation Controlled Molecular Excitation“. In: *Phys. Rev. Lett.* 110.12 (Mar. 2013), p. 123003. DOI: 10.1103/PhysRevLett.110.123003 (cit. on pp. 87, 97).

[119] Edvin Olofsson and Jan Marcus Dahlström. „Photoelectron signature of dressed-atom stabilization in an intense XUV field“. In: *Phys. Rev. Res.* 5.4 (Oct. 2023), p. 043017. DOI: 10.1103/PhysRevResearch.5.043017 (cit. on p. 87).

[120] K. P. Heeg et al. „Spectral narrowing of x-ray pulses for precision spectroscopy with nuclear resonances“. In: *Science* 357.6349 (July 2017), pp. 375–378. DOI: 10.1126/science.aan3512 (cit. on pp. 89, 91).

[121] Jinyue Gao et al. „Observation of light amplification without population inversion in sodium“. In: *Optics Communications* 93.5 (Oct. 1992), pp. 323–327. DOI: 10.1016/0030-4018(92)90193-U (cit. on p. 89).

[122] G. Grynberg, M. Pinard and P. Mandel. „Amplification without population inversion in a V three-level system: A physical interpretation“. In: *Physical Review A* 54.1 (July 1996), pp. 776–785. DOI: 10.1103/PhysRevA.54.776 (cit. on p. 89).

[123] W. E. Van Der Veer, R. J.J. Van Diest, A. Dönszelmann and H. B. Van Linden Van Den Heuvell. „Experimental demonstration of light amplification without population inversion“. In: *Physical Review Letters* 70.21 (May 1993), pp. 3243–3246. DOI: 10.1103/PhysRevLett.70.3243 (cit. on p. 89).

[124] A. S. Zibrov et al. „Experimental Demonstration of Laser Oscillation without Population Inversion via Quantum Interference in Rb“. In: *Physical Review Letters* 75.8 (Aug. 1995), pp. 1499–1502. DOI: 10.1103/PhysRevLett.75.1499 (cit. on p. 89).

[125] P. Y. Wen et al. „Reflective Amplification without Population Inversion from a Strongly Driven Superconducting Qubit“. In: *Physical Review Letters* 120.6 (Feb. 2018), p. 063603. DOI: 10.1103/PhysRevLett.120.063603 (cit. on p. 89).

[126] O. A. Kocharovskaia and Ia. I. Khanin. „Coherent amplification of an ultrashort pulse in a three-level medium without population inversion“. In: *PZETF* 48 (1988), pp. 581–584 (cit. on p. 89).

[127] Olga Kocharovskaya and Paul Mandel. „Amplification without inversion: The double-Λ scheme“. In: *Physical Review A* 42.1 (July 1990), pp. 523–535. DOI: 10.1103/PhysRevA.42.523 (cit. on p. 89).

[128] Olga Kocharovskaya. „Amplification and lasing without inversion“. In: *Physics Reports* 219 (3-6 Oct. 1992), pp. 175–190. DOI: 10.1016/0370-1573(92)90135-M (cit. on p. 89).

[129] A. Lyras, X. Tang, P. Lambropoulos and Jian Zhang. „Radiation amplification through autoionizing resonances without population inversion“. In: *Physical Review A* 40.7 (Oct. 1989), pp. 4131–4134. DOI: 10.1103/PhysRevA.40.4131 (cit. on p. 89).

[130] V. G. Arkhipkin and Yu I. Heller. „Radiation amplification without population inversion at transitions to autoionizing states“. In: *Physics Letters A* 98 (1-2 Oct. 1983), pp. 12–14. DOI: 10.1016/0375-9601(83)90533-9 (cit. on p. 89).

[131] Jan-Erik Rubensson. „RIXS dynamics for beginners“. In: *Journal of Electron Spectroscopy and Related Phenomena* 110-111 (2000), pp. 135–151. DOI: 10.1016/S0368-2048(00)00161-4 (cit. on p. 91).

[132] J. Itatani et al. „Attosecond Streak Camera“. In: *Phys. Rev. Lett.* 88.17 (Apr. 2002), p. 173903. DOI: 10.1103/PhysRevLett.88.173903 (cit. on p. 93).

[133] Siqi Li et al. „Characterizing isolated attosecond pulses with angular streaking“. In: *Opt. Express* 26.4 (Feb. 2018), pp. 4531–4547. DOI: 10.1364/OE.26.004531 (cit. on p. 93).

[134] Saikat Nandi et al. „Generation of entanglement using a short-wavelength seeded free-electron laser“. In: *Science Advances* 10.16 (2024), eado0668. DOI: 10.1126/sciadv.ado0668 (cit. on pp. 93, 97).

[135] Oliver G. Alexander, Jon P. Marangos, Marco Ruberti and Morgane Vacher. „Chapter Three - Attosecond electron dynamics in molecular systems“. In: *Advances in Atomic, Molecular, and Optical Physics*. Ed. by Louis F. DiMauro, Hélène Perrin and Susanne F. Yelin. Vol. 72. Advances In Atomic, Molecular, and Optical Physics. Academic Press, 2023, pp. 183–251. DOI: 10.1016/bs.aamop.2023.05.001 (cit. on p. 94).

[136] Jordan T. O'Neal et al. „Electronic Population Transfer via Impulsive Stimulated X-Ray Raman Scattering with Attosecond Soft-X-Ray Pulses“. In: *Phys. Rev. Lett.* 125.7 (Aug. 2020), p. 073203. DOI: 10.1103/PhysRevLett.125.073203 (cit. on pp. 97, 107, 111).

[137] L.S. Cederbaum and J. Zobeley. „Ultrafast charge migration by electron correlation“. In: *Chemical Physics Letters* 307.3 (1999), pp. 205–210. DOI: https://doi.org/10.1016/S0009-2614(99)00508-4 (cit. on p. 97).

[138] Yen-Cheng Lin et al. „Coupled nuclear-electronic decay dynamics of O_2 inner valence excited states revealed by attosecond XUV wave-mixing spectroscopy“. In: *Faraday Discussions* (2020). DOI: 10.1039/d0fd00113a (cit. on pp. 98, 101, 106, 107).

[139] Henry Timmers, Niranjan Shivaram and Arvinder Sandhu. „Ultrafast dynamics of neutral superexcited oxygen: A direct measurement of the competition between autoionization and predissociation“. In: *Physical Review Letters* 109.17 (Oct. 2012), p. 173001. DOI: 10.1103/PhysRevLett.109.173001 (cit. on pp. 98, 101, 106, 107).

[140] M. Evans, S. Stimson, C. Y. Ng and C. W. Hsu. „High-resolution pulsed field ionization photoelectron study of O_2: Predissociation lifetimes and high-n Rydberg lifetimes converging to $O_2^+(c\ ^4\Sigma_u^-, v^+=0,1)$“. In: *The Journal of Chemical Physics* 109.4 (July 1998), p. 1285. DOI: 10.1063/1.476678 (cit. on p. 101).

[141] Y Hikosaka et al. „Competition between autoionization and dissociation in the $[O_2^+(B\ ^2\Sigma_g^-)]$nl and $[O_2^+(c\ ^4\Sigma_u^-)]$nl Rydberg states investigated by photon-induced dissociation to neutral fragments“. In: *J. Phys. B: At. Mol. Opt. Phys.* 36 (2003), p. 4311. DOI: 10.1088/0953-4075/36/21/010 (cit. on p. 101).

[142] H. Liebel et al. „De-excitation dynamics of Rydberg states in O_2: I. Total cross sections for O I fluorescence emission following predissociation of $2\sigma_u^{-1}(c\ ^4\Sigma_u^-)n\sigma_g\ ^3\Sigma_u^-$ states“. In: *Journal of Physics B: Atomic, Molecular and Optical Physics* 35.4 (Feb. 2002), p. 895. DOI: 10.1088/0953-4075/35/4/313 (cit. on p. 101).

[143] Ph V. Demekhin et al. „Investigation of photoionization and photodissociation of an oxygen molecule by the method of coupled differential equations“. In: *Optics and Spectroscopy* 102.3 (Mar. 2007), pp. 318–329. DOI: 10.1134/S0030400X07030022 (cit. on p. 101).

[144] K Codling, L J Frasinski and K J Randall. „Competition between autoionisation and predissociation in the Rydberg series approaching the $c\ ^4\Sigma_u^-$ state of O_2^+“. In: *Journal of Physics B: Atomic and Molecular Physics* 18.9 (May 1985), p. L251. DOI: 10.1088/0022-3700/18/9/003 (cit. on p. 101).

[145] Atia-tul-noor et al. „Sub-50 fs temporal resolution in an FEL-optical laser pump-probe experiment at FLASH2“. In: *Opt. Express* 32.4 (Feb. 2024), pp. 6597–6608. DOI: 10.1364/OE.513714 (cit. on p. 101).

[146] Miles Mountney et al. *Formation of two singly-ionized Oxygen atoms during the breakup of O_2 driven by an XUV pulse*. 2024. arXiv: 2403.20098 [physics.atom-ph] (cit. on pp. 106, 112).

[147] Xinyao Liu et al. „Machine learning for laser-induced electron diffraction imaging of molecular structures“. In: *Communications Chemistry* 4.1 (Nov. 2021), pp. 1–7. DOI: 10.1038/s42004-021-00594-z (cit. on p. 107).

B. Acknowledgment

This doctoral thesis was facilitated by a great deal through other people. In fact, the list of people is likely to be too long for mentioning all of them without forgetting anyone. Therefore, I would rather make two general acknowledgments, hoping all individuals who I owe my dept of gratitude can recognize themselves in these statements.

From a professional perspective, working with scientific and non-scientific colleagues was essential for this thesis. From building setups to writing code, running experiments, evaluating data, discussing results and writing publications as well as, eventually, this thesis, has been a necessity and a pleasure likewise. I appreciate the fun times, the achievements and failures, the coffees drunk together, as well as the shared sorrows and troubles. Furthermore, the exchange with a broad international community of scientific experts and enthusiasts was essential for shaping my interest for, understanding of, and love-hate-relationship with all those quantum particles. Participating in international conferences and collaborations made feel like being a real scientist. Research seems to be a human business after all.

On a personal level, the last nearly five years have been quite a trip. The underlying psychological and emotional dynamics of this time are hard to describe, reconstruct or evaluate—even with the best of neural networks, our own **schmunzel**. It was a time of extensive personal growth, and even more than on the professional level, I am grateful to all the people participating in the trip. This goes especially to family and friends, to which many of the above mentioned colleagues can be counted as well. But also to all the smaller and shorter encounters in everyday life, unexpected connections, perspectives and teachings arising from them—contributing in the long run. Whoever made it to this point of the thesis, please feel free to reach out and ask how a coffee on the other side of the planet or learning dance moves keeps a quantum physicist sane.

To all of you shaping this time and these memories,

Thank you. All of you.